



The University of
Nottingham

School of Electrical and Electronic Engineering

**Characterisation, Emulation and
By-Emitter Degradation Analysis of
High Power Semiconductor Laser Diodes**

by

Christian Kwaku AMUZUVI

BSc, MSc

GEORGE GREEN LIBRARY OF
SCIENCE AND ENGINEERING

Thesis submitted to the University of Nottingham for
the degree of Doctor of Philosophy

September 2010

Contents

Acknowledgement	vii
List of Common Symbols and Abbreviations.....	ix
List of Figures.....	xi
List of Tables	xix
Abstract.....	xx
 Chapter 1	 1
Introduction.....	1
References	9
 Chapter 2	 14
Semiconductor Laser Principles, Technology and Applications.....	14
2.1 Optical Processes in Semiconductors	15
2.1.1 Band-to-band optical transition	20
2.1.2 Absorption, spontaneous and stimulated emissions.....	22
2.1.3 Probability of emission and absorption phenomena	23
2.1.4 Population inversion	26
2.2 The Idea of the Laser	27
2.3 Semiconductor Lasers	30
2.3.1 Principle of semiconductor laser operation.....	30
2.3.2 The threshold condition in lasers	32
2.3.3 Lasing wavelength and longitudinal modes.....	35
2.4 Properties of Laser Beams	37
2.4.1 Beam Quality	38
2.4.1.1 Astigmatism	39
2.4.1.2 Brightness.....	41
2.4.1.3 M^2 factor.....	42
2.5 Introduction to High Power Laser Diodes	43
2.5.1 The nature of semiconductor lasers	43

2.5.2	Structure of semiconductor lasers	44
2.5.3	Homostructure and Heterostructure Lasers.....	45
2.5.4	Broad waveguide lasers	47
2.5.5	Broad area lasers	48
2.5.6	Tapered lasers	50
2.5.7	Quantum well (QW) lasers	51
2.5.7.1	<i>QW structures</i>	51
2.5.7.2	<i>Strained QW lasers</i>	53
2.5.7.3	<i>Absorption and emission in QWs</i>	54
2.6	Typical Laser Diode Structures – Arrays and Stacks	55
2.6.1	A typical 1 cm bar laser structure	56
2.7	Mounting Technology and Heatsinks	58
2.8	Applications of High Power Laser Diodes	59
	References	61

Chapter 3 67

Degradation of High Power Laser Diodes and the Description of the Emulation Tool..... 67

3.1	Degradation of High Power Laser Diode.....	68
3.1.1	Classification of degradation modes	68
3.2	Degradation Mechanisms.....	73
3.3	Spatial Location of the Degradation	75
3.3.1	Internal degradation	75
3.3.2	External degradation	76
3.3.3	Suppression and elimination of facet degradation	77
3.4	Degradation of Single Emitters/Bars	79
3.5	Reliability of Lasers Degradation of Single Emitters/Bars.....	81
3.6	Semiconductor Laser Emulation Tool	83
3.6.1	Device Structure	84
3.6.2	Effective index approximation	84
3.6.3	Complex refractive index perturbation	85
3.6.4	Numerical solution procedure.....	85

3.6.5 Output Characteristics.....	88
3.6.6 Light-current characteristic.....	88
3.6.7 Model Validation.....	89
3.6.8 Summary.....	90
References.....	91

Chapter 4 97

Experimental Techniques and the Presentation and Analysis of Experimental Results..... 97

4.1 Experimental Techniques.....	100
4.1.1 Photo- and electroluminescence imaging measurements.....	100
4.1.2 Near-field Observations.....	102
4.1.3.1 <i>How a laser bar is mounted on the motion control unit</i>	103
4.1.3.2 <i>Power-current characteristics of emitters within a laser bar</i>	105
4.2 Devices Examined, Why Studied, and Techniques Used.....	106
4.2.1 Technologies used to study the laser degradations.....	108
4.3 Study 1.....	109
4.3.1 Observations using optical microscopy (650 nm bars).....	109
4.3.2 Presentation of experimental results.....	111
4.3.3 Analysis of experimental results (650 nm bars).....	114
4.4 Study 2.....	115
4.4.1 Observations using optical microscopy.....	115
4.4.2 Presentation of experimental results (975 nm bars).....	117
4.4.2.1 <i>Results for bar 16022</i>	118
4.4.2.2 <i>Results for bar 16023</i>	120
4.4.2.3 <i>Results for bar 16024</i>	122
4.4.2.4 <i>Results for bar 16025</i>	125
4.4.3 Global trends observed in the bars (975 nm bars).....	128
4.5 Analysis of Experimental Results.....	133
4.5.1 Bar 16022.....	133
4.5.2 Bar 16023.....	137
4.5.3 Bar 16024.....	140

4.5.4	Bar 16025	142
4.6	Conclusion of Experimental By-emitter Degradation Studies of these Bars	144
	References	146
Chapter 5		149
By-Emitter Degradation Analysis of High Power Laser Diodes Using the Emulation Tool		149
5.1	LabVIEW Control Interface.....	150
5.1.1	The <i>Barlase</i> control interface.....	150
5.1.2	The laser bar model.....	151
5.2	Overview of the Operation of the LabVIEW Control Interface	152
5.3	Testing of the <i>Barlase</i> Control Interface.....	155
5.3.1	Investigation of some factors affecting laser degradation processes	158
5.3.1.1	<i>Effect of introducing defects through nonradiative recombination centres</i>	158
5.3.1.2	<i>Effect of increased heatsink temperature</i>	162
5.3.1.3	<i>Effect of packaging-induced strain</i>	165
5.3.2	Summary of single emitter simulation scenarios	168
5.3.3	Multi-emitter simulations.....	169
5.3.3.1	<i>Scenario 1: Random low-level of defects distributed across the bar ...</i>	170
5.3.3.2	<i>Scenario 2: Damaged single emitter randomly located in the bar</i>	174
5.3.3.3	<i>Scenario 3: Curved temperature (frown) profile with the maximum temperature at the centre of the bar.....</i>	178
5.3.4	Summary of multiple emitter simulation scenarios	183
5.3.5	General summary and outlook	183
	References	185

Chapter 6	186
Modification of the Emulation Tool for Improved By-Emitter Degradation Analysis.....	186
6.1 Aging Models.....	187
6.2 Spectral Laser Model Enhancement	188
6.2.1 Spatially variable trap density distribution	188
6.2.2 Case study 1 (single emitter) – uniform QW trap density	190
6.2.3 Case study 2 (single emitter) – local QW trap density	191
6.2.4 Case study 3 (multiple emitters i.e. bars) – uniform QW trap density	194
6.2.5 Case study 4 (multiple emitters i.e. bars) – local QW trap density.....	196
6.3 Conclusion	199
References	200
Chapter 7	201
Emulation of the Degradation of a Calibrated 975 nm High Power Tapered Laser Bars	201
7.1 Structure of the Device Being Studied: 975 nm Tapered Bars Fabricated by Alcatel-Thales III-V Lab.....	202
7.1.1 Calibration of the laser	203
7.2 Emulation of the Degradation of a Calibrated Single Emitter	204
7.3 Multiple Emitter Degradation Emulation of the Calibrated Bar.....	206
7.4 By-Emitter Emulation of Real Bars (975 nm Laser Bars with 16 Tapered Emitters).....	209
7.5 Presentation and Analysis of Simulation Results at Time 0	210
7.5.1 Emulation results (unaged) of bar 16022 (bar physically damaged at two ends)	210
7.5.2 Emulation results (unaged) of bar 16024	218
7.6 The Enhancement of the Emulation Tool Using A Global Thermal Solver..	222
7.6.1 Bar emulation enhancement using a global thermal solver	222
7.6.2 Analysis and observations made	225

7.7	Summary	227
	References	228
	Chapter 8	230
	Conclusions and Further Study.....	230
	References	237
	Appendix	238
	List of Publications	238

Acknowledgement

Everything that has a beginning has an end and nothing that is achieved is achieved in isolation and hence my indebtedness to the following, who made contributions either great or small in making this piece of work a reality. First of all I must say, unto the Lord, be the glory great things he has done and greater things he will do. I say 'ayekoo' to my beloved and helpful wife Enyo, who joined me on this journey and who has been there throughout the way, for her support, encouragement and love. I am grateful to all my sibling Francisca, Florence and Emily, family members and friends back in Ghana who took care of business on my behalf while away and who prayed for me throughout my stay in the United Kingdom in pursuance of the degree of PhD.

I am indebted to my first supervisor Professor E.C. Larkins, for believing in me and accepting me into his group to pursue this programme. I thank my second supervisor Dr S. Sujecki who complemented the effort of my first supervisor to bring this work into fruition. I must say your invaluable contributions and support has broadened my scope in life and lifted that can do attitude in me which I will never depart from. I would also want to thank Dr A. Kalashnikov for stepping in to help get my recommendation letter sorted out from my former University in the Ukraine (National Technical University in Kharkov) prior to my admission into my programme. I say thank you because you played your part.

The broad scope of this thesis makes it impossible for one person to take credit for, and therefore, I would like to show my appreciation to these three persons who contributed immensely for this work to see the light of the day. These three persons are: Dr Stephen Bull, Dr Jun Jun Lim and Mr Rod Dykeman. Dr Bull, who is a mentor and friend introduced me to the characterization aspect of my work, to the Optical Measurement and Evaluation Systems (OMES) laboratory and taught me how to use the equipment and software of the OMES facility. He was always at hand to facilitate anything I needed to progress in my work. He helped me a great deal in the learning of the Labview program which I used as a control interface to communicate with *Speclase*. Dr Lim being the brain behind the software *Speclase*, played a fundamental role in this piece of work. The running of thousands of simulations, and the plotting of same, ends up on his table for a discussion on how to better improve the results achieved. His calmness in the midst of difficulty is just unparalleled. I cannot also relegate to the background, the contribution and support from Mr Dykeman during my short spell in the Clean Room (yellow room) learning about some fabrication techniques. He told me Christian; you need to work and clean-up at the same time to save time and energy. I think that advice pertains to almost everything because procrastination is a thief of time.

I also wish to thank our partners who provided the devices used in my characterisation work. The 650 nm red-emitting BA lasers were fabricated by Ferdinand-Braun-Institut für Höchstfrequenztechnik and the 980 nm infrared tapered lasers fabricated by Alcatel-Thales III-V Lab. I also thank them for their initial positive comments about this work.

I gratefully acknowledge the financial support offered me by the Ghana Education Trust Fund (GETFund) that funded my PhD and made my stay in the United Kingdom possible and to the staff at the Ghana High Commission. My thanks also go to the University of

Mines and Technology, Tarkwa, for nominating me for this award and especially to the Vice Chancellor Professor Daniel Mireku-Gyimah for yielding to my perseverance through my hard work all to the cause of the University. I am very grateful to you for giving me the opportunity to represent the University on this stage. I say a big thank you also to my department, faculty and UTAG members and the entire University Community for your support and prayers. Mr Andy Lumor in London, coordinator of the overseas office of Universities in Ghana, I say thank you.

I would like to recognize my mates for their support and love; Dr Rod MacKenzie, Dr V.K. Sundaramoorthy, Dr M.P. Dlubek, Dr Havey Padda, Dr Sheng Chao, Dr Weisheng Lu, Dr Zhichao Zhang, Dr S. Kaunga-Nyirenda, Mr Lei Lang, Mr TianJian Zuo, Mr Abisayo Aladeloba, Mr Hasula Dias, Mr Suhaila Isaak, Mrs Suejit Pechprasarn, Leah Ridgway and Priyanka Desai. My special thanks also go to Mr Everton Blake and Rebecca Dowsette.

The Radford Methodist Church provided me with the spiritual upliftment that my family and I needed, and we are so grateful to Rev Sandy Osgerby and her husband, Mrs Lucille Allen, Mr Alan Clark, Mr Gary Robbins, Mr Gary Brown, and the entire membership of the church.

I wish to also show my gratitude to the following for their immense support and great friendship; Mr Jojo Kwetey and wife, Hon. Fiifi Kwetey and wife, Aseye and family, Mr J.P.L Darabor, Dr Ekwow Spio-Garbrah, Mr Kwesi Fletcher, Mr Anthony Akussah and wife, Mr Joe Amewornu and family, Mrs Patricia Mireku-Gyimah, Dr Grace Sarpomah Ofori-Sarpong, Mr A.K. Dakubo, Prof. Amankwah and family, Mr Jenkins Awumee and family, Mr & Mrs Prempeh, Mr & Mrs Daboni and family, Ms Dorcas Akyeampong, Ms Edith Amo-Mensah, Dr & Mrs Abruquah, Auntie Berkie, Frau Zimmerman, Ms Rita Aryee, Herr & Frau Michael Boateng, Mr & Mrs Dumenya, Mr & Mrs Wuddah, Artus & Grace, Kumi & Pamela, Uncle Joe & Kate, Dr Atsu Dordor and wife, Mr Emmanuel Buaba and family, Mr Simon Agbenu and family, Charles Appiah and wife, Deldar Singh (Danny), Mrs Bathia, the list is endless...so forgive me if you are left out.

Finally, I dedicate this thesis to the memory of my departed sister Gifty and parents, Daniel and Lucia, who I believe are smiling out there in appreciation to what has been achieved by their brother and son. I have really missed them especially on this occasion but God knows best. Thank you everybody and God Bless us All.

List of Common Symbols and Abbreviations

Symbols

α	Absorption Coefficient
γ_{12}	Absorption Rate
$\gamma_{21(spon)}$	Spontaneous Emission Rate
$\gamma_{21(stim)}$	Stimulated Emission Rate
η	Efficiency
λ	Wavelength
ν	Optical Frequency
τ	Exposure Time
Γ	Confinement Factor
A	Area
A_{12}	Spontaneous Emission Transition Probability
B_{12}	Absorption Transition Probability
B_{21}	Stimulated Emission Transition Probability
c	Velocity of Light in a Vacuum
f_1, f_2	Occupation Probabilities
F_n, F_p	Quasi-Fermi Levels
$g(E)$	Material Gain
$G(E)$	Optical Gain
h	Planck's Constant
I	Current
$I(x)$	Optical Intensity
M^2	Times-Diffraction-Limit Factor
n	Refractive Index
P	Power
q	Electronic Charge
r	Resistance
R_1, R_2	Reflection Coefficients
V	Voltage

Abbreviations

AR	Anti-Reflection
BA	Broad Area
BW	Broad Waveguide
CB	Conduction Band
CCD	Charge Coupled Device
COMD	Catastrophic Optical Mirror Damage
CMD	Catastrophic Mirror Damage
CW	Continuous Wave
DC	Direct Current
DFB	Distributed Feedback
DH	Double Heterostructure
DLD	Dark Line Defect
DSD	Dark Spot Defect
EHP	Electron Hole Pair
EL	Electroluminescence
ELM	Electroluminescence Microscopy
ELS	Electroluminescence Spectrum

FFP	Far-Field Pattern
FFT	Fast Fourier Transform
FP	Fabry-Perot
GTS	Global Thermal Solver
GRIN	Graded Refractive Index
HPLD	High Power Laser Diode
HR	High-Reflection
IR	Infrared
LCFP	Liquid Crystal Fabry-Perot
ND	Neutral Density
NFP	Near-Field Pattern
NFS	Near-Field Spectra
OMES	Optical Materials Evaluation System
PC	Photocurrent
PCS	Photocurrent Spectroscopy
PL	Photoluminescence
PLM	Photoluminescence Microscopy
QW	Quantum Well
REDR	Recombination Enhanced Defect Reaction
RW	Ridge Waveguide
SCH	Separate Confinement Heterostructure
S-ELM	Spectroscopically Resolved ELM
S-PLM	Spectroscopically Resolved PLM
SNR	Signal to Noise Ratio
VB	Valence Band



List of Figures

Fig. 2.1 Optical transition in a direct-gap semiconductor [10] p. 822.	21
Fig. 2.2 Schematic illustration of radiation and absorption processes: (a) absorption, (b) spontaneous emission, and (c) stimulated emission.	22
Fig. 2.3 Energy levels with population N_1 , N_2 and degeneracies g_1 , g_2 respectively.	25
Fig. 2.4 An elemental change dF , in the photon flux density F , for a plane electromagnetic wave travelling a distance dz , through a material [18] p 5.	27
Fig. 2.5 (a) An oscillator circuit and (b) a laser oscillator circuit.	29
Fig. 2.6 Fabry-Perot interferometer: (a) laser and (b) laser diode [6] p. 58.	29
Fig. 2.8 Schematic diagram illustrating a semiconductor laser diode and its associated FP interferometer. The cleaved facets act like partially reflecting mirrors.	33
Fig. 2.9 Light output of laser diode above and below the laser threshold current.	35
Fig. 2.10 The relationship between the gain spectra and longitudinal modes.	36
Fig. 2.11 Light intensity versus photon energy for laser diodes: (a) incoherent emission: below threshold; (b) laser modes: at threshold; and (c) dominant laser mode: above threshold.	36
Fig. 2.12 Properties of laser light.	37
Fig. 2.13 Schematic diagram showing the problem of astigmatism.	40
Fig. 2.14 Simple structure of semiconductor laser.	44
Fig. 2.15 Schematic illustration of (a) a homostructure and (b) a double-heterostructure laser. The vicinity of the homojunction is the depletion region. The shaded area shows the thin ($\sim 0.2 \mu\text{m}$) active layer of a semiconductor material, whose bandgap energy is slightly lower than that of the surrounding cladding layers [30] p. 2.	46
Fig. 2.16 Schematic illustration of the simultaneous confinement of the charge carriers and the optical mode to the active region occurring in a DH semiconductor laser [30] p. 3.	47
Fig. 2.17 Plan view schematic diagram of a tapered laser.	50
Fig. 2.18 Examples of typical QW active region structure.	53
Fig. 2.19 The energy levels in a single finite quantum well showing the confined energy levels of the electrons and holes.	55
Fig. 2.20 Schematic diagram of electrically and optically separated single emitters of a HPLD bar.	56
Fig. 2.21 A drawing showing a typical 1-cm-bar with a cavity length of 2 mm and a thickness of $100 \mu\text{m}$ [77] p. 218.	57
Fig. 2.22 Schematic diagram of a mounted laser bar [77] p. 218.	59

Fig. 3.1 Degradation modes at constant current and constant power of laser diodes. ...	69
Fig. 3.2 Flow chart of catastrophic optical damage process: (a) Henry et al., 1979 (b) Chen et al., 1993.	72
Fig. 3.3 Basic concept of point defect: (a) vacancy, (b) interstitial atom [3] p. 119.	75
Fig. 3.4 Schematic configuration of a laser mounted on a heatsink [3] p. 116.	77
Fig. 3.5 Schematic illustration of the COD mechanism [3] p. 135.	78
Fig. 3.6 Cross-section schematic of the laser structure. The x-origin is at the centre of the stripe of width w and the y-origin is at the centre of the active layer.	84
Fig. 4.1 Schematic diagram of the PLM/ELM setup.	102
Fig. 4.2 Schematic diagram of an experimental system for simultaneously measuring the NFP and NFS of individual emitters within a laser bar.	103
Fig. 4.3 Sample representation of (a) 650 nm red emitting and (b) 975 nm infrared emitting laser bars.	104
Fig. 4.4 Photographs of how the laser bar is mounted and connected to the motion control unit in the OMES Lab at the University of Nottingham.	105
Fig. 4.5 Typical P-I characteristic for a laser diode showing the threshold current (I_{th}) and the external differential efficiency (η_{ext}).	106
Fig. 4.6 12 magnified images taken before and after by-emitter measurements to ascertain the facet integrity of the bar (bar 05x1).	110
Fig. 4.7 Power against emitter number for the three 650 nm bars at $I_{BAR} = 8$ A at aging times of 0 hrs, 100 hrs and 700 hrs respectively. (a) Bar 05x1, (b) bar 0519, and (c) bar 0521.	112
Fig. 4.8 Graphs of emitter temperature versus emitter number after different aging times (courtesy of J. Tomm, Max-Born Institute).	113
Fig. 4.9 Graphs of strain-induced shift of substrate PL versus emitter number after different aging times (courtesy of J. Perraud and J. Nagle, Thales Research and Technology).	113
Fig. 4.10 Graphs of near infrared EL signal versus emitter number after different aging times (courtesy of J. Tomm, Max-Born Institute).	114
Fig. 4.11 22 magnified images taken before and after by-emitter measurements to ascertain the facet integrity of the bar (bar 16022).	116
Fig. 4.12 22 magnified images taken before and after by-emitter measurements at to ascertain the facet integrity of the bar (bar 16023).	117
Fig. 4.13 Emitter group power versus emitter number for various I_{BAR} currents (15 A, 20 A, and 25 A) after aging for (a) 0 hrs, (b) 100 hrs, and (c) 600 hrs.	118

Fig. 4.14 Graphs of (a) emitter temperature versus emitter group number, (b) emitter temperature versus emitter power at 25 A for 0 hrs (courtesy of J. Tomm, Max-Born Institute).	119
Fig. 4.15 Graphs of (a) bandedge measured by photocurrent in the QW versus emitter group number, (b) bandedge measured by photocurrent in the waveguide (WG) versus emitter group number (courtesy of J. Tomm, Max-Born Institute).	119
Fig. 4.16 Graphs of (a) near infrared EL signal versus emitter group number, (b) strain-induced shift of substrate PL versus emitter group number (courtesy of J. Tomm, Max-Born Institute and J. Perraud and J. Nagle, Thales Research and Technology).	120
Fig. 4.17 Emitter group power versus emitter number for various I_{BAR} currents (15 A, 20 A, and 25 A) after aging for (a) 0 hrs, (b) 100 hrs, and (c) 600 hrs.	121
Fig. 4.18 Graphs of (a) emitter temperature versus emitter group number, (b) emitter temperature versus emitter power at 25 A for 0 hrs (courtesy of J. Tomm, Max-Born Institute).	121
Fig. 4.19 Graphs of (a) bandedge measured by photocurrent in the QW versus emitter group number, (b) bandedge measured by photocurrent in the WG versus emitter group number (courtesy of J. Tomm, Max-Born Institute).	122
Fig. 4.20 Graphs of (a) near infrared EL signal versus emitter group number, (b) strain-induced shift of substrate PL versus emitter group number. (courtesy of J. Tomm, Max-Born Institute and J. Perraud and J. Nagle, Thales Research and Technology).	122
Fig. 4.21 Emitter group power versus emitter number for various I_{BAR} currents (15 A, 20 A, and 25 A) after aging for (a) 0 hrs, (b) 100 hrs, and (c) 600 hrs.	123
Fig. 4.22 Graphs of (a) temperature versus emitter group number, (b) temperature versus power at 25 A for 0 hrs (courtesy of J. Tomm, Max-Born Institute).	124
Fig. 4.23 Graphs of (a) bandedge measured by photocurrent in the QW versus emitter group number, (b) bandedge measured by photocurrent in the WG versus emitter group number (courtesy of J. Tomm, Max-Born Institute).	124
Fig. 4.24 Graphs of (a) near infrared EL signal versus emitter group number, (b) strain-induced shift of substrate PL versus emitter group number. (courtesy of J. Tomm, Max-Born Institute and J. Perraud and J. Nagle, Thales Research and Technology).	125
Fig. 4.25 Emitter group power versus emitter number for various I_{BAR} currents (15 A, 20 A, and 25 A) after aging for (a) 0 hrs, (b) 100 hrs, and (c) 600 hrs.	126
Fig. 4.26 Graphs of (a) temperature versus emitter group number, (b) temperature versus power at 25 A for 0 hrs (courtesy of J. Tomm, Max-Born Institute).	126

Fig. 4.27 Graphs of (a) bandedge measured by photocurrent in the QW versus emitter group number, (b) bandedge measured by photocurrent in the WG versus emitter group number (courtesy of J. Tomm, Max-Born Institute).	127
Fig. 4.28 Graphs of (a) near infrared EL signal versus emitter group number, (b) strain-induced shift of substrate PL versus emitter group number. (courtesy of J. Tomm, Max-Born Institute and J. Perraud and J. Nagle, Thales Research and Technology).	127
Fig. 4.29 Acoustic micrographs from bar IAF-16001: (a) In solder between bar and Cu microchannel heatsink (n-contact removed); (b) In solder between Au top ribbon and bar (courtesy of J. Perraud and J. Nagle, Thales Research and Technology).	133
Fig. 4.30 Images of weaker emitters within an emitter group observed by NF imaging.	135
Fig. 4.31 Emitter group emission intensity versus emitter number for various I_{BAR} currents (a) bar current of 6 A, (b) bar current of 8 A, and (c) bar current of 10 A.	135
Fig. 4.32 (a) Emission group emission intensity versus emitter number at various I_{BAR} currents (a) bar current of 4 and 5 A, (b) bar current of 6 A, 7 A and 8 A, and (c) bar current of 15 A, 20 A and 25 A.	136
Fig. 4.33 Emission intensity versus emitter number at $I_{BAR} = 5$ A and 25 A, respectively.	136
Fig. 4.34 Graphs of (a) lasing intensity, (b) temperature profile and (c) NIR defect EL intensity of the emitter groups (temperature and NIR EL data courtesy of J. Tomm, Max-Born Institute).	137
Fig. 4.35 (a) Typical image from bar 16023, (b) typical image from bar 16022.	138
Fig. 4.36 (a) Emitter group emission intensity versus emitter number for various I_{BAR} currents (a) bar current of 4 and 5 A, (b) bar current of 6 A, 7 A and 8 A, and (c) bar current of 15 A, 20 A and 25 A.	139
Fig. 4.37 (a) NF pattern and microscope image of emitter group number 13; (b) temperature and (c) NIR defect luminescence profiles (temperature and NIR EL data courtesy of J. Tomm, Max-Born Institute).	140
Fig. 4.38 (a) Emitter group emission intensity versus emitter number for various I_{BAR} currents (a) bar current of 4 and 5 A, (b) bar current of 6 A, 7 A and 8 A, and (c) bar current of 15 A, 20 A and 25 A.	141
Fig. 4.39 (a) NF pattern and microscopic image of emitter group number 5; (b) temperature and (c) NIR defect luminescence profiles. (Temperature and NIR EL data courtesy of J. Tomm, Max-Born Institute).	142

Fig. 4.40 Emitter group intensity versus emitter number for various I_{BAR} currents (a) bar current of 4 and 5 A, (b) bar current of 6 A, 7 A and 8 A, and (c) bar current of 15 A, 20 A and 25 A	143
Fig. 4.41 (a) Temperature and (b) NIR defect luminescence profiles. (Temperature and NIR EL data courtesy of J. Tomm, Max-Born Institute).	144
Fig. 5.1 Flow chart showing the communication between Speclase and Barlase.	150
Fig. 5.3 Front panel of the LabVIEW interface control program.	155
Fig. 5.4 A hypothetical standard 975 nm tapered laser structure.	156
Fig. 5.5 Power-current characteristics (a) and the maximum temperature in the QW (b) as a function of current for simulations with different QW trap densities.	159
Fig. 5.6 Power-voltage characteristics (a) and the maximum temperature in the QW as a function of voltage (b) for simulations with different QW trap densities.	160
Fig. 5.7 Current-voltage characteristics (a) and the maximum temperature in the QW as a function of voltage (b) for simulations with different QW trap densities.	160
Fig. 5.8 Dependence of threshold current (a) and slope efficiency (b) on the QW trap density.	161
Fig. 5.9 Percentage change in current (a) and output power (b) for simulations with different QW trap densities relative to the standard QW trap density of $2 \times 10^{15} \text{ cm}^{-3}$	161
Fig. 5.10 Power-current characteristics (left), the maximum temperature in the QW as a function of current (right).	162
Fig. 5.11 Graphs showing the dependence of threshold current (a) and efficiency (b) on heatsink temperature.	163
Fig. 5.12 (a) Current-voltage characteristics, (b) power-voltage characteristics, (c) and the maximum temperature in the QW versus voltage for simulations at different heatsink temperatures.	164
Fig. 5.13 Graphs showing the percentage change in current (left) and power (right) in simulations at different heatsink temperatures relative to the standard heatsink temperature of 300 K.	165
Fig. 5.14 Power-current characteristics (a) and the maximum temperature in the QW as a function of current (b) for simulations with different levels of packaging-induced strain.	166
Fig. 5.15 Power-voltage characteristics (a) and the maximum temperature in the QW as a function of voltage (b) for simulations with different levels of packaging-induced strain.	166

Fig. 5.16 Percentage change in current (a) and power (b) in simulations at different levels of packaging-induced strain relative to the standard case of no packaging-induced strain.	167
Fig. 5.17 QW trap densities (a) and table showing the values of QW trap densities assigned to each emitter in the bar (b).	170
Fig. 5.18 Power-current characteristics of the full bar (left) and of the individual emitters (right).	171
Fig. 5.19 Current-voltage characteristics of the full bar (left) and of the individual emitters (right).	172
Fig. 5.20 Variation of threshold current (apparent threshold current) (a) and slope efficiency (apparent slope efficiency) (b) of individual emitters.	172
Fig. 5.21 (a) Distribution of the emitter currents, (b) emitter powers and (c) maximum emitter QW temperatures across the bar at a total bar bias current of 2A.	173
Fig. 5.22 (a) Distribution of the emitter currents, (b) emitter powers and (c) maximum emitter QW temperatures across the bar at a total bar bias current of 10 A.	174
Fig. 5.24 (a) Bar power-current characteristics of the full bar, (b) emitter power-emitter current characteristics, (c) and emitter power-individual emitter voltage characteristics.	176
Fig. 5.25 Variation of the threshold current and apparent threshold current (a), and the slope efficiency and the apparent slope efficiency (b) of the individual emitters.	176
Fig. 5.26 (a) Distribution of the emitter currents, (b) the emitter powers and (c) the maximum emitter QW temperatures across the bar for a total bar bias current of 2 A.	177
Fig. 5.27 (a) Distribution of the emitter currents, (b) the emitter powers and (c) the maximum emitter QW temperatures across the bar for a total bar bias current of 10 A.	178
Fig. 5.28 Heatsink temperature profile (a) and table showing the values of heatsink temperatures assigned to each emitter in the bar (b).	179
Fig. 5.29 (a) Bar power-current characteristics of the full bar, (b) emitter power-emitter current characteristics, (c) and emitter power-individual emitter voltage characteristics.	180
Fig. 5.30 Graphs showing the variation of the threshold current and the apparent threshold current (a), and the slope efficiency and the apparent slope efficiency (b) of the individual emitters.	181

Fig. 5.31 (a) Graphs showing the distribution of the emitter currents, (b) the emitter powers and (c) the maximum emitter QW temperatures across the bar for a total bar bias current of 2 A.	182
Fig. 5.32 (a) Graphs showing the distribution of the emitter currents, (b) the emitter powers and (c) the maximum emitter QW temperatures across the bar for a total bar bias current of 10 A.	182
Fig. 6.1 3D plots of (a) uniform trap density (b) local trap density and (c) QW temperature profile.	189
Fig. 6.2 Graphs with uniform trap density for: (a) emitter power versus aging time and (b) % power loss with respect to the unaged emitter.	190
Fig. 6.3 Graphs with local trap density for: (a) emitter power versus aging time, (b) % power loss with respect to the unaged emitter.	191
Fig. 6.4 Graphs of: (a) threshold current versus aging time, (b) slope efficiency versus aging time, for a device with a local trap density.	192
Fig. 6.5 (a) Bar power loss at maximum $T_{\text{Heatsink}} = 315 \text{ K}$, (b) bar power loss at maximum $T_{\text{Heatsink}} = 330 \text{ K}$ and their equivalent temperature distributions.	195
Fig. 6.6 (a) Emitter power losses at maximum $T_{\text{Heatsink}} = 315 \text{ K}$, (b) emitter power losses at maximum $T_{\text{Heatsink}} = 330 \text{ K}$	195
Fig. 6.7 (a) Bar power loss at maximum $T_{\text{Heatsink}} = 330 \text{ K}$, (b) percentage bar power loss at maximum $T_{\text{Heatsink}} = 330 \text{ K}$	196
Fig. 6.8 (a) Bar threshold current, and (b) bar slope efficiency at maximum $T_{\text{Heatsink}} = 330 \text{ K}$	197
Fig. 6.9 (a) QW temperature profile at maximum $T_{\text{Heatsink}} = 330 \text{ K}$, (b) emitter current at maximum $T_{\text{Heatsink}} = 330 \text{ K}$	198
Fig. 6.10 (a) Emitter powers losses at maximum $T_{\text{Heatsink}} = 330 \text{ K}$, (b) percentage emitter power at maximum $T_{\text{Heatsink}} = 330 \text{ K}$	198
Fig. 6.11 (a) Emitter threshold current and (b) emitter slope efficiency at maximum $T_{\text{Heatsink}} = 330 \text{ K}$	199
Fig. 7.1 (a) Structure of the investigated laser bar: 16 emitter tapered laser bar with each group of 4 mini-array emitters, (b) NF image of 4 sub-emitter groups, (c) taper structure dimensions and (d) bar dimensions.	203
Fig. 7.2 Graphs of the experimental and calibrated (accepted P-I for emulation) laser bar at 0 hours.	204
Fig. 7.3 Graphs of (a) emitter output power, (b) % power loss against aging time.	205

Fig. 7.4 QW trap densities (a) and table showing the values of QW trap densities assigned to each emitter in the bar (b).....	207
Fig. 7.5 Degradation of a bar using the non-uniform temperature profile and values in Fig. 7.4: (a) Emitter power levels and (b) emitter current competition.	208
Fig. 7.6 Graphs of: (a) output power, (b) current and (c) QW temperature versus emitter group number at zero aging time (view legend in the graphs for the conditions simulated).	209
Fig. 7.7 Emulation inputs: (a) Experimental temperature profile against emitter group number in degrees Celsius, (b) NIR EL signal (a.u.) and equivalent lifetime(s) versus emitter group number.	211
Fig. 7.8 Bar currents of 15 A, 20 A and 25 A: (a) Power, (b) QW temperature and (c) emitter current against emitter group numbers.	213
Fig. 7.9 Bar currents of 15 A, 20 A and 25 A: (a) Power, (b) QW temperature and (c) emitter current against emitter group numbers.	214
Fig. 7.10 (a) Initial emulation, (b) modified emulation.	215
Fig. 7.11 Experimental and simulated temperature profiles of bar number 16022: (a) real temperature, (b) normalised temperature.	215
Fig. 7.12 Comparison of power distribution profiles of bar 16022: (a) experimental output power, (b) initial emulated output power without the modification of the input parameters, and (c) initial emulated output power with the modification of the input parameters by increasing defect levels by 3.	216
Fig. 7.13 Emulation inputs: (a) Experimental temperature profile against emitter group number in degrees celsius, (b) NIR EL signal (a.u.) and equivalent lifetime (s) against emitter group number.	219
Fig. 7.14 Bar currents of 15 A, 20 A and 25 A: (a) Power, (b) QW temperature and (c) emitter current against emitter group numbers.	220
Fig. 7.15 Experimental and simulated temperature profiles of bar number 16024: (a) real temperature, (b) normalised temperature.	220
Fig. 7.16 Comparison of power distribution profiles of bar 16024: (a) experimental output power, (b) simulated output power.	221
Fig. 7.17 Flow diagram of the global thermal solver showing the electro-optical communication in the bar emulation tool (courtesy of Dr Jun Lim).	222
Fig. 7.18 (a) Top view of bar and (b) transverse cross section of the bar.	224
Fig. 7.19 (a) Current and (b) power versus emitter group numbers.	225
Fig. 7.20 (a) Front facet profile of the bar and (b) back facet profile of the bar.	226

List of Tables

Table 2.1 Relationship between electrons energies and optical transitions. 16

Table 2.2 Applications of HPLDs according to their wavelengths. 60

Table 2.3 Wavelength ranges of differential material systems of HPLDs. 60

Table 3.1 Parts, causes and main enhancement factors in HPLDs..... 73

Table 4.1 Techniques and some important specifications..... 99

Table 5.1 Data obtained from single emitter simulations performed in constant current and power modes..... 157

Table 6.1 Changes in threshold current and slope efficiency during aging. 193

Table 6.2 Maximum changes in the QW temperature during aging (K) with respect to time zero. 194

Table 7.1 Comparison of apparent threshold and slope efficiency. 221

Table 7.2 Comparison of the experimental and emulated output power distributions for bar 16022 for the initial emulated output power without the modification of the input parameters. 217

Table 7.3 Comparison of the experimental and emulated output power distributions for bar 16022 with the modification of the input parameter by increasing the defect level by 3. 217

Table 7.4 Comparison of the output power distributions for bar 16024. 221

Abstract

The characterisation, emulation and by-emitter degradation analysis of two types of high power semiconductor laser diodes are presented in this thesis as part of an European Union (EU) project. An attempt is made using an accurate laser simulator called *Speclase* to learn more about the degradation of high power semiconductor laser diodes. *Speclase* being a single emitter simulation tool was transformed to model a bar i.e. multiple emitters, which we have named *Barlase*, through an external control interface written in Labview. The concept of *Barlase* was based on the fact that a bar is a monolithic block of multiple emitters connected in parallel with each other with a common voltage connected across them.

This tool is capable of performing simulation in different modes of operation (i.e. constant current or constant power). The tool is designed to examine and emulate the degradation processes at both the laser bar and individual emitter levels of operation. It is known that, emitter degradation is faster for emitters within a bar than for identical single emitters due to a combination of packaging-induced strain and current competition between emitters amongst others.

This tool shows clear evidence of the benefits of using by-emitter degradation analysis for gaining detailed understanding of individual emitters operating in a bar and for determining bar degradation mechanisms. The tool complement to the by-emitter analysis, allowing the effects of certain factors that affect the degradation of laser bars to be investigated.

Various intervention measures were taken to improve upon the results of the emulation such as modifying the trap density through local heating and the use of the global thermal solver. The modification of the trap density allowed the acceptance of a spatially variable local trap density distribution that gave a more realistic and accurate simulation of the degradation behaviour. The introduction of the global thermal solver allowed the modelling of thermal cross-talk communication between the emitters, which brings about the frown shaped current/power profiles for the unaged bars (though not as pronounced as in the experiment).

An attempt was made to employ this tool in the emulation of experimentally-observed degradation behaviour in a 975 nm, 16 emitter infrared tapered laser bar with each group of 4 mini-array emitters. The laser bar was first calibrated to achieve a reasonable agreement between the experimental P-I curves of unaged emitters assuming identical emitters with the simulated P-I curves. The simulated P-I curve was then used to perform simulations to emulate the degradation of the laser.

The simulated output power profile did not correspond well with the experimental power profile, but a good agreement was realised between the combined output powers of the bar. Better correlation was observed between the experimental and the simulated temperature profiles. This was expected since the experimental temperature was set as input for the heatsink temperature profile. This agreement therefore must not be over-emphasised.

The bar emulation model was enhanced by including a global thermal solver to model the thermal crosstalk between emitters. Emulations using this model showed a clearly defined frown shaped profile in the output current and power profiles but the change was minimal. As the emulation of laser bar degradation has not been attempted before, this work is still at a very early stage. Therefore, further work is needed to achieve better agreement in the output current/power profiles and to better the model.

Chapter 1

Introduction

The motivation for this work was borne from the convergence of the numerical modelling tool (*Speclase*) [1, 2] and the experimental by-emitter degradation analysis work on high power laser diodes (HPLDs). The potential of using the modelling tool in conjunction with the by-emitter analysis opened exciting new opportunities for improving our understanding of laser degradation processes. Apart from its contribution to all stakeholders in the field of HPLDs, it promises holding the key to the future of HPLDs which are now being considered as a pump source for the generation of green electricity by nuclear fusion [3]. The idea of emulating the degradation of HPLD bars using numerical methods and computer simulation is vital if the improvement in the quality and reliability of this device is to be addressed. The unfolding demand for quality, reliability and affordability of HPLDs puts more pressure on the industry to evolve in order to meet the challenges ahead head-on.

Historically, the development of lasers began as an extension of stimulated amplification techniques used in the microwave region. Masers, coined from Microwave Amplification by Stimulated Emission of Radiation, served as

sensitive preamplifiers in microwave receivers and in 1954, the first maser was built by C. Townes [4] and utilised the population inversion between two molecular levels of ammonia to amplify radiation at a wavelength around 1.25 cm.

In 1958, A. Schawlow and C. Townes [4] proposed extending the maser principle to optical frequencies and the use of a Fabry-Perot resonator for feedback. They, however, did not find a suitable material or means of exciting it to the required degree of population inversion. It was T. Maiman who built the first laser in 1960 using a pink ruby crystal. The ruby was optically pumped by a helical flashlamp that surrounded the cylindrical laser crystal to produce a laser with an output wavelength of 694 nm.

Maiman also coined the name “laser”, in analogy to maser, as an abbreviation of Light Amplification by Stimulated Emission of Radiation, finding its earliest application in active range-finding, by measuring the time of flight of a laser pulse reflected from a target. The invention of the ruby laser triggered an intensive research into other materials. Subsequently, an extraordinary number of different types of lasers have been invented using a wide range of active media and pump techniques to create population inversion.

Consequently, laser research and engineering has developed into many specialised disciplines depending on the laser medium (solid-state, semiconductor, neutral or ionised gas, liquid, free electron) and the excitation mechanism (optical pumping, electric current, gas discharge, chemical reaction, electron beam) [4].

To gain wider acceptance in manufacturing processes, the reliability of the laser systems needed improvement and the operation of the lasers had to be simplified.

During the 1970s, efforts concentrated on engineering improvements, such as an increase in component and system lifetime and reliability. The early-lasers often worked poorly and had severe reliability problems. At the component level, damage resistant optical coatings and high-quality laser crystals had to be developed; and the lifetime of flash lamps and arc lamps had to be drastically improved. On the system side, the problems requiring solutions were associated with water leaks, corrosion of metal parts by the cooling fluid, deterioration of seals and other parts in the pump cavity due to the ultraviolet radiation of the flashlamps, arcing within the high-voltage section of the laser, and contamination of optical surfaces caused by the environment.

Semiconductor laser pumping can in principle be achieved and indeed has been achieved in a number of ways, e.g., by using either the beam of another laser or an auxiliary electron beam to excite, transversely or longitudinally, the bulk semiconductor. By far the most convenient way of excitation, however, involves using the semiconductor laser in the form of a diode, with excitation produced by current flowing in the forward direction of the junction. [5].

Laser action in a semiconductor was in fact first observed in 1962 by using a p-n junction diode; the observation was made almost simultaneously by four groups, [6-10] three of which were using GaAs. Devices developed during the early stage of semiconductor laser research used the same material for both the p and n sides of the junction; therefore these are referred to as homojunction lasers. The homojunction laser is now only of historic importance, since it was superseded by the double-heterostructure (DH) laser, whose active medium is, sandwiched between p and n materials that differ from the active material. Homojunction

lasers in fact operate CW only at cryogenic temperatures ($T = 77\text{ K}$); only after the invention of the heterojunction laser was it possible to operate semiconductor lasers CW at room temperature. This development occurred 7 years after the invention of the homojunction laser (1969) [10-13], opening the way to the great variety of applications for which semiconductor lasers are currently used.

Following the developments made in the semiconductor laser industry, diode lasers are finding many applications in the manufacturing field (e.g. material processing, welding, cutting [14, 15]), in the field of medicine (e.g. treatment of tumours with photodynamic therapy, cosmetic surgery, ophthalmology [16-18]), in telecommunications (e.g. fibre lasers and amplifiers [19-22]), as pump sources for solid-state lasers [3, 23, 24] and in the space industry/forestry applications (e.g. for light detection and ranging (LIDAR) [25, 26] and laser interferometer space antenna (LISA) [27]). In all of these applications, reliability is essential, hence the quest to finding more ways of understanding better the anatomy of HPLDs even though great strides have been made in the development of highly reliable, high power laser diode sources [28-33].

This thesis presents both experimental and simulation work in the understanding of HPLDs. The experimental work involves the use of some of the experimentally investigated techniques below, some of which are performed in our state-of-the-art laboratory known as the Optical Measurement and Evaluation Systems (OMES) laboratory, described in chapter 4 of this thesis. The experimental techniques are: micro-photoluminescence (μ -PL), which has been used extensively in the study of packaging-induced strain [34-37] and PL microscopy (PLM), often used for the observance and identification of extended defects [38].

Micro-Raman spectroscopy [35-37], photocurrent spectroscopy (PCS) [35-37, 39] and electroluminescence (EL) studies [40, 41] coupled with a fast Fourier transform (FFT) analysis [41-43] have been used to study the impact of strain and defects.

In the advent of computers and the development of software's, it has become important to use numerical simulations in conjunction with the design and optimisation of laser diodes. The use of simulation in this work has become necessary in order to underpin experimental studies and gain a greater understanding of interactions between individual emitters within a laser bar. In this thesis, we have attempted the use of simulation tools to emulate the degradation of emitters and bars. The use of simulations has become an integral part of every field of engineering nowadays in the bid to optimise device layouts using beam propagation methods (BPM) simulation programs [44, 45]. Simulations are also done to optimise device structures before they are actually fabricated which buttresses the important role they play today in optoelectronic devices [46-48]. Simulations are significantly based on numerical models in order to establish a relationship between experimental results and simulation results [49-53]. This is done to simplify the otherwise complex nonlinear equations that are involved in semiconductor optoelectronic devices. Simulations form the other aspect of my thesis [54] together with the experimental work by the characterisation of the devices.

The principal objective of using simulation is the virtual nature of investigating a real situation, thereby saving cost and time. Using simulations, we can investigate the degradation of individual emitters in laser bars, by looking at effects including defects, packaging-induced stress and current competition between the emitters.

Using simulation tools, a wide parameter space can be investigated to provide data that can be compared with experimentally-observed degradation behaviour. The laser simulation tool used in this thesis is called *Speclase*, designed to simulate/emulate the degradation of a single emitter. Other researchers are using simulation tools to estimate the end of life of optoelectronic systems [55].

It is well known that within a bar, the emitter degradation rate is much faster than that of identical single emitters, but the reasons for this are not well understood. Many studies in the past have looked at the reliability and degradation of single emitters but much less attention was given to understanding the details of the degradation dynamics of high-power laser bars. The quest for more insight into this has led to the development of the by-emitter degradation analysis method. The work by Xia *et al.*, [36], Tomm *et al.*, [35] and Bull *et al.*, [56, 57] have provided new understanding of the behaviour and degradation of individual emitters within a laser bar.

This thesis presents the emulation of by-emitter degradation in high-power laser diode bars using advanced simulation tools [58]. This work is designed to provide further insight into laser bar degradation and also to allow a more thorough analysis and understanding of experimental by-emitter degradation studies.

What is *Speclase*? It is a state-of-the-art simulation tool developed by UNott's, which was initially designed for the simulation of single emitters. It is a 2.5D spectral laser model, the full details of which have been published elsewhere [1, 2]. Because *Speclase* was initially designed for single emitters, there was a need to find a way to integrate it into a software control interface, so that it can work for multiple emitters as well. This assignment is one of the most important

achievements of this thesis. The software control interface was developed in LabVIEW to control multiple instances of *Speclase* and to run these instances simultaneously for each emitter in a laser bar.

Since bars are made up of multiple emitters, the software control interface provides an innovative way to include the interactions between the individual emitters within the bar. This gave rise to the *Barlase* concept, where a bar is considered as a monolithic block of multiple emitters connected in parallel with each other with a common voltage connected across them. In the resulting circuit, each emitter is biased with a common voltage, but the emitter currents and powers change depending on the conditions of the individual emitters and their environment [59]. *Barlase* is also able to emulate different modes of operation (i.e. constant current or constant power).

Four main contributions can be credited to this thesis. Firstly, the characterisation aspect of all the high power laser diode devices carried out at UNotts as per Table 4.1 before and after aging and their analysis. Secondly, the development of a software control interfaces in LabVIEW to control *Speclase* leading to the development of *Barlase*. Thirdly, the test of *Barlase* using a hypothetical laser bar to investigate experimentally-observed degradation behaviour, including defects, temperature, packaging-induced stress and current competition between the emitters. The fourth is the use of *Barlase* to emulate the degradation of a real bar.

This thesis is structured into eight chapters. The first chapter is the introductory one, which talks a bit about the history of semiconductor laser devices and followed by what the thesis entails. Chapter 2 looks at the basic principles of optical processes which occur in semiconductors, the technology and the various

applications of semiconductor laser devices. Chapter 3 reviews the degradation of high power laser diodes and the description of the emulation tool. Some of the experimental techniques being used in this thesis are briefly outlined and the experimental results and analysis presented in chapter 4. Chapter 5 describes how the by-emitter degradation analysis methodology for high power laser diodes is used to complement the emulation of a hypothetical bar. In chapter 6, an improved by-emitter degradation analysis tool is used for the emulation of a bar. In chapter 7, an attempt is made to emulate the degradation of a real bar. Chapter 8 is the closing chapter, where recommendations, conclusions and suggestions for further study are presented.

Lists of publications from this work are presented in the thesis as an appendix.

References

- [1] J. J. Lim, S. Sujecki, L. Lang, Z. C. Zhang, D. Paboeuf, G. Pauliat, G. Lucas-Leclin, P. Georges, R. C. I. MacKenzie, P. Bream, S. Bull, K. H. Hasler, B. Sumpf, H. Wenzel, G. Erbert, B. Thestrup, P. M. Petersen, N. Michel, M. Krakowski, and E. C. Larkins, "Design and Simulation of Next-Generation High-Power, High-Brightness Laser Diodes," *IEEE Journal of Selected Topics in Quantum Electronics*, vol. 15, pp. 993-1008, May-Jun 2009.
- [2] J. J. Lim, R. MacKenzie, S. Sujecki, M. Sadeghi, S. M. Wang, Y. Q. Wei, J. S. Gustavsson, A. Larsson, P. Melanen, P. Sipila, P. Uusimaa, A. A. George, P. M. Smowton, and E. C. Larkins, "Simulation of double quantum well GaInNAs laser diodes," in *21st Conference on Semiconductor Integrated Optoelectronics (SIOE)*, Cardiff, WALES, 2007, pp. 259-265.
- [3] K. Ertel, S. Banerjee, P. D. Mason, C. Hernandez-Gomez, and J. L. Collier, "HiPER and ELI: multi-kilojoule-class DPSSLs for laser fusion and ultra high intensity research," *2nd High Power Diode Lasers and Systems Meeting (HPDLS)*, Coventry, UK, KEYNOTE, 2009.
- [4] W. Koechner and M. Bass, *Solid-State Lasers: A Graduate Text*: Springer, 2003.
- [5] N. G. Basov, O. N. Krokhin, and Y. M. Popov, "Production of negative-temperature states in p-n junctions of degenerate semiconductors," *Soviet Physics Jetp-USSR*, vol. 13, pp. 1320-1321, 1961.
- [6] M. I. Nathan, W. P. Dumke, G. Burns, F. H. Dill, and G. Lasher, "Stimulated emission of radiation from GaAs p-n junctions," *Applied Physics Letters*, vol. 1, pp. 62-64, 1962.
- [7] R. N. Hall, R. O. Carlson, T. J. Soltys, G. E. Fenner, and J. D. Kingsley, "Coherent light emission from GaAs junctions," *Physical Review Letters*, vol. 9, pp. 366-&, 1962.
- [8] N. Holonyak and S. F. Bevacqua, "Coherent (visible) light emission from Ga(As_{1-x}P_x) junctions," *Applied Physics Letters*, vol. 1, pp. 82-83, 1962.
- [9] T. M. Quist, R. H. Rediker, R. J. Keyes, W. E. Krag, B. Lax, A. L. McWhorter, and H. J. Zeigler, "Semiconductor maser of GaAs," *Applied Physics Letters*, vol. 1, pp. 91-92, 1962.
- [10] O. Svelto, *Principles of Lasers* Springer; 4th ed. Corr. 5th printing edition, 1998.
- [11] Z. I. Alferov, V. M. Andreev, V. I. Korolkov, E. L. Portnoi, and Tretyako.Dn, "Coherent radiation of epitaxial heterojunction structures in AlAs-GaAs system," *Soviet Physics Semiconductors-Ussr*, vol. 2, pp. 1289-&, 1969.
- [12] I. Hayashi, M. B. Panish, and P. W. Foy, "A low-threshold room-temperature injection laser," *IEEE Journal of Quantum Electronics*, vol. QE 5, pp. 211-&, 1969.

- [13] H. Kressel and H. Nelson, "Close-confinement gallium arsenide pn junction lasers with reduced optical loss at room temperature," *Rca Review*, vol. 30, pp. 106-114, 1969.
- [14] H. G. Treusch, A. Ovtchinnikov, X. He, M. Kanskar, J. Mott, and S. Yang, "High-brightness semiconductor laser sources for materials processing: Stacking, beam shaping, and bars," *IEEE Journal of Selected Topics in Quantum Electronics*, vol. 6, pp. 601-614, Jul-Aug 2000.
- [15] W. Schulz and R. Poprawe, "Manufacturing with novel high-power diode lasers," *IEEE Journal of Selected Topics in Quantum Electronics*, vol. 6, pp. 696-705, Jul-Aug 2000.
- [16] I. Gannot and R. W. Waynant, "Introduction to the issue on lasers in medicine and biology," *IEEE Journal of Selected Topics in Quantum Electronics*, vol. 7, pp. 873-873, Nov-Dec 2001.
- [17] R. W. Waynant and I. Gannot, "Introduction to the issue on lasers in medicine and biology," *IEEE Journal of Selected Topics in Quantum Electronics*, vol. 5, pp. 893-894, Jul-Aug 1999.
- [18] R. W. Waynant, I. K. Ilev, and I. Gannot, "Medical applications of infrared fibers and waveguides," in *Infrared Optical Fibers and Their Applications*, vol. 3849, M. Saad and J. A. Harrington, Eds. Bellingham: Spie-Int Soc Optical Engineering, 1999, pp. 2-6.
- [19] G. P. Agrawal, *Fibre-Optic Communication Systems*: Wiley, New York; 3rd edition, 1997.
- [20] A. Yariv, *Optical Electronics in Modern Communications*: Oxford University Press, New York; 5th edition, 1997.
- [21] H. Po, J. D. Cao, B. M. Laliberte, R. A. Minns, R. F. Robinson, B. H. Rockney, R. R. Tricca, and Y. H. Zhang, "High-power neodymium-doped single transverse-mode fiber laser," *Electronics Letters*, vol. 29, pp. 1500-1501, Aug 1993.
- [22] E. Rochat, K. Haroud, and R. Dandliker, "High-power Nd-doped fiber amplifier for coherent intersatellite links," *IEEE Journal of Quantum Electronics*, vol. 35, pp. 1419-1423, Oct 1999.
- [23] K. Shigihara, Y. Nagai, S. Karakida, A. Takami, Y. Kokubo, H. Matsubara, and S. Kakimoto, "High-power operation of broad-area laser-diodes with GaAs and AlGaAs single quantum-wells for Nd-YAG laser pumping," *IEEE Journal of Quantum Electronics*, vol. 27, pp. 1537-1543, Jun 1991.
- [24] G. T. Maker and A. I. Ferguson, "Frequency-modulation mode-locking and q-switching of diode-laser-pumped Nd-YLF laser," *Electronics Letters*, vol. 25, pp. 1025-1026, Aug 1989.
- [25] K. Clem, "Rendezvous Sensor Technology Launches on Next Space Shuttle Flight," *Johnson Space Center, Houston*, 2010.

- [26] T. J. Hawbaker, T. Gobakken, A. Lesak, E. Tromborg, K. Contrucci, and V. Radeloff, "Light Detection and Ranging-Based Measures of Mixed Hardwood Forest Structure," *Forest Science*, vol. 56, pp. 313-326, Jun 2010.
- [27] K. Hausler, U. Zeimer, B. Sumpf, G. Erbert, and G. Trankle, "Degradation model analysis of laser diodes," *Journal of Materials Science-Materials in Electronics*, vol. 19, pp. S160-S164, 2008.
- [28] A. AlMuhanna, L. J. Mawst, D. Botez, D. Z. Garbuzov, R. U. Martinelli, and J. C. Connolly, "14.3 W quasicontinuous wave front-facet power from broad-waveguide Al-free 970 nm diode lasers," *Applied Physics Letters*, vol. 71, pp. 1142-1144, Sep 1997.
- [29] A. Knauer, G. Erbert, H. Wenzel, A. Bhattacharya, F. Bugge, J. Maege, W. Pittroff, and J. Sebastian, "7W CW power from tensile-strained GaAsyP1-y/AlGaAs ($\lambda = 735$ nm) QW diode lasers," *Electronics Letters*, vol. 35, pp. 638-639, Apr 1999.
- [30] X. He, A. Ovtchinnikov, S. Yang, J. Harrison, and A. Feitisch, "Efficient high power reliable InGaAs/AlGaAs (940nm) monolithic laser diode arrays," *Electronics Letters*, vol. 35, pp. 1739-1740, Sep 1999.
- [31] M. Jansen, P. Bournes, P. Corvini, F. Fang, M. Finander, M. Hmelar, T. Johnston, C. Jordan, R. Nabiev, J. Nightingale, M. Widman, H. Asonen, J. Aarik, A. Salokatve, J. Nappi, and K. Rakennus, "High performance laser diode bars with aluminum-free active regions," *Optics Express*, vol. 4, pp. 3-11, Jan 1999.
- [32] M. M. Apter and F. Leibreich, "High-power diode-laser bars come of age," *Laser Focus World*, 2006.
- [33] H. Huang*, J. Wang, M. DeVito, L. Bao, A. Hodges, S. Zhang, D. Wise, M. Grimshaw, D. Xu, and C. Bai, "High Power High Brightness 808nm QCW Laser Diode Mini Bars," *nLight Corporation, 5408 NE 88th Street, Bldg E, Vancouver, WA 98665*, 2010.
- [34] E. Martin, J. P. Landesman, J. P. Hirtz, and A. Fily, "Microphotoluminescence mapping of packaging-induced stress distribution in high-power AlGaAs laser diodes," *Applied Physics Letters*, vol. 75, pp. 2521-2523, Oct 1999.
- [35] J. W. Tomm, A. Gerhardt, T. Elsaesser, D. Lorenzen, and P. Hennig, "Simultaneous quantification of strain and defects in high-power diode laser devices," *Applied Physics Letters*, vol. 81, pp. 3269-3271, Oct 2002.
- [36] R. Xia, E. C. Larkins, I. Harrison, S. R. A. Dods, A. Andrianov, J. Morgan, and J. P. Landesman, "Mounting-induced strain threshold for the degradation of high-power AlGaAs laser bars," *IEEE Photonics Technology Letters*, vol. 14, pp. 893-895, Jul 2002.
- [37] J. W. Tomm, A. Gerhardt, R. Muller, V. Malyarchuk, Y. Sainte-Marie, P. Galtier, J. Nagle, and J. P. Landesman, "Spatially resolved spectroscopic strain measurements on high-power, laser diode bars," *Journal of Applied Physics*, vol. 93, pp. 1354-1362, Feb 2003.

- [38] A. V. Andrianov, S. R. A. Dods, J. Morgan, J. W. Orton, T. M. Benson, I. Harrison, E. C. Larkins, F. X. Daiminger, E. Vassilakis, and J. P. Hirtz, "Optical and photoelectric study of mirror facets in degraded high power AlGaAs 808 nm laser diodes," *Journal of Applied Physics*, vol. 87, pp. 3227-3233, Apr 2000.
- [39] J. W. Tomm, A. Gerhardt, R. Muller, M. L. Biermann, J. P. Holland, D. Lorenzen, and E. Kaulfersch, "Quantitative strain analysis in AlGaAs-based devices," *Applied Physics Letters*, vol. 82, pp. 4193-4195, 2003.
- [40] S. Bull, A. V. Andrianov, I. Harrison, M. Dorin, R. B. Kerr, J. Noto, and E. C. Larkins, "A spectroscopically resolved photo- and electroluminescence microscopy technique for the study of high-power and high-brightness laser diodes," *IEEE Transactions on Instrumentation and Measurement*, vol. 54, pp. 1079-1088, Jun 2005.
- [41] R. Xia, A. V. Andrianov, S. Bull, I. Harrison, J. P. Landesman, and E. C. Larkins, "Micro-electroluminescence spectroscopy investigation of mounting-induced strain and defects on high power GaAs/AlGaAs laser diodes," *Optical and Quantum Electronics*, vol. 35, pp. 1099-1106, Sep 2003.
- [42] A. Klehr, G. Beister, G. Erbert, A. Klein, J. Maege, I. Rechenberg, J. Sebastian, H. Wenzel, and G. Trankle, "Defect recognition via longitudinal mode analysis of high power fundamental mode and broad area edge emitting laser diodes," *Journal of Applied Physics*, vol. 90, pp. 43-47, 2001.
- [43] P. Lambkin, C. Percival, and B. Corbett, "Reflectivity measurements of intracavity defects in laser diodes," *IEEE Journal of Quantum Electronics*, vol. 40, pp. 10-17, Jan 2004.
- [44] K. Boucke and I. IEEE, "Numerical simulations of new high-power, high-brightness diode laser structures," in *2000 IEEE 17th International Semiconductor Laser Conference, Conference Digest* New York: IEEE, 2000, pp. 99-100.
- [45] K. Boucke, J. Rogg, M. Kelemen, R. Poprawe, and G. Weimann, "Numerical simulations of novel high-power, high-brightness diode laser structures," in *Physics and Simulation of Optoelectronic Devices IX*, vol. 4283, Y. Arakawa, P. Blood, and M. Osinski, Eds. Bellingham: Spie-Int Soc Optical Engineering, 2001, pp. 586-592.
- [46] K. H. Hasler, H. Wenzel, A. Klehr, and G. Erbert, "Simulation of the generation of high-power pulses in the GHz range with three-section DBR lasers," *Optoelectronics, IEE Proceedings -*, vol. 149, pp. 152-160, 2002.
- [47] S. Kallenbach, M. T. Kelemen, R. Aidam, R. Losch, G. Kaufel, M. Mikulla, and G. Weimann, "High-power high-brightness ridge-waveguide tapered diode lasers at 14xx nm," in *Novel In-Plane Semiconductor Lasers IV*, vol. 5738, C. Mermelstein and D. P. Bour, Eds. Bellingham: Spie-Int Soc Optical Engineering, 2005, pp. 406-415.
- [48] H. Odriozola, J. M. G. Tijero, L. Borruel, S. Sujecki, E. C. Larkins, I. Esquivias, and IEEE, "Simulation of tapered lasers with separate contacts," in *2007 Spanish Conference on Electron Devices, Proceedings* New York: IEEE, 2007, pp. 56-59.

- [49] E. Gehrig, O. Hess, and R. Wallenstein, "Modeling of the performance of high-power diode amplifier systems with an optothermal microscopic spatio-temporal theory," *Quantum Electronics, IEEE Journal of*, vol. 35, pp. 320-331, 1999.
- [50] S. Mariojouis, S. Morgott, A. Schmitt, M. Mikulla, J. Braunstein, G. Weimann, F. Lozes, and S. Bonnefont, "Modeling of the performance of high-brightness tapered lasers," in *Physics and Simulation of Optoelectronic Devices VIII*, San Jose, CA, USA, 2000, pp. 395-406.
- [51] G. Romo, T. Smy, D. Walkey, and B. Reid, "Modeling facet heating in ridge lasers," *Microelectronics Reliability*, vol. 43, pp. 99-110, 2003.
- [52] P. J. Bream, S. Bull, I. Harrison, S. Sujecki, and E. C. Larkins, "Fourier transform analysis method for modeling the positions and properties of cavity defects in Fabry-Perot laser diodes," *Applied Physics Letters*, vol. 86, pp. 061104-3, 2005.
- [53] F. Gity, V. Ahmadi, and M. Noshiravani, "Numerical analysis of void-induced thermal effects on GaAs/Al_xGa_{1-x}As high power single-quantum-well laser diodes," *Solid-State Electronics*, vol. 50, pp. 1767-1773, 2006/12//.
- [54] C. K. Amuzuvi, J. J. Lim, S. Bull, and E. C. Larkins, "Describing the state-of-the-art laser diode emulation tool," *in preparation to be submitted*, 2010.
- [55] C. Aupetit-Berthelomot, L. Bechou, A. Guerin, A. Julie-Vergonjanne, and C. Tronche, "End of life optoelectronic system performance estimation using a system simulator," in *International symposium on reliability of optoelectronics for space (ISROS), April 28-30, 2010, Organised by <http://www.isros.org>* Cagliari, Sardinia (Italy), 2010.
- [56] S. Bull, J. W. Tomm, M. Oudart, J. Nagle, C. Scholz, K. Boucke, I. Harrison, and E. C. Larkins, "By-emitter degradation analysis of high-power laser bars," *Journal of Applied Physics*, vol. 98, p. 063101, 2005.
- [57] S. Bull, C. K. Amuzuvi, T. J.W., X. R., L. J.J., S. S., and L. E.C., "By emitter degradation analysis in high power laser bars: Experiment and emulation," in *High Power Diode Lasers and Systems Conference, Coventry (UK) 2008. HPD 2008*, 2008.
- [58] C. K. Amuzuvi, J. J. Lim, S. Bull, and E. C. Larkins, "Investigating a hypothetical single emitter/bar using a laser diode emulation tool," *in preparation to be submitted*, 2010.
- [59] C. K. Amuzuvi, S. Bull, J. J. Lim, S. Sujecki, and E. C. Larkins, "Numerical emulation of the degradation of 975nm high power tapered laser bars," in *High Power Diode Lasers and Systems Conference, Coventry (UK) 2009. HPD 2009*, 2009, pp. 1-2.

Chapter 2

Semiconductor Laser Principles, Technology and Applications

This chapter focuses on the principles, technology and applications of high power laser diode devices. Optical processes in semiconductors will be discussed briefly to distinguish between absorption, spontaneous and stimulated emissions. Population inversion will also be discussed, leading to the concept of lasing in semiconductors.

Next to be considered will be the technology of high power laser diodes. In view of the technological advancements in the manufacture of HPLDs, more applications have evolved such as the use of stacks of HPLDs as pump sources [1] in the generation of green electricity. Other traditional applications include material processing, printing, medicine and entertainment, and recently in the space industry. In the space industry/forestry, applications include light detection and ranging (LIDAR) [2, 3] and laser interferometer space antenna (LISA) [4].

Finally, a discussion on some of the various applications of these devices and different material systems employed to achieve different wavelengths of interest is presented.

2.1 Optical Processes in Semiconductors

The operation of a laser is based on the physical principles governing the interaction of radiation with matter. Atomic systems can exist only in discrete energy states. An optical transition is a change from one energy state to another which is accompanied with either an emission or absorption of a photon. The wavelength of the absorbed or emitted radiation is given by Bohr's frequency relation of Eq. 2.1.

$$E_2 - E_1 = h\nu_{21}, \quad (2.1)$$

where E_2 (higher energy state) and E_1 (lower energy state) are two discrete energy levels, ν_{21} is the frequency, and h is Planck's constant. At thermal equilibrium, the lower energy states in the medium are more heavily populated than the higher energy states. The operation of a laser requires that the energy equilibrium of a laser material be changed, so that more atoms (ions, molecules) populate higher rather than lower energy states. An electron transition from E_2 to E_1 with their corresponding wave vectors k_2 and k_1 accompanied by the emission of a photon with energy $h\nu$ and wave vector k_p occurs only if the conservation of energy and momentum (or wave vector) is maintained according to Eq. 2.1 and Eq. 2.2:

$$k_2 = k_1 + k_p \quad (2.2)$$

The absolute value of the wave vector for a photon is given by:

$$|k_p| = 2\pi / \lambda \quad (2.3)$$

with λ denoting the wavelength of light. For optical frequencies, the momentum k may be neglected in Eq. 2.2 yielding:

$$k_2 = k_1 . \quad (2.4)$$

The transition according to Eqs. 2.1 and 2.4 is called a direct transition and semiconductors that permit a direct transition are called direct bandgap semiconductors. [5]. Optical transitions have a relationship with electron energies and show whether absorption occurs or emission occurs. This can be demonstrated in Table 2.1 [6].

Table 2.1 Relationship between electrons energies and optical transitions.

Optical Transition	Energy of the electron
Absorption	Low energy to high energy
Emission	High energy to low energy

In a laser, an electron transition from a high energy level to a low energy level is normally accompanied by the emission of light. However, nonradiative transitions may occur when the electron encounters a trap on its way from the high energy (conduction band) to the low energy (valence band). Auger recombination, which is also nonradiative, gives off energy in the form of kinetic energy to another electron or hole.

The fundamental nature of an induced or stimulated emission process was described by Albert Einstein and Max Planck [7]. The basic ideas underlying the operation of semiconductor lasers will be discussed but in-depth treatment of laser physics can be found in [8, 9]. All laser amplifiers have at least two elements in common: a laser medium in which a population inversion can be achieved, and a

pump process to supply energy to the system in order to maintain a nonequilibrium state. For a laser oscillator, a feedback mechanism is also required to allow the radiation to build up. Typically, two mirrors facing each other provide this feedback. Distributed feedback (DFB) laser use gratings which act as wavelength selectors for at least one of the mirrors and provides the feedback by reflecting light back into the cavity to form the resonator. In a distributed Bragg reflector (DBR) laser, the laser resonator is made with at least one distributed Bragg reflector (DBR) outside the gain medium (the active region).

Whether a population inversion occurs within atoms, ions, or molecules, and whether the pump energy supplied to the medium is in the form of optical radiation, electrical current, kinetic energy due to electron impact in a gas discharge, or an exothermic reaction, depends on the type of laser required and the type of active medium being used, i.e., solid-state, liquid, semiconductor, or gas.

In semiconductor lasers, also referred to as injection lasers, radiation is emitted as a consequence of carrier injection in a forward-biased semiconductor p-n junction. Since the junction defines a diode, the laser is commonly called a diode laser. Energy levels in a semiconductor are defined by the conduction band and the valence band separated by a bandgap. The p-n junction is made of p-type semiconductor material, which contains impurities that accept electrons (or produces holes or positive carriers). The n-type material contains impurities that donate excess electrons (or negative carriers).

The n-type material with a large electron density in the conduction band is brought into intimate contact with the p-type material with a large hole density in the valence band. In a forward biased p-n junction, current will flow and electrons

in the n-type material are injected into the p-type region, while positive holes from the p-region are injected into the n-type region.

Radiative recombination

The electron-hole recombination process in a semiconductor is the transition of an electron from an occupied state at a higher energy to an empty state at a lower energy. This is accompanied by the release of the energy difference between the two states. This process can be either radiative or nonradiative. In a radiative recombination, the energy released is emitted as electromagnetic radiation. In a nonradiative recombination, the energy released is eventually converted to thermal energy in the form of lattice vibrations. Only radiative processes are useful to the function of semiconductor lasers [10].

Radiative efficiency

The total recombination rate for the excess carriers in a semiconductor can be expressed as the sum of radiative and nonradiative recombination rates:

$$R = R_{rad} + R_{nonrad} \quad (2.5)$$

The lifetime of an excess electron-hole pair (ehp) associated with radiative recombination is called the radiative carrier lifetime, τ_{rad} . This is associated with nonradiative recombination which is also called the nonradiative carrier lifetime, τ_{nonrad} . They are related to the total spontaneous carrier recombination lifetime, τ_s , of the excess carriers by:

$$1/\tau_s = 1/\tau_{rad} + 1/\tau_{nonrad} \quad (2.6)$$

The spontaneous carrier recombination rate, γ_s , is defined as $\gamma_s = 1/\tau_s$. This parameter is the total rate of carrier recombination including the contributions from

all, i.e., radiative, nonradiative, and spontaneous emission recombination processes, but excluding the contribution from the stimulated emission recombination process. Including the presence of stimulated emission, the effective recombination rate of the carriers can be much higher than γ_s .

Nonradiative recombination mechanisms

Electrons and holes are also capable of recombining nonradiatively, in which case there will be no emission of light. Nonradiative mechanisms play an important role in device degradation; common examples include: Shockley-Read-Hall (SRH) recombination, Auger recombination, surface recombination and multi-phonon emission [11]. In the SRH recombination process, the electrons and holes recombine at localised defect centres. These defect centres first capture an electron (hole) and then a hole (electron) to return back to their original charge state. When an electron is captured, it transfers its excess energy to the lattice as heat through the emission of a phonon.

The Auger recombination process is known to be a major nonradiative recombination mechanism in narrow-gap semiconductors. [12-14]. Auger recombination is responsible for the strong temperature dependence of the threshold current in long-wavelength semiconductor lasers. The Auger effect is a three-body phenomenon [15, 16], where a hole and an electron recombine and the annihilation energy and momentum are donated to another electron or hole. The electron or hole is then excited high into either the conduction or the valence band, in such a way that both energy and momentum are conserved. The effect of surface recombination plays a vital role when an electron or hole falls within a diffusion length from a surface. A large concentration of defect levels can occur at

a surface and these can act as efficient recombination centers. These defects can exist because the lattice is strongly perturbed at the edges and many dangling bonds [11] are generated. Recombination through this continuum of surface states of electrons and holes can form a transition which is nonradiative, releasing a series of phonons [17].

2.1.1 Band-to-band optical transition

The characteristics of optical transitions between energy levels are very peculiar in semiconductors. In semiconductors, the states of all the valence electrons collectively form an energy band of electron population. This is governed by the Fermi-Dirac distribution function because the state of an electron is not independent of the other electrons. For a solid material in thermal equilibrium at a temperature T , the probability of any electronic state at an energy E being occupied by an electron is given by the Fermi-Dirac distribution function:

$$f(E) = \frac{1}{e^{(E-E_F)/k_B T} + 1}, \quad (2.7)$$

where E_F is the Fermi level of the material and k_B is the Boltzmann constant [10]. A band-to-band transition in a semiconductor takes place through the transition of such an electron between a valence band state and a conduction band state. Consequently, when considering a band-to-band optical transition, the characteristics of the band structure have to be considered.

Two types of band-to-band transitions exist in a semiconductor. The first is a direct transition, which takes place when an electron makes an upward or downward transition without the participation of a phonon. The second is when an electron makes an indirect transition, where a phonon is absorbed or emitted

(thereby exchanging energy and momentum with the crystal lattice) in order to complete the transition. The probability of a transition varies significantly between a direct process and an indirect process. The conditions for direct band-to-band transition with the absorption or emission of a photon are:

$$E_2 - E_1 = h\nu \quad \text{and} \quad k_2 = k_1 + k_{\text{photon}} \approx k_1 \quad (2.8)$$

where E_1 and E_2 are valence and conduction band energies and k_1 and k_2 are valence and conduction band wavevectors respectively. This expresses the need to satisfy the conservation of energy and momentum principles in order to complete the transition.

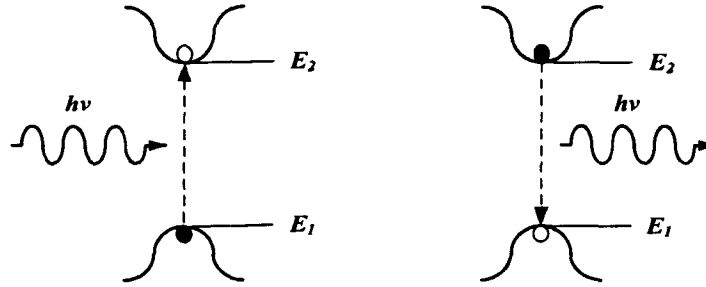


Fig. 2.1 Optical transition in a direct-gap semiconductor [10] p. 822.

In Fig. 2.1, direct transitions are shown between two states at the conduction and valence band edges (broken arrow in Fig. 2.1 shows the direction of direct transition from E_1 to E_2 and vice versa). Band-to-band absorption in a direct-gap semiconductor normally occurs through a direct absorption or annihilation process of a photon of energy $h\nu = E_2 - E_1 > E_g$. Band-to-band recombination normally occurs through a direct recombination process with the emission of a photon of energy $h\nu = E_2 - E_1 > E_g$. The conditions in Eq. 2.2 for direct transition processes are easily satisfied, and therefore increase the probability of radiative recombination in a direct-gap semiconductor, which leads to a short radiative lifetime and a high

radiative efficiency [6].

2.1.2 Absorption, spontaneous and stimulated emissions

There are three optical transition processes in semiconductors: absorption, spontaneous emission, and stimulated emission. Electrons finding their way into the conduction band from the valence band will always exhibit instability in satisfaction to the natural laws of nature. When an external stimulus is applied to an electron at the ground level E_1 , it will be raised or excited to a high level E_2 and undergo a transition. This process is termed absorption (Fig. 2.2a).

The electron at E_2 can spontaneously decay or relax to E_1 , characterised by the emission of a photon of energy $E_2 - E_1 = h\nu_{21}$ when the electron decays from level 2 to level 1 in Fig. 2.2b. This process is also called spontaneous (or radiative) emission. The frequency ν_{21} of the radiated wave is then given by Eq. 2.1. Note that radiative emission is just one of several possible ways for the electron to decay (e.g. spontaneous emission, stimulated emission, Shockley-Read-Hall recombination, Auger recombination, multiphonon emission etc.) and that decay can be nonradiative. In the case of a nonradiative decay, the energy delivered may go into the kinetic or internal energy of the surrounding electrons.

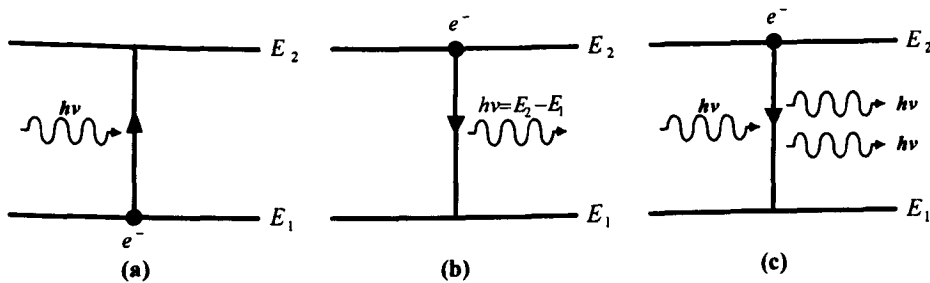


Fig. 2.2 Schematic illustration of radiation and absorption processes: (a) absorption, (b) spontaneous emission, and (c) stimulated emission.

An electron may also be forced to undergo a transition from E_2 to E_1 when incident light induces a radiative transition of an excited electron. This is the phenomenon of stimulated emission (Fig. 2.2c). The emitted light that evolves due to the stimulated emission has the same wavelength, phase and direction as the incident light. This process can also lead to optical amplification [18].

2.1.3 Probability of emission and absorption phenomena

To introduce probabilities for these emission and absorption phenomena, let N_i (population of the level) be the number of electrons per unit volume that at time t occupy a given energy level, i .

For the case of spontaneous emission, the probability that the process occurs can be defined as the rate of decay of the upper state population being proportional to the population N_2 . We can write this as:

$$\left(\frac{dN_2}{dt} \right)_{sp} = -AN_2 = -A_{21}N_2 \quad (2.9)$$

where the minus sign shows that the time derivative is negative. The coefficient A_{21} , is a positive constant called the rate of spontaneous emission or the Einstein A coefficient. The quantity $\tau_{sp} = 1/A_{21}$ is the spontaneous emission (or radiative) lifetime. Likewise, for nonradiative decay, we can generally write:

$$\left(\frac{dN_2}{dt} \right)_{nr} = -\frac{N_2}{\tau_{nr}} \quad (2.10)$$

where τ_{nr} is the nonradiative decay lifetime which depends on the transition and the characteristics of the surrounding medium.

For stimulated processes (emission or absorption), we can write the rate as:

$$\left(\frac{dN_2}{dt} \right)_{st} = -B_{21}N_2 \quad (2.11)$$

where $(dN_2/dt)_{st}$ is the rate at which transitions from E_2 to E_1 occur as a result of stimulated emission and B_{21} is the rate of stimulated emission. The coefficient B_{21} has a dimension s^{-1} and depends not only on the particular transition but also on the intensity of the incident light. More precisely, for a plane wave, we can write:

$$B_{21} = \sigma_{21}F \quad (2.12)$$

where F is the photon flux density of the wave and σ_{21} is a quantity having the dimension of area (the stimulated emission cross section) which depends on the characteristics of the given transition.

As in Eq. 2.1.3.3, the absorption rate B_{12} can be defined using the equation:

$$\left(\frac{dN_1}{dt} \right)_a = -B_{12}N_1 \quad (2.13)$$

where $(dN_1/dt)_a$ is the rate of transitions from E_1 to E_2 due to absorption and N_1 is the population of level 1. Similarly as in Eq. 2.12, we can write:

$$B_{12} = \sigma_{12}F, \quad (2.14)$$

where σ_{12} is some characteristic area (the absorption cross section), which depends only on the particular transition. Einstein showed that, if the two levels are nondegenerate, then $B_{21} = B_{12}$ and thus $\sigma_{21} = \sigma_{12}$. If levels 1 and 2 are g_1 -fold and g_2 -fold degenerate, respectively, then:

$$g_1 B_{12} = g_2 B_{21}$$

that is

$$g_1 \sigma_{12} = g_2 \sigma_{21}$$

The Einstein coefficients (A_{12} , B_{12} , B_{21}) are related by the Einstein relations given by Eq. 2.15 [19]:

$$A_{21} = \frac{8\pi^3 E_{21}^2}{h^3 c^3} B_{21}, \quad (2.15)$$

$$B_{12} = B_{21}, \quad (2.16)$$

where h is Plank's constant, c is the speed of light in a vacuum and n is the refractive index of the material.

The fundamental processes of spontaneous emission, stimulated emission, and optical absorption can be described in terms of the absorbed or the emitted photons as follows (Fig. 2.3):

- (a) In the absorption process, the incident photon is absorbed to produce a transition from E_1 to E_2 . Each optical emission process creates a photon, whereas each optical absorption process annihilates a photon.
- (b) In the spontaneous emission process, the electron decays from level 2 to level 1 through the emission of a photon.
- (c) In the stimulated emission process, the incident photon stimulates the transition from level 2 to level 1, so that there are two photons (the stimulating one and the stimulated one) [19].

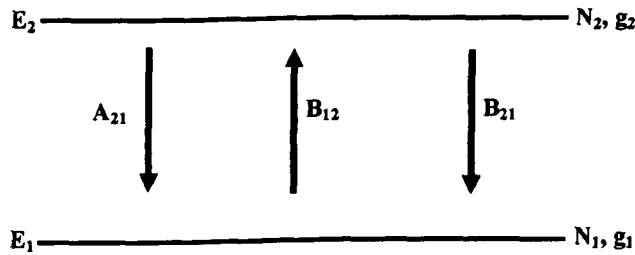


Fig. 2.3 Energy levels with population N_1 , N_2 and degeneracies g_1 , g_2 respectively.

2.1.4 Population inversion

According to the Boltzmann distribution of Eq. 2.17, in a collection of atoms at thermal equilibrium, there will always be fewer atoms in the higher energy level E_2 than in the lower energy level E_1 [7]. The population difference of $N_1 - N_2$ will therefore be always positive.

$$\frac{N_2}{N_1} = \exp\left(\frac{-(E_2 - E_1)}{kT}\right) \quad (2.17)$$

However, from Eq. 2.17, the transition probabilities of band-to-band absorption and stimulated emission are equal. Hence to ensure that the stimulated emission process dominates, a population inversion must be achieved. This means that stimulated absorption becomes stimulated emission or amplification. The essential criterion for amplification is that more electrons are present in the conduction band than in the valence band i.e.

$$N_2 > N_1 \quad \text{if} \quad E_2 > E_1. \quad (2.18)$$

The population difference which is negative in this instance on this transition is called population inversion and the point at which both population states are equal is called the “inversion threshold”. This condition actually makes population inversion not a normal phenomenon and can never be observed at thermal equilibrium. Emission will predominate and radiation enhanced when there are more electrons at the higher energy level than the lower level [7].

For this to occur, a source of energy is required to populate the upper energy level. We call this the pump energy. The quantum of inverted population difference is reduced not only by the amplification process, but also by spontaneous emission which always tends to return the energy level populations

to their thermal equilibrium values.

In semiconductor lasers, a population inversion at a p - n junction can occur if [16, 19]:

$$F_n - F_p \geq E_g , \quad (2.19)$$

where F_n and F_p are the quasi-Fermi levels of the electrons and holes, respectively. To fulfil this condition, the quasi-Fermi levels must lie outside of the bandgap on at least one side of the junction and this can be achieved by applying a sufficiently large forward bias across the p - n junction.

2.2 The Idea of the Laser

A plane wave with a photon flux density F , travelling in a direction in a material (Fig. 2.2.1), with elemental change dF of this flux density along the elemental length dz of the material, is attributed to both stimulated absorption and emission processes occurring in the shaded region of Fig. 2.4.

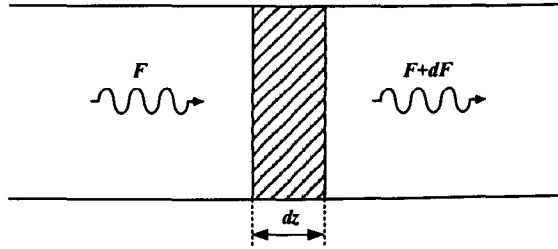


Fig. 2.4 *An elemental change dF , in the photon flux density F , for a plane electromagnetic wave travelling a distance dz , through a material [18] p 5.*

The change in number between outgoing and incoming photons in the shaded volume per unit distance, dz is SdF , where S is the cross-sectional area of the beam. Each stimulated emission process creates a photon whilst each absorption

process removes a photon. Therefore, SdF must equal the difference between the number of stimulated emission and absorption events occurring in the shaded volume per unit distance, dz .

From Eqs. 2.11 and 2.13, we can write that: $SdF = (B_{21}N_2 - B_{12}N_1)(Sdz)$, where Sdz is the volume of the shaded region. From Eqs. 2.12, 2.14, and 2.16, we can obtain:

$$dF = \sigma_{21}F \left[N_2 - \left(\frac{g_2 N_1}{g_1} \right) \right] dz. \quad (2.20)$$

Nonradiative decay does not add new photons, while photons created by spontaneous emission are emitted in any direction and thus give negligible contribution to the incoming photon flux density F . At thermal equilibrium, populations are described by Boltzmann statistics. If N_1^e and N_2^e are the thermal equilibrium populations of the two levels, then:

$$\frac{N_2^e}{N_1^e} = \frac{g_2}{g_1} \exp\left(-\frac{E_2 - E_1}{kT}\right) \quad (2.21)$$

where k is Boltzmann's constant and T is the absolute temperature of the material. If the nonequilibrium condition is achieved for which $N_2 > g_2 N_1 / g_1$, then the material is said to act as an amplifier and population inversion in the material is achieved. The material in which this population inversion is produced is referred to as an *active medium*. If the transition frequency falls in the optical region, the amplifier is called a laser amplifier. To make an oscillator from an amplifier, a suitable positive feedback is required [18].

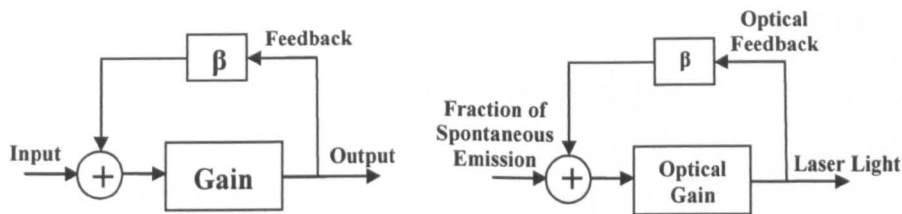


Fig. 2.5 (a) An oscillator circuit and (b) a laser oscillator circuit.

In general, an oscillator has *gain*, amplifies an input signal and returns a fraction of the output signal through a feedback loop as shown in Fig. 2.5a [6]. The difference between the output and the input is used as a means of control. In a laser (Fig. 2.5b), the feedback signal which is obtained by placing the active material between two highly reflecting mirrors, such as the plane parallel mirrors in Fig. 2.6 is repetitively amplified until oscillation starts when the net gain exceeds the internal loss and mirror loss of the oscillator. The light travels in a direction perpendicular to the mirrors bounces back and forth between the two mirrors (Fabry-Perot arrangement), amplified on each passage through the active material.

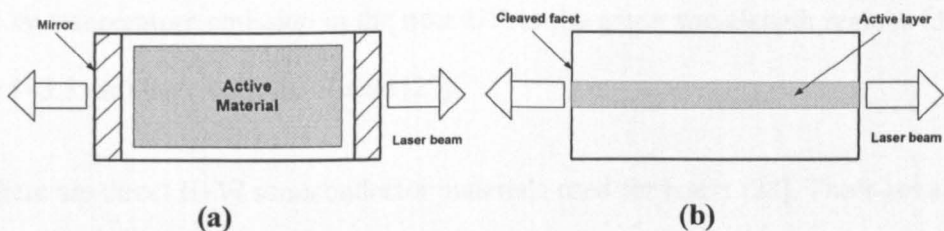


Fig. 2.6 Fabry-Perot interferometer: (a) laser and (b) laser diode [6] p. 58.

It must be noted though that, not all the spontaneously emitted light is used as input, because they have different wavelengths, phases, and propagation directions. Only spontaneous emission which obtains sufficient optical gain is amplified by stimulated emission and therefore has the same wavelength, phase,

and propagation direction as the input light. For this reason, laser sources are highly monochromatic, coherent, bright, and directional [6].

2.3 Semiconductor Lasers

Semiconductor lasers represent one of the most important classes of laser in use today, due to its large variety of direct applications. They also find a widespread use as pumps for solid-state lasers [20, 21]. The active medium of semiconductor lasers requires a direct-gap material, so normal elemental semiconductors (e.g., Si or Ge) are not used. Semiconductor laser materials are often based on a combination of elements in the third group of the periodic table (such as Al, Ga, In) and the fifth group (such as N, P, As, Sb). These are referred to as III–V compounds. Examples include the well-known GaAs [22, 23], as well as some ternary (e.g., AlGaAs, InGaAs) [24] and quaternary (e.g., InGaAsP) [25] alloys.

The CW laser emission wavelength of these III–V compounds recently ranges from 400–1600 nm. Currently, InGaN semiconductor lasers [26], providing CW room-temperature emission in the near UV to the green wavelength regions (380 to 543.5 nm) have been developed [27].

There are direct II–VI semiconductor materials used for lasers [28]. There are also some III–V materials which are indirect (e.g. $\text{Al}_x\text{Ga}_{1-x}\text{As}$: $x \geq 0.45$) [29].

2.3.1 Principle of semiconductor laser operation

Fig. 2.7 which shows the semiconductor valence band VB and conduction band CB separated by the energy gap E_g can be used to explain the operating principles of a semiconductor laser. For simplicity, we first assume that the semiconductor is

held at a temperature $T = 0$ K. For a nondegenerate semiconductor, the valence band is completely filled with electrons, while the conduction band is completely empty (see Fig. 2.7a; the hatched area is completely filled by electrons).

If some electrons are raised from the valence band to the conduction band by a suitable pumping mechanism, then after a very short time (~ 200 fs), electrons in the conduction band drop to the lowest unoccupied levels of this band. Any electron near the top of the valence band also drops to the lowest unoccupied levels, thus leaving holes at the top of the valence band (Fig. 2.7b). This introduces the quasi-Fermi levels F_n for the conduction band and F_p for the valence band.

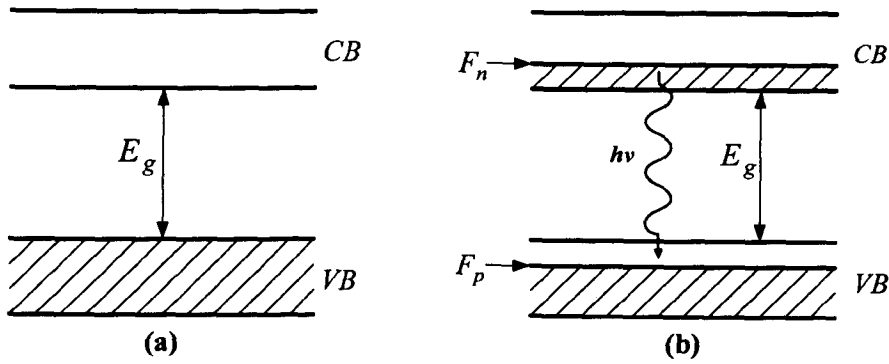


Fig. 2.7 The principle of operation of a semiconductor laser.

Light emission can now occur when an electron in the conduction band falls to the valence band to recombine with a hole. Stimulated emission from this recombination is what leads to laser action. This facilitates the condition for a photon to be amplified rather than absorbed by the semiconductor and is given by:

$$E_g \leq h\nu \leq F_n - F_p \quad (2.22)$$

Laser action then occurs when the total gain overcomes total cavity losses [30].

2.3.2 The threshold condition in lasers

As discussed earlier, two basic physical structures are required in all lasers:

1. A medium within which the optical gain occurs;
2. A mechanism of sustained laser oscillation through an optical feedback system.

Fig. 2.3.2.1 illustrates the fundamental structure of a laser diode (LD) with a Fabry-Perot (FP) cavity. Laser action will occur in the active medium when the round trip gain of the cavity balances that of the losses in the cavity. In other words, when the number of generated photons through stimulated emission equals the number of photons lost through absorption, scattering inside the cavity and emission through the mirror. This condition is called the threshold condition for a laser. This can be expressed as [31]:

$$G_{th} = \alpha_i + \frac{1}{2L} \ln \left(\frac{1}{R_1 R_2} \right), \quad (2.23)$$

where G_{th} is the modal gain at threshold, α_i is the internal loss in the cavity per unit length (this includes optical scattering and free carrier absorption), L is the cavity length and R_1 and R_2 are the mirror reflectivities [30].

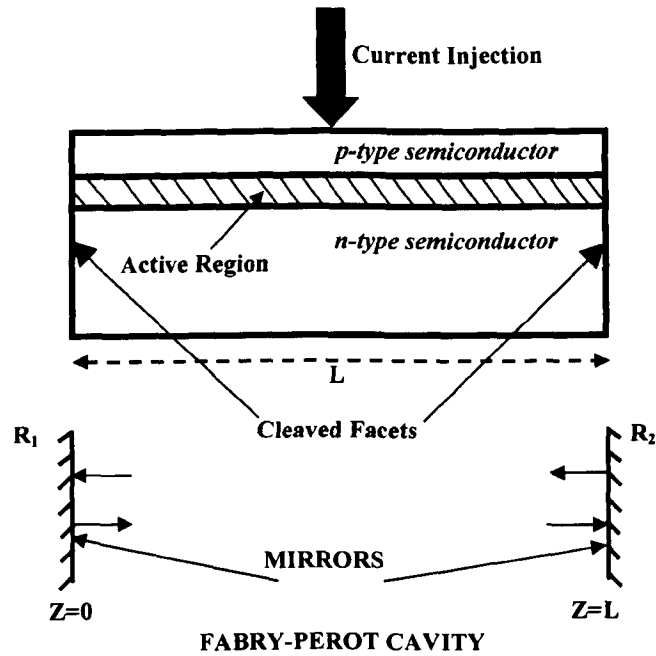


Fig. 2.8 Schematic diagram illustrating a semiconductor laser diode and its associated FP interferometer. The cleaved facets act like partially reflecting mirrors.

Also in Fig. 2.8, the optical intensity increases along the laser cavity with an initial intensity of I_0 from one end, R_1 , to the other end, R_2 , with a half trip intensity of $R_2 I_0 \exp(G - \alpha_i)L$. The total intensity for a trip will therefore be equal to $R_1 R_2 I_0 \exp(G - \alpha_i)2L$.

The active region of the material provides the gain for the photons. In modern LDs, where the active region is sandwiched between two cladding (or waveguiding) layers, the optical field penetrates into the cladding regions and the gain is only coupled to that part of the optical mode which is contained within the active region of the laser. Consequently, the modal gain G is related to the material gain g by a confinement factor Γ , which is defined as:

$$G = \Gamma g \quad (2.24)$$

The confinement factor is the overlap of the optical mode profile with the active region of the device and is defined by Eq. 2.25:

$$\Gamma = \frac{\int_{-d/2}^{+d/2} I(x) dx}{\int_{-\infty}^{+\infty} I(x) dx}, \quad (2.25)$$

where $I(x)$ is the intensity distribution of the optical mode and d is the width of the active region. Γ ($0 < \Gamma < 1$) gives the fraction of optical intensity in the active region and is a dimensionless quantity. Γ can have a typical value of less than 0.05 [19] for QW lasers where the active region thickness is 5-10 nm. It can approach unity when the thickness of the active region is larger than 0.2 μm .

The gain medium is normally electrically pumped using a forward-biased p - n diode structure with the injection of electrons and holes in the active layer which provides the gain. The laser is therefore controlled by the injection of current. This implies that the excitation density is controlled by the injected current density J . The value of J that is needed to overcome the cavity losses is referred to as the threshold current density J_{th} . Below this value, spontaneous emission predominates and there will be no lasing. Therefore, any increase above the J_{th} will lead to a strong rise in light emission. The characteristics in Fig. 2.9 [32, 33] show the emission of a LD above and below threshold.

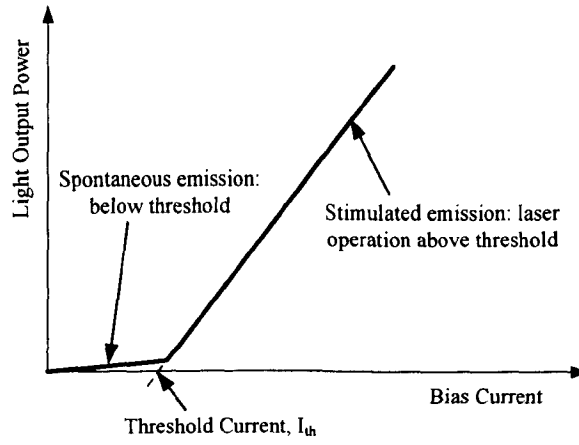


Fig. 2.9 Light output of laser diode above and below the laser threshold current.

2.3.3 Lasing wavelength and longitudinal modes

The condition for lasing described earlier does not in itself satisfy all the conditions necessary for lasing with regard to the threshold gain. Several longitudinal modes exist at threshold relative to the increase in current. The multimode nature of semiconductor lasers was a concern in the early days [34, 35]. Spontaneous emission is believed to have played an important role in determining the spectral characteristics of a semiconductor laser [36-40].

The longitudinal mode of lasing, must also satisfy the round trip phase matching condition [41], where the phase of the light after a complete round trip coincides with its initial phase. Algebraically, this can be written as:

$$m\lambda_m = 2L \quad (m = 1, 2, 3, \dots), \quad (2.26)$$

where m is the mode number and λ_m is the mode wavelength in the optical cavity.

If the refractive index of the waveguide is n_r , then Eq. 2.26 becomes:

$$m(\lambda_0 / n_r) = 2L \quad (m = 1, 2, 3, \dots), \quad (2.27)$$

where λ_0 is the wavelength in vacuum. Lasing occurs at wavelengths satisfying Eq. 2.27 when the gain reaches the threshold level. The gain profile is usually broad, as shown in Fig. 2.10. It shows the gain profile, Fabry-Perot modes and the corresponding lasing spectra. Due to the broadness of the gain profile, multiple modes can achieve the threshold condition and lase simultaneously. However, a few modes can predominate due to mode competition [42]. After the mode competition above threshold, single mode lasing can be achieved. Examples of multi-mode emission spectra and single mode emission after mode competition are shown in Fig. 2.11 [32] to illustrate the transformations.

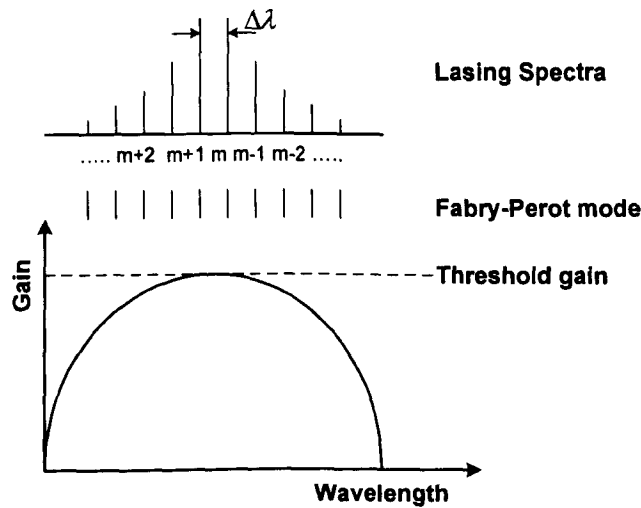


Fig. 2.10 The relationship between the gain spectra and longitudinal modes.

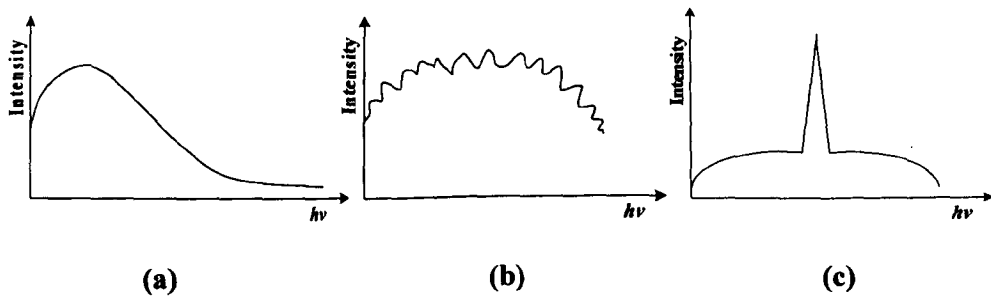


Fig. 2.11 Light intensity versus photon energy for laser diodes: (a) incoherent emission: below threshold; (b) laser modes: at threshold; and (c) dominant laser mode: above threshold.

2.4 Properties of Laser Beams

Laser radiation can be elucidated as being with an extremely high degree of monochromaticity, coherence, directionality, and brightness as will be discussed. Fig. 2.12 briefly explains and summarises some of the important properties of lasers [43].

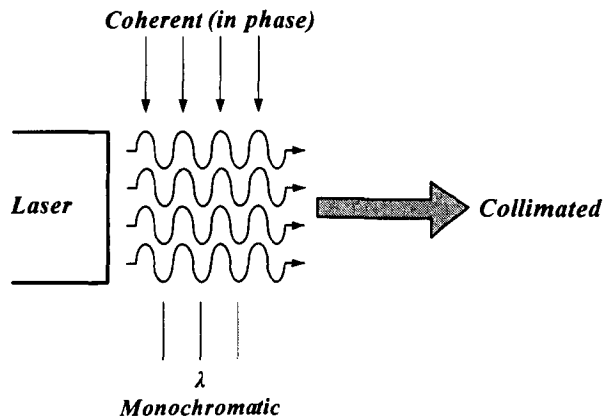


Fig. 2.12 Properties of laser light.

Generally, most lasers are monochromatic (single coloured) and nominally emit only one wavelength of light. In actual fact, lasers emit a range of wavelengths of light, but the range is so narrow it can often be considered as a single wavelength for most purposes [44]. Laser coherence is when all the light waves are in phase with one another, where all the peaks and valleys are lined up with each other. The more monochromatic a laser is the more coherent it is and the better the directionality of the beam. The collimation of a laser reduces the divergence of the beam and increases its brightness. It must be noted though that, brightness characterizes a laser beam as a whole, rather than being a spatially variable quality such as the intensity.

2.4.1 Beam Quality

The beam quality of a laser gives a measure of how well it can be focused. The beam quality of a laser beam can be defined in different ways, but it is essentially a measure of how tightly a laser beam can be focused under certain conditions (e.g. with a limited beam divergence). To achieve a good beam quality with a high optical output power, lateral mode profiles must be carefully controlled. In trying to control the lateral modes, the presence of higher order modes and filamentation increases the number of size of virtual sources inside of the cavity. This in turn limits the maximum achievable power density and prevent efficient fibre coupling [45, 46]. There are a variety of parameters used to characterise a laser beam and very different ways of determining them, including the beam divergence, beam astigmatism and the times-diffraction-limit factor or M^2 . The most common ways to quantify beam qualities are:

- the beam parameter product (BPP), i.e., the product of beam radius at the beam waist with the far-field beam divergence angle,
- the M^2 factor, defined as the beam parameter product divided by the corresponding product for a diffraction-limited Gaussian beam with the same wavelength,
- the inverse M^2 factor, which is high (ideally 1) for beams with high beam quality.

It is possible to some extent to improve the beam quality of a laser beam with a nonresonant mode cleaner or a mode cleaner cavity. This, however, leads to some

loss of optical power. Beam quality deterioration of lasers is possible and can be caused by intracavity beam distortions [47].

The brightness of a laser is determined by its output power together with its beam quality. According to ISO Standard 11146 [48], the beam quality factor M^2 can be calculated [49] with a fitting procedure, applied to the measured evolution of the beam radius along the propagation direction. For correct results, the exact definition of the beam radius must be clearly defined. A high beam quality can be important e.g. when strong focusing of a beam is required. In the area of laser material processing, printing, marking, cutting and drilling require high beam qualities. Welding and various kinds of surface treatment are less critical in this respect, because they work with larger spots, so that direct application of high-power laser diodes with poor beam quality is acceptable.

2.4.1.1 Astigmatism

Astigmatism is the cause of the elliptical shape beam (shown in Fig. 2.22) of a laser diode. This is because a beam has different virtual point sources for the parallel (top view) and perpendicular (side view) directions on the active layer of laser diode. For this reason a laser diode with a large astigmatism must incorporate external lenses if the beam is to be accurately focused or collimated. Fig. 2.13 is a schematic diagram showing the problem of astigmatism. The angle of the parallel ($8^\circ - 10^\circ$) and perpendicular ($30^\circ - 70^\circ$) axis of the elliptically shaped beam is known as the beam divergence.

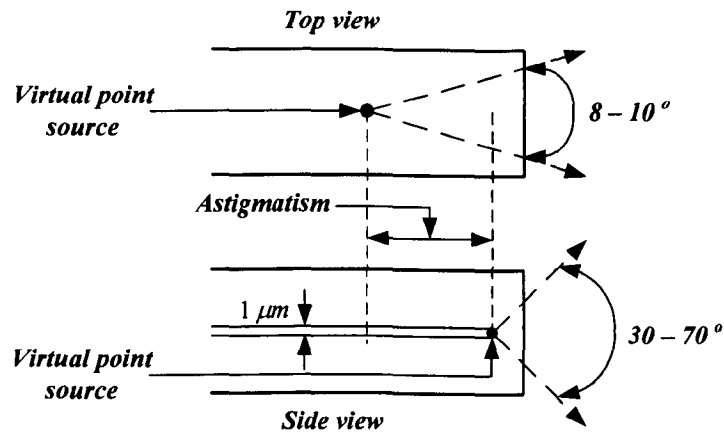


Fig. 2.13 Schematic diagram showing the problem of astigmatism.

The divergence of the beam is due to diffraction as a beam of light passes through an aperture. A spreading of the beam occurs because of diffraction as the beam passes through an aperture. Near-field or Fresnel diffraction is observed when the observed point is close to the diffracting aperture. Far-field or Fraunhofer diffraction is observed when the observed point is much further away from the diffracting aperture. If the distance between the diffracting aperture and the observation point is L and s is half the largest diameter of the diffracting aperture, then at a wavelength of λ_0 , the near-field diffraction is observed when $L < s^2 / \lambda_0$ and far-field diffraction is observed when $L > s^2 / \lambda_0$. Diffraction effects are most noticeable when the size of the opening is comparable to the wavelength of the light passing through it [46, 50]. Astigmatism therefore can be defined as the difference in virtual point source of the parallel and perpendicular beams.

Several methods have been commercially used to circularize beams from diode lasers. The most popular include prism pairs, cylindrical lenses, spatial filters, and perpendicular bi-focal cylindrical lenses. However, none of the approaches have yielded perfect Gaussian beams.

2.4.1.2 Brightness

The term brightness is often used in the context of lasers and laser beams, but often with a purely descriptive, non-quantitative meaning. Brightness is related to the output power and beam quality of a laser. It is quantitatively synonymous with luminance. In the context of laser technology, the brightness of a laser source (in a quantitative sense) is generally understood as being equivalent to its radiance, which is the total power divided by the product of the mode area in the focus and the solid angle in the far-field; the units are then usually $W.sr^{-1}.cm^{-2}$.

For a diffraction-limited beam with moderate divergence, the relation between beam divergence and beam radius can be used to obtain:

$$B = \frac{P}{\pi w_0 \pi \theta^2} = \frac{P}{\pi w_0 \pi \left(\frac{\lambda}{\pi w_0} \right)^2} = \frac{P}{\lambda^2}, \quad (2.28)$$

where w_0 is the beam radius at the beam waist, θ is beam divergence, λ the wavelength and P is power. This shows that apart from the power and beam quality, the brightness depends on the wavelength. For a non-diffraction-limited beam, the brightness is reduced by a factor which is the product of the M^2 beam quality factors.

Another possible definition is to take the optical power divided by the product of M^2 factors. For diffraction-limited beams, this quantity is identical with the optical power, and in general it is a good measure of the maximum optical intensity of a focus which can be generated with a certain aperture and working distance, i.e., with a limited beam divergence.

It must be noted that brightness characterizes a laser beam as a whole, rather than being a spatially variable quality such as the intensity.

2.4.1.3 M^2 factor

The M^2 factor, which is also called *beam quality factor* or *beam propagation factor*, is a parameter for quantifying the beam quality of laser beams. According to ISO Standard 11146 [48], it is defined as the beam parameter product divided by λ/π , the latter being the *beam parameter product* for a diffraction-limited Gaussian beam with the same wavelength. In other words, the half-angle beam divergence is

$$\theta = M^2 \frac{\lambda}{\pi w_0}, \quad (2.29)$$

where w_0 is the beam radius at the beam waist and λ the wavelength. A laser beam is often said to be “ M^2 times diffraction-limited”. To properly evaluate the quality of a laser beam, Siegman introduced the times diffraction-limited, M^2 [51, 52].

A diffraction-limited beam has an M^2 factor of 1, and is a Gaussian beam. Smaller values of M^2 are physically not possible. For a real laser beam, the M^2 factor must be greater than or equal to unity. The lower the value of M^2 , the better is the beam quality and the smaller is the spot of the focused laser beam.

The M^2 factor of a laser beam limits the degree to which the beam can be focused for a given beam divergence angle, which is often limited by the numerical aperture of the focusing lens. Together with the optical power, the beam quality factor determines the brightness (more precisely, the radiance) of a laser beam.

2.5 Introduction to High Power Laser Diodes

Three important improvements in the manufacture of HPLDs are known to have led to the success they enjoy in the past 20 years. These are: i) the use of quantum well heterostructures in the active regions to achieve low threshold current and high differential quantum efficiency; ii) the use of mirror coatings to reduce rapid mirror degradation and catastrophic optical mirror damage; iii) the use of efficient heat removal techniques. Some of the techniques used in HPLDs will be discussed in this section.

2.5.1 The nature of semiconductor lasers

Semiconductor lasers generate light from the recombination of EHPs at a forward-biased junction. The power of the light output is proportional to the drive current, with the output wavelength depending on the material's bandgap energy. Laser diodes produce low levels of incoherent emission when the current passing through them is below the threshold current necessary for lasing. For lasing to occur, the current concentration must be high enough for stimulated emission from the EHPs to dominate over absorption at the junction. In other words, there must be a population inversion at the junction as discussed earlier.

Spontaneous emission can go in any direction, but in lasers a pair of reflective surfaces help confine the stimulated emission to a certain direction. Typically, structures within the laser confine the stimulated emission to a stripe in the junction plane, as shown in Fig. 2.14. The structure in Fig. 2.14 is more simple than actual semiconductor lasers [44]. Some lasers emit from both facets.

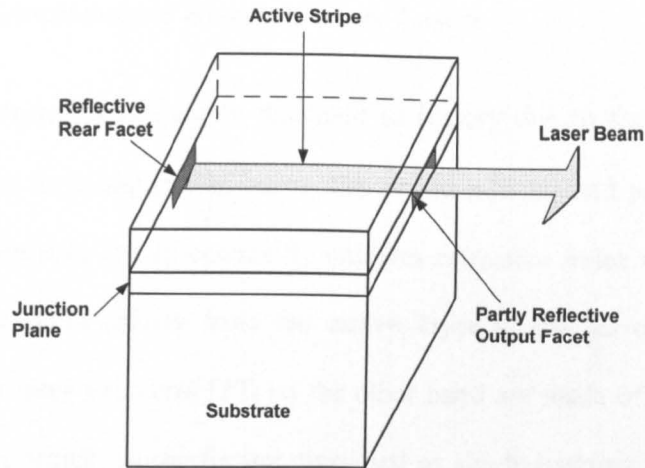


Fig. 2.14 Simple structure of semiconductor laser.

2.5.2 Structure of semiconductor lasers

Semiconductor laser action was first observed in 1962 simultaneously by four groups [53-56], three of which were using a GaAs p - n junction diode. The devices developed used the same material for both the p and n sides of the junction and therefore are referred to as homojunction lasers. Homojunction lasers are now only of historical importance and have been replaced by the double-heterostructure (DH) laser, whose active medium is sandwiched between p and n materials that differ from the active material. The invention of the heterojunction laser diode led to the operation of the semiconductor laser in CW at room temperature. Other structures have evolved such as quantum well (QW), quantum wire (QWR), and quantum dot (QD) laser diodes. The structures studied in this thesis are based on the QW and therefore will be considered in more detail in this chapter.

2.5.3 Homostructure and Heterostructure Lasers

Homojunction lasers were quickly relegated to history due to their inefficiency. This is because in homojunction lasers, the semiconductor had poor carrier and photon confinements. It had essentially uniform refractive index throughout and therefore light could diffuse from the active layer to the surrounding layers. Heterojunction laser structures [57] on the other hand are made of two dissimilar semiconductors which can be further classified as single-heterostructure (SH) or double-heterostructure (DH) devices. The classification is based on whether the active region is surrounded on one side or both sides by a cladding layer of higher bandgap. Fig. 2.15 shows the schematic structures of both the homostructure and the heterostructure laser [30]. The advantage of using different materials is that they confine light better in the active region, making stimulated emission more efficient. Heterojunction structures confine the injected electrons and holes in a narrow region which requires less current to establish the required concentration of electrons for population inversion. The construction of a dielectric waveguide around the optical gain region also increases the photon concentration which in turn increases the probability of stimulated emission.

However, they also require careful matching of the lattice constants of the two semiconductors. Two physical reasons account for the reduction in the threshold current density of a heterostructure device [58]: i) higher bandgap of the cladding layer which helps to better confine electrons and holes in the active layer; ii) the lower refractive index difference confines the optical mode close to the active layer, which significantly reduces internal losses [59]. Fig. 2.16 [30] shows the

schematic illustration of the simultaneous confinement of the charge carriers and the optical mode to the active region occurring in a DH semiconductor laser.

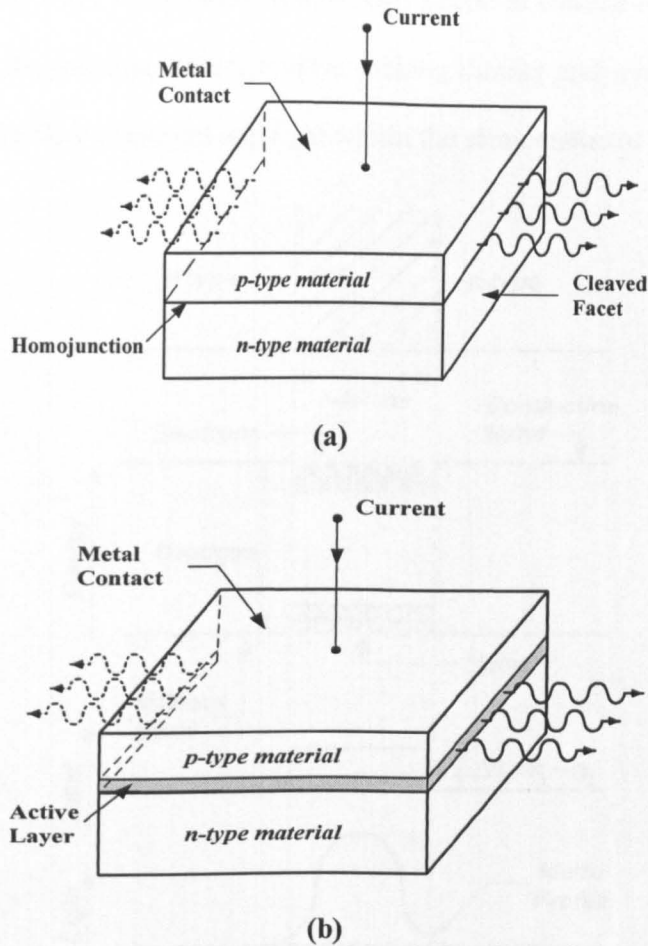


Fig. 2.15 Schematic illustration of (a) a homostructure and (b) a double-heterostructure laser. The vicinity of the homojunction is the depletion region. The shaded area shows the thin ($\sim 0.2 \mu\text{m}$) active layer of a semiconductor material, whose bandgap energy is slightly lower than that of the surrounding cladding layers [30] p. 2.

The DH semiconductor laser shown in Fig. 2.15 is sometimes called a broad-area (BA) laser because it has no extrinsic mechanism for the lateral confinement of the injected current or the optical mode. (Lateral optical confinement relies on

gain guiding.) DH lasers are more efficient and can generate a CW beam at room temperature. This approach is used in all commercial diode lasers, and has been refined in many ways. While some refinements intend to confine light to a narrow stripe within the junction, others involve making thinner and thinner layers that also control the flow of current and light within the semiconductor [44].

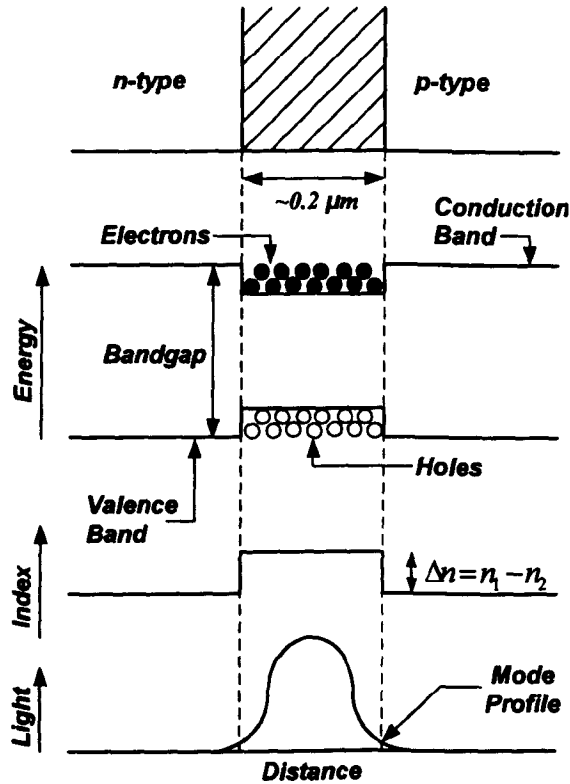


Fig. 2.16 Schematic illustration of the simultaneous confinement of the charge carriers and the optical mode to the active region occurring in a DH semiconductor laser [30] p. 3.

2.5.4 Broad waveguide lasers

The transverse spot of the optical mode has to be large to minimize the optical power density at the facet of a laser. This leads to the design of the broad waveguide (BW) or the large optical cavity (LOC) lasers. The waveguiding layer

is made thick ($1\ \mu\text{m}$) in order to reduce the optical confinement factor, Γ . The increase in the equivalent optical spot size d/Γ (where d is active layer thickness and Γ is the confinement factor) has also been shown to reduce filamentation effects [60]. Filamentations are caused due to beam self-focusing, forming optical filaments which lead to non-uniform optical distribution.

High CW powers of broad waveguide lasers have been demonstrated [61]. This BW device had a low internal loss of between $1\text{--}1.5\ \text{cm}^{-1}$, high external differential quantum efficiency of 72% and good wallplug efficiency of 47%. Lower internal losses and longer cavity lengths can help reduce the current density and junction heating [62].

2.5.5 Broad area lasers

Broad area laser diodes (also called *broad stripe* or *broad emitter laser diodes*) are edge-emitting laser diodes where the emitting region at the front facet has the shape of a broad stripe. They have typical dimensions of e.g. $1\ \mu\text{m} \times 100\ \mu\text{m}$. Due to the asymmetry of the emitter, the beam properties are also completely different in both the vertical (fast axis) and the longitudinal (slow axis) directions.

The broader the stripe, the higher is the achievable power, but the worse is the beam quality in the “slow” direction. The technological trend is to obtain higher and higher powers even from narrow stripes, but this is limited by the high optical intensity at the front facet (which can lead to catastrophic failure) and possibly by thermal issues. Special techniques of facet passivation can be used to allow for higher powers. For a $100\ \mu\text{m}$ wide aperture, the output power of a commercial device is typically a few watts or up to the order of 10 W.

The strongly asymmetric beam profile and the large divergence in the “fast” direction requires special care, e.g. for properly collimating the output of a broad area laser. A common method is the use of a cylindrical “fast axis collimator” lens with high numerical aperture in close proximity to the diode facet. Such a lens collimates the beam in the fast axis direction, before the beam radius becomes too large. A second cylindrical lens at a larger distance may then be used for collimation in the slow axis direction. By choosing lenses with suitable focal lengths, a circular beam can be obtained, which however will have different divergence angles in the two directions due to the different beam quality values.

Broad area laser diodes are often used for pumping solid-state lasers. A device with a 200 μm broad emitter may emit e.g. 2–4 W, so that the pumped laser may emit up to ~ 2 W. The laser diode is often mounted on a thermoelectric cooler, which makes it possible to tune the emission wavelength within a few nanometers, so that the emission peak can be matched to the absorption maximum of the laser crystal.

The combination of several broad area emitters in a single device leads to a diode bar, which can emit tens of watts and more than 100 W of optical power. This has been the approach employed in many commercial high power lasers, because it is relatively simple to fabricate. High CW powers of broad area lasers have been demonstrated [63-66]. However, a diode bar has a lower brightness than a single-emitter laser, despite the higher output power, because the beam quality is much lower. For that reason, the design of a diode-pumped laser is generally simpler when using broad-area diodes for pumping. To achieve even higher powers, these

laser bars can be combined in a two dimensional (2D) ‘rack-and-stack’ configuration to produce powers of up to several kilowatts.

2.5.6 Tapered lasers

The design of high brightness tapered lasers has received great attention due to the technological simplicity of their fabrication. A number of groups have reported on their improved beam quality and high output powers at different wavelengths [67-70]. A generic tapered laser consists of a ridge waveguide (RW) section and a tapered amplifier section, shown in the schematic diagram of Fig. 2.17.

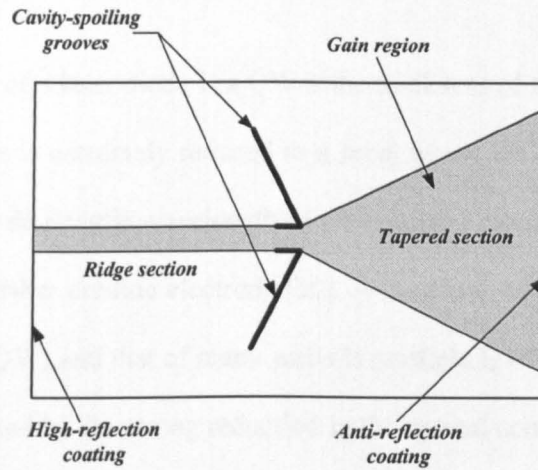


Fig. 2.17 Plan view schematic diagram of a tapered laser.

The straight waveguide section serves as a modal filter and ensures that the tapered amplifier is only excited by the fundamental transverse mode of the straight waveguide. Fundamental transverse modes are desired because in optics and particularly in laser physics, laser beams often occur in the form of Gaussian beams. The transverse profile of the optical intensity of the beam with a power P

can be described with a Gaussian function. Gaussian beams are usually considered in situations where the beam divergence is relatively small.

The tapered amplifier section allows the optical beam to spread out gradually (without exciting the higher order lateral modes), so as to lower the optical power density at the facet. Cavity spoiling grooves may also be etched at the narrow end of the taper to suppress Fabry-Perot cavity modes which oscillate parallel to the two facets. Such Fabry-Perot modes can introduce unwanted higher order modes in the taper gain section and can cause absorption in the unpumped regions.

2.5.7 Quantum well (QW) lasers

The active region of a laser diode is a QW if the thickness of the active layer (<10 nm) of a DH laser is extremely reduced to a level where the dimension becomes comparable to the de Broglie wavelength of the confined electron or hole [18, 71]. This is done to further confine electrons [30]. A structure with one well is called the single QW (SQW) and that of many wells is multiple QW (MQW). QW lasers are however affected by the strong reduction in the optical confinement factor due to the reduced layer thickness. To improve beam quality in the QW direction, a separate confinement structure is used.

2.5.7.1 QW structures

The fundamental QW structure alone does not answer all the questions in improving the carrier confinement and optical confinement in the well and therefore needs some modification to achieve that. The separate confinement structure is used to further improve upon the optical confinement. Two examples of such structures are available: the separate confinement heterostructure (SCH)

and the graded refractive index separate confinement heterostructure (GRINSCH), shown in Figs. 2.18 (b), (c) and (d) respectively. Fig. 2.18 (a) shows the basic structure of the QW laser structure.

In the SCH and GRINSCH laser structures, the refractive indices of the layers adjacent to the well are set at values higher than those of the outside layers in order to improve upon the confinement of light into the SCH and GRINSCH regions. In both structures, the carriers are confined by the QW structure, while the optical mode is confined by the step index or graded index profile.

Due to the strong reduction in the active layer thickness, there is further reduction in the threshold current density J_{th} . This threshold current density reduction is made possible by the combination of the following features:

- 1) Reduction by the strong decrease in the layer thickness once the problem of beam confinement is overcome by the introduction of a separate confinement structure.
- 2) Provision of the separate confinement structure, which increases the differential gain in a QW compared to a corresponding bulk material.

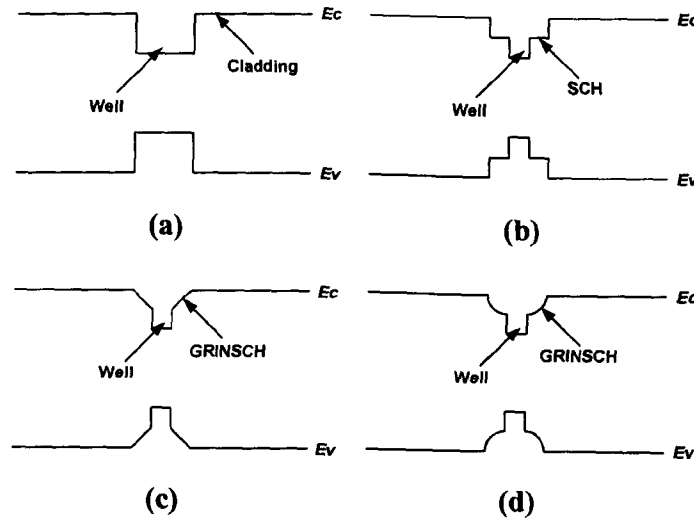


Fig. 2.18 Examples of typical QW active region structure.

2.5.7.2 Strained QW lasers

In DH lasers, a precise lattice match between two heterostructures (within better than 0.1%) must be achieved. However, in a strained QW, some level of lattice mismatch with the surrounding layers (up to ~1–3%) can be tolerated without creating excessive misfit dislocations (these can introduce defects which can severely degrade the device during operation) [72]. The strained QW structure therefore introduces a compressive or tensile strain in the QW due to the lattice mismatch. This strain can be exploited to control the emission wavelength to achieve wavelengths that previously could not be achieved. This means that if the lattice mismatch is less than a few percent and the well width is less than some critical thickness, then a QW without any misfit dislocations can be formed from two semiconductors with different lattice constants. This type of well is called a pseudomorphically strained QW.

Two main advantages can be derived from strained QWs: 1. They can produce laser action at wavelengths previously not attainable (e.g., 900–1100 nm for

$\text{In}_x\text{Ga}_{1-x}\text{As}/\text{GaAs}$); 2. They can increase the differential gain and thereby reduce the threshold current density and improve the efficiency. Also, this kind of structure can result in a further reduction in the threshold current density by changing the optical density of states of the QW gain material [33]. Due to the degree of confinement of carriers, the dispersion relation along the confinement direction is changed. The change in dispersion relation results in a change in the density of states. The density of states for a QW is a step function with steps occurring at the energy of each quantised level and therefore close to the bandedge than corresponding bulk material [73].

2.5.7.3 Absorption and emission in QWs

The properties of optical absorption in QWs were first reported by Dingle *et al.* [74] and Chang *et al.* [75]. It is therefore evident that the absorption and emission processes in a QW are different to those in bulk semiconductors (e.g. in a DH laser). When the thickness of the active layer (L_z) is comparable to the de Broglie wavelength in Fig. 2.19, the kinetic energy corresponding to the carrier motion along the z direction is quantised into discrete energy levels. The energy levels of the carriers can be obtained by solving the Schrödinger equation for a one-dimensional potential well [30]. Fig 2.19 shows the energy levels of electrons and holes confined within a quantum well [30]. The peak energy position of the QW emission is given by:

$$h\nu = E_g + E_e + E_h, \quad (2.30)$$

where E_g is the bandgap energy of the well material. The carrier energy levels are denoted by E_{1c} , E_{2c} and E_{3c} for electrons, E_{1hh} , E_{2hh} and E_{3hh} for heavy holes and

E_{1lh} and E_{2lh} for the light holes. These energy levels are a function of the well width, L_z .

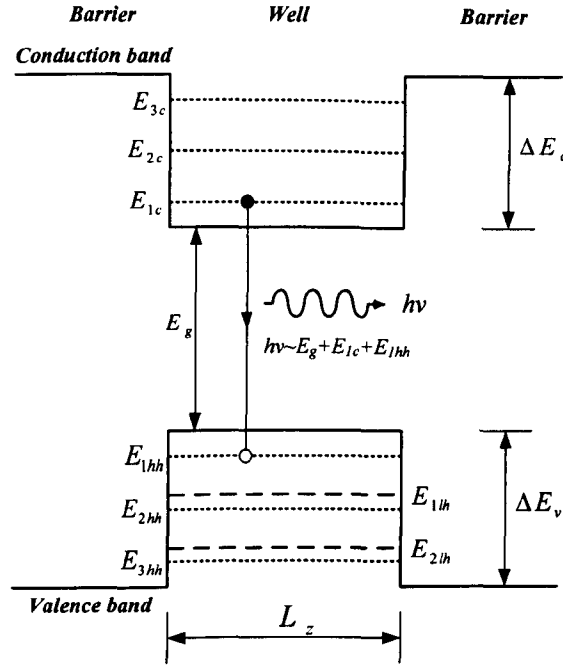


Fig. 2.19 The energy levels in a single finite quantum well showing the confined energy levels of the electrons and holes.

Both conduction and valence band edges are shifted due to strain. The dependence of the energy levels on L_z leads to a shift in the band edge absorption and emission energies. The tensile strain causes a decrease of the bandgap energy and a compressive strain causes an increase of the bandgap energy.

2.6 Typical Laser Diode Structures – Arrays and Stacks

Appropriate designs of laser diodes can help in the optimisation of the output powers. The most common method used to achieve this is the use of linear arrays of broad area emitters typically fabricated as a 1 cm wide bar. A bar often contains between 20 and 50 emitters (cavity lengths between 600 and 900 μm),

which are electrically and optically isolated from each other. The emitters are, however, connected in parallel with a common anode and cathode, and mounted on a common heatsink. The schematic diagram of such a monolithic block, consisting of arrays of emitters, is shown in Fig. 2.20.

Many commercially available high-power lasers employ this approach to fabricate and achieve high output powers. A single 1 cm bar of continuous wave can produce powers of over 700 W [76]. Also, commercial laser diode stacks can achieve output powers in excess of 5000 W, but may compromise on good beam quality.

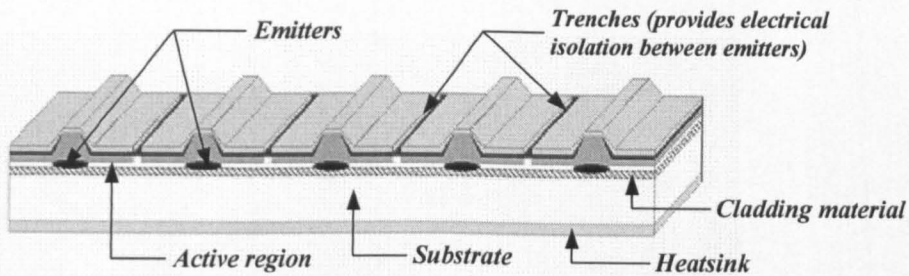


Fig. 2.20 Schematic diagram of electrically and optically separated single emitters of a HPLD bar.

2.6.1 A typical 1 cm bar laser structure

Laser diodes are connected in parallel to form a laser bar as shown in Fig. 2.21 in order to increase the output power [77]. The individual laser diodes which constitute the bar are known as emitters. These emitters are optically isolated by a deep etching of the active material between adjacent emitters or by the introduction of absorbing materials in the inter-emitter region. The laser bar can be referred to as constituting an array of emitters forming a monolithic block. The laser bar processing defines the array dimensions of a bar, such as the emitter width and the number of emitters per bar (which is 20 emitters in Fig. 2.21).

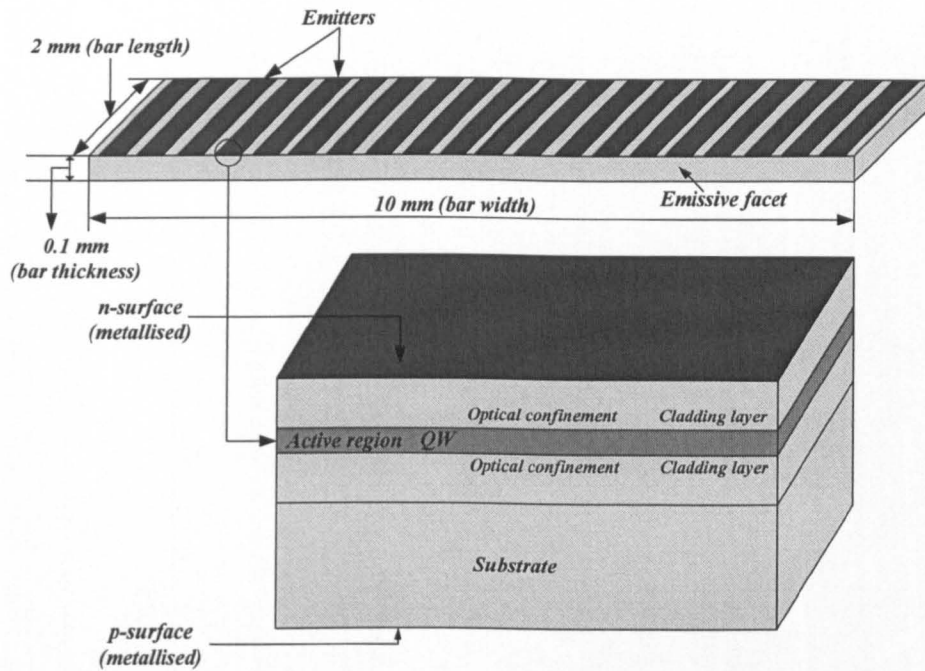


Fig. 2.21 A drawing showing a typical 1-cm-bar with a cavity length of 2 mm and a thickness of 100 μm [77] p. 218.

The fill factor is a parameter of a laser bar which is directly related to the bar output power. It is defined as the ratio of the total width of the emitters (defined by the emitter width multiplied by the number of emitters) to the total bar width. The length of a bar corresponds to the cavity length and not to the highest dimension of the bar (called the bar width).

The issue of thermal crosstalk between emitters will always limit the power density of the individual emitters. The issue of temperature has been looked at extensively in the investigations described later in this thesis. The bottom line is the cost implication and the intended application of the laser diode bar. Low fill factor's show generally superior performance in many applications, but high fill factor's need significantly less semiconductor material as explained by R. Fehse *et al.* [78] and J Boucart *et al.* [79].

2.7 Mounting Technology and Heatsinks

Laser diodes are being pushed to higher power levels. Therefore, the dissipation of heat is crucial especially in the centre of bars. It is also very important that lasers are effectively packaged and mounted [16, 80] in order to minimise packaging-induced strain [81]. For example, it is well established that the threshold current of a laser diode increases and its external quantum efficiency decreases as temperature increases. Therefore, when the temperatures of a bar go unchecked, central emitters within a bar are the worst affected even though they may emit more power initially. They will continue to give off more power as long as they remain undegraded until degradation sets in, which is precipitated by the continuous increase in temperature. Thus, for the efficient and effective performance of laser diodes, the rise in temperature must be checked and made as small as possible.

The mounting of the laser diode on the heatsink permits the removal of heat and establishes the electrical contact for both sides (p and n sides) of the laser. The narrow waveguide in the direction of the pn -junction ('optical fast axis') produces a high beam divergence and the wide emitter stripe on the plane of the pn -junction ('slow axis') produces a smaller beam divergence, as shown in Fig. 2.22. This results in the intensity distribution of the beam, having an elliptical shape, as seen in Fig 2.22. Fig. 2.22 [77] shows schematically a mounted laser bar, indicating the 'fast axis' and the 'slow axis'. This also relates to the astigmatism of the larger beam. Fig. 2.22 also shows the mounting of a laser bar with the p-surface facing down and close to the heatsink. This is to ensure that the QW active region is as

close as possible to the heatsink to enhance efficient heat dissipation from the device.

The choice of solder and heatsink is dictated by the thermal conductivities, the solder temperature, and the coefficient of thermal expansion of the materials (heatsink and bar materials). The reason for this is to achieve the lowest possible thermal resistance while simultaneously avoiding stress and strain induced by the packaging.

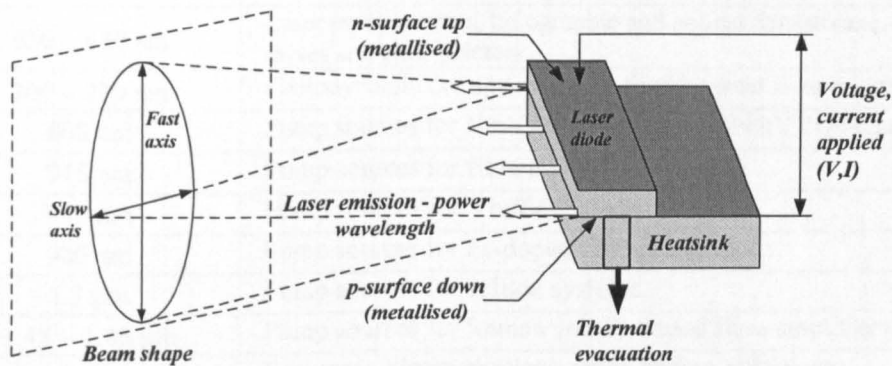


Fig. 2.22 Schematic diagram of a mounted laser bar [77] p. 218.

For effective dissipation of heat, bars are usually packaged by soldering their active side onto heat spreaders with low thermal resistance, e.g. diamond or Cu-W. The heat spreaders are soldered onto the heatsink with an In-based soft solder or an AuSn-based hard solder [33]. Bars are also sometimes soldered directly onto a heatsink without the use of heat spreaders.

2.8 Applications of High Power Laser Diodes

The technological advancement in the manufacture of HPLDs has brought in its wake improved efficiency and reliability. This has also attracted a surge in its application. A list of typical applications are summarised in Table 2.2 [30, 41, 82].

These applications require some emission wavelength material systems to achieve them and these are shown in Table 2.3.

Table 2.2 Applications of HPLDs according to their wavelengths.

Wavelength	Applications
375 nm	Excitation of Hoechst stain (fluorescent stains for labeling DNA in fluorescence microscopy).
400 nm	Recording sources for next generation optical disks.
405 nm	Flourescence spectroscopy imaging for PPT
500 – 600 nm	Laser projectors and pointers.
630 nm	Photodynamic therapy, display related applications.
650 – 680 nm	Laser pump sources, holographic and optical data storage, DVD drives and laser pointers.
700 – 780 nm	Photodynamic therapy, printing, femtosecond laser pumping.
808 nm	Pump sources for Nd:YAG, Nd:YLF and Nd:YVO4 lasers.
915 nm	Pump sources for fibre lasers.
940 nm	Pump sources for Yb:YAG lasers.
980 nm	Pump sources for Er-doped fibre amplifiers.
1.3 μm	Pump sources for soliton systems.
1.45 – 1.48 μm	Pump sources for Raman and Er-doped fibre amplifiers.
1.5 – 1.6 μm	Free-space communications, range finding and surgery.
1.7 – 5.0 μm	Laser radar (LIDAR), remote sensing and laser medicine.

Table 2.3 Wavelength ranges of differential material systems of HPLDs.

Material System	Wavelength Range (μm)	Substrate
$\text{Al}_x\text{Ga}_{1-x}\text{N}$	0.2 – 0.36	Sapphire/SiC
$\text{In}_x\text{Ga}_{1-x}\text{N}$	0.36 – 0.6	Sapphire/SiC
$\text{Al}_x\text{Ga}_{1-x}\text{As}$	0.6 – 0.9	GaAs
$\text{In}_x\text{Ga}_{1-x}\text{As}$	0.6 – 1.3	GaAs
$\text{In}_x\text{Al}_y\text{Ga}_{1-x-y}\text{As}$	0.9 – 1.4	GaAs
$\text{In}_{1-x}\text{Ga}_x\text{As}_{1-y}\text{P}_y$	1.1 – 1.65	InP
$\text{Ga}_x\text{As}_{1-x}\text{P}$	0.6 – 0.9	GaAs
$\text{InAs}_x\text{P}_{1-x}$	0.93 – 3	InP
$\text{In}_x\text{Al}_y\text{Ga}_{1-x-y}\text{P}$	0.6 – 0.8	InP
$\text{In}_x\text{Ga}_x\text{As}_{1-y}\text{Sb}_y$	1.7 – 5	GaSb

References

- [1] K. Ertel, S. Banerjee, P. D. Mason, C. Hernandez-Gomez, and J. L. Collier, "HiPER and ELI: multi-kilojoule-class DPSSLs for laser fusion and ultra high intensity research," *2nd High Power Diode Lasers and Systems Meeting (HPDLS), Coventry, UK, KEYNOTE*, 2009.
- [2] K. Clem, "Rendezvous Sensor Technology Launches on Next Space Shuttle Flight," *Johnson Space Center, Houston*, 2010.
- [3] T. J. Hawbaker, T. Gobakken, A. Lesak, E. Tromborg, K. Contrucci, and V. Radeloff, "Light Detection and Ranging-Based Measures of Mixed Hardwood Forest Structure," *Forest Science*, vol. 56, pp. 313-326, Jun 2010.
- [4] K. Hausler, U. Zeimer, B. Sumpf, G. Erbert, and G. Trankle, "Degradation model analysis of laser diodes," *Journal of Materials Science-Materials in Electronics*, vol. 19, pp. S160-S164, 2008.
- [5] K. Petermann, *Laser Diode Modulation and Noise*: Kluwer Academic Publishers; Tokyo : KTH Scientific Publishers, 1988.
- [6] T. Numai, *Fundamentals of Semiconductor Lasers (Springer Series in Optical Sciences)*: Springer-Verlag, New York, 2004.
- [7] W. Koechner and M. Bass, *Solid-State Lasers: A Graduate Text*: Springer, 2003.
- [8] A. Yariv, *Quantum Electronics*: Wiley, New York, 4th ed., 1991.
- [9] A. E. Siegman, *Lasers*: University Science Books, Mill Valley, California, 1986.
- [10] J.-m. Liu, *Photonic Devices*: Cambridge University Press, 2005.
- [11] P. Y. Yu and M. Cardona, *Fundamentals of Semiconductors*: Springer-Verlag Berlin and Heidelberg GmbH & Co. K; 2nd edition, 1999.
- [12] Y. Horikoshi and Y. Furukawa, "Temperature sensitive threshold current of InGaAsP-InP double heterostructure lasers," *Japanese Journal of Applied Physics*, vol. 18, pp. 809-815, 1979.
- [13] N. K. Dutta and R. J. Nelson, "Temperature-dependence of threshold of InGaAsP-InP double-heterostructure lasers and Auger recombination," *Applied Physics Letters*, vol. 38, pp. 407-409, 1981.
- [14] A. Sugimura, "Band-to-band Auger recombination effect on InGaAsP laser threshold," *IEEE Journal of Quantum Electronics*, vol. 17, pp. 627-635, 1981.
- [15] A. M. Stoneham, *Theory of defects in solids*: Oxford Univ. Press, 1975.
- [16] H. Kressel and J. K. Butler, *Semiconductor Lasers and Heterojunction LEDs*: Academic Press, Inc., London, 1977.
- [17] C. Kittel, *Introduction to Solid State Physics*: Wiley & Sons, Inc., NY, Chichester, Brisbane, Toronto, Singapore, 7th edition 1996.

- [18] O. Svelto, *Principles of Lasers* Springer; 4th ed. Corr. 5th printing edition, 1998.
- [19] H. C. Casey and M. B. Panish, *Heterostructure Lasers, Part A: Fundamental Principles*: Academic Press Ltd.; London, 1978.
- [20] G. P. Agrawal, *Semiconductor Lasers: Past, Present, Future*: Amer Inst of Physics, Woodbury, New York, 1995.
- [21] G. P. Agrawal and N. K. Dutta, *Long Wavelength Semiconductor Lasers*: Springer; 1 edition, 1986.
- [22] Z. C. Niu, S. Y. Zhang, H. Q. Ni, D. H. Wu, H. Zhao, H. L. Peng, Y. Q. Xu, S. Y. Li, Z. H. He, Z. W. Ren, Q. Han, X. H. Yang, Y. Du, and R. H. Wu, "GaAs-based room-temperature continuous-wave 1.59 μm GaInNAsSb single-quantum-well laser diode grown by molecular-beam epitaxy," *Applied Physics Letters*, vol. 87, pp. 231121-3, 2005.
- [23] N. Yamamoto, K. Akahane, S. Gozu, and N. Ohtani, "Over 1.3 μm continuous-wave laser emission from InGaSb quantum-dot laser diode fabricated on GaAs substrates," *Applied Physics Letters*, vol. 86, pp. 203118-3, 2005.
- [24] G. W. Yang, R. J. Hwu, Z. T. Xu, and X. Y. Ma, "Design consideration and performance of high-power and high-brightness InGaAs-InGaAsP-AlGaAs quantum-well diode lasers ($\lambda=0.98 \mu\text{m}$)," *IEEE Journal of Selected Topics in Quantum Electronics*, vol. 6, pp. 577-584, Jul-Aug 2000.
- [25] T. Fukushima, T. Tanaka, and T. Harayama, "Ring and axis mode switching in multielectrode strained InGaAsP multiple-quantum-well quasistadium laser diodes," *Applied Physics Letters*, vol. 87, pp. 191103-3, 2005.
- [26] L. Marona, P. Wisniewski, P. Prystawko, I. Grzegory, T. Suski, S. Porowski, P. Perlin, R. Czernecki, and M. Leszczynski, "Degradation mechanisms in InGaN laser diodes grown on bulk GaN crystals," *Applied Physics Letters*, vol. 88, pp. 201111-3, 2006.
- [27] T. Meyer, H. Braun, U. T. Schwarz, S. Tautz, M. Schillgalies, S. Lutgen, and U. Strauss, "Spectral dynamics of 405 nm (Al,In)GaN laser diodes grown on GaN and SiC substrate," *Optics Express*, vol. 16, pp. 6833-6845, May 2008.
- [28] W. Faschinger and J. Nurnberger, "Green II-VI light emitting diodes with long lifetime on InP substrate," *Applied Physics Letters*, vol. 77, pp. 187-189, 2000.
- [29] I. V. Berman, E. V. Bogdanov, H. Kissel, N. Y. Minina, S. S. Shirokov, and A. E. Yunovich, "Electroluminescence in quantum well heterostructures $\text{p-Al}_x\text{Ga}_{1-x}\text{As/GaAs}_{1-y}\text{P}_y/\text{n-Al}_x\text{Ga}_{1-x}\text{As}$ under uniaxial stress," *Physica Status Solidi B-Basic Solid State Physics*, vol. 246, pp. 522-526, Mar 2009.
- [30] G. P. Agrawal and N. K. Dutta, *Semiconductor Lasers*: Kluwer Academic Publishers; 2nd Revised edition edition, 1993.
- [31] P. Bhattacharya, *Semiconductor Optoelectronic Devices*: Prentice Hall Inc., Englewood Cliffs, New Jersey, 1994.
- [32] B. G. Streetman, *Semiconductor Optoelectronic Devices*: Prentice-Hall Inc., Englewood Cliffs, New Jersey; 4th edition, 1995.

- [33] M. Fukuda, *Reliability and Degradation of Semiconductor Lasers and LEDs*: Artech House, Boston, first citation in article, 1991.
- [34] H. Statz, J. M. Lavine, and C. L. Tang, "Spectral output of semiconductor lasers," *Journal of Applied Physics*, vol. 35, pp. 2581-2585, 1964.
- [35] M. J. Adams, Grundorf.S, B. Thomas, C. F. L. Davies, and D. Mistry, "Time delays and Q-switching in homostructure and heterostructure injection lasers," *IEEE Journal of Quantum Electronics*, vol. QE 9, pp. 328-337, 1973.
- [36] L. W. Casperson and M. S. Shekhani, "Mode properties of annular gain lasers," *Applied Optics*, vol. 14, pp. 2653-2661, 1975.
- [37] Y. Suematsu, S. Akiba, and T. Hong, "Measurement of spontaneous-emission factor of AlGaAs double-heterostructure semiconductor-lasers," *IEEE Journal of Quantum Electronics*, vol. 13, pp. 596-600, 1977.
- [38] D. Renner and J. E. Carroll, "Analysis of the effect of spontaneous-emission coupling on the number of excited longitudinal modes in semiconductor-lasers," *Electronics Letters*, vol. 14, pp. 779-781, 1978.
- [39] W. Streifer, D. R. Scifres, and R. D. Burnham, "Analysis of diode-laser properties," *IEEE Journal of Quantum Electronics*, vol. 18, pp. 1918-1929, 1982.
- [40] T. P. Lee, C. A. Burrus, J. A. Copeland, A. G. Dentai, and D. Marcuse, "Short-cavity InGaAsP injection-lasers - dependence of mode spectra and single-longitudinal-mode power on cavity length," *IEEE Journal of Quantum Electronics*, vol. 18, pp. 1101-1113, 1982.
- [41] P. Unger, *Topics in Applied Physics*: 78, pp. 1-53, 2000.
- [42] G. H. B. Thompson, *Physics of Semiconductor Laser Devices*: John Wiley & Sons Ltd., New York, 1980.
- [43] M. Csele, *Fundamentals of light sources and lasers*: John Wiley & Sons, Inc., Hoboken, New Jersey, 2004.
- [44] J. Hecht, *Understanding Lasers: An Entry-Level Guide* 2nd ed. New York: IEEE Press Understanding Science & Technology Series, 1994.
- [45] M. Fukuda, *Optical Semiconductor Devices*: Wiley, NY, 1999.
- [46] M. Young, *Optics and Lasers*: Springer-Verlag, Berlin, 2000.
- [47] R. Paschotta, "Beam quality deterioration of lasers caused by intracavity beam distortions" *Opt. Express* 14 (13), 6069, 2006.
- [48] I. S. 11146, *Lasers and laser-related equipment – Test methods for laser beam widths, divergence angles and beam propagation ratios*: International Organisation for Standardisation, 2005.
- [49] T. F. J. Johnston, "Beam propagation (M^2) measurement made as easy as it gets: the four-cuts method," *Appl. Opt.* 37 (21), 4840, 1998.

- [50] F. L. Pedrotti and L. S. Pedrotti, *Introduction to Optics*: Prentice-Hall International Inc., London, 1987.
- [51] A. E. Siegman, "New developments in laser resonators," *Proc. SPIE* 1224, 2, 1990.
- [52] A. E. Siegman, "Defining, measuring, and optimizing laser beam quality," *Proc. SPIE Vol. 1868*, pp. 2-12, 1993.
- [53] M. I. Nathan, W. P. Dumke, G. Burns, F. H. Dill, and G. Lasher, "Stimulated emission of radiation from GaAs p-n junctions," *Applied Physics Letters*, vol. 1, pp. 62-64, 1962.
- [54] R. N. Hall, R. O. Carlson, T. J. Soltys, G. E. Fenner, and J. D. Kingsley, "Coherent light emission from GaAs junctions," *Physical Review Letters*, vol. 9, pp. 366-368, 1962.
- [55] N. Holonyak and S. F. Bevacqua, "Coherent (visible) light emission from Ga(As_{1-x}P_x) junctions," *Applied Physics Letters*, vol. 1, pp. 82-83, 1962.
- [56] T. M. Quist, R. H. Rediker, R. J. Keyes, W. E. Krag, B. Lax, A. L. McWhorter, and H. J. Zeigler, "Semiconductor Maser of GaAs," *Applied Physics Letters*, vol. 1, pp. 91-92, 1962.
- [57] Z. I. Alferov, "The history and future of semiconductor heterostructures from the point of view of a Russian scientist," *Physica Scripta*, vol. T68, pp. 32-45, 1996.
- [58] H. Kroemer, "A proposed class of heterojunction injection lasers," *Proceedings of the IEEE*, vol. 51, pp. 1782-1783, 1963.
- [59] H. Kressel and H. Nelson, "Close-confinement gallium arsenide pn junction lasers with reduced optical loss at room temperature," *Rca Review*, vol. 30, pp. 106-&, 1969.
- [60] A. Al-Muhanna, L. J. Mawst, D. Botez, D. Z. Garbuzov, R. U. Martinelli, and J. C. Connolly, "14.3 W quasicontinuous wave front-facet power from broad-waveguide Al-free 970 nm diode lasers," *Applied Physics Letters*, vol. 71, pp. 1142-1144, 1997.
- [61] L. J. Mawst, A. Bhattacharya, J. Lopez, D. Botez, D. Z. Garbuzov, L. DeMarco, J. C. Connolly, M. Jansen, F. Fang, and R. F. Nabiev, "8 W continuous wave front-facet power from broad-waveguide Al-free 980 nm diode lasers," *Applied Physics Letters*, vol. 69, pp. 1532-1534, 1996.
- [62] C. Hanke, L. Korte, B. Acklin, J. Luft, S. Grotsch, G. Herrmann, Z. Spika, M. Marciano, B. De Odorico, and J. Wilhelmi, "Highly reliable 40W-CW-InGaAlAs/GaAs-808 nm laser bars," in *In-Plane Semiconductor Lasers Iii*. vol. 3628, H. K. Choi and P. S. Zory, Eds. Bellingham: Spie-Int Soc Optical Engineering, 1999, pp. 64-70.
- [63] X. He, A. Ovtchinnikov, S. Yang, J. Harrison, and A. Feitisch, "Efficient high power reliable InGaAs/AlGaAs (940nm) monolithic laser diode arrays," *Electronics Letters*, vol. 35, pp. 1739-1740, Sep 1999.

- [64] X. He, M. Ung, S. Srinivasan, and R. Patel, "155W CW optical power from 1 cm monolithic AlGaAs/InGaAs laser diode array," *Electronics Letters*, vol. 33, pp. 1221-1222, Jul 1997.
- [65] M. Sakamoto, J. G. Endriz, and D. R. Scifres, "120W CW output power from monolithic AlGaAs (800 nm) laser diode-array mounted on diamond heatsink," *Electronics Letters*, vol. 28, pp. 197-199, Jan 1992.
- [66] M. Jansen, P. Bournes, P. Corvini, F. Fang, M. Finander, M. Hmelar, T. Johnston, C. Jordan, R. Nabiev, J. Nightingale, M. Widman, H. Asonen, J. Aarik, A. Salokatve, J. Nappi, and K. Rakennus, "High performance laser diode bars with aluminum-free active regions," *Optics Express*, vol. 4, pp. 3-11, Jan 1999.
- [67] K. A. Williams, R. V. Penty, I. H. White, D. J. Robbins, F. J. Wilson, J. J. Lewandowski, and B. K. Nayar, "Design of high-brightness tapered laser arrays," *IEEE Journal of Selected Topics in Quantum Electronics*, vol. 5, pp. 822-831, May-Jun 1999.
- [68] S. Kristjansson, N. Eriksson, P. Modh, and A. Larsson, "Grating-based surface-emitting tapered unstable resonator lasers simulations and experiments," *IEEE Journal of Quantum Electronics*, vol. 37, pp. 1441-1448, Nov 2001.
- [69] B. Sumpf, R. Hulsewede, G. Erbert, C. Dzionk, J. Fricke, A. Knauer, W. Pittroff, P. Ressel, J. Sebastian, H. Wenzel, and G. Trankle, "High-brightness 735 nm tapered diode lasers," *Electronics Letters*, vol. 38, pp. 183-184, Feb 2002.
- [70] R. Bedford and M. Fallahi, "Semiconductor unstable resonators with laterally finite mirrors," *IEEE Journal of Quantum Electronics*, vol. 38, pp. 716-723, Jul 2002.
- [71] J. J. Coleman, "Strained-layer InGaAs quantum-well heterostructure lasers," *IEEE Journal of Selected Topics in Quantum Electronics*, vol. 6, pp. 1008-1013, Nov-Dec 2000.
- [72] G. C. Osbourn, L. R. Dawson, R. M. Biefeld, T. E. Zipperian, I. J. Fritz, and B. L. Doyle, "III-V strained layer superlattices for long-wavelength detector applications - recent progress," *Journal of Vacuum Science & Technology a-Vacuum Surfaces and Films*, vol. 5, pp. 3150-3152, Sep-Oct 1987.
- [73] S. M. Sze and K. K. Ng, *Physics of semiconductor devices*: Wiley-Interscience, 2006.
- [74] R. Dingle, W. Wiegmann, and C. H. Henry, "Quantum states of confined carriers in very thin $\text{Al}_x\text{Ga}_{1-x}\text{As}$ -GaAs- $\text{Al}_x\text{Ga}_{1-x}\text{As}$ heterostructures," *Physical Review Letters*, vol. 33, pp. 827-830, 1974.
- [75] L. L. Chang, L. Esaki, and R. Tsu, "Resonant tunneling in semiconductor double barriers," *Applied Physics Letters*, vol. 24, pp. 593-595, 1974.
- [76] H. X. Li, I. Chyr, X. Jin, F. Reinhardt, T. Towe, D. Brown, T. Nguyen, M. Berube, T. Truchan, D. Hu, R. Miller, R. Srinivasan, T. Crum, E. Wolak, R. Bullock, J. Mott, and J. Harrison, ">700W continuous-wave output power from single laser diode bar," *Electronics Letters*, vol. 43, pp. 27-28, 2007.

- [77] J. Tomm and J. Jiménez, *Quantum-Well Laser Array Packaging*: McGraw-Hill Professional; 1 edition, 2006.
- [78] R. Fehse, H. König, G. Grönniger, C. Lauer, U. Strauß, H. Kissel, M. Puschmann, and J. Biesenbach, "Low fill factor diode laser bars with high brilliance from 808 nm to 1020 nm for fibre coupling," *2nd High Power Diode Lasers and Systems Meeting (HPDLS)*, Coventry, UK, (Invited), 2009.
- [79] J. Boucart, S. Pawlik, A. Guarino, B.Sverdlov, J. Mueller, R.Todt, M. Krejci, and N. Lichtenstein, "Design and realization of high power semiconductor Lasers," *2nd High Power Diode Lasers and Systems Meeting (HPDLS)*, Coventry, UK, (Invited), 2009.
- [80] P. Bhattacharya, "Semiconductor Optoelectronic Devices," *Prentice Hall Inc.*, Englewood Cliffs, NJ, 1994.
- [81] J. W. Tomm, R. Muller, A. Barwolff, T. Elsaesser, D. Lorenzen, F. X. Daiminger, A. Gerhardt, and J. Donecker, "Direct spectroscopic measurement of mounting-induced strain in high-power optoelectronic devices," *Applied Physics Letters*, vol. 73, pp. 3908-3910, Dec 1998.
- [82] K. Shigihara, Y. Nagai, S. Karakida, A. Takami, Y. Kokubo, H. Matsubara, and S. Kakimoto, "High-power operation of broad-area laser-diodes with GaAs and AlGaAs single quantum-wells for Nd-YAG laser pumping," *IEEE Journal of Quantum Electronics*, vol. 27, pp. 1537-1543, Jun 1991.

Chapter 3

Degradation of High Power Laser Diodes and the Description of the Emulation Tool

The first part of this chapter will focus on the background of degradation in high power laser diodes. It is well known that within a bar, the emitter degradation rate is much faster than that of identical single emitters, but the reasons for this are not well understood. Many studies have looked at the reliability and degradation of single emitters but much less attention was given to understanding the details of the degradation dynamics of high-power laser bars. A tone will be set for the degradation of laser diodes prior to the introduction of the emulation tool.

The last part of this chapter will describe the emulation tool and explain how it has been transformed to emulate the degradation of semiconductor laser bars. It must be said from the onset that the anatomy of this tool is not within the scope of this thesis. One significant contribution of this thesis is the transformation of the emulation tool, which was initially designed for a single emitter to emulate the degradation of laser bars. This led to the development of a LabVIEW control

interface called *Barlase* which is used to control multiple instances of *Speclase* and run these instances simultaneously for each emitter in a laser bar.

3.1 Degradation of High Power Laser Diode

The performance in the operation of high power laser diode reduces with the passage of time i.e. it is time dependent. That notwithstanding, the rate of degradation is an important aspect that needs to be reduced. The requirements of laser bars have become stringent in modern times, increasing the pressure for improved reliability and enhanced lifetime. Numerous factors influence the degradation of HPLDs. Some of the factors include: material defects, temperature, packaging-induced strain caused mainly due to soldering to a heatsink [1] and the degradation of the solder itself. Degradation is characterised usually by an increase in the threshold current with a corresponding decrease in the external quantum efficiency [2]. Devices are normally operated in two modes: constant current mode and constant power mode. A device is deemed to have failed if it drops more than 20% of its power in the constant current mode or requires more than a 20% increase in current in the constant power mode of operation [3].

3.1.1 Classification of degradation modes

Degradation modes can be classified into three categories according to their dependence on time: rapid, gradual (slow) and catastrophic (sudden). These different categories of degradation modes are often related to different types of defects and are enhanced by different factors. Fig. 3.1 shows the temporal evolution of operating power under constant current mode and the operating current under constant power mode.

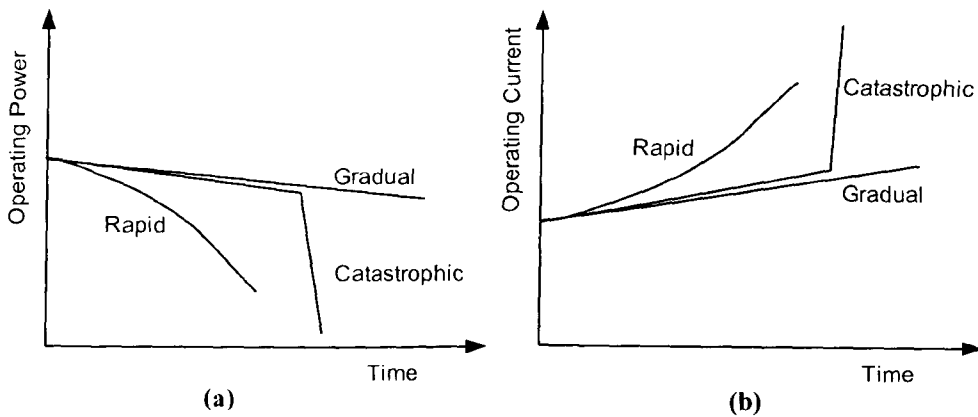


Fig. 3.1 Degradation modes at constant current and constant power of laser diodes.

Rapid degradation

Rapid degradation normally occurs within the first 100 hrs of operation of a device. It is characterised by a decrease in the optical output power or quick increase in the threshold current and a gradual decrease in the quantum efficiency. It is often associated with the formation of dark regions in the active region of the device through nonradiative recombination. Two main dark regions are possible: dark-line defects (DLD's) and dark-spot defects (DSD's). The nonradiative recombination of minority carriers is responsible for the generation of dark defects in the active region of devices. The defect formation is driven by the energy released by the nonradiative recombination process, so that these processes are known as the recombination enhanced defect reactions (REDR) [4, 5]. These dark region defects appear at very low or even dark luminescence efficiency, with experiments revealing the DLDs and DSDs [3].

Gradual degradation

Gradual degradation is the most important mode of degradation because practical bars must degrade slowly. Such bars represent a slow and progressive decrease in the optical output power along the device life. They are seldom formed by point defects caused by REDR [4, 6, 7]. Deep levels are observed by deep level transient spectroscopy (DLTS) in AlGaAs/GaAs DH lasers with the concentration of those levels increasing with operating time [8-10]. Gradual degradation can sequentially be described as follows: Nonradiative recombination at an existing point defect produces a new point defect aided by REDR. The point defect acts as a nonradiative recombination centre that reduces the light-generation efficiency to form new point defects by REDR. A feedback mechanism is established which leads to the migration and condensation of point defects, forming small dislocation loops which lowers the quantum efficiency of devices. These small dislocation loops and microloops can be observed in EL images as small DSDs. DLDs are also common in gradual degradation phenomenon [9].

Catastrophic degradation

Catastrophic degradation (CD) occurs with a sudden drop in the optical output power. It is often associated with a catastrophic optical damage of the facets. It can also occur in the inner part of the cavity and is referred to as catastrophic degradation. The high intensity of power present at the facets of lasers contribute directly to the catastrophic optical mirror damage (COMD) [3]. The high power at the facets, heats up the active layer, which in turn lowers the bandgap energy [11]. This increases the optical absorption, which causes further heating of the facet.

The process gives rise to a positive feedback loop, which ultimately leads to irreversible optical mirror damage [12].

CD is irreversible because it affects the mirror facets which are critical for laser diode reliability [13]. The lifetime of low power laser diodes is limited by gradual degradation, but that of high power laser diodes is mostly limited by the catastrophic optical mirror damage through the destruction of the mirror facets under laser action. This mode of degradation has received tremendous attention because it is one of the main factors limiting the lifetime of HPLDs. The mechanism leading to catastrophic optical damage which was revealed by Henry *et al.* in 1979 [14] and later by Chen *et al.* in 1993 [15] can be summarised in the following sequential steps:

- i. Nonradiative recombination at the mirror facet increases the local temperature
- ii. The bandgap shrinks
- iii. Optical-absorption at the facet is increased
- iv. Free carriers are generated
- v. Free carriers recombine nonradiatively, increasing further the temperature of the facet region.

The positive feedback loop generated as a consequence of this sequence leads to thermal runaway of the mirror facet that can locally melt (Henry *et al.*, 1979) [14]. Chen and Tien (Chen *et al.*, 1993) [15] proposed a similar scheme for this thermal runaway model, as shown in Fig. 3.1.1.2.

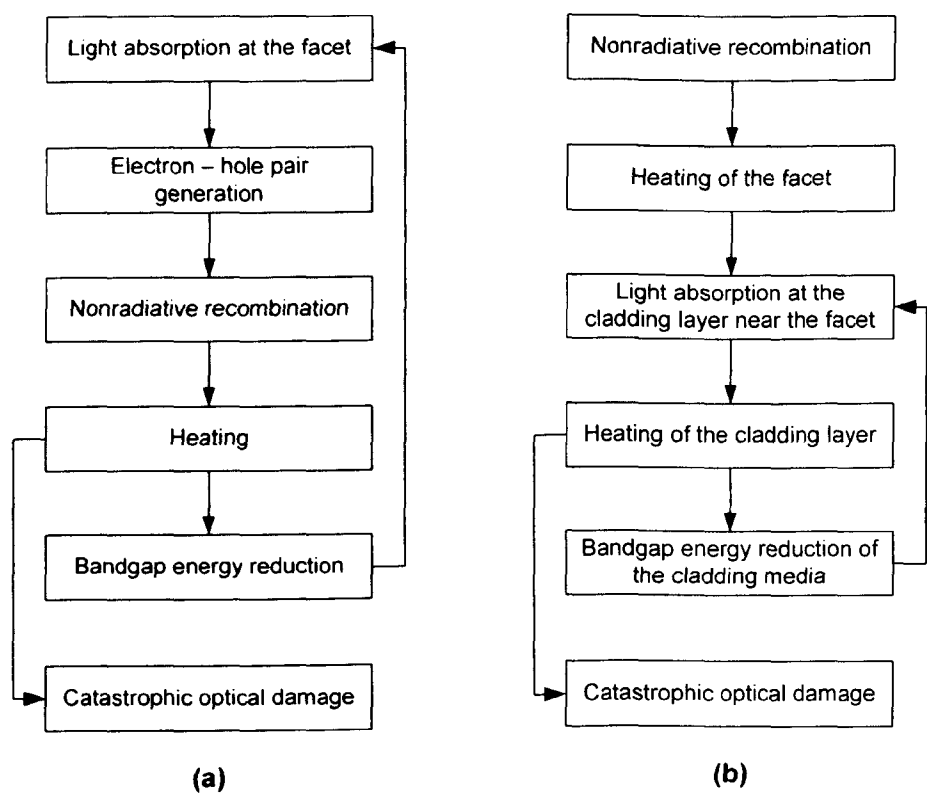


Fig. 3.2 Flow chart of catastrophic optical damage process: (a) Henry et al., 1979 (b) Chen et al., 1993.

One or several factors may contribute to the degradation of HPLDs. Defects, which eventually lead to degradation may be introduced via the crystal growth process, the fabrication process, and the packaging process. The correlation between the degradation region, the mechanisms causing the degradation of the region, and the factors that enhance the rapid degradation of lasers is summarised in Table 3.1.

Crystal defects such as dislocations are the main defects responsible for causing internal degradation in the active region. These defects are intrinsic because they occur during the growth of the crystal [16]. We can also have extrinsic processing-induced strain in the inner region.

Table 3.1 Parts, causes and main enhancement factors in HPLDs.

Part	Cause	Main enhancement factors
Inner region	Dislocation Precipitation	Current Ambient temperature (heat, light)
Facet (surface)	Oxidation	Light, moisture
Electrode	Metal diffusion, Alloy reaction	Current Ambient temperature (heat)
Bonding part	Solder instability (reaction and migration) Stress Strain	Ambient temperature (heat) Current Packaging
Heatsink	Separation of metal	Ambient temperature (heat) Current

The presence of aluminium causes oxidation of the facet, especially in GaAs/AlGaAs lasers and introduces defects. Aluminium free laser diodes are less susceptible to oxidation and therefore have a reduction in nonradiative recombination centres leading to an increase in efficiency and reliability [17, 18]. The absence of aluminium in the active layer reduces the generation of DLDs and DSDs, which can be assisted by REDR to cause COD if these defects are close to the facet [10].

3.2 Degradation Mechanisms

Degradation is always characterised by an increase in the threshold current with an accompanying decrease in the external differential quantum efficiency [2]. Fabrication processes including epitaxy, device processing and bonding are some of the dominant mechanisms responsible for device degradation.

Three categories can be considered under degradation mechanisms as: i) defect formation in the active region of the device; ii) catastrophic mirror damage at high

power densities; and iii) degradation of current-confining junctions [2]. As already discussed, lasers operate under high injection current densities and hence will create high-energy ehrs, thermal potential for strain fields, and high nonradiative recombination centres in the active region. Such factors will generate defects and will significantly degrade the performance of devices.

Types of defects

Any deviation in a crystal from a perfect periodic lattice or structure is an imperfection that can affect a device made from it. Real crystals are always imperfect in nature but efforts are always made to minimise the departure from perfection. Defects known to degrade the performance of semiconductor devices can broadly be classified as point defects and extended defects [3]. Common point defects include impurities, vacant lattice sites, interstitial and substitutional defects, and complex defects which are made up of a combination of different point defects. On the other hand, common extended defects are dislocations (and dislocation complexes) which can propagate from the substrate into the active region during the epitaxial growth stages.

Defects in the lattice, such as vacancies and impurities are very important because they give rise to deep trap levels which are closely related to nonradiative recombination and hence the quantum efficiency of the device. They are fundamental in the degradation process because nonradiative recombination supplies energy in the form of heat for REDR mechanisms leading to laser degradation.

3.3 Spatial Location of the Degradation

The inspection of a laser diode after degradation reveals two distinct degradation modes: internal and external degradations.

3.3.1 Internal degradation

Internal degradations are usually found in the active region of laser diodes. They are mostly strongly related or linked to crystal-defect reactions (e.g., diffusion, generation, and motion of defects) which occur during the operation of laser diodes [9]. Material properties are known to play a major role in this degradation mode and are accelerated by strain, temperature, injection current and light power. Crystals contain imperfections that disturb the local regular arrangement of the atoms. The imperfections are point, line, and plane defects [19]. Fig. 3.3a show typical point defects where there is a vacancy and an interstitial atom. Other crystal imperfections are caused by plane defects and dislocation networks [20].

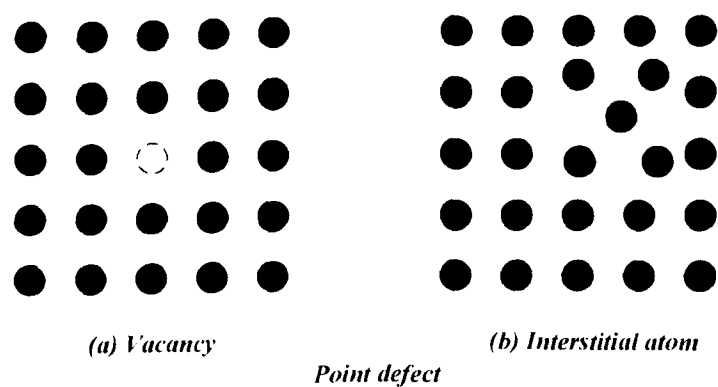


Fig. 3.3 Basic concept of point defect: (a) vacancy, (b) interstitial atom [3] p.

3.3.2 External degradation

External degradation can occur anywhere on a device. However, mirror facet degradations are critical links for external laser diode degradations. This is because the mirror facet is so sensitive and various causes can lead to their fatal failure. Oxidation of the cleaved facet of lasers is one of the most common processes which can lead to failure. This though, can be reduced by facet passivation by coating with a dielectric layer [13, 21]. Unfortunately, facet degradation appears as a thermal runaway process; therefore, a COD level must not be exceeded [22]. The COD level is defined as the maximum optical output power density allowed without catastrophic damage.

Other external links are the electrodes, heatsink bonding and metal coating the heatsink. The electrodes usually degrade by metal electromigration inside the lasers. This condition is enhanced by current injection and temperature. The heatsink bonding to the layer is crucial for the effective dissipation of heat during laser operation. Poor soldering can lead to poor heat management by the creation of solder voids. The coating of the heatsink can also degrade due to poor adherence of the metal to the heatsink [23]. Fig. 3.4 shows the schematic configuration of a laser mounted on a heatsink.

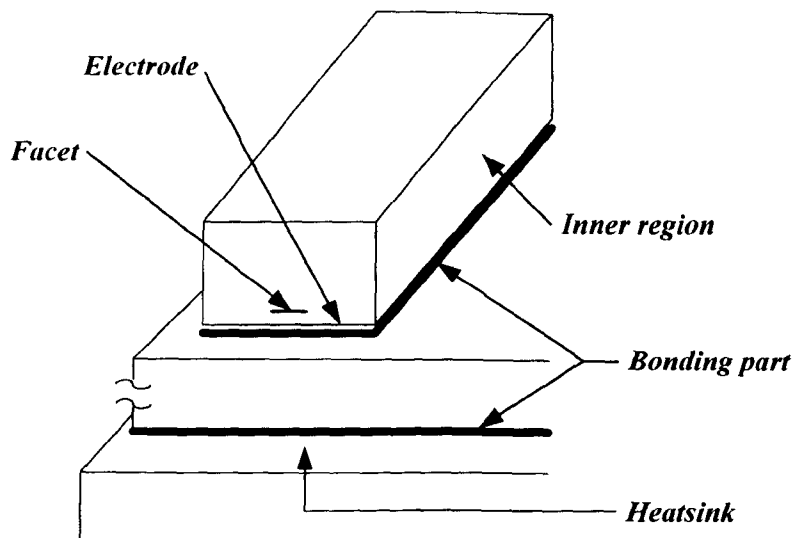


Fig. 3.4 Schematic configuration of a laser mounted on a heatsink [3] p. 116.

3.3.3 Suppression and elimination of facet degradation

Facet oxidation and COD as already explained depend on the properties of the semiconductor surface and are enhanced or generated by the existence of light. In electron beam induced current (EBIC) image or EL topograph, DLD perpendicular to the facet in the $\langle 110 \rangle$ direction is always observed after COD [24]. The $\langle 110 \rangle$ DLD corresponds to the trace of propagation of the molten part into the inner region.

The propagation direction of the molten part corresponds to the direction in which the optical intensity is maximum. Dislocation loops and networks are observed with transmission electron microscopy (TEM) [14, 25, 26] after rapid cooling of the molten part and rapid recrystallisation occurs. A dislocation loop is formed under direct current operation. Thus, the trace of the penetration of the molten part is observed as a $\langle 110 \rangle$ DLD. This COD procedure is demonstrated in Fig. 3.5.

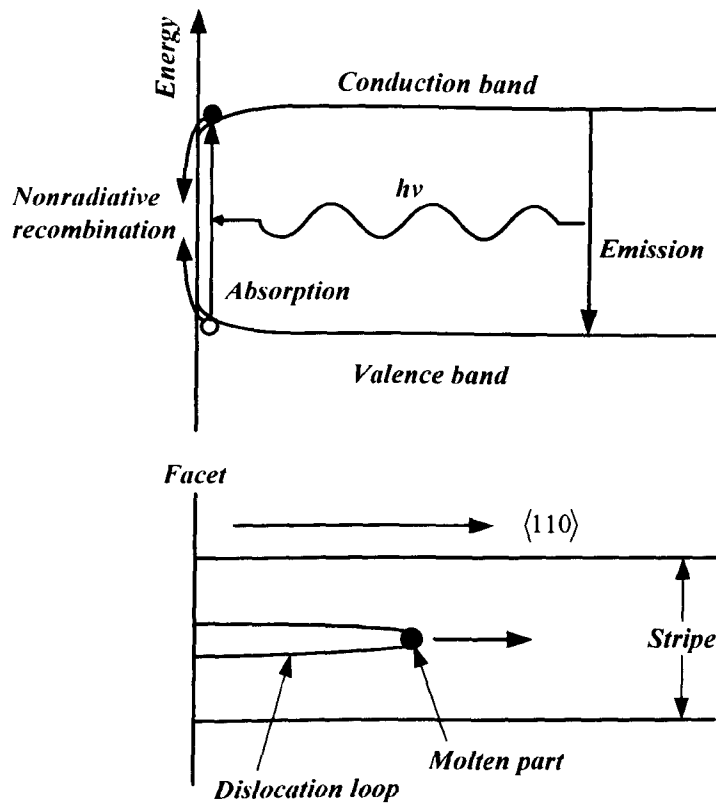


Fig. 3.5 Schematic illustration of the COD mechanism [3] p. 135.

The rate of facet oxidation becomes high and the COD level decreases if the emitted light shortens [14, 26]. Facet degradation is more of a challenge in AlGaAs/GaAs lasers. This has led to the development of several suppression or elimination methods. These include the reduction of light absorption, a reduction in light density, and a separation of the facet from the atmosphere. A facet coating with dielectric film such as Al_2O_3 , SiO_2 , and SiNx , is generally used [27-30] to separate the facet from the atmosphere. Facet oxidation is sufficiently suppressed by these means because the facet is no longer exposed to the atmosphere. Facet coatings are also effective at increasing the COD level because the density of the surface state relative to nonradiative recombination is decreased. The temperature increase at the facet can also be suppressed by the coatings [31].

The COD level is physically determined by the light density at the facet. This is done by the reduction of the light density at the facet which allows an apparent high light output power operation. It can be achieved by thinning the active layer thickness to decrease the optical confinement into the active layer or by employing a large optical cavity structure [32]. Non absorbing mirror lasers have been demonstrated to improve COD levels compared to standard lasers by a factor of 2.6 [33]. This is achieved without the use of good quality anti-reflection/high-reflection coatings.

3.4 Degradation of Single Emitters/Bars

Single emitter degradation processes are less complicated than bar degradation due to the fact that bar behaviour is the sum of the behaviour of many emitters. The emitters do not necessarily degrade via the same mechanism due to the intrinsic nonuniformity of some processes. For example, mounting can induce a large strain, which produces packaging-induced defects in a spatially variable distribution. Mounting also induces variable evolution related to strain relaxation or thermal resistance changes associated with solid-phase reactions at the metal-solder interface and within the solder material. These effects combine with others and come into play in single emitters and contribute to make the interpretation of bar aging at short times more sophisticated. In particular, current competition effects between emitters can change the relative operating conditions of individual emitters within a bar during aging. This holds for bars coming from the same wafer and more true when comparing batches of bars that are not from the same wafer [9].

Factors that contribute to failure

Failure is introduced into a laser diode during the fabrication and packaging processes. Laser structures are normally grown on a GaAs substrate, which is the most common. The growth of the epitaxial layer is done using one of the two modern industrial growth techniques: molecular-beam epitaxy (MBE) or metal organic chemical vapour deposition (MOCVD) on a GaAs substrate. These layers constitute the active region, which include: the quantum well, optical confinement, and cladding layers (Fig. 2.21). The quality of the deposited material is one major issue in terms of the optical performance and lifetime. Lattice mismatch between layers is also important. These layers can be stressed in compression or in tension, affecting the bandgap energy and must be taken into account when designing the sandwiched layer structure [34, 35]. The stress state also changes with temperature as a consequence of the different coefficients of thermal expansion of the constituent materials. Additional stress is introduced during packaging. Care must be taken not to exceed a level of stress above which lattice defects are likely to be created. At higher stress levels, damage to the semiconductor becomes evident through microcracks and subsequent failure of the device.

It is very important to minimise defect creation in the active material. This is critical to the performance of the laser. Intrinsic defects (e.g., vacancies, interstitials) and extrinsic defects (e.g., impurity-related) lead to residual absorption, increased internal losses in the cavity, and increased nonradiative recombination. All of this results in higher threshold currents and reduced optical efficiencies. Dislocations must also be avoided to stop DLDs during operation.

After the growth process, the laser diode is processed by metallisation and photolithography and in some cases etching and dielectric deposition. The output power is increased usually by connecting emitters in parallel to form a laser bar (as shown in Figs. 2.20 and 2.21).

Another important process is the cleavage of the laser diode, which determines the length of the laser cavity. The final process is the mounting of the laser diode on the heatsink (Fig. 3.4). This has been explained in section 2.7. A further concern which occurs during packaging is to keep the “smile” of the bar to a minimum [9]. A flat line array of emitters can result in emitters along the bar having different thermal contacts with the solder material and heatsink. Heating effects play a significant role in degradation and therefore can vary considerably from emitter to emitter because of the smile. Solder integrity must be maintained to avoid solder voids in the solder joints.

3.5 Reliability of Lasers Degradation of Single Emitters/Bars

The performance of a semiconductor laser degrades during its operation. The dominant mechanism responsible for degradation is determined by one or several of the fabrication processes, including epitaxy, device processing, and bonding. Also, the degradation rate of lasers processed from a given wafer depends on the operating conditions, namely, the operating temperature and injection current. For many applications, laser sources are expected to operate reliably over a period of time, say in excess of 10 years. For this reason, appropriate reliability assurances become necessary – especially for applications such as undersea lightwave transmission systems, where laser replacement cost is prohibitive [36, 37].

Laser failure can occur by several means, such as: a) infant mortality i.e. laser with intrinsic defects that degrade very quickly; b) chance failures, these could be catastrophic damage due to external factors; and c) a gradual degradation mechanism in which some characteristic of the laser operation (e.g., the threshold current) changes slowly with time. The central point to the determination of the expected operating lifetime is the concept of thermally accelerated aging, the validity of which for AlGaAs injection lasers was shown by Hartman and Dixon [38]. The lifetime τ at a temperature T is empirically found to vary as:

$$\tau = \tau_0 \exp\left(\frac{E_a}{k_B T}\right) \quad (3.1)$$

where E_a is the activation energy and τ_0 is a constant. An important measure of the reliability of semiconductor lasers is the mean time to failure (MTTF). For instance, the MTTF at an operating temperature of 10°C (the ocean-bottom temperature) is then obtained using Eq. 3.1 and an activation energy of 0.9 eV. This represents a 25 year equivalent operating lifetime at 10°C, which is the expected cable lifetime and temperature of submarine lightwave systems [39]. A similar relation of Eq. 3.1 also holds for the degradation rate of semiconductor devices which was used as the aging model in section 5.1.2. It must be pointed out though, that the simple Arrhenius-type relationship in section 5.1.2 may not apply under all aging conditions and that the measured activation energy may differ under different aging conditions and temperature ranges [40]. Numerous articles have been written on semiconductor laser reliability [41-45]. More information on laser reliability can be found in a book specially dedicated solely to it and published in 1991 [3].

3.6 Semiconductor Laser Emulation Tool

Introduction

A semiconductor laser model that accurately includes all the physical processes in a real device is important both for understanding the operating behaviour of the device and allowing the optimisation of the design of the device. To this end, several models have been introduced in the literature with varying degrees of complexity [46-60]. The majority of the earlier models [46-54] attempted to explain the kinks in the LI characteristics of stripe geometry lasers by including changes in the laser medium induced by the optical field. However, these models only considered the lateral variation of the field profile (along the plane of the junction) and ignored any longitudinal effects.

These earlier models were therefore only accurate for describing the laser behaviour near threshold and could not be used for devices which possessed some form of longitudinal variation in the design, such as in tapered lasers [61] and unstable resonator lasers [62]. More accurate models were introduced to circumvent this problem by using the BPM [55, 57-60, 63, 64], together with the Fox and Li [65] approach of propagating the lateral field back and forth in the laser cavity until a self-consistent solution was found. However, until recently [66-68], most of the BPM models employed a simple diffusion equation to model the carrier distribution in the lateral direction. In *Speclase*, a more complete treatment of the carrier distribution is obtained from solving the full semiconductor device equations in the transverse xy slice as described in the dissertation of Dr Jun Lim [69]. The changes in the carrier distribution are then coupled to a 2D wide angle FD-BPM model (xz directions) that provides an accurate description of the longitudinal

variation of the optical field.

The effective index approximation is used to reduce the complexity of the full wave equation from three to two spatial dimensions. This is followed by a description of the changes in the complex refractive index that would result from the injection of carriers in the device. After obtaining a self-consistent solution for all physical variables in the device, some post-processing of the data is done to enable the evaluation and optimization of the laser design.

3.6.1 Device Structure

The device structure used in the *Speclase* model was assumed to have the cross-sectional structure of the general stripe-geometry laser as shown in Fig. 3.6.

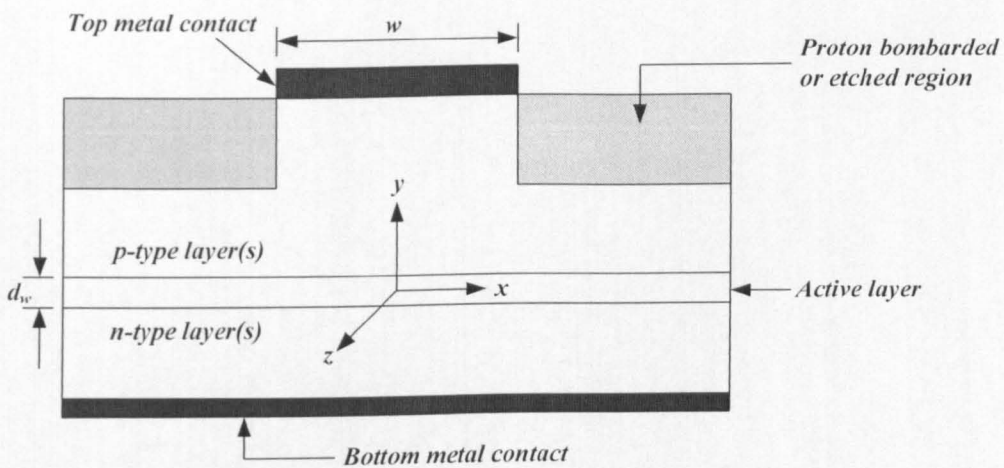


Fig. 3.6 Cross-section schematic of the laser structure. The x -origin is at the centre of the stripe of width w and the y -origin is at the centre of the active layer.

3.6.2 Effective index approximation

It would seem necessary to solve the full 3D wave equation as the laser structure has three dimensions (transverse, lateral and longitudinal). However, to consider all three dimensions would incur a major computational penalty. Therefore, *Speclase* used the effective index method [70] to reduce the optical problem to include only

the lateral and longitudinal dimensions (x and z respectively). The effective index method was compared with a full 3D model developed independently in-house and was shown to be sufficiently accurate for most high power/high brightness lasers [71].

The effective index method assumes that the electric field can be separated into a field component perpendicular to the junction and a field component parallel to the plane of the junction. Details of the method are demonstrated in the dissertation of Dr Jun Lim [69].

3.6.3 Complex refractive index perturbation

The refractive index $n(x, y, z)$ is generally complex. Changes to the refractive index can be due to several physical mechanisms such as carrier injection, temperature and strain variations. An efficient approach is to treat the changes as small perturbations to the eigenvalue problem. The use of this method is justified for semiconductor lasers, because the vertical waveguide is designed to strongly support a single mode. The detail of the method is demonstrated in the dissertation of Dr Jun Lim [69].

3.6.4 Numerical solution procedure

The simulation tool is UNott's 2.5D spectral laser model, the full details of which have been published elsewhere [72, 73]. In brief, this model is based on a single wavelength steady state CW model and consists of 2D optical (x - z) and electro-thermal (x - y) solvers. The electro-thermal model is coupled to the optical model through carrier-induced changes in the complex refractive index. The optical model is coupled to the electro-thermal model through stimulated emission/absorption and spontaneous emission coupling. The optical model

propagates multiple wavelengths between electro-thermal slices using the 2D Wide-Angle Finite-Difference Beam Propagation Method (WA-FD-BPM), where the effective index assumption has been used. The electrical model calculates the carrier density profile for a series of 2D transverse slices along the laser cavity and includes drift-diffusion transport and the capture/escape processes between the bound and unbound states of the QW(s). The self-heating effect is included by solving the classical heat flux equation including all relevant heating terms. The lattice heat flux equation is solved iteratively with the semiconductor device equations until a self-consistent solution is found. The photon density distribution at each wavelength is provided as an input to the electro-thermal solver. The gain and spontaneous emission spectra, which are dependent on the electron and hole densities and temperature are obtained from an externally calculated gain table and used by the optical model to propagate the fields to the next electro-thermal slice. The electro-thermal and optical models are solved self-consistently, following an accelerated Fox-Li iterative approach.

The basic (steady state) electrical equations solved in the device simulator are the Poisson equation and the continuity equations for electrons and holes. They are:

$$\text{div}(\epsilon \cdot \text{grad}\psi) = q \cdot (n - p - C_{\text{net}}), \quad (3.2)$$

$$\text{div } J_n = q R, \quad (3.3)$$

$$\text{div } J_p = -q R. \quad (3.4)$$

The unknown quantities in Eqs. (3.2) to (3.4) are the electrostatic potential ψ , and the electron and hole concentrations, n and p , respectively. C_{net} denotes the net concentration of the ionized dopants and other charged defects, ϵ is the dielectric permittivity of the semiconductor or insulator, and R is the net recombination rate.

The current densities in Eqs. (3.3) and (3.4) are given by the drift-diffusion relations:

$$J_n = \mu_n n \left(\text{grad}(E_C) - \frac{k_B T}{N_C} \text{grad}(N_C) \right) + \mu_n k_B T \text{grad}(n), \quad (3.5)$$

$$J_p = \mu_p p \left(\text{grad}(E_V) + \frac{k_B T}{N_V} \text{grad}(N_V) \right) - \mu_p k_B T \text{grad}(p). \quad (3.6)$$

The drift-diffusion current relations which are used in the simulator can be derived from the Boltzmann transport equation by the method of moments [74]. These current relations account for the position-dependent band edge energies, E_C and E_V , and for position-dependent effective masses which are included in the effective density of states, N_C and N_V [75].

A numerical solution of the semiconductor device equations (3.2) to (3.6) is exploited because no closed form analytical solution can be found without the introduction of unrealistic simplifications. Numerical modelling of semiconductor devices is a well-established field. Simulations are used routinely in the design and optimisation of devices – especially in the field of very large semiconductor integration (VLSI) microelectronics [76]. Methods developed in this field [77] are adopted directly to efficiently model the electrical behaviour of semiconductor laser diodes.

The equations involved in the solution are nonlinear. Therefore, the use of iterative methods is appropriate. The methods that could be used to solve the semiconductor device equations include Gummel's method and Newton's method. Newton's method was used because it is highly stable and robust, allowing an accurate solution to be obtained within ~15 iterations. The convergence rate of

Newton's method can be shown to be quadratic [78]. Further details are presented in the dissertation of Dr Jun Lim [69].

3.6.5 Output Characteristics

In order to assess the performance of a semiconductor laser and to compare simulation results with experiment, the output characteristics of a semiconductor laser must be determined. These output characteristics are obtained after the iterative scheme has produced a converged self-consistent solution. Among the main characteristics required from the simulation are: i) light-current, ii) voltage-current and iii) spatial mode distribution. The simulations performed are entirely in the steady-state at a fixed optical frequency; therefore the spectral and dynamic characteristics of the laser are not obtainable. This was acceptable in the present application context, since high-power broad area lasers are generally operated in continuous wave mode and the beam quality is of greater significance than the spectral content of the laser beam or dynamic effects (e.g. mode-beating).

3.6.6 Light-current characteristic

The light emitted by the output facet is commonly measured as a function of the injected current, producing a curve known as the light-current characteristic. The amount of light emitted is measured in terms of the output power P_{out} (W), which can be calculated from the energy flux density S (Wcm^2) integrated over the area of the output facet multiplied by the power transmission from the output facet. The details of the calculations are presented in the dissertation of Dr Jun Lim [69].

3.6.7 Model Validation

Speclase was validated against an in-house laser simulator developed under the EC project Ultrabright. This in-house laser simulator is known as *Conan* and was developed independently and in parallel to the laser model *Speclase*. *Conan* has demonstrated good qualitative and quantitative agreement with experiments [68]. The equations solved by *Conan* and *Speclase* were essentially the same. However, there were slight differences between the two laser simulators.

Firstly, *Conan* includes a thermal solver which computes the temperature distribution throughout the device. However, the influence of thermal effects is largely variable and dependent upon the cooling system employed and has been found to be less significant than the carrier induced nonlinear effects [64] in *Speclase*. Secondly, *Conan* does not incorporate the Prony method [Jun] and hence does not produce any modal discrimination information. Thirdly, *Conan* only simulates a single bias point at a time and has difficulty calculating the threshold condition. *Speclase* on the other hand readily calculates the threshold condition and solves for higher bias levels incrementally from threshold. The starting solution guess for each bias level is taken from the solution of the previous bias level. In this way, the present laser simulator is able to obtain the LI curve automatically and increases its computational efficiency compared to *Conan*.

Speclase was used to simulate a tapered laser and the results were compared with those obtained from *Conan*. There was good agreement between *Conan* and the present laser model. As further comparison, the photon density and carrier density distribution at the output facet of the tapered laser for two different bias levels was done. The results from *Speclase* showed excellent agreement with those generated

by *Conan*. The results obtained from *Conan* had been validated against experiment and therefore *Speclase* can be relied upon to produce realistic results in good agreement with experiment.

3.6.8 Summary

The optical and electrical models developed were coupled together to produce *Speclase*. The complexity of the problem was reduced from 3D to 2D using the effective index method. The contributions to the effective index change due to carrier injection and other loss mechanisms were considered. To obtain a self-consistent solution, the Fox-Li iteration method was used. There were several methods of obtaining output characteristics from the steady-state solution of *Speclase*. These output characteristics were used to evaluate and optimize the design of a stripe geometry semiconductor laser. The semiconductor laser model was validated against an in-house laser simulator. The in-house laser simulator had shown good agreement with experiments giving confidence in the results obtained using the laser simulator *Speclase*.

References

- [1] J. W. Tomm, R. Muller, A. Barwolff, T. Elsaesser, D. Lorenzen, F. X. Daiminger, A. Gerhardt, and J. Donecker, "Direct spectroscopic measurement of mounting-induced strain in high-power optoelectronic devices," *Applied Physics Letters*, vol. 73, pp. 3908-3910, Dec 1998.
- [2] G. P. Agrawal and N. K. Dutta, *Semiconductor Lasers*: Kluwer Academic Publishers; 2nd Revised edition edition, 1993.
- [3] M. Fukuda, *Reliability and Degradation of Semiconductor Lasers and LEDs*: Artech House, Boston, first citation in article, 1991.
- [4] L. C. Kimerling, "Recombination enhanced defect reactions," *Solid-State Electronics*, vol. 21, pp. 1391-1401, 1978.
- [5] M. Vanzi, G. Salmini, and R. De Palo, "New FIB/TEM evidence for a REDR mechanism in sudden failures of 980 nm SL SQW InGaAs/AlGaAs pump laser diodes," *Microelectronics Reliability*, vol. 40, pp. 1753-1757, Aug-Oct 2000.
- [6] I. Rechenberg, A. Klehr, U. Richter, W. Erfurth, F. Bugge, and A. Klein, "Interdiffusion-induced degradation of 1017 nm ridge waveguide laser diodes," *Journal of Crystal Growth*, vol. 210, pp. 307-312, 2000.
- [7] J. Jimenez, "Laser diode reliability: crystal defects and degradation modes," *Comptes Rendus Physique*, vol. 4, pp. 663-673, Jul-Aug 2003.
- [8] T. Uji, T. Suzuki, and T. Kamejima, "Deep-level changes in (Al,Ga)As double-heterostructure lasers degraded during accelerated aging at high temperatures," *Applied Physics Letters*, vol. 36, pp. 655-657, 1980.
- [9] J. Tomm and J. Jiménez, *Quantum-Well Laser Array Packaging*: McGraw-Hill Professional; 1 edition, 2006.
- [10] R. W. Lambert, T. Ayling, A. F. Hendry, J. M. Carson, D. A. Barrow, S. McHendry, C. J. Scott, A. McKee, and W. Meredith, "Facet-passivation processes for the improvement of Al-containing semiconductor laser diodes," *Journal of Lightwave Technology*, vol. 24, pp. 956-961, Feb 2006.
- [11] Y. P. Varshni, "Temperature dependence of energy gap in semiconductors," *Physica*, vol. 34, pp. 149-154, 1967.
- [12] U. Martin, *COMD Behavior of Semiconductor Laser Diodes*: Annual Report 1999, Dept. of Optoelectronics, University of Ulm, 1999.
- [13] R. E. Sah, *Silicon Nitride, Silicon Dioxide Thin Insulating Films, and Other Emerging Dielectrics VIII 2005*: Electrochemical Society, 2005.
- [14] C. H. Henry, P. M. Petroff, R. A. Logan, and F. R. Merritt, "Catastrophic damage of $\text{Al}_x\text{Ga}_{1-x}\text{As}$ double-heterostructure laser material," *Journal of Applied Physics*, vol. 50, pp. 3721-3732, 1979.

- [15] G. Chen and C. L. Tien, "Facet heating of quantum-well lasers," *Journal of Applied Physics*, vol. 74, pp. 2167-2174, Aug 1993.
- [16] A. Moser, E. E. Latta, and D. J. Webb, "Thermodynamics approach to catastrophic optical mirror damage of AlGaAs single quantum well lasers," *Applied Physics Letters*, vol. 55, pp. 1152-1154, Sep 1989.
- [17] D. Pendse, A. Chin, F. Dabkowski, and E. Clausen, "Reliability comparison of GaAlAs/GaAs and aluminum-free high-power laser diodes," in *Semiconductor Lasers III*, vol. 3547, Q. Wang, L. J. Davis, and S. Forouhar, Eds. Bellingham: Spie-Int Soc Optical Engineering, 1998, pp. 79-85.
- [18] N. University, "<http://cqd.eecs.northwestern.edu/research/alfree.php>," Center for Quantum Devices, Evanston, Illinois, United States, 1991.
- [19] D. Hall and D. J. Bacon, *Introduction to dislocations*: Pergamon Press, Oxford; 2nd Revised edition, 1975.
- [20] P. Petroff and R. L. Hartman, "Defect structure introduced during operation of heterojunction GaAs lasers," *Applied Physics Letters*, vol. 23, pp. 469-471, 1973.
- [21] V. A. Kheraj, C. J. Panchal, P. K. Patel, B. M. Arora, and T. K. Sharma, "Optimization of facet coating for highly strained InGaAs quantum well lasers operating at 1200 nm," *Optics & Laser Technology*, vol. 39, pp. 1395-1399, 2007.
- [22] S. N. Elliott, P. M. Snowton, M. Ziegler, J. W. Tømm, and U. Zeimer, "Time resolved studies of catastrophic optical mirror damage in red-emitting laser diodes," *Journal of Applied Physics*, vol. 107, pp. 123116-7, 2010.
- [23] V. V. Parashchuk, G. I. Ryabtsev, A. K. Belyaeva, T. V. Bezyazychnaya, V. V. Baranov, E. V. Telesh, D. M. Vu, V. L. Vu, and V. T. Pham, "Improving the efficiency of high-power diode lasers using diamond heat sinks," *Quantum Electronics*, vol. 40, pp. 301-304, 2010.
- [24] B. W. Hakki and F. R. Nash, "Catastrophic failure in GaAs double-heterostructure injection lasers," *Journal of Applied Physics*, vol. 45 Issue: 9, pp. 3907 - 3912, Jul 1974.
- [25] S. Mahajan, H. Temkin, and R. A. Logan, "Formation of optically induced catastrophic degradation lines in InGaAsP epilayers," *Applied Physics Letters*, vol. 44, pp. 119-121, 1984.
- [26] O. Ueda, "Degradation of III-V opto-electronic devices," *Journal of the Electrochemical Society*, vol. 135, pp. C11-C22, Jan 1988.
- [27] I. Ladany, M. Ettenberg, H. F. Lockwood, and H. Kressel, "Al₂O₃ half-wave films for long-life cw lasers," *Applied Physics Letters*, vol. 30, pp. 87-88, 1977.
- [28] Y. Shima, N. Chinone, and R. Ito, "Effects of facet coatings on the degradation characteristics of GaAs/Ga_{1-x}Al_xAs DH lasers," *Applied Physics Letters*, vol. 31, pp. 625-627, 1977.

- [29] H. Namizaki, S. Takamiya, M. Ishii, and W. Susaki, "High power density single mode operation of GaAs/GaAlAs TJS lasers utilizing Si₃N₄ plasma deposition for facet coating," *Journal of Applied Physics*, vol. 50, pp. 3743-3745, 1979.
- [30] T. Yuasa, K. Endo, T. Torikai, and H. Yonezu, "Facet protection of (AlGa)As lasers using SiO₂ sputter deposition," *Applied Physics Letters*, vol. 34, pp. 685-687, 1979.
- [31] H. Brugger and P. W. Epperlein, "Mapping of local temperatures on mirrors of GaAs/AlGaAs laser diodes," *Applied Physics Letters*, vol. 56, pp. 1049-1051, 1990.
- [32] J. Buus, "Threshold currents for GaInAsP lasers emitting at 1.55 μm ," *Optics Letters*, vol. 5, pp. 211-213, 1980.
- [33] C. L. Walker, A. C. Bryce, J. H. Marsh, and I. IEEE, "Non absorbing mirror laser with improved catastrophic optical damage level," in *2002 IEEE/Leos Annual Meeting Conference Proceedings, Vols 1 and 2* New York: IEEE, 2002, pp. 643-644.
- [34] N. W. Carlson, *Monolithic Diode-Laser Arrays*: Springer Series in Electronics and Photonics 33. New York: Springer, 1994.
- [35] L. A. Coldren and S. W. Corzine, *Diode Lasers and Photonic Integrated Circuits*: Wiley-Interscience Publication, 1995.
- [36] F. R. Nash, W. J. Sundburg, R. L. Hartman, J. R. Pawlik, D. A. Ackerman, N. K. Dutta, and R. W. Dixon, "Implementation of the proposed reliability assurance strategy for an InGaAsP/InP, planar mesa, buried heterostructure laser operating at 1.3 μm for use in a submarine cable," *At&T Technical Journal*, vol. 64, pp. 809-860, 1985.
- [37] R. L. Easton, R. L. Hartman, and F. R. Nash, "Assuring high-reliability of lasers and photodetectors for submarine lightwave cable systems - Introduction," *At & T Technical Journal*, vol. 64, pp. 661-669, 1985.
- [38] R. L. Hartman and R. W. Dixon, "Reliability of DH GaAs lasers at elevated temperatures," *Applied Physics Letters*, vol. 26, pp. 239-242, 1975.
- [39] P. K. Runge, "Undersea lightwave communications," *Journal of Lightwave Technology*, vol. 2, pp. 742-743, 1984.
- [40] W. B. Joyce, K. Y. Liou, F. R. Nash, P. R. Bossard, and R. L. Hartman, "Methodology of accelerated aging," *At & T Technical Journal*, vol. 64, pp. 717-764, 1985.
- [41] D. Gallant, "Diode array reliability experiment," in *High-Power Diode Laser Technology and Applications II*. vol. 5336, M. S. Zadiker, Ed. Bellingham: Spie-Int Soc Optical Engineering, 2004, pp. 212-217.
- [42] B. L. Meadows, F. Amzajerdian, B. W. Barnes, N. R. Baker, R. P. Baggott, U. N. Singh, and M. J. Kavaya, "Reliability of long pulsewidth high power laser diode arrays," in *Advanced Devices and Materials for Laser Remote Sensing*. vol. 883, A. Aksnes, F. Amzajerdian, D. Killinger, and L. Merhari, Eds. Warrendale: Materials Research Society, 2005, pp. 99-109.

- [43] A. Vasilyev, E. Troupaki, G. R. Allan, N. B. Kashem, and M. A. Stephen, "The reliability of the laser diode arrays," in *Photonics for Space Environments XI*, vol. 6308, E. W. Taylor, Ed. Bellingham: Spie-Int Soc Optical Engineering, 2006, pp. U152-U161.
- [44] B. Sumpf, M. Zorn, R. Staske, J. Fricke, P. Ressel, G. Erbert, M. Weyers, and G. Trankle, "5-W reliable operation over 2000 h of 5-mm-wide 650-nm AlGaInP-GaInP-AlGaAs laser bars with asymmetric cladding layers," *IEEE Photonics Technology Letters*, vol. 18, pp. 1955-1957, Sep-Oct 2006.
- [45] A. Yuen, "Telecom packaging improves reliability of high-power lasers," *Laser Focus World*, July 2007.
- [46] N. Chinone, "Nonlinearity in power-output-current characteristics of stripe-geometry injection-lasers," *Journal of Applied Physics*, vol. 48, pp. 3237-3243, 1977.
- [47] P. A. Kirkby, A. R. Goodwin, G. H. B. Thompson, and P. R. Selway, "Observations of self-focusing in stripe geometry semiconductor-lasers and development of a comprehensive model of their operation," *IEEE Journal of Quantum Electronics*, vol. 13, pp. 705-719, 1977.
- [48] R. Lang, "Lateral transverse-mode instability and its stabilization in stripe geometry injection-lasers," *IEEE Journal of Quantum Electronics*, vol. 15, pp. 718-726, 1979.
- [49] P. M. Asbeck, D. A. Cammack, J. J. Daniele, and V. Klebanoff, "Lateral-mode behaviour in narrow stripe lasers," *IEEE Journal of Quantum Electronics*, vol. 15, pp. 727-733, 1979.
- [50] K. A. Shore, T. E. Rozzi, and G. H. Intveld, "Semiconductor-laser analysis - general-method for characterizing devices of various cross-sectional geometries," *IEE Proceedings-I Communications Speech and Vision*, vol. 127, pp. 221-229, 1980.
- [51] W. Streifer, R. D. Burnham, and D. R. Scifres, "Channeled substrate nonplanar laser analysis. Part 1. Formulation and the plano-convex wave-guide laser," *IEEE Journal of Quantum Electronics*, vol. 17, pp. 736-744, 1981.
- [52] D. P. Wilt and A. Yariv, "A self-consistent static model of the double-heterostructure laser," *IEEE Journal of Quantum Electronics*, vol. 17, pp. 1941-1949, 1981.
- [53] M. Ueno, R. Lang, S. Matsumoto, H. Kawano, T. Furuse, and I. Sakuma, "Optimum designs for InGaAsP/InP ($\lambda=1.3\ \mu\text{m}$) planoconvex waveguide lasers under lasing conditions," *IEE Proceedings-I Communications Speech and Vision*, vol. 129, pp. 218-228, 1982.
- [54] J. K. Butler and D. Botez, "Lateral-mode discrimination and control in high-power single-mode diode-lasers of the large-optical-cavity (LOC) type," *IEEE Journal of Quantum Electronics*, vol. 20, pp. 879-891, 1984.

- [55] G. P. Agrawal, W. B. Joyce, R. W. Dixon, and M. Lax, "Beam-propagation analysis of stripe-geometry semiconductor lasers: threshold behaviour," *Applied Physics Letters*, vol. 43, pp. 11-13, 1983.
- [56] G. P. Agrawal, "Fast-Fourier-Transform based beam-propagation model for stripe-geometry semiconductor-lasers – inclusion of axial effects," *J. Appl. Phys.*, vol. Vol. 56, p. p. 3100, 1984.
- [57] G. P. Agrawal, "Lateral analysis of quasi-index-guided injection lasers: transition from gain to index guiding," *Journal of Lightwave Technology*, vol. 2, pp. 537-543, 1984.
- [58] P. Meissner, E. Patzak, and D. Yevick, "A self-consistent model of stripe geometry lasers based on the beam propagation method," *IEEE Journal of Quantum Electronics*, vol. 20, pp. 899-905, 1984.
- [59] R. Baets and P. E. Lagasse, "Longitudinal static-field model for DH lasers," *Electronics Letters*, vol. 20, pp. 41-42, 1984.
- [60] R. Baets, J. P. Vandecapelle, and P. E. Lagasse, "Longitudinal analysis of semiconductor lasers with low reflectivity facets," *IEEE Journal of Quantum Electronics*, vol. 21, pp. 693-699, 1985.
- [61] J. N. Walpole, "Semiconductor amplifiers and lasers with tapered gain regions," *Optical and Quantum Electronics*, vol. 28, pp. 623-645, Jun 1996.
- [62] S. A. Biellak, G. Fanning, Y. Sun, S. S. Wong, and A. E. Siegman, "Reactive-ion-etched diffraction-limited unstable resonator semiconductor lasers," *IEEE Journal of Quantum Electronics*, vol. 33, pp. 219-230, Feb 1997.
- [63] G. P. Agrawal, "Fast-Fourier-Transform based beam-propagation model for stripe-geometry semiconductor-lasers – inclusion of axial effects," *J. Appl. Phys.*, vol. Vol. 56, p. p. 3100, 1984.
- [64] K. A. Williams, R. V. Penty, I. H. White, D. J. Robbins, F. J. Wilson, J. J. Lewandowski, and B. K. Nayar, "Design of high-brightness tapered laser arrays," *IEEE Journal of Selected Topics in Quantum Electronics*, vol. 5, pp. 822-831, May-Jun 1999.
- [65] G. Fox and T. Li, "Resonant modes in a maser interferometer," *Bell Syst. Tech. J.*, vol. Vol. 40, pp. 453-488, 1961.
- [66] L. Borruel, S. Sujecki, I. Esquivias, J. Wykes, P. Sewell, T. M. Benson, E. C. Larkins, J. Arias, and B. Romero, "Selfconsistent electrical, thermal and optical model of high brightness tapered lasers," in *Physics and Simulation of Optoelectronic Devices X*, vol. 4646, P. Blood, M. Osinski, and Y. Arakawa, Eds. Bellingham: Spie-Int Soc Optical Engineering, 2002, pp. 355-366.
- [67] J. G. Wykes, L. Borruel, S. Sujecki, P. Sewell, T. M. Benson, E. C. Larkins, and I. Esquivias, "Convergence behavior of coupled electromagnetic/electronic high power laser models," *Proc. IEE CEM2002 (Bournemouth, UK)*, 2002.
- [68] S. Sujecki, L. Borruel, J. Wykes, P. Moreno, B. Sumpf, P. Sewell, H. Wenzel, T. A. Benson, G. Erbert, I. Esquivias, and E. C. Larkins, "Nonlinear properties of

- tapered laser cavities," *IEEE Journal of Selected Topics in Quantum Electronics*, vol. 9, pp. 823-834, May-Jun 2003.
- [69] Jun Jun Lim, "Investigation of Factors Influencing the Brightness of High-Power, High-Brightness Laser Diodes," University of Nottingham: Thesis for Doctor's Degree, 2003.
- [70] J. Buus, "The effective index method and its application to semiconductor lasers," *IEEE Journal of Quantum Electronics*, vol. 18, pp. 1083-1089, 1982.
- [71] J. G. Wykes, L. Borruel, S. Sujecki, I. Esquivias, P. Sewell, T. M. Benson, E. C. Larkins, P. Moreno, and M. Krakowski, "Hot-cavity modelling of high-power tapered laser diodes using wide-angle 3D FD-BPM," *IEEE Lasers and Electrooptics Society Annual Meeting*, 2002.
- [72] J. J. Lim, S. Sujecki, L. Lang, Z. C. Zhang, D. Paboeuf, G. Pauliat, G. Lucas-Leclin, P. Georges, R. C. I. MacKenzie, P. Bream, S. Bull, K. H. Hasler, B. Sumpf, H. Wenzel, G. Erbert, B. Thestrup, P. M. Petersen, N. Michel, M. Krakowski, and E. C. Larkins, "Design and Simulation of Next-Generation High-Power, High-Brightness Laser Diodes," *IEEE Journal of Selected Topics in Quantum Electronics*, vol. 15, pp. 993-1008, May-Jun 2009.
- [73] J. J. Lim, R. MacKenzie, S. Sujecki, M. Sadeghi, S. M. Wang, Y. Q. Wei, J. S. Gustavsson, A. Larsson, P. Melanen, P. Sipila, P. Uusimaa, A. A. George, P. M. Smowton, and E. C. Larkins, "Simulation of double quantum well GaInNAs laser diodes," in *21st Conference on Semiconductor Integrated Optoelectronics (SIOE)*, Cardiff, WALES, 2007, pp. 259-265.
- [74] S. Selberherr, *Analysis and Simulation of Semiconductor Devices*: Wien, New York: Springer, 1984.
- [75] S. Selberherr, "Device Modeling and Physics," *Physica Scripta*, vol. T35, pp. 293-298, 1991.
- [76] M. R. Pinto, C. S. Rafferty, and R. W. Dutton, *PISCES-II User's Manual*: Stanford Electron. Labs., Stanford, CA, 1984.
- [77] R. E. Bank, D. J. Rose, and W. Fichtner, "Numerical-methods for semiconductor-device simulation," *IEEE Transactions on Electron Devices*, vol. 30, pp. 1031-1041, 1983.
- [78] O. E. Akcasu, "Convergence properties of Newton's method for the solution of the semiconductor transport-equations and hybrid solution techniques for multidimensional simulation of VLSI devices," *Solid-State Electronics*, vol. 27, pp. 319-328, 1984.

Chapter 4

Experimental Techniques and the Presentation and Analysis of Experimental Results

The experimental techniques used in the analysis of the devices investigated in this thesis will be briefly discussed in this chapter. A state-of-the-art laboratory, called the Optical Measurement and Evaluation Systems (OMES) laboratory, is dedicated to the measurement and characterisation of semiconductor optoelectronic devices at the University of Nottingham. The laboratory is capable of performing the following experiments on laser bars: photoluminescence microscopy (PLM), micro-photoluminescence spectroscopy (μ -PLS), electroluminescence microscopy (ELM), micro-electroluminescence spectroscopy (μ -ELS), measurement of near-field patterns and spectra (NFP and NFS), photocurrent spectroscopy PCS) and micro-photocurrent spectroscopy (μ -PCS). Some of the experimental techniques mentioned above will be discussed briefly prior to the presentation of the experimental results. All of the techniques mentioned above are nondestructive. This means that the bars are carefully mounted and handled in such a way that no damage is caused to them during the measurement process.

A presentation and analysis of the experimental results will also be discussed in this chapter for two different bars. The experiments performed were μ -PLS [1-4], laser beam induced current (LBIC), PCS [2-5], thermal imaging [1], PLM [6], ELM [7, 8], NFP measurements [7], and ELS [7, 8]. The measurements performed at UNott are PLM, ELM, NFP and ELS. The additional measurements mentioned above, were carried out by other partners included in the Brighter Project [9]. More information is given in Table 4.1.

The degradation of the individual emitters [10] in the laser bars was critically studied, looking at the impact of defects, temperature, packaging-induced stress and current competition between the emitters.

Table 4.1 Techniques and some important specifications.

Technique	Partner	Details	Output(s)
μ -Photoluminescence Spectroscopy (μ -PL)	TRT	1 scan along each device $\sim 50\ \mu\text{m}$ from the active region, with data acquisition every $10\ \mu\text{m}$	Local position versus peak PL wavelength data
Laser Beam Induced Current (LBIC)	MBI	2 scans along each device, with data points every $10\ \mu\text{m}$	Photo-response versus local position
Photocurrent Spectroscopy (PCS)	MBI	Either overview-spectra or scans along bars, with 1 measurement per emitter	Absorption properties of devices or single-emitters within bars
Thermocamera (Thermo)	MBI	Images of the devices measured in the MIR or NIR	Temperature and information on defect-related electroluminescence
Microscopic optical photography	UNott	12-22 images ($\sim 300 \times 400\ \mu\text{m}$) taken of the facet of each bar before and after measurements.	Images of all bars from each study
Photoluminescence Microscopy (PLM)	UNott	1 scan of ~ 50 images along the facet of each device using Ar^+ excitation	Details of dark spots, dark lines, and facet contaminations etc. observed and their locations
Electroluminescence Microscopy (ELM)	UNott	1 scan of ~ 50 images along the facet of each device with very low bias (typically $10\ \text{mA}$)	Details of uneven intensities especially at higher currents observed and their locations
Near-Field Patterns (NFP)	UNott	Images of each individual emitter at 5 or more bias currents (above and below I_{th})	NFP shape, apparent threshold and efficiency of each emitter, relative power distribution between emitters
Electroluminescence Spectra (ELS)	UNott	Spectra of each individual emitter at 5 or more bias currents (above and below I_{th})	Peak wavelength and FWHM of each emitter as a function of current

4.1 Experimental Techniques

4.1.1 Photo- and electroluminescence imaging measurements

PLM and ELM are powerful, non-destructive tools used for the study of degradation and defects in semiconductor materials and devices [11]. The PLM technique is intrinsically sensitive to the impact of nonradiative recombination centres or defects on optical processes. No sample preparation is required for PLM when it is used to observe facet defects in laser diodes. ELM on the other hand, is used to complement PLM and uses very low current densities. Measurement at specific emission wavelengths can also be implemented, providing additional information on defects. PL and EL measurements are based on the recombination processes of ehps in a semiconductor material [12]. The energy required to excite the semiconductor for PL measurements is sourced from an external light source. For EL measurements, the energy source is a bias current connected across the device.

Micro-PL is a topographical technique and therefore does not “image” and thus does not need a camera. On the other hand, PLM is an imaging technique, so it does not require a scanned excitation source.

In EL imaging, the optical excitation source is replaced by a power supply unit, which provides either continuous or pulsed current. PLM and ELM imaging systems can be constructed based on the basic principles discussed above. The components needed for the construction of such a system are enumerated below:

1. The sample to be imaged must be illuminated by an external light source (i.e. laser sources or lamp sources.) Independent of the light source used, the

excitation light needs filtering out to preserve the much weaker PL signal i.e. cutoff filters are needed to block the wavelength of the excitation sources.

2. Further filtering is needed for spectroscopic studies. For spectral resolution of 0.45 to 1.10 nm in the near-infrared region [13, 14], systems that uses a liquid-crystal Fabry-Perot (LCFP) filter can be implemented [7, 15].
3. Collection of the image is by a microscope objective. For the greatest image efficiency, the objective must have the largest numerical aperture and highest transmission possible at the luminescence wavelengths of interest.
4. A major component of the PLM/ELM system is the detector i.e. the charged coupled device (CCD) camera. In selecting a detector, the first consideration has to be the choice of an appropriate imaging wavelength. We next consider the issues of sensitivity and dark current. For long exposure times (when measuring very weak PL signals), a very low dark current and excellent sensitivity are required. In addition to choosing a good detector, it often requires cooling the detector head.
5. The mounting and movement of the sample automatically and data processing are very crucial. The sample is mounted on a motorised motion control unit, which allows series of images to be taken and large amount of data to be collected and stored on a computer. This also allows various image processing functions (e.g. dark signal subtraction) to be performed.

The specific PLM/ELM system used for the collection of the experimental data in this thesis is shown in Fig. 4.1 [16]. The sample is mounted on xyz translation stage and excited by an Ar⁺ laser source. A dc power supply is used for the ELM measurements. The image of the sample is focussed onto a 1024×1024 pixel silicon CCD array, which is cooled by liquid nitrogen to improve the signal-to-

noise ratio (SNR). A microscope objective and a set of lenses and filters are used to collect the light and focus the image.

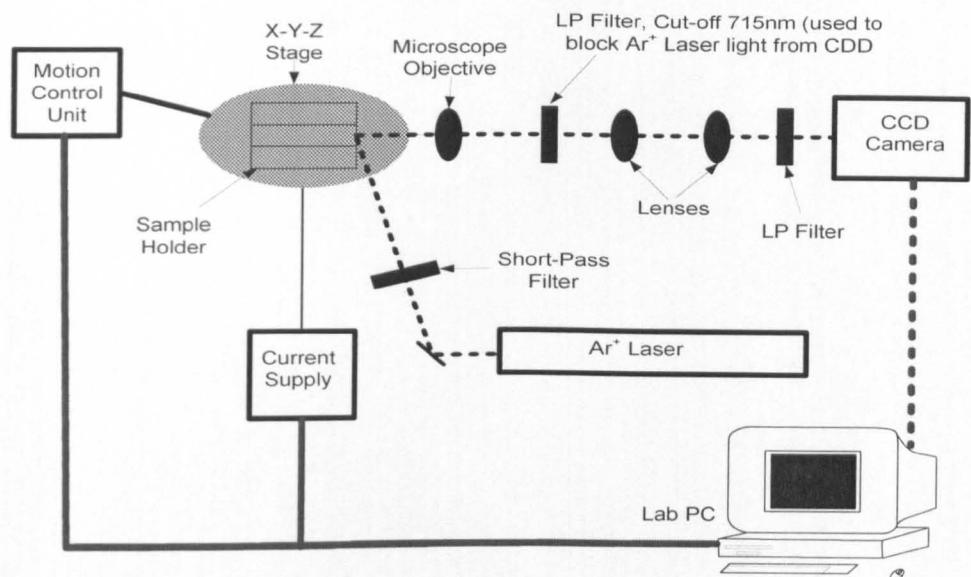


Fig. 4.1 Schematic diagram of the PLM/ELM setup.

4.1.2 Near-field Observations

Earlier in this chapter, very low current ELM measurements (in conjunction with PLM) were discussed. Here, the focus will be on the NF observation of a laser facet at high bias currents – where we observe both the NFPs and the NFS by ELM. The focus is on the measurement of the NF of the individual emitters within the HPLD bars. The use of the fast Fourier transform (FFT) technique on the EL spectrum [8, 17, 18] can also be used to reveal information about defects within a laser cavity from nondestructive measurements made at the facet.

The degradation of single-emitter lasers is slower than the degradation rate of identical individual emitters within a HPLD bar. The reasons for this are complex, but three factors that can be identified are: 1. inhomogeneous packaging-induced strain; 2. current competition between the emitters within the bar; and 3. thermal

crosstalk between the emitters. The analysis of bars within this context has been termed by-emitter analysis [3, 8, 19]. “By-emitter analysis is a methodology for studying the behaviour and degradation on individual emitters, which are operating in the context of a parallel connected array sharing the same physical substrate and heatsink” [20]. Fig. 4.2 presents a suitable system for the rapid measurement of spectra and NF images from the individual emitters within a bar. NF images can be produced for a range of bias currents above and below the lasing threshold, using neutral density (ND) filters to prevent saturation of the camera. Two CCD cameras are used in this setup. One records the image of the NFP (1st CCD camera), while the other simultaneously records the emission spectra from the individual emitters (2nd CCD camera).

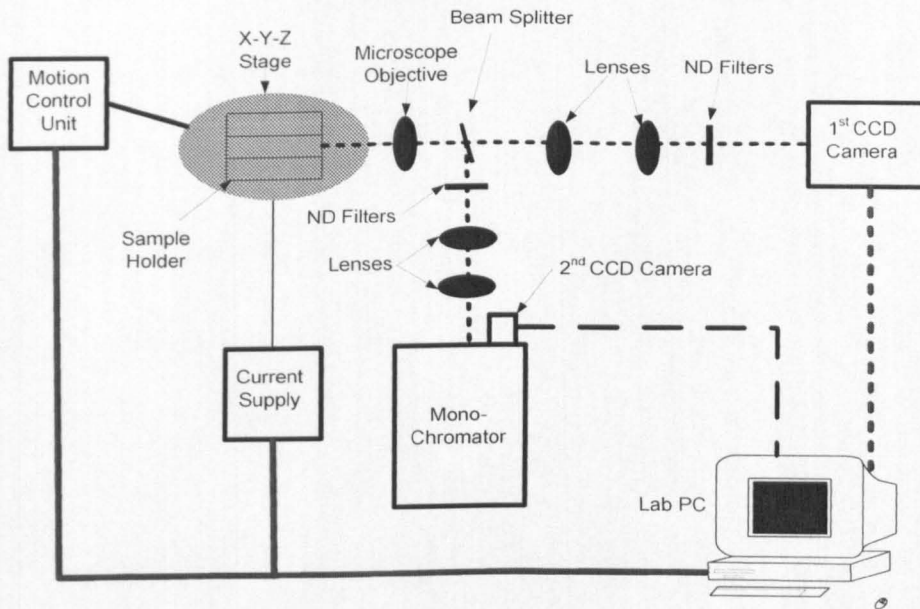


Fig. 4.2 Schematic diagram of an experimental system for simultaneously measuring the NFP and NFS of individual emitters within a laser bar.

4.1.3.1 How a laser bar is mounted on the motion control unit

Fig. 4.3a and b shows sample representations (pictures) of the 650 nm and the 975 nm laser bars measured using the by-emitter analysis described above. Fig. 4.4

demonstrates how the bars are mounted on the *X-Y-Z* motion control unit stage. It also shows how the laser is connected to the power supply.

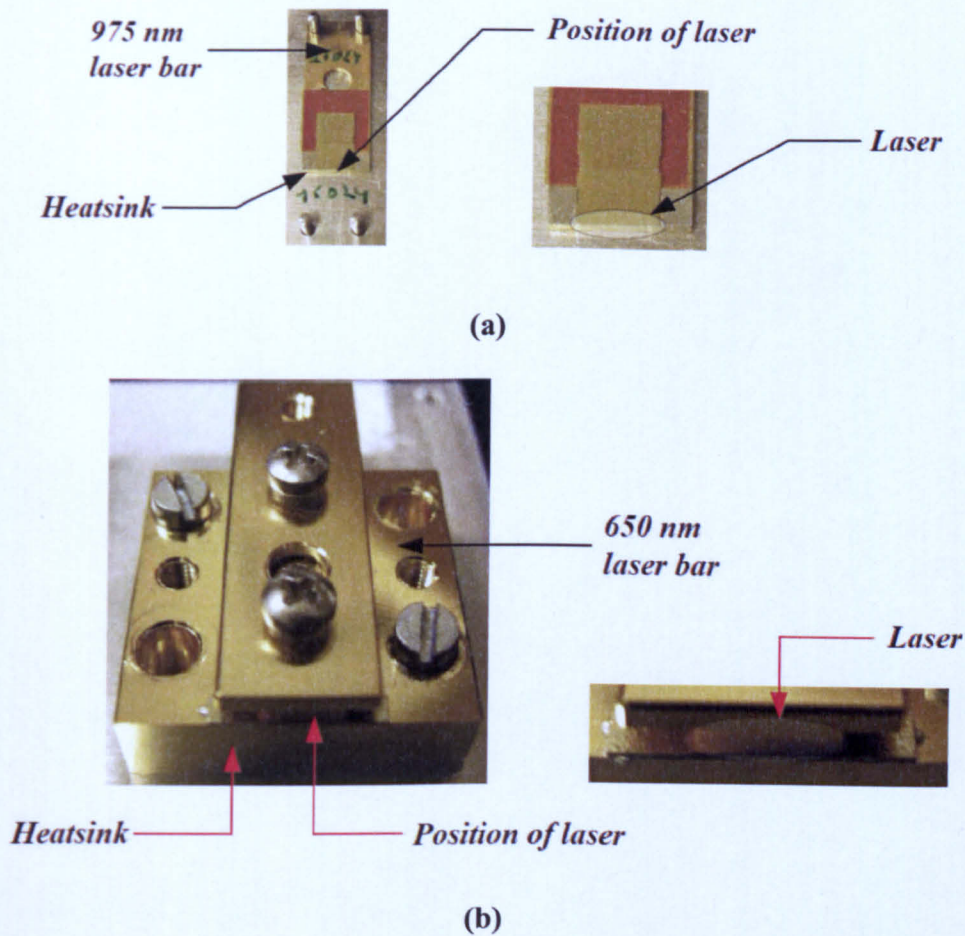


Fig. 4.3 Sample representation of (a) 650 nm red emitting and (b) 975 nm infrared emitting laser bars.

Fig. 4.4a shows the base and top copper blocks, the laser power connector leads and the laser bar. Fig. 4.4b shows the laser mounted on the base copper block and the water hose which facilitates the cooling of the bar. Fig. 4.4c also shows the top block that clamps the laser down unto the base block and the insulating plate that insulates the laser block from the motion control unit. Finally, Fig. 4.4d shows the laser block mounted unto the motion control unit with the power supply connected to the laser bar.

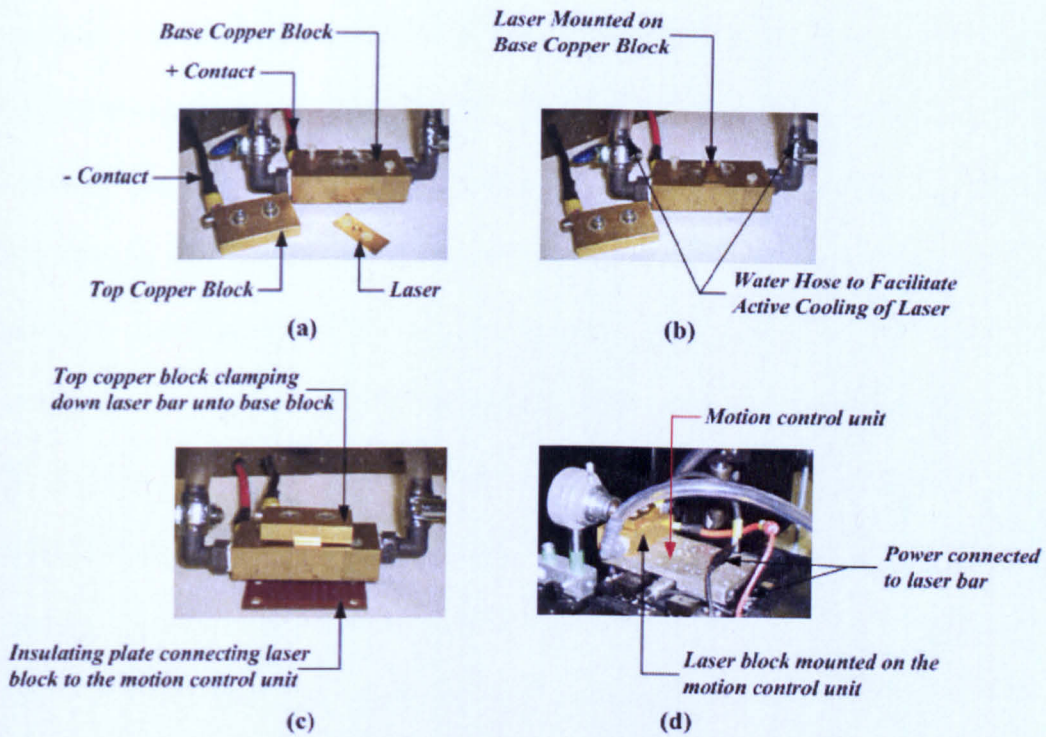


Fig. 4.4 Photographs of how the laser bar is mounted and connected to the motion control unit in the OMES Lab at the University of Nottingham.

4.1.3.2 Power-current characteristics of emitters within a laser bar

The performance of a laser diode is often measured in terms of its power-current (P-I) characteristics, where the threshold current I_{th} and the external differential efficiency η_{ext} can be extracted. I_{th} and η_{ext} of a single emitter can be extracted from the P-I characteristics in the manner indicated in Fig. 4.5. However, a diode laser bar is a parallel-connected array of emitters sharing the same anode and cathode. It is therefore not possible to determine the currents of the individual emitters. Thus, the values of I_{th} and η_{ext} cannot be determined. We can only determine an “apparent” threshold current of the i_{th} emitter (I_{th_app}) and the “apparent” external differential efficiency of the η_{ext} emitter (η_{ext_app}).

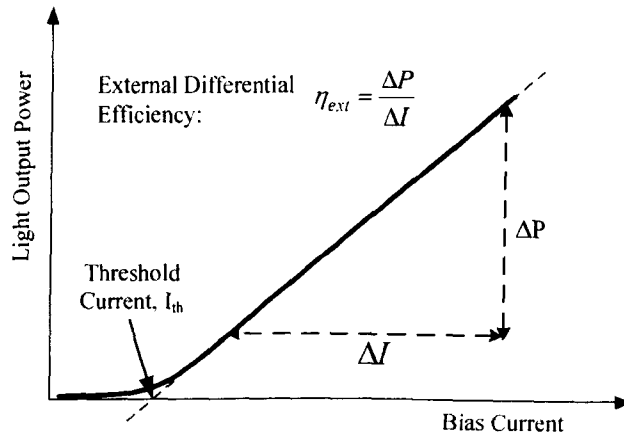


Fig. 4.5 Typical P - I characteristic for a laser diode showing the threshold current (I_{th}) and the external differential efficiency (η_{ext}).

These quantities are determined from the P_i – versus – I_{BAR} curves of the individual emitters, where P_i is the power of the individual emitter, but I_{BAR} is the total bar current [3]. These two quantities allow a qualitative comparison between individual emitters within a laser bar. Note that these quantities differ from the actual I_{th} and η_{ext} in important ways, which will be discussed later.

4.2 Devices Examined, Why Studied, and Techniques Used

The devices chosen include: 1. three 650 nm red-emitting broad area (BA) laser bars fabricated by Ferdinand-Braun-Institut für Höchstfrequenztechnik (FBH) [21]; and 2. four 975 nm infrared tapered laser bars with QW active regions fabricated by Alcatel-Thales III-V Lab. and mounted on expansion-matched heatsinks. Much more analysis was done on the 975 nm bars in study 2 to support the emulation work using *Barlase* in chapter 7 of this thesis.

Study 1 – Red-emitting BA laser bars

Batch #3	λ_o (nm)	Active Region	Emitter Geometry	Heatsink Details	Solder	Supplier
Bar 05x1 Bar 0519 Bar 0521	650	QW	Broad Area	CuW (passive)	AuSn	FBH

The 650 nm lasers consisted of 12 BA emitters (width = 60 μm) with a QW active region, mounted by FBH on CuW passively cooled heatsinks with AuSn solder (i.e. laser diode bar and CuW submount) is mounted on a standard conduction cooled package with a footprint of 25×25 mm². The optimized layer structure consists of GaInP quantum wells embedded in AlGaInP waveguide layers. The n-cladding layer consists of AlInP, the p-cladding layer of AlGaAs with a GaAs substrate [22, 23]. They were 6 mm wide, 1.5 mm long and had an emitter pitch of 500 μm .

Study 2 – Laser bars with QW active regions

Batch #6	λ_o (nm)	Active Region	Emitter Geometry	Heatsink Details	Solder	Supplier
Bar 16022 Bar 16023 Bar 16024 Bar 16025	975	QW	Tapered	Expansion - matched (active)	In	Alcatel Thales III-V LAB

The 975 nm narrow-angle (<1°) tapered laser bars consisted of 16 groups of 4 tapered emitter mini arrays (200 μm wide), mounted by Fraunhofer Institut für Lasertechnik (ILT) with indium solder on expansion-matched Cu heatsinks with active cooling. The expansion-matched cooling uses additional expansion-matched submounts, mounted between the copper heatsink and the laser bar [24]. Active cooling is provided from the mains water supply which runs through water cooling channels beneath the bar to cool it. The optimized layer structure consists

of GaInAs quantum wells embedded in GaInAsP waveguide layers. The n-cladding layer consists of AlGaAs, the p-cladding layer of AlGaAs with a GaAs substrate [25].

The bars were 6.4 mm wide, 2.4 mm long, consisting of a 200 μm ridge waveguide and a 2200 μm tapered amplifier and had an emitter group pitch of 400 μm . The front and rear facet reflectivities were 3% and 90%, respectively.

4.2.1 Technologies used to study the laser degradations

The experimental techniques applied between the various burn-in and subsequent aging tests are described in this section. This characterisation was performed by researchers at Max-Born Institute (MBI), Thales Research and Technology (TRT) and UNott. In addition, standard electro-optical characterisation was performed at the start and end of each aging test. This was done to safeguard and ascertain the facet integrity of the devices before and after the measurements. The techniques and some important specifications are detailed in Table 4.1. The by-emitter experiments performed on these bars are summarised in Table 4.1 and are also described in [1, 3, 10, 25].

Photoluminescence microscopy measures defects and is sensitive to nonradiative recombination centres [6]. Micro-PL is used to measure the bandgap energy in the centre of the substrate and is sensitive to packaging-induced strain [1]. Electroluminescence microscopy is used to measure near field patterns, defects, and relative emitter power. ELM is sensitive to nonradiative recombination centres, temperature, change in bandgap energy (ΔE_g) and scattering losses [8].

I_{th_app} and η_{ext_app} can be obtained from the relative emitter power as a function of current. The electroluminescence spectra measures defects and $\Delta\lambda/\lambda$, which are

sensitive to extended areas of nonradiative recombination and temperature [8]. LBIC measures the sub-band-gap absorption and is sensitive to defects and shifts in the absorption edge [5]. Finally, photocurrent spectroscopy measures QW-transition energies, the bandgap energy of the waveguide and band to trap transitions (e.g., $E_t - E_v$ or $E_c - E_t$). The band edge transitions are sensitive to packaging-induced strain [26].

The NF images and spectra were taken from each emitter using electroluminescence microscopy and spectroscopy. To avoid saturation of the CCD camera, a series of ND filters were employed to attenuate the EL signal. The relative power of each emitter was extracted by integrating its NF image intensities and correcting for the ND filters used.

The bulk temperatures within the bars are measured using a THERMOSENSORIK CMT384 camera equipped with a 45° tilted protection filter and a spectral band-pass filter being transparent in the 3.4–6 μm spectral range. The bars are stabilized to $25.0^\circ\text{C} \pm 0.2^\circ\text{C}$. The temperature sensitivity of the system was calibrated by taking images of the entire bar assembly at elevated temperatures. Typical temperature sensitivities are 25 counts/K. This calibration is cross-checked with data obtained by analysis of the spectral shift of the emission wavelength as described by Ziegler *et al.* [27].

4.3 Study 1

4.3.1 Observations using optical microscopy (650 nm bars)

In order to safeguard and ascertain the facet integrity of the devices, quality control measures were undertaken using optical microscopy when devices were received for by-emitter degradation analysis. In these devices, 12 images at 500

μm intervals were taken, with each image capturing one emitter. No changes were observed in the appearance of the front facet before and after the by-emitter measurements. Fig. 4.6 shows a representative picture of the optical microscopic images taken for bar 05x1. The other two bars also had clean facets and no damage to the bars whatsoever.

Optical microscopic features of bar 05x1

- Clean facet and no damage to bar ends observed

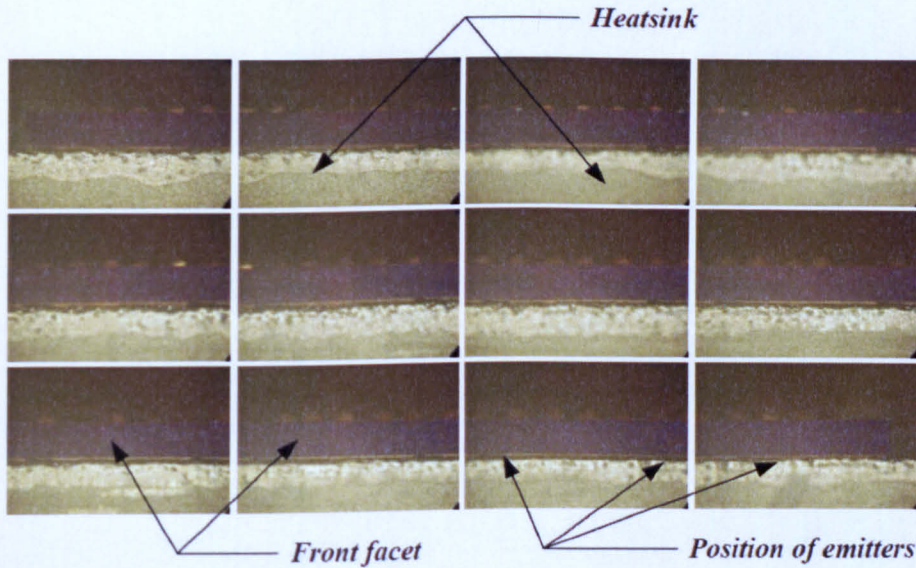


Fig. 4.6 12 magnified images taken before and after by-emitter measurements to ascertain the facet integrity of the bar (bar 05x1).

4.3.2 Presentation of experimental results

The first by-emitter degradation analysis study was performed on 7 W red laser bars emitting at 650 nm. These bars, made by FBH, were comprised of 12 BA emitters (emitter width = 60 μm). Three bars (05x1, 0519, and 0521) were characterised before burn-in.

The red laser bars were selected for by-emitter degradation analysis, since high-power red laser diode bars are relatively recent additions to the family of high-power laser bars. Consequently, comparatively little was known about their degradation behaviour. The aging of these bars showed excellent reliability. This is consistent with other aging tests on the 650 nm bars, which showed the first device failure at 2,100 hours and a mean time to failure (MTTF) of 8,850 hours.

We observed a frown shaped profile in the power distributions (Fig. 4.7), meaning that there were higher powers and temperatures (Fig. 4.8) at the centre of the bars at zero aging time (unaged bars). The frown shaped profile however, changed to a smile shaped profile as the aging progressed, with the central emitters losing more power. A redistribution of power occurred during the aging process. The reason for this power redistribution is explained in the analysis of these bars in section 4.3.3.

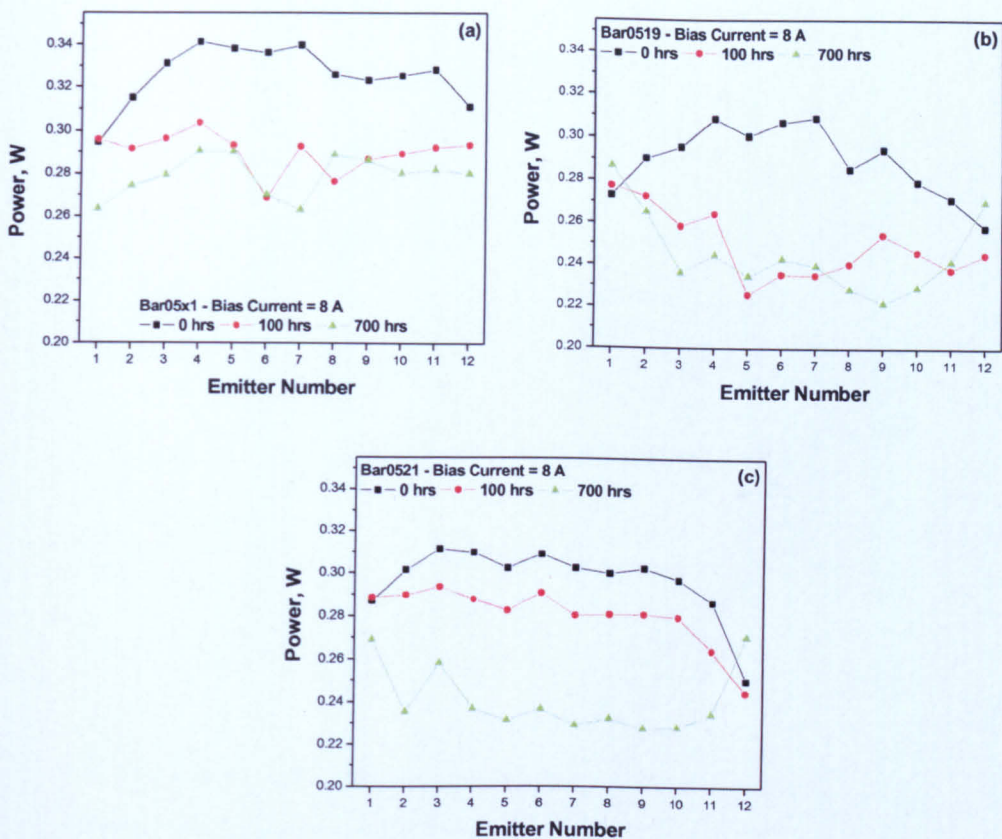


Fig. 4.7 Power against emitter number for the three 650 nm bars at $I_{BAR} = 8 A$ at aging times of 0 hrs, 100 hrs and 700 hrs respectively. (a) Bar 05x1, (b) bar 0519, and (c) bar 0521.

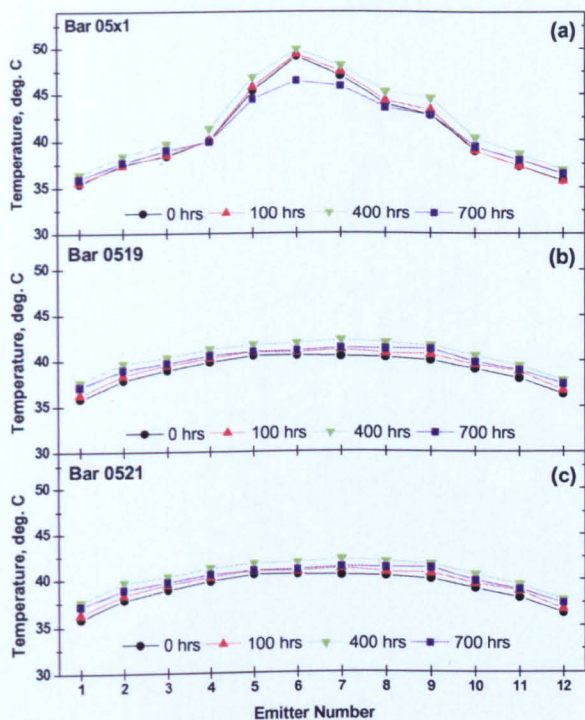


Fig. 4.8 Graphs of emitter temperature versus emitter number after different aging times (courtesy of J. Tomm, Max-Born Institute).

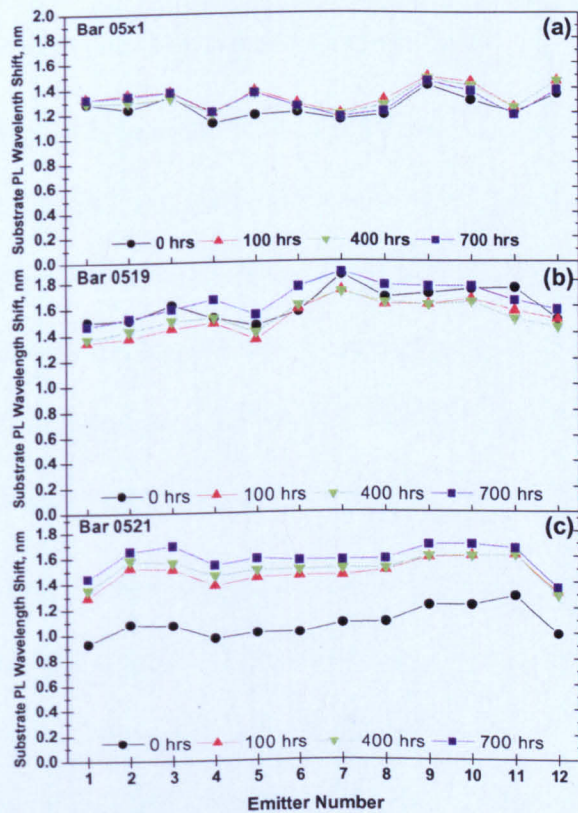


Fig. 4.9 Graphs of strain-induced shift of substrate PL versus emitter number after different aging times (courtesy of J. Perraud and J. Nagle, Thales Research and Technology).

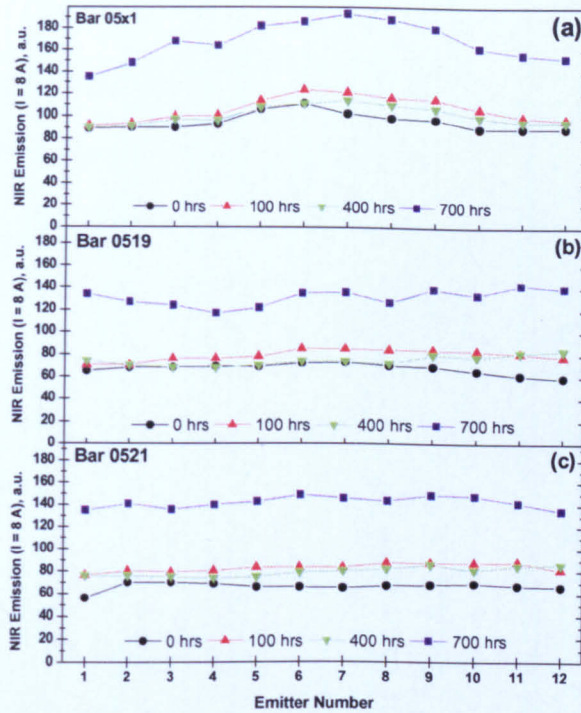


Fig. 4.10 Graphs of near infrared EL signal versus emitter number after different aging times (courtesy of J. Tomm, Max-Born Institute).

4.3.3 Analysis of experimental results (650 nm bars)

There is no evidence of defects in the near-field patterns. All three bars exhibited reasonably uniform power emission, with variations of $\sim 6\%$ between emitters (Fig. 4.7) – even after 700 hours of aging. A slight frown-shaped profile is evident in the profile of the emitter powers across the unaged bars [28]. After aging, the frown-shaped profile turns into a smile-shaped profile (particularly for bar 0519 and bar 0521), with the centre emitters providing less power [28, 29].

Degradation emulation studies suggest that the frown-shaped power profile of the unaged bars is probably a result of the higher temperature of the centre emitters compared to those at the edges of the bar (Fig. 4.8). The higher emitter temperature at the centre of the bar causes the bandgap energy to decrease slightly, so that the turn-on voltages of these emitters decrease relative to those of the cooler edge emitters. This causes these emitters to draw more current and emit

more power than the edge emitters. As the centre emitters are being driven harder than the edge emitters, their performance also degrades faster. This causes the frown-shaped power profile to turn into a smile-shaped profile after aging and degradation. A slight decrease in the temperature of the degraded emitters at the centre of the bar is also observed (Fig. 4.8). (Similar behaviour is also observed in the 975 nm laser bars in study 2, as discussed later.) Nevertheless, it should be noted that both the power variation across these bars and the subsequent power loss during aging is quite small in the 975 nm devices.

Inhomogeneous packaging induced strain has often been related to faster bar degradation [15, 30]. Fig. 4.9 shows that the shift in the PL transition energy of the substrate is very small (<0.3 nm), indicating that any packaging induced strain is homogenous across the bar. Furthermore, the strain induced shift in the substrate PL does not change appreciably during aging. (The profile at 0 hours for bar 0521 is an exception, which is not fully understood, but appears more consistent with an error in the measurement.) These observations are consistent with a good soldering process and the excellent reliability achieved with these bars.

4.4 Study 2

4.4.1 Observations using optical microscopy

In order to safeguard and ascertain the facet integrity of the devices, quality control measures were undertaken using optical microscopy by UNott when devices were received for by-emitter degradation analysis. In these devices, 22 images were taken at 400 μm intervals, with each image capturing at least one group of 4 emitters. No changes were observed in the appearance of the front facet

before and after the by-emitter measurements. Fig. 4.11 shows a representative picture of the optical microscopic images taken for bar 16022. A critical observation of this figure shows the damage (broken edges) at both ends of the bar. Fig. 4.12 on the other hand reveals large number of features observed on the facet of bar 16023 from the optical microscopy analysis. The other two bars (bar 16024 and bar 16025) had clean facets and no damage to the bars whatsoever.

Optical microscopic features of bar 16022

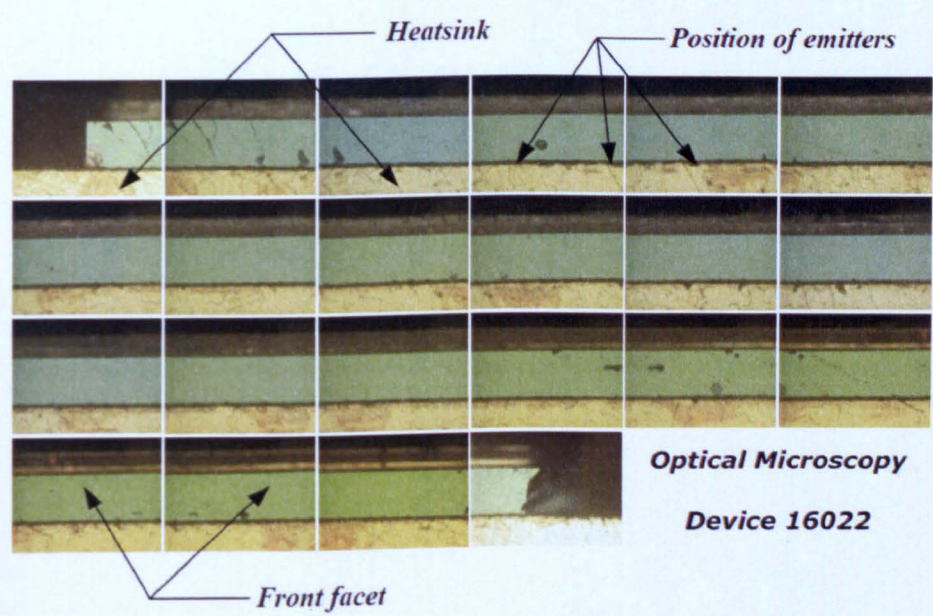


Fig. 4.11 22 magnified images taken before and after by-emitter measurements to ascertain the facet integrity of the bar (bar 16022).

Optical microscopic features of bar 16023

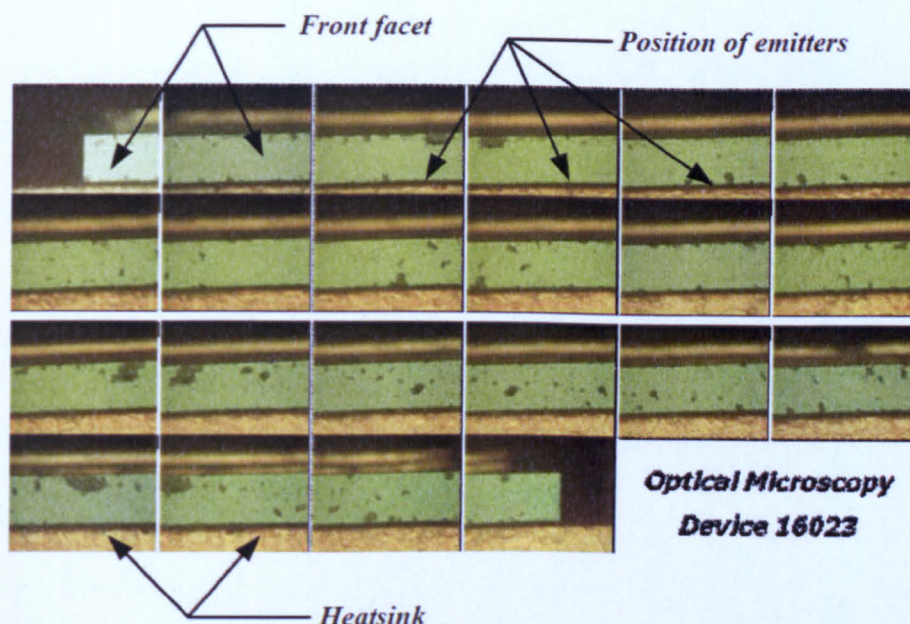


Fig. 4.12 22 magnified images taken before and after by-emitter measurements at to ascertain the facet integrity of the bar (bar 16023).

4.4.2 Presentation of experimental results (975 nm bars)

The presentation of experimental results from these bars is done separately due to some departures from what is expected. For instance, the power distributions of the bars typically have a frown-shaped profile, so that higher emission power is observed for the emitters at the middle of the bar. However, some bars did not show this profile. Bar 16024, and especially bar 16023, deserve special attention to enquire if the lack of correlation between the substrate PL shift and the QW bandgap energies was due to a compositional variation in the epitaxial material.

4.4.2.1 Results for bar 16022

The emission power of this bar follows the frown shape expected with high emission power at the centre of the bar (hotter emitters). However, because the emitters at both edges of this bar were broken (Fig. 4.11), emitter groups 1 and 16 recorded a significant drop in emission power. This corresponds to high temperatures recorded at both edges of the bar. The emitter group with the highest power throughout the aging process (emitter group #9 of 1.054 W @ 25 A) degraded by 9.6% at 100 hrs and 12.9% at 600 hrs, respectively. This trend is typical for most laser bars, where the hottest emitters (recording the highest power) are located somewhere near the centre of the bar.

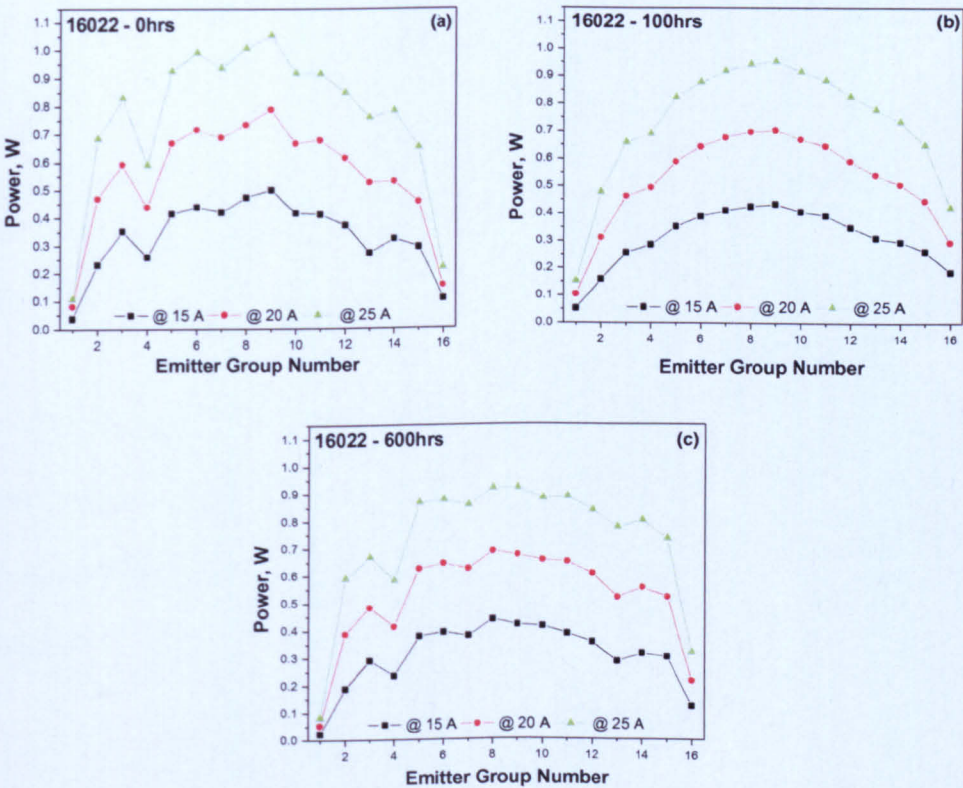


Fig. 4.13 Emitter group power versus emitter number for various I_{BAR} currents (15 A, 20 A, and 25 A) after aging for (a) 0 hrs, (b) 100 hrs, and (c) 600 hrs.

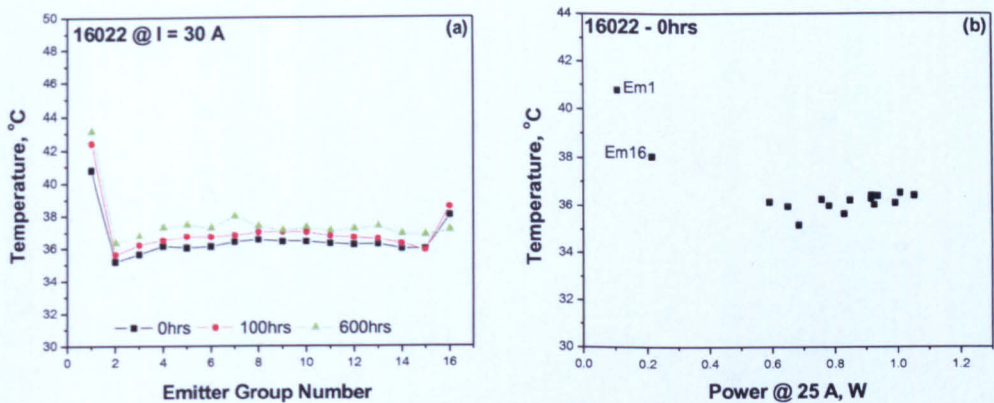


Fig. 4.14 Graphs of (a) emitter temperature versus emitter group number, (b) emitter temperature versus emitter power at 25 A for 0 hrs (courtesy of J. Tomm, Max-Born Institute).

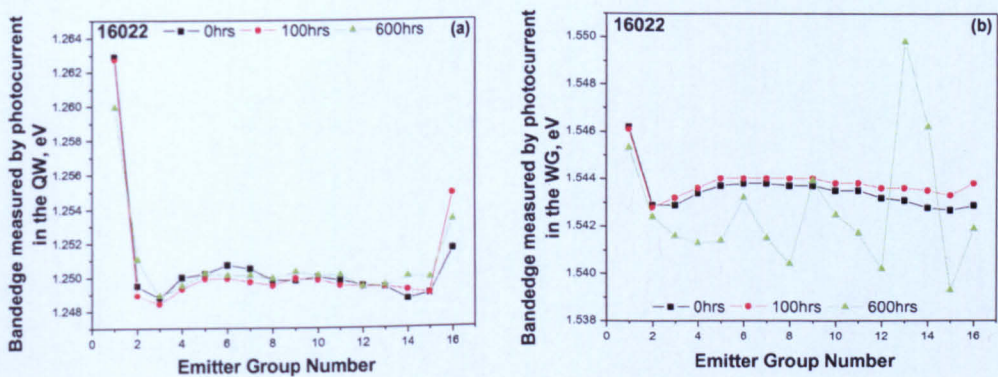


Fig. 4.15 Graphs of (a) bandedge measured by photocurrent in the QW versus emitter group number, (b) bandedge measured by photocurrent in the waveguide (WG) versus emitter group number (courtesy of J. Tomm, Max-Born Institute).

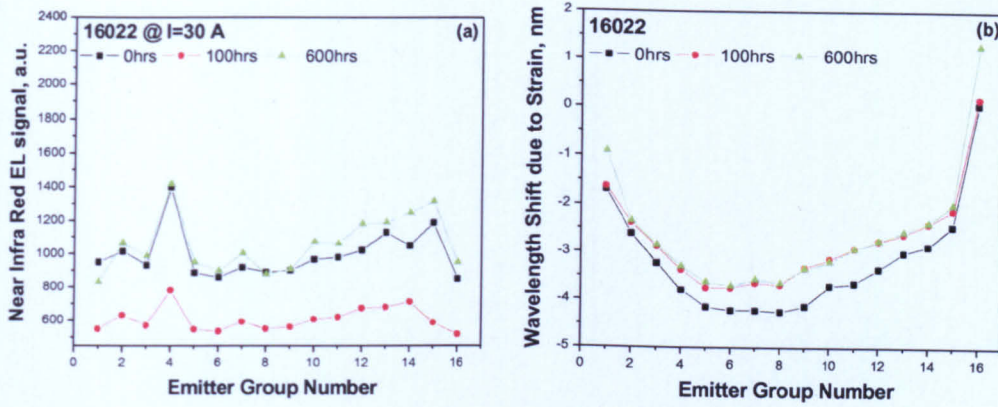


Fig. 4.16 Graphs of (a) near infrared EL signal versus emitter group number, (b) strain-induced shift of substrate PL versus emitter group number (courtesy of J. Tomm, Max-Born Institute and J. Perraud and J. Nagle, Thales Research and Technology).

4.4.2.2 Results for bar 16023

The emission power of this bar does not have the typical frown shaped profile, but has an almost flat emission power profile at the centre of the bar. There is an increase in power at the right hand edge of the bar. This corresponds to an increase in temperature, but this power drops as the degradation progresses. The emitter group with the highest power at 0 hrs (emitter group #14 of 0.736 W @ 25 A) increased in power by 7.5% at 100 hrs, but degraded by 15.8% at 600 hrs. In this bar, the emitter with the highest recorded power changed during the degradation process from emitter group #14 at 0 hrs to emitter #15 at 100 hrs, and emitter #5 at 600 hrs.

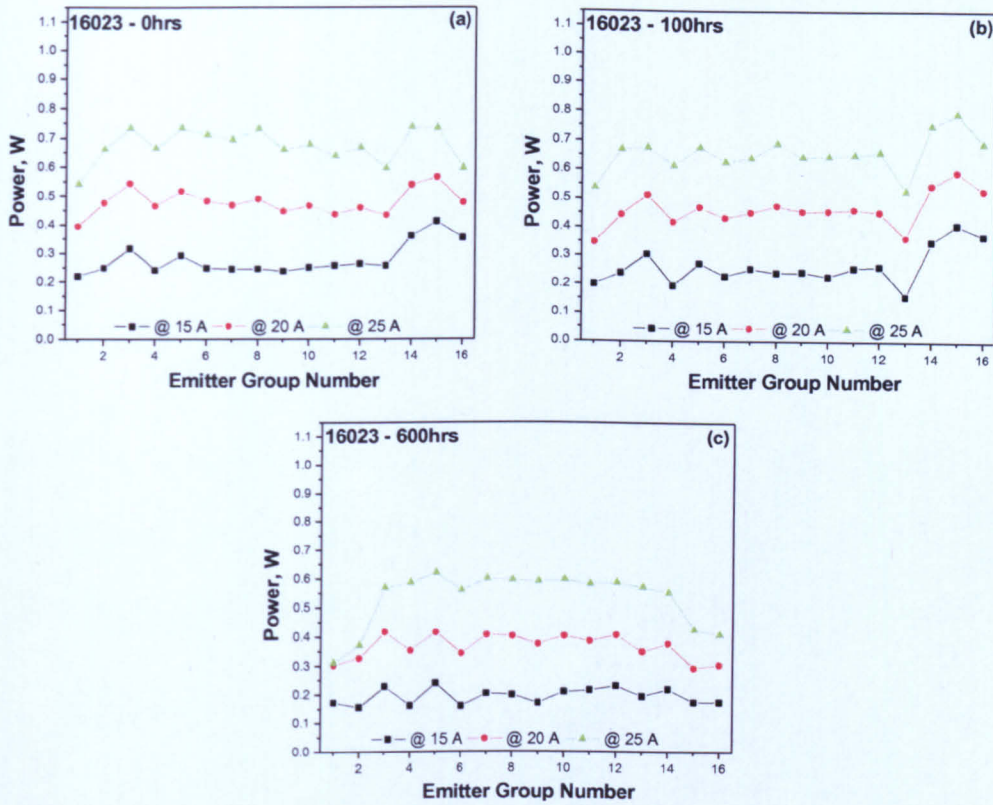


Fig. 4.17 Emitter group power versus emitter number for various I_{BAR} currents (15 A, 20 A, and 25 A) after aging for (a) 0 hrs, (b) 100 hrs, and (c) 600 hrs.

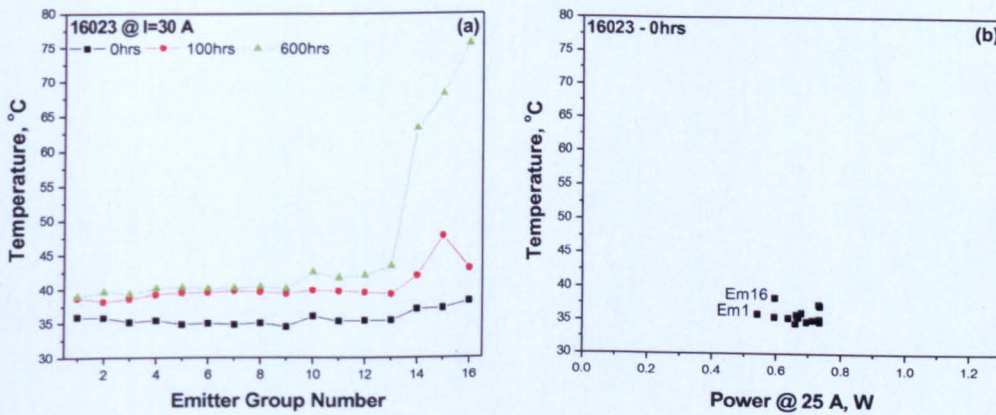


Fig. 4.18 Graphs of (a) emitter temperature versus emitter group number, (b) emitter temperature versus emitter power at 25 A for 0 hrs (courtesy of J. Tomm, Max-Born Institute).

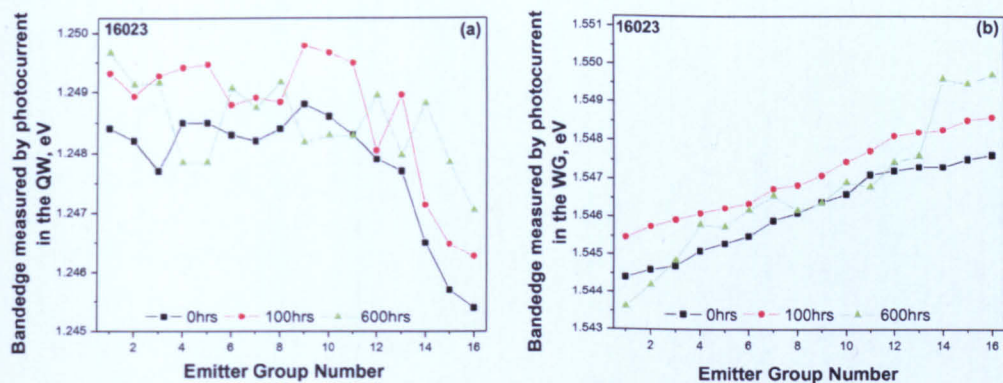


Fig. 4.19 Graphs of (a) bandedge measured by photocurrent in the QW versus emitter group number, (b) bandedge measured by photocurrent in the WG versus emitter group number (courtesy of J. Tomm, Max-Born Institute).

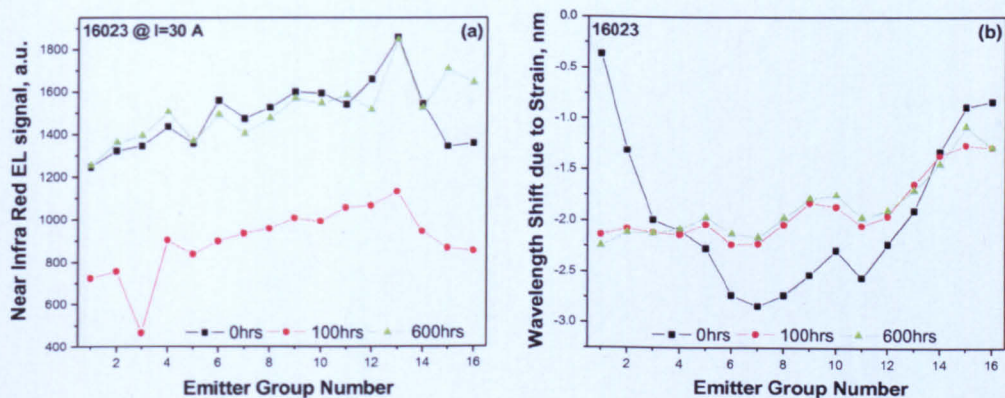


Fig. 4.20 Graphs of (a) near infrared EL signal versus emitter group number, (b) strain-induced shift of substrate PL versus emitter group number. (courtesy of J. Tomm, Max-Born Institute and J. Perraud and J. Nagle, Thales Research and Technology).

4.4.2.3 Results for bar 16024

The power profile of this bar has the expected frown shaped profile with high emission power at the centre of the bar (hotter emitters). Emitter group number 5 has an abnormally high temperature compared to all of the other emitters and has

a correspondingly high NIR defect EL. The emitter group with the highest power at 0 hrs (emitter group #6 of 1.022 W @ 25 A) degraded by 2.8% at 100 hrs and by 9.6% at 600 hrs, respectively. In this bar, the emitter with the highest recorded power also changed from emitter group #6 at 0 hrs and 100 hrs to emitter #4 at 600 hrs.

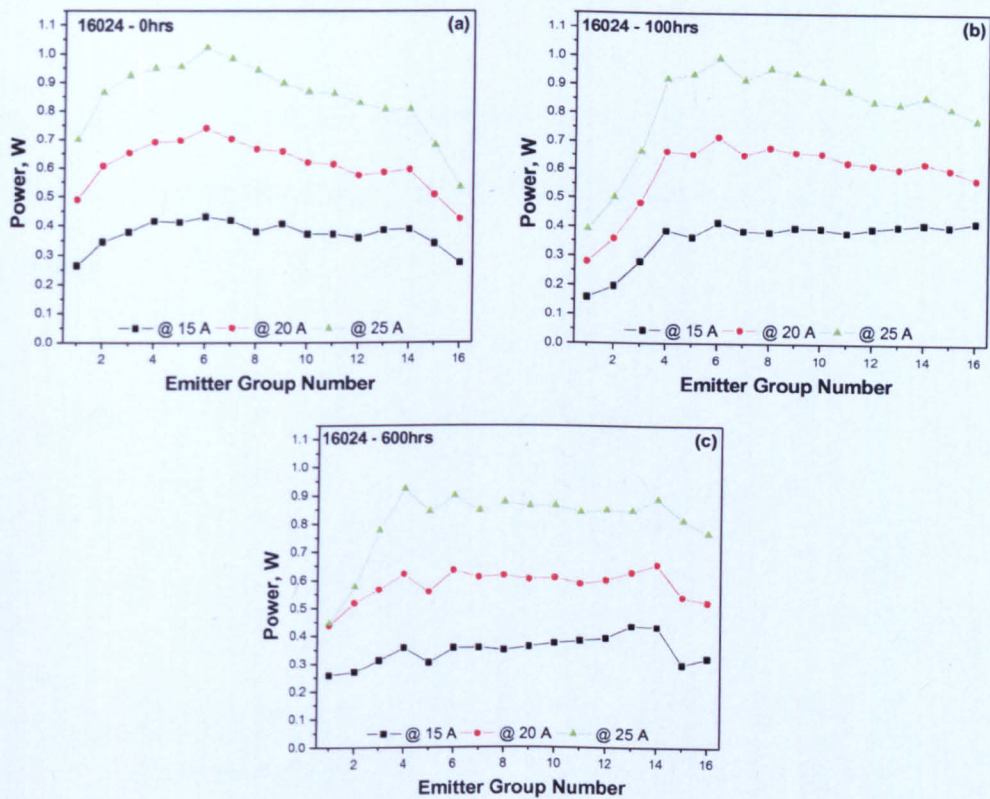


Fig. 4.21 Emitter group power versus emitter number for various I_{BAR} currents (15 A, 20 A, and 25 A) after aging for (a) 0 hrs, (b) 100 hrs, and (c) 600 hrs.

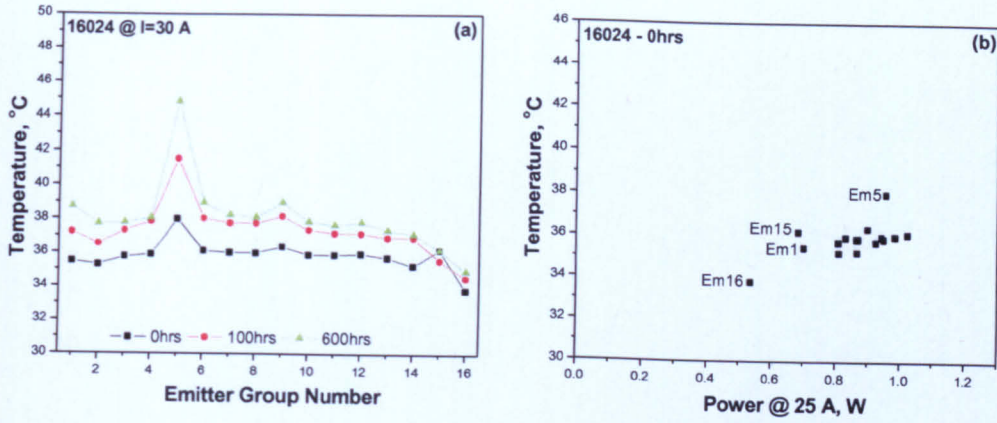


Fig. 4.22 Graphs of (a) temperature versus emitter group number, (b) temperature versus power at 25 A for 0 hrs (courtesy of J. Tomm, Max-Born Institute).

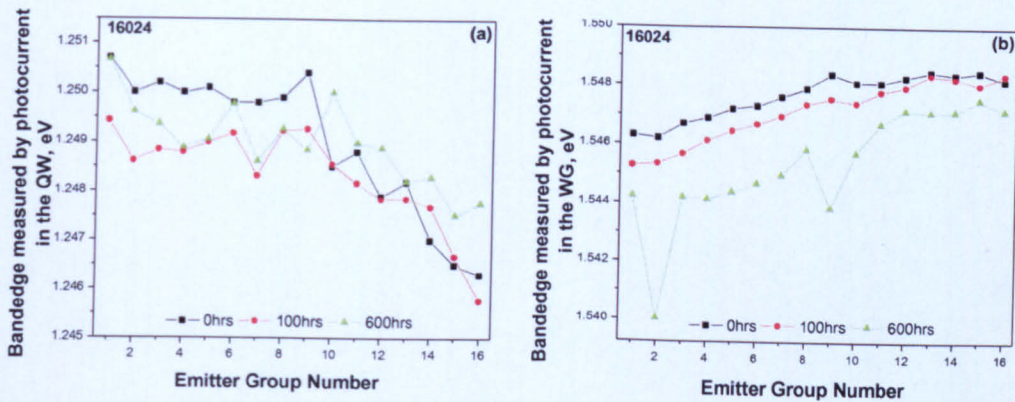


Fig. 4.23 Graphs of (a) bandedge measured by photocurrent in the QW versus emitter group number, (b) bandedge measured by photocurrent in the WG versus emitter group number (courtesy of J. Tomm, Max-Born Institute).

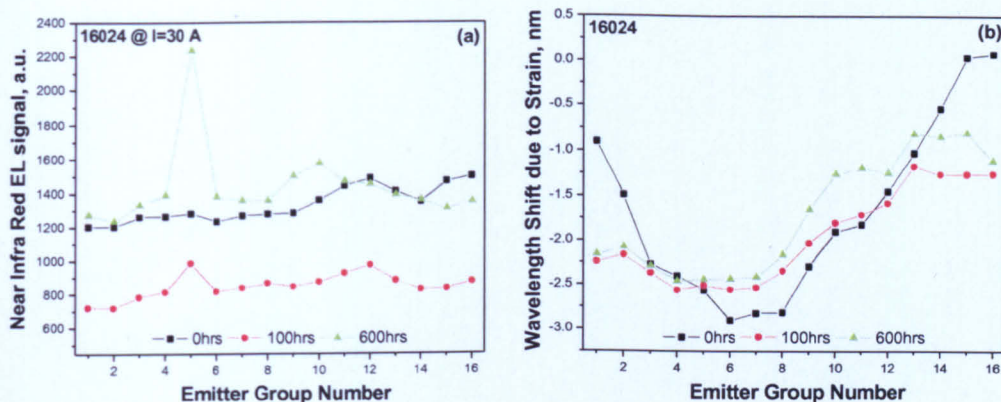


Fig. 4.24 Graphs of (a) near infrared EL signal versus emitter group number, (b) strain-induced shift of substrate PL versus emitter group number. (courtesy of J. Tomm, Max-Born Institute and J. Perraud and J. Nagle, Thales Research and Technology).

4.4.2.4 Results for bar 16025

The emission power of this bar has the expected frown shaped profile, with high emission power at the centre of the bar (hotter emitters). The emitter group with the highest power at 0 hrs (emitter group #8 of 1.004 W @ 25 A) degraded by 4% at 100 hrs and by 10.6% at 600 hrs, respectively. As mentioned earlier, this is the expected trend for most laser bars.

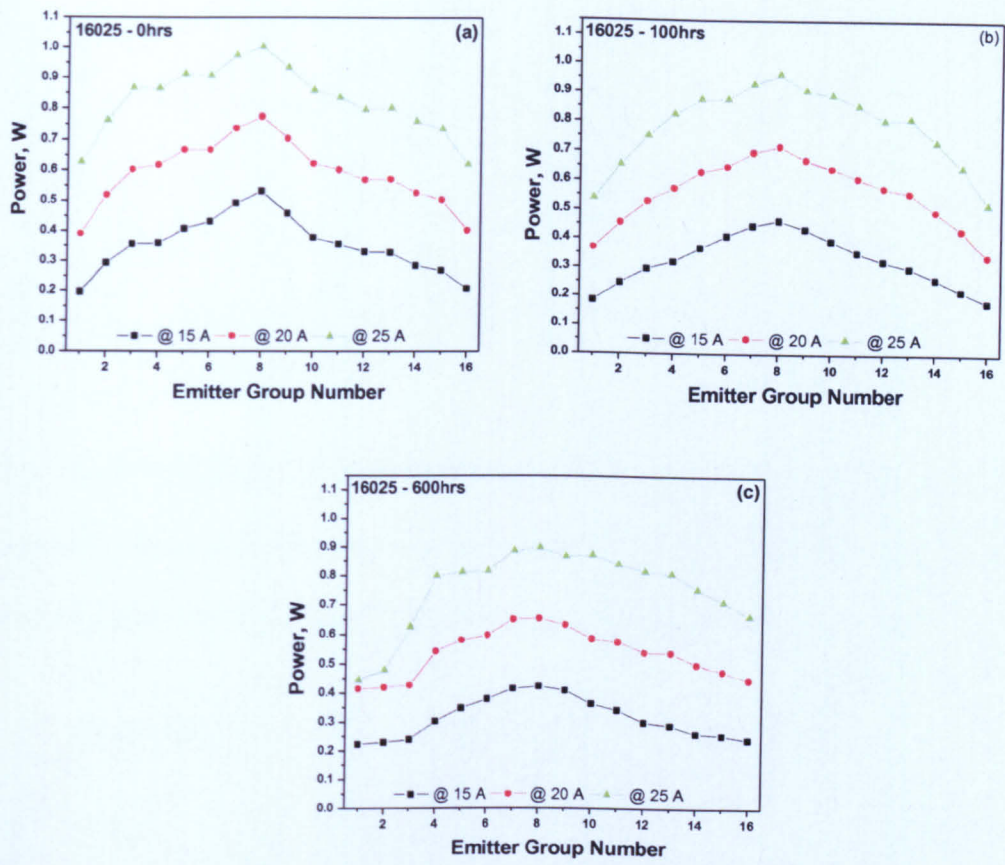


Fig. 4.25 Emitter group power versus emitter number for various I_{BAR} currents (15 A, 20 A, and 25 A) after aging for (a) 0 hrs, (b) 100 hrs, and (c) 600 hrs.

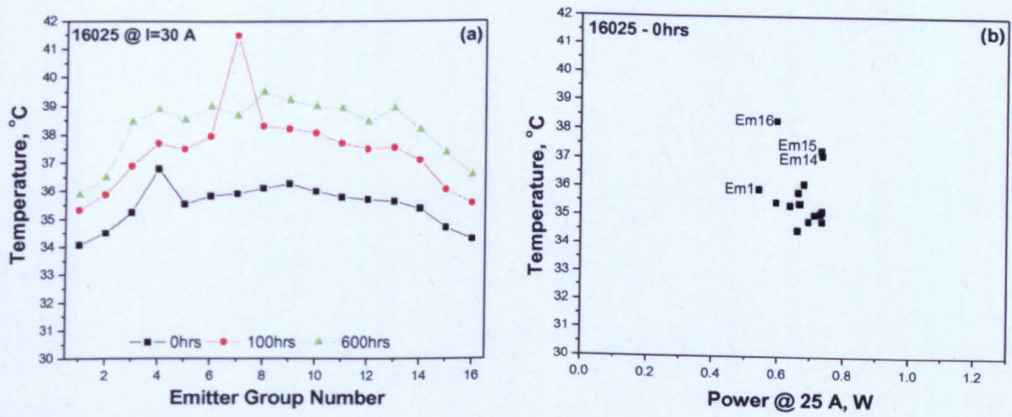


Fig. 4.26 Graphs of (a) temperature versus emitter group number, (b) temperature versus power at 25 A for 0 hrs (courtesy of J. Tomm, Max-Born Institute).

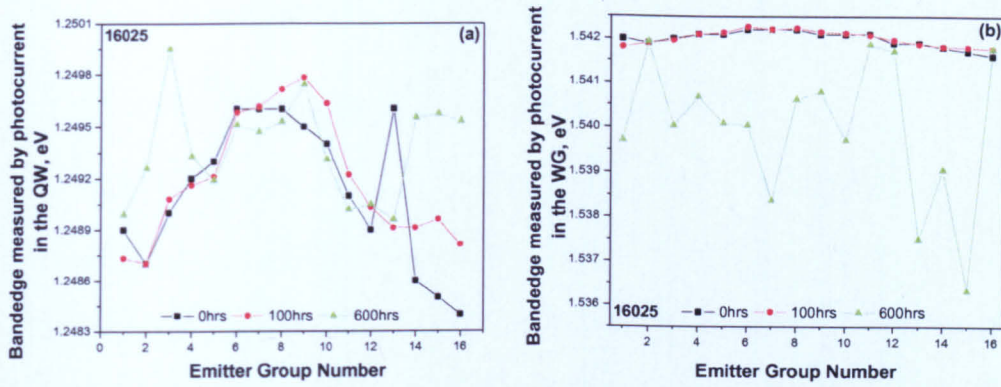


Fig. 4.27 Graphs of (a) bandedge measured by photocurrent in the QW versus emitter group number, (b) bandedge measured by photocurrent in the WG versus emitter group number (courtesy of J. Tomm, Max-Born Institute).

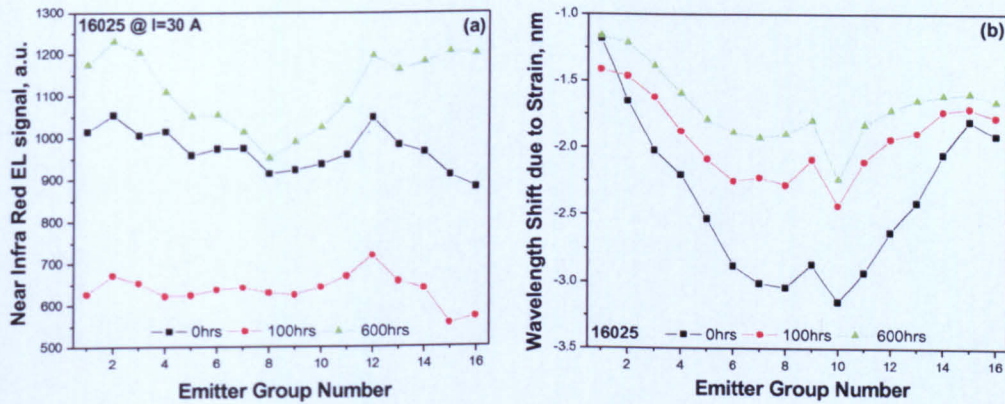


Fig. 4.28 Graphs of (a) near infrared EL signal versus emitter group number, (b) strain-induced shift of substrate PL versus emitter group number. (courtesy of J. Tomm, Max-Born Institute and J. Perraud and J. Nagle, Thales Research and Technology).

4.4.3 Global trends observed in the bars (975 nm bars)

Correlation between power and temperature distributions

A general correlation can be observed between the temperature and power distributions of undegraded bars. The power distributions of the bars typically have a frown-shaped profile (Figs. 4.13, 4.21, and 4.25), so that higher emission powers are observed for the emitters near the middle of the bar. At the same time, the typical temperature profile of the bars is also frown-shaped. (The temperature and power distributions of bar 16023, show a marked departure from this trend for reasons, which will be discussed shortly.)

Two things must be kept in mind when using the measured temperature profiles. Firstly, the measurement underestimates the actual temperature of the active region, since the spatial resolution of the thermal imaging camera ($\sim 30\text{ }\mu\text{m}$) is much larger than the thickness of the QW active region. Simulations suggest that the actual self-heating could be larger than indicated by the thermal camera. Secondly, the thermal camera measures the bulk temperature, so it may not accurately reflect the temperature near the facet – particularly if there is degradation in this region.

At first glance, this correlation between the temperature and power profiles seems surprising. For example, it is well established that the threshold current of a laser increases and its external quantum efficiency decreases as the temperature increases. Nevertheless, this correlation between the temperature and power profiles is correct and is reproduced in the bar degradation emulation work discussed in chapter 7 (section 7.3). It can be understood as follows: The emitters at the centre of the bar are hottest because they are being heated by neighbouring

emitters. (Alternatively, the emitters at the edges of the bar experience more effective heat dissipation.) The bandgap energy (E_g) decreases with temperature according to the relation: $E_g(T) = E_g(0) - \frac{\alpha T^2}{T + \beta}$, where α and β are fitting parameters [31]. For example, in GaAs the bandgap change with temperature is $dE_g / dT = -0.45 \text{ meV} / K$ at room temperature. This means that the turn-on voltage of the emitter drops as E_g decreases, so that hotter emitters turn on earlier (i.e. at a lower voltage)¹. There is an underestimation in the measurement of temperature in the experiment due to the low spatial resolution of the thermal imaging camera ($\sim 30 \text{ } \mu\text{m}$) by a factor of ~ 1.4 . This means that $(T_{real} - T_{ref}) = (1.4 T_{measured} - T_{ref})$, where T_{ref} is 15°C for the 650 nm and 25°C for the 975 nm bars, respectively, are the heatsink temperatures. T_{real} and $T_{measured}$ are the expected and measured temperatures respectively. Therefore, for a measured temperature variation of typically $\sim 2^\circ\text{C}$, the temperature induced variation in the bandgap energy is about $\sim 2\text{--}3 \text{ meV}$. Consequently, the emitters at the centre of the bar draw more current and hence emit more power (as long as they have not degraded). This is because all of the emitters share the same bias voltage. (One should note, however, that this trend does not continue unchecked, as the defect-related recombination rate also increases rapidly with temperature.)

Finally, the emitters at the centre of the bar, (which are hotter and are being driven harder), also tend to suffer faster degradation. This is completely expected. For

¹ Note that the simple long-base diode equation: $I = qn_i^2 A \left(\frac{D_p}{N_a L_p} + \left(\frac{D_n}{N_a L_n} \right) \right) \left[\exp\left(\frac{qV}{kT}\right) - 1 \right]$, can be expressed as $I = qAN_c N_v \left(\frac{D_p}{N_a L_p} + \left(\frac{D_n}{N_a L_n} \right) \right) \left[\exp\left(\frac{qV - E_g}{kT}\right) - 1 \right]$ using the relation $n_i^2 = N_c N_v \exp\left(\frac{-E_g}{kT}\right)$. This shows that the turn-on voltage is related to E_g .

example, higher currents or higher temperatures are often used to accelerate aging processes in laser diode degradation tests.

Correlation between power and packaging induced strain

The peak emission wavelength of the GaAs substrate, measured by micro-PL measurements, has a smile-shaped profile. The substrate emission wavelength is shorter near the centre of the bar than at the edges (Figs. 4.16b, 4.20b, 4.24b, and 4.28b). Thus, packaging induced strain increases the bandgap energy of the substrate near the middle of the bar. Furthermore, there is a correlation between the strain and the bandgap energy of the InGaAs QW active layer (Figs. 4.15a and 4.27a) and the bandgap energy of the InGaAsP confinement region (Figs. 4.15b and 4.27b). Although bars 16023 and 16024 exhibit an almost linear bandgap energy profiles from one end of the bar to the other, these also have a small downward curvature. (The linear component of the bandgap profile is believed to be due to compositional inhomogeneity and is discussed separately.)

The smile-shaped profile of the peak PL wavelength of the substrate is a consequence of packaging induced strain [1]. The peak emission wavelength of the GaAs substrate depends on strain. The soldering process introduces strain in the laser bar as the device cools, due to the thermal expansion mismatch of the semiconductor and heatsink. This typically results in a higher strain at the centre of the bar, which increases the bandgap energy.

A correlation between power and packaging induced strain is expected using the same arguments made for the correlation between the emitter temperature and power. However, the apparent correlation has the wrong dependence on bandgap energy – the power should decrease at the centre of the bar. This is because the

strain-induced changes in the bandgap energies of the QW and of the confinement layer are only $\sim 0.7\text{--}1$ meV. Thus, the strain-induced bandgap energy change is dominated by the larger temperature-induced changes – which have the same shape, but change in the opposite direction.

Impact of compositional inhomogeneity

Bar 16024 and especially bar 16023 deserve special attention. Both bars show a smile-shaped profile in the PL emission wavelength of the substrate. This indicates that the profile of the packaging induced strain is typical for the soldering process used. What makes these two bars different from the other bars in this study is that the profiles of the bandgap energies of the InGaAs QW and InGaAsP confinement region do not correlate with the substrate PL shift. Instead, there is a strong, nearly linear variation of $2\text{--}3$ meV in the bandgap energies from one end of the bar to the other – with the two bandgap energies moving in the opposite directions. At the same time, the power profile of the bars does not show the usual frown-shaped profile.

The only reasonable explanation for this behaviour is a compositional variation in the epitaxial material of these bars. (Unfortunately, attempts to check this were unsuccessful, since the original positions of the bars on the epitaxial wafer were not recorded.) A 3 meV increase in the bandgap energy would only require an increase of ~ 0.004 in the phosphorus mole fraction or a decrease of ~ 0.002 in the indium mole fraction across the 6.4 mm wide bar. Although it is clear that the change in bandgap energy has a significant impact on the power distribution across the bar, it is difficult to explain this impact in a simple manner. This is due

to the fact that the QW and confinement layer bandgap energies change in opposite directions and the fact that the strain also changes.

Finally, the point defect density also appears to change, as seen by the nearly linear change in the intensity of the near-infrared electroluminescence across the bar (Figs. 4.20a and 4.24a). Nevertheless, the dramatic decrease in the QW energy of emitters 14–16 of bar 16023 does appear to correlate with a noticeable increase in power (and temperature) in these emitters (Figs. 4.17a-b and 4.18a). These emitters are also the first to degrade, as seen from the drop in power and increase in temperature after 600 hours of aging (Figs. 4.17c and 4.18a).

Impact of solder voids

All of the bars considered (16022–16025) show a significant aging induced change in the profile of the peak PL emission wavelength from the substrate (Figs. 4.16b, 4.20b, 4.24b, and 4.28b). As discussed above, the profile of the substrate PL emission energy is caused by and directly related to the profile of the packaging induced strain. Acoustic microscopy and destructive measurements at TRT have revealed extensive solder voids in other bars (from a separate by-emitter degradation study using bars from Fraunhofer-Institut für Angewandte Festkörperphysik (IAF)) packaged with the same process at about the same time. Solder voids are observed both between the bar and the heatsink (Fig. 4.29a) and between the n-contact ribbon and the bar (Fig. 4.2b). Furthermore, as these strain profile changes are unusually large compared to other previously observed bars, it is believed that this might have been caused by numerous voids in the solder.

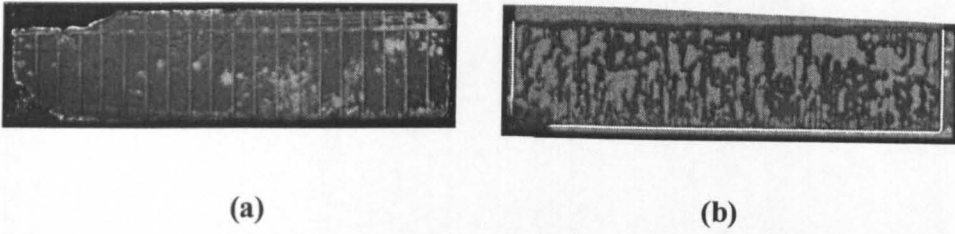


Fig. 4.29 Acoustic micrographs from bar IAF-16001: (a) In solder between bar and Cu microchannel heatsink (n-contact removed); (b) In solder between Au top ribbon and bar (courtesy of J. Perraud and J. Nagle, Thales Research and Technology).

Common signatures of emitter degradation

Emitters which degraded during aging (i.e. a noticeable drop in output power) often showed either a marked increase in the near-infrared electroluminescence from defects or a marked increase in temperature. Examples of this behaviour include: emitter 4 of bar 16022, emitters 13–16 of bar 16023; emitters 1–3 and 5 of bar 16024; emitters 1–3 of bar 16025. Although this correlation is not perfect, it does suggest that there may be two different manifestations (or even causes) of defect degradation – one due to radiative deep level defects and one due to nonradiative recombination.

4.5 Analysis of Experimental Results

4.5.1 Bar 16022

By-emitter analysis was performed on each of the four batch #6 devices (bars 16022, 16023, 16024 and 16025). The relative powers of each emitter group were extracted by integrating their NF image intensities and correcting for the ND filters used.

At high currents, there was a distinct emission intensity distribution of the emitter groups in bar 16022. There was poor performance at the ends of the bar (emitter groups 1 and 16) and also for emitter group number 4 (see Fig. 4.30) as expected due to high temperature and high NIR EL defect density. The emitter groups in the centre began lasing at lower total bar currents (Fig. 4.31); i.e. lasing occurred even before the threshold current was reached. Fig. 4.32 shows some graphs of the intensity of the 16 emitter groups for various I_{BAR} currents.

Results from the by-emitter analysis show that the poor emitter performances correlate well with the NIR EL (defects) from emitter group number 4 (Fig. 4.34c). The results from MBI show elevated temperatures at the edge emitter groups (Fig. 4.34b). In general, there was very good correspondence between the lasing intensity (Fig. 4.34a) and the NIR defect EL intensity of the emitter groups.

An examination of the performance of the poorly performing emitter groups reveals a correlation with features observed by optical microscopy. The observance of weaker emitters within an emitter group (mini arrays of emitters) was seen by NF imaging (Fig. 4.30). This can also be clearly seen in the emission intensity versus emitter number (Fig. 4.33) for emitter group number 4 A and B especially at $I_{BAR} = 5$ A and 25 A.

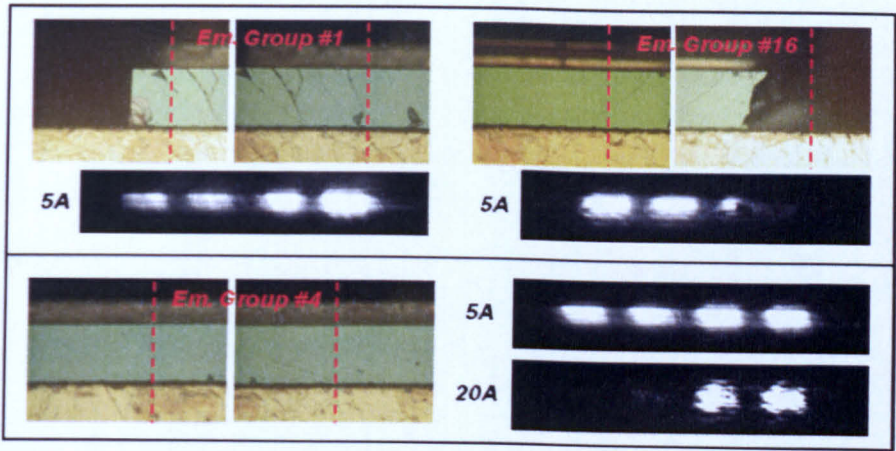


Fig. 4.30 Images of weaker emitters within an emitter group observed by NF imaging.

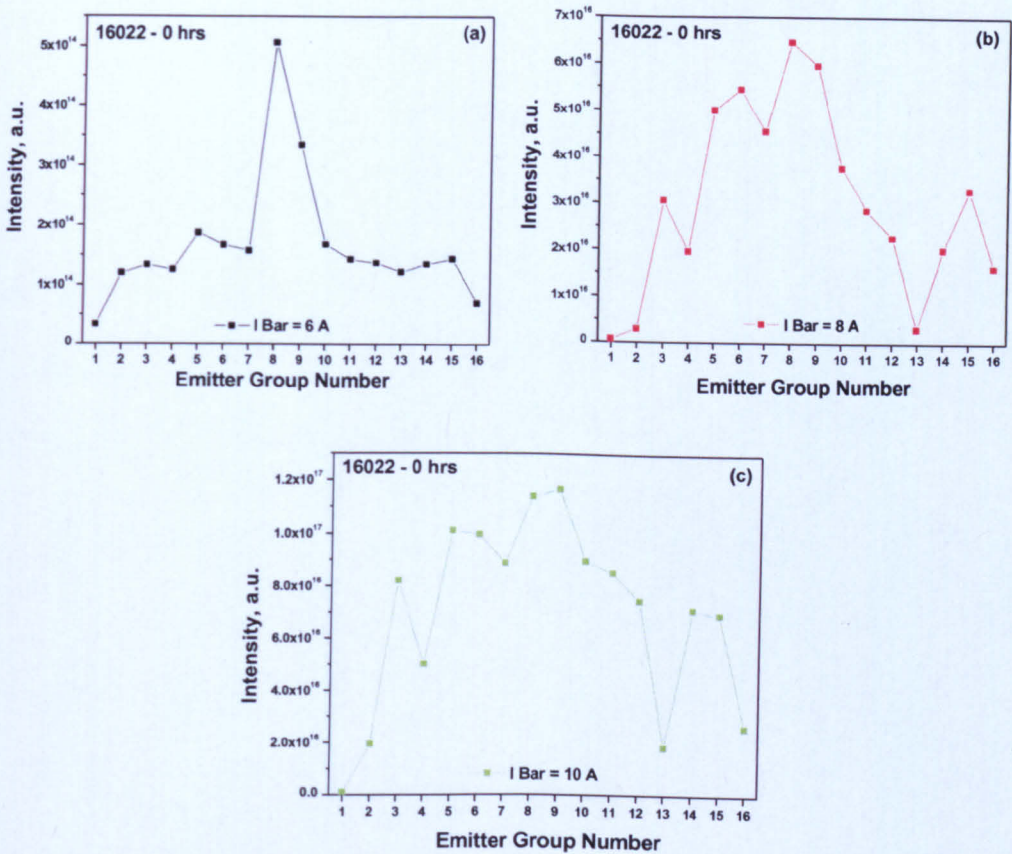


Fig. 4.31 Emitter group emission intensity versus emitter number for various I_{BAR} currents (a) bar current of 6 A, (b) bar current of 8 A, and (c) bar current of 10 A.

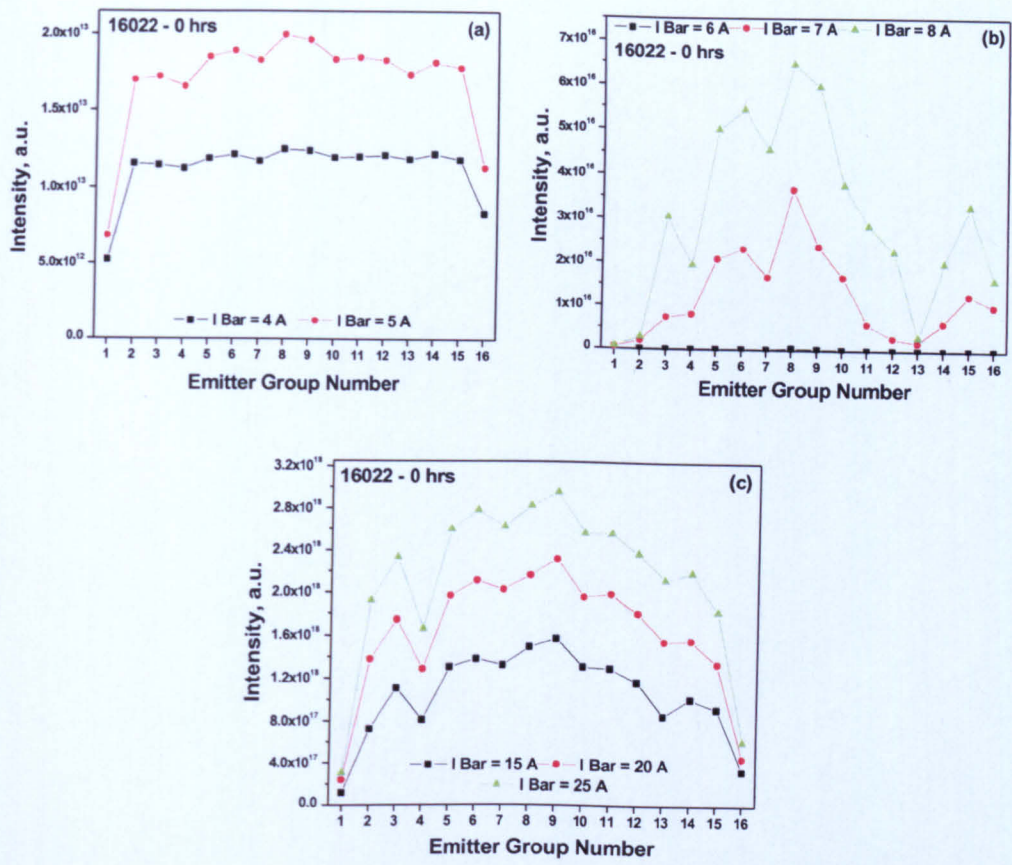


Fig. 4.32 (a) Emission group emission intensity versus emitter number at various I_{BAR} currents (a) bar current of 4 and 5 A, (b) bar current of 6 A, 7 A and 8 A, and (c) bar current of 15 A, 20 A and 25 A.

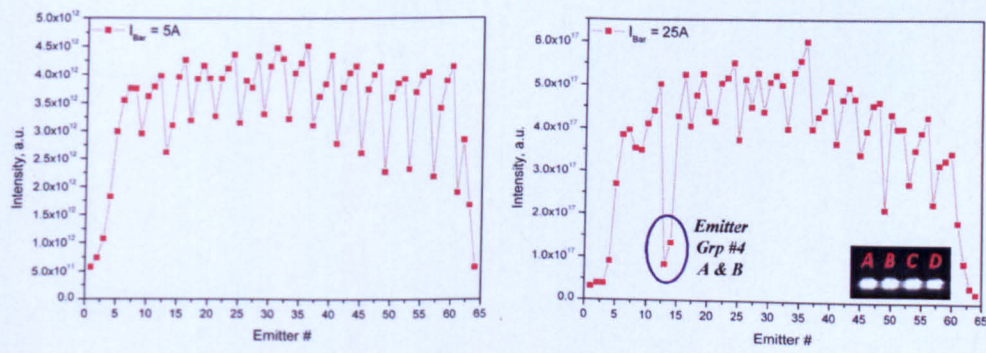


Fig. 4.33 Emission intensity versus emitter number at $I_{BAR} = 5 A$ and 25 A, respectively.

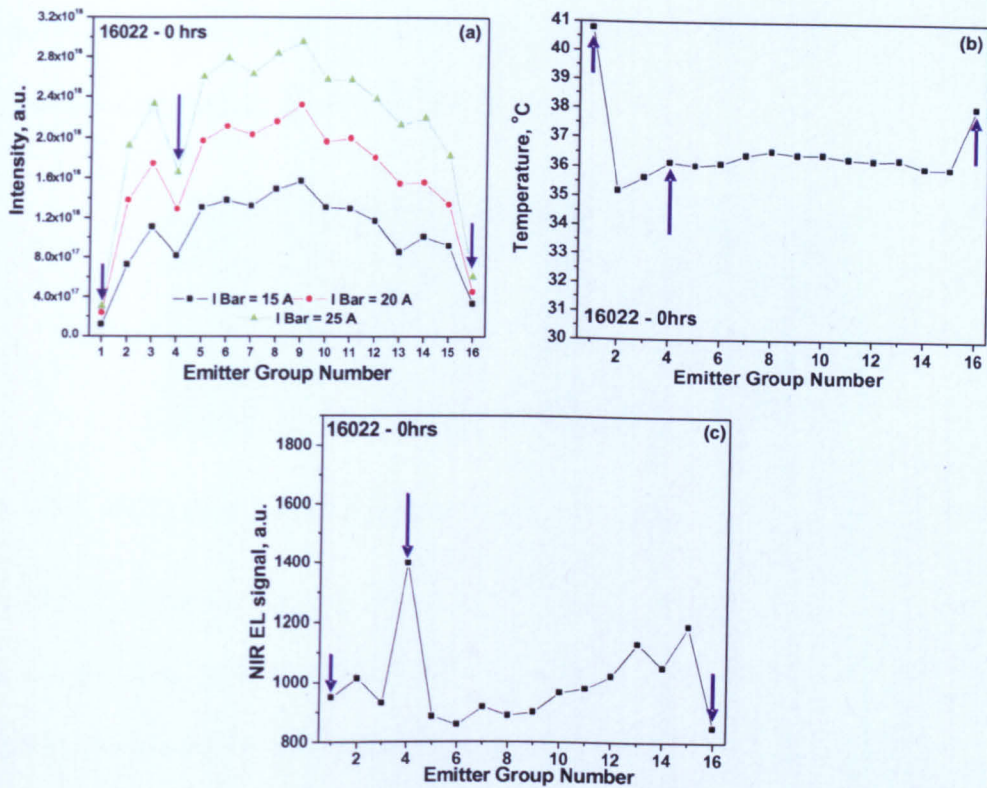


Fig. 4.34 Graphs of (a) lasing intensity, (b) temperature profile and (c) NIR defect EL intensity of the emitter groups (temperature and NIR EL data courtesy of J. Tomm, Max-Born Institute).

The images in Fig. 4.30 show a drop in intensity of the poorly performing emitter groups. Further analysis of the individual emitters within a group gave greater insight into the power distribution in the mini arrays. Emitters with the poorest performance are visible within the emitter group (e.g. at a bar current of 25 A of Fig. 4.30).

4.5.2 Bar 16023

A large number of features were observed on the facet of bar 16023 by optical microscopy (Fig. 4.12). This correlates with the many bright regions observed by PLM in regions, where the facet is damaged and/or contaminated. These features are not observed on the clean facets of other bars (Fig. 4.35b). In spite of the

numerous features seen on the facet, there was a relatively uniform performance across all of the emitter groups within this bar.

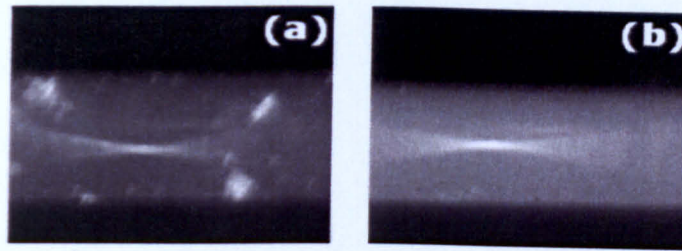


Fig. 4.35 (a) Typical image from bar 16023, (b) typical image from bar 16022.

The emitter groups at the right hand end of the bar began to lase at a bar current which was lower than the bar threshold current of 8 A. These emitters were also hotter in thermocamera measurements made at MBI. Fig. 4.36 shows the intensity of the 16 emitter groups versus emitter number for various I_{BAR} currents.

A prominent damage feature is observed in emitter group number 13 by optical microscopy (Fig. 4.37a) and is also seen in the NF images. There is a correlation between the damaged emitter within emitter group number 13 and the increased NIR defect luminescence (measured at MBI), Fig. 4.37c.

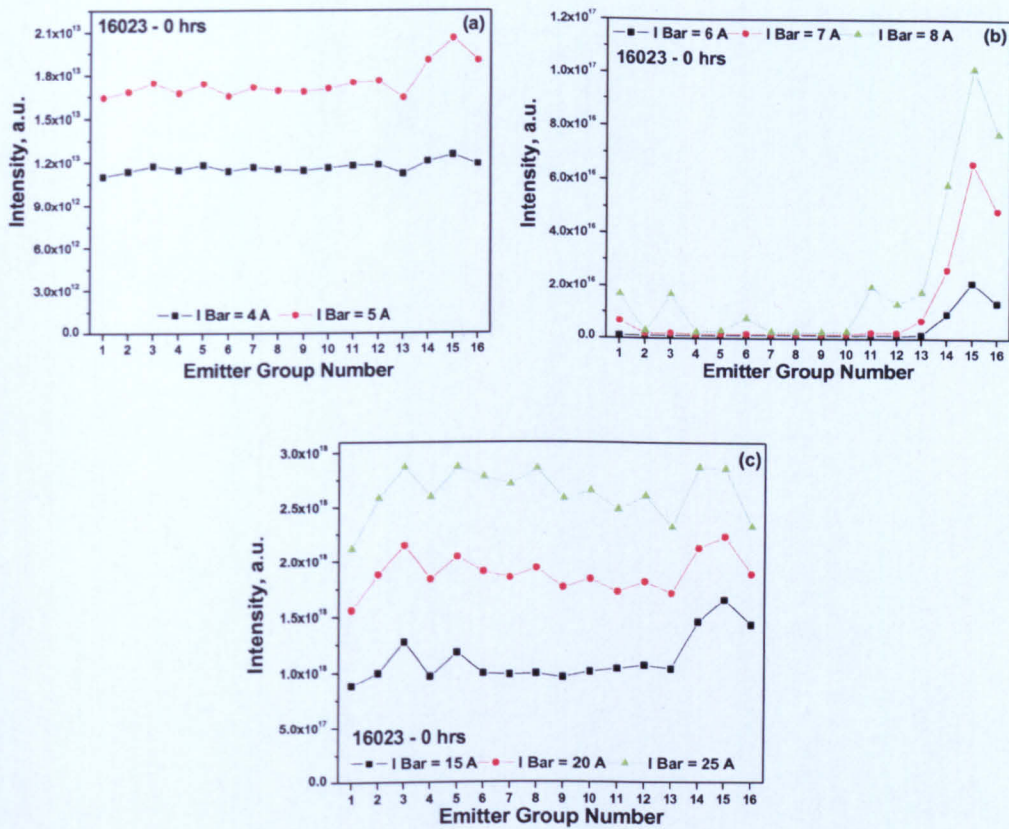


Fig. 4.36 (a) Emitter group emission intensity versus emitter number for various I_{BAR} currents (a) bar current of 4 and 5 A, (b) bar current of 6 A, 7 A and 8 A, and (c) bar current of 15 A, 20 A and 25 A.

Fig. 4.37a looks at the weakest emitter in emitter group number 13, where there is a virtual absence of mini emitter number B at a bar current of 25 A. This can also be seen at the facet of the bar, as indicated by the arrow in the ELM image of Fig. 4.5.2.3a. There is a good correspondence between the NF pattern, the microscope image of the facet of emitter group number 13, the NIR defect luminescence profile and the temperature profile.

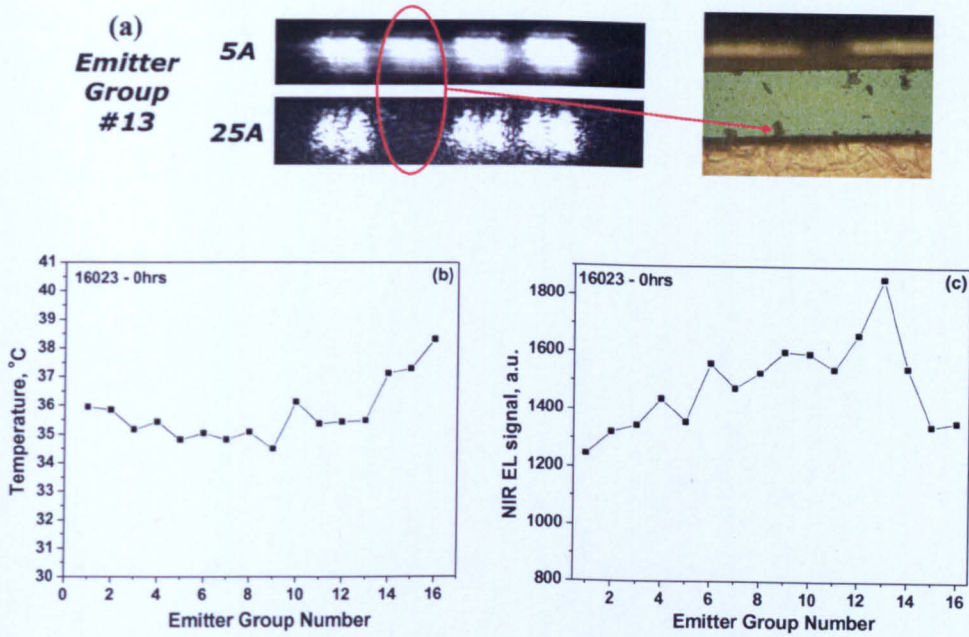


Fig. 4.37 (a) NF pattern and microscope image of emitter group number 13; (b) temperature and (c) NIR defect luminescence profiles (temperature and NIR EL data courtesy of J. Tomm, Max-Born Institute).

4.5.3 Bar 16024

This bar had a relatively uniform performance across all emitter groups within it. The emitter groups at the right hand end of the bar began to lase below the bar threshold current of 7.2 A. This phenomenon can be verified in the graphs of the intensity versus emitter number for various I_{BAR} currents of the 16 emitter groups (Fig. 4.38).

There was also a correlation between the NF images, visual inspections and temperature data of the emitters in this bar (Fig. 4.39). However, although there was a low optical efficiency in some emitters, there was no increase in the level of NIR defect EL. This was also correlated with a hot emitter (emitter group number 5), which could be due to a solder void under this emitter.

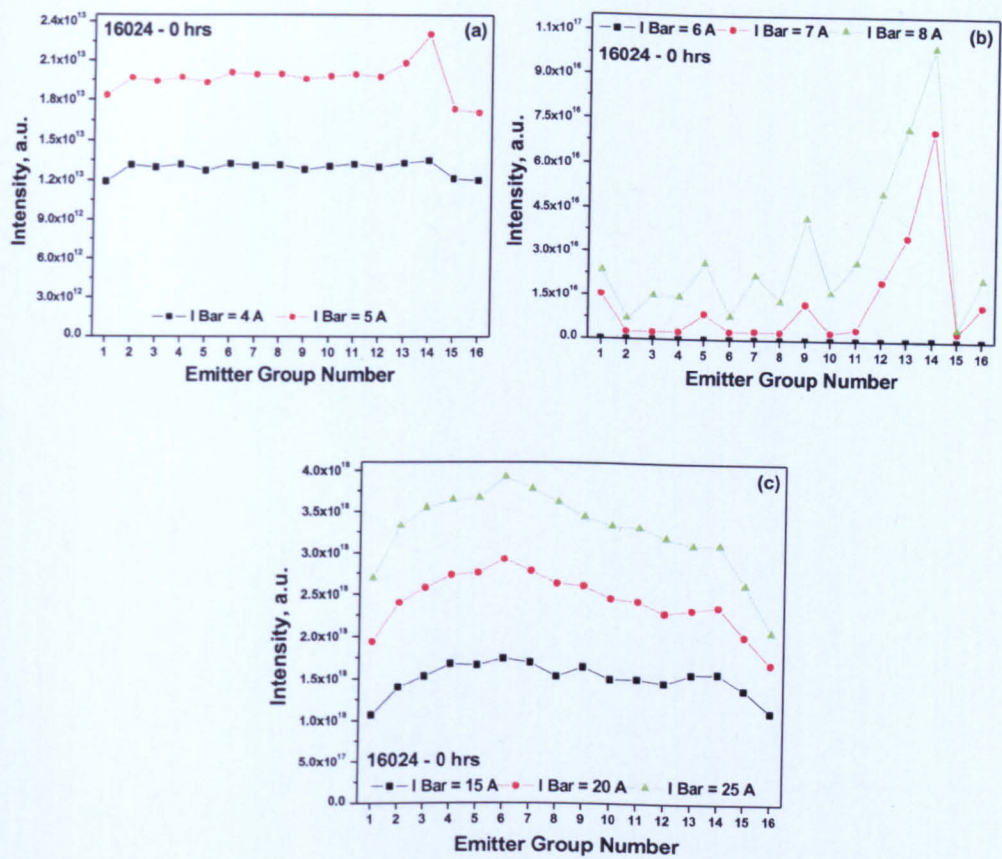


Fig. 4.38 (a) Emitter group emission intensity versus emitter number for various I_{BAR} currents (a) bar current of 4 and 5 A, (b) bar current of 6 A, 7 A and 8 A, and (c) bar current of 15 A, 20 A and 25 A.

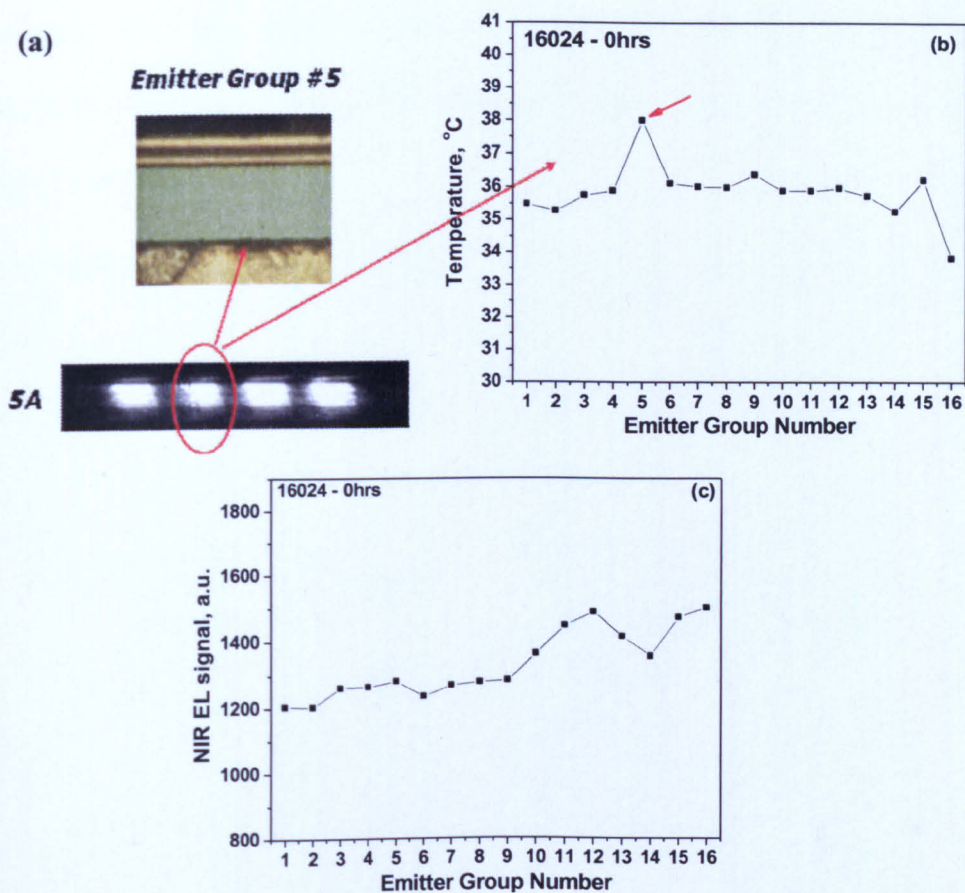


Fig. 4.39 (a) NF pattern and microscopic image of emitter group number 5; (b) temperature and (c) NIR defect luminescence profiles. (Temperature and NIR EL data courtesy of J. Tomm, Max-Born Institute).

4.5.4 Bar 16025

Bar 16025 has a relatively uniform performance across all emitter groups above threshold (Fig. 4.40c). The optical microscopy images show that the facet was very clean. The emitter groups near the centre of the bar begin to lase first, with a bar threshold current of 6.2 A. Fig. 4.40 shows graphs of the emission intensity of the 16 emitter groups versus emitter number for various I_{BAR} currents.

There was a uniform NIR defect EL across the bar. The temperature distribution was hottest near the centre of the bar, which is consistent with the higher power

emanating from the central emitters. Emitter group number 4 has a higher temperature and has a reduced intensity/power (Fig. 4.41a), which could indicate a high defect density.

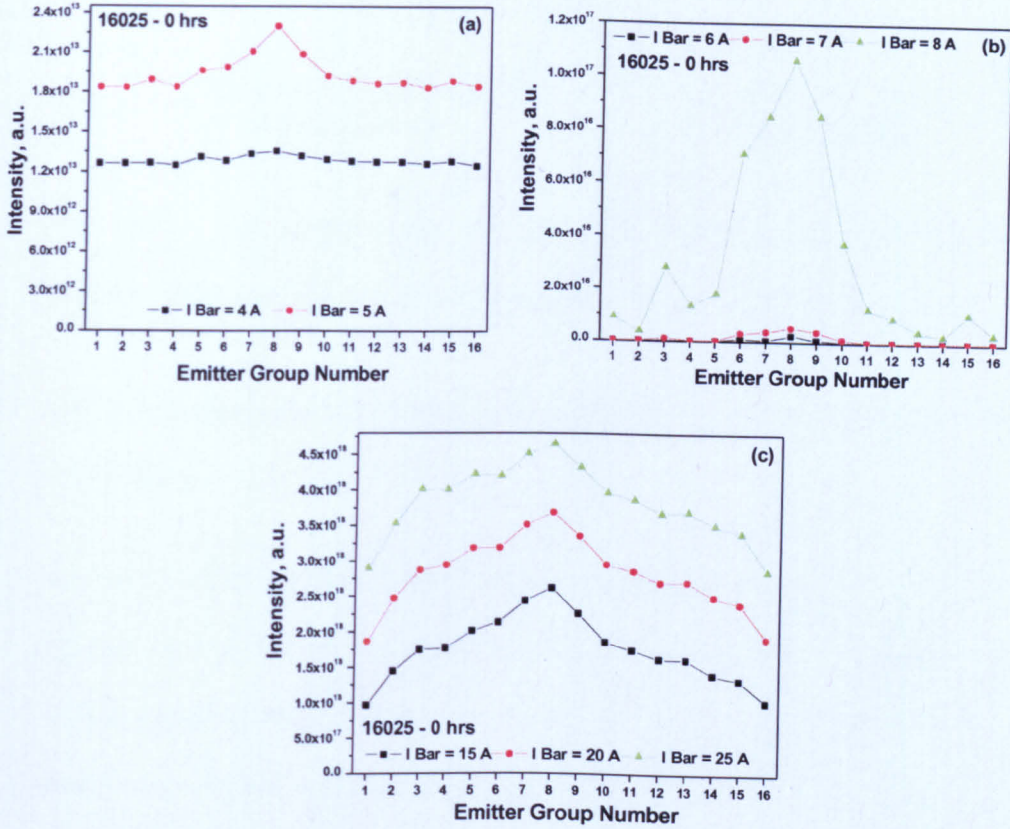


Fig. 4.40 Emitter group intensity versus emitter number for various I_{BAR} currents (a) bar current of 4 and 5 A, (b) bar current of 6 A, 7 A and 8 A, and (c) bar current of 15 A, 20 A and 25 A.

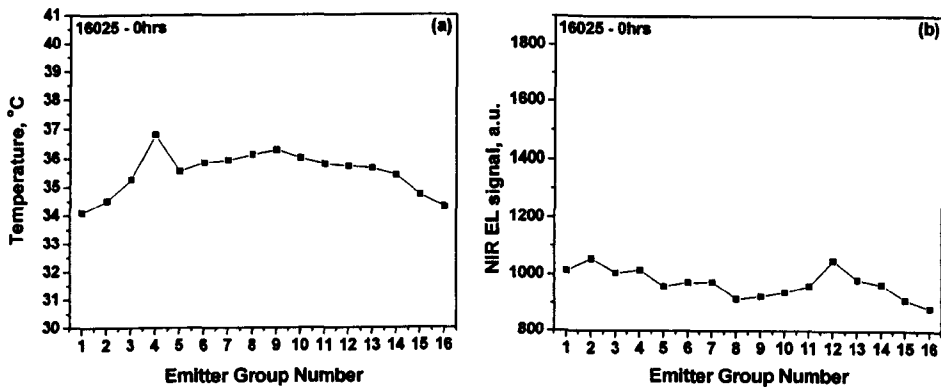


Fig. 4.41 (a) Temperature and (b) NIR defect luminescence profiles. (Temperature and NIR EL data courtesy of J. Tamm, Max-Born Institute).

4.6 Conclusion of Experimental By-emitter Degradation Studies of these Bars

We have studied extensively the behaviour of these two types of bars. All three 650 nm bars exhibited reasonably uniform power emission, with variations of ~6% between emitters – even after 700 hours of aging. A slight frown-shaped profile was evident in the profile of the emitter powers across the unaged bars. This profile turned into a smile-shaped profile after aging, with the centre emitters providing less power. The strain induced shift in the substrate PL was very homogenous across the bars and did not change appreciably during aging.

In the 975 nm bars, a general correlation was observed between the temperature and power distributions of the unaged bars. The power distributions of the bars typically have frown-shaped profiles, so that higher emission powers are observed for the emitters near the middle of the bar. At the same time, the typical temperature profile of the bars was also frown-shaped. This surprising occurrence is explained by the relationship between the bandgap energy and temperature, so

that the hotter central emitters have low turn-on voltages. The strain-induced bandgap energy change was dominated by the larger temperature-induced changes. These results suggest that the inhomogeneous temperature distribution played a larger role in the bar degradation. Poorly performing emitters in the unaged bars were often found to correlate with damage at the facet observed by optical microscopy and PLM/ELM. Emitters which degraded during aging (noticeable drop in output power) often showed either a marked increase in the near-infrared electroluminescence from defects or a marked increase in temperature.

Finally bar 16024 and especially bar 16023 deserve special attention. They show a smile-shaped profile in the PL emission wavelength of the substrate, which indicates that the profile of the packaging induced strain, is typical for the soldering process used. However, the lack of the correlation between the substrate PL shift, the QW and the corresponding bandgap energy shifts is believed to be due to a compositional variation of the epitaxial material across the bar, which affects the operation (and hence degradation) of the bar.

References

- [1] E. Martin, J. P. Landesman, J. P. Hirtz, and A. Fily, "Microphotoluminescence mapping of packaging-induced stress distribution in high-power AlGaAs laser diodes," *Applied Physics Letters*, vol. 75, pp. 2521-2523, Oct 1999.
- [2] J. W. Tomm, A. Gerhardt, T. Elsaesser, D. Lorenzen, and P. Hennig, "Simultaneous quantification of strain and defects in high-power diode laser devices," *Applied Physics Letters*, vol. 81, pp. 3269-3271, Oct 2002.
- [3] R. Xia, E. C. Larkins, I. Harrison, S. R. A. Dods, A. Andrianov, J. Morgan, and J. P. Landesman, "Mounting-induced strain threshold for the degradation of high-power AlGaAs laser bars," *IEEE Photonics Technology Letters*, vol. 14, pp. 893-895, Jul 2002.
- [4] J. W. Tomm, A. Gerhardt, R. Muller, V. Malyarchuk, Y. Sainte-Marie, P. Galtier, J. Nagle, and J. P. Landesman, "Spatially resolved spectroscopic strain measurements on high-power, laser diode bars," *Journal of Applied Physics*, vol. 93, pp. 1354-1362, Feb 2003.
- [5] J. W. Tomm, A. Gerhardt, R. Muller, M. L. Biermann, J. P. Holland, D. Lorenzen, and E. Kaulfersch, "Quantitative strain analysis in AlGaAs-based devices," *Applied Physics Letters*, vol. 82, pp. 4193-4195, 2003.
- [6] A. V. Andrianov, S. R. A. Dods, J. Morgan, J. W. Orton, T. M. Benson, I. Harrison, E. C. Larkins, F. X. Daiminger, E. Vassilakis, and J. P. Hirtz, "Optical and photoelectric study of mirror facets in degraded high power AlGaAs 808 nm laser diodes," *Journal of Applied Physics*, vol. 87, pp. 3227-3233, Apr 2000.
- [7] S. Bull, A. V. Andrianov, I. Harrison, M. Dorin, R. B. Kerr, J. Noto, and E. C. Larkins, "A spectroscopically resolved photo- and electroluminescence microscopy technique for the study of high-power and high-brightness laser diodes," *IEEE Transactions on Instrumentation and Measurement*, vol. 54, pp. 1079-1088, Jun 2005.
- [8] R. Xia, A. V. Andrianov, S. Bull, I. Harrison, J. P. Landesman, and E. C. Larkins, "Micro-electroluminescence spectroscopy investigation of mounting-induced strain and defects on high power GaAs/AlGaAs laser diodes," *Optical and Quantum Electronics*, vol. 35, pp. 1099-1106, Sep 2003.
- [9] "WWW.BRIGHTER.EU [Project]," <http://www.ist-brighter.eu/index.htm>.
- [10] S. Bull, J. W. Tomm, M. Oudart, J. Nagle, C. Scholz, K. Boucke, I. Harrison, and E. C. Larkins, "By-emitter degradation analysis of high-power laser bars," *Journal of Applied Physics*, vol. 98, p. 063101, 2005.
- [11] M. Baeumler and W. Jantz, "Photoluminescence Imaging": Microprobe characterization of optoelectronic materials. London: Taylor and Francis. (Optoelectronic properties of semiconductors and superlattices 17), pp. 1-88 (Chapter I), 2003.

- [12] E. W. Williams and H. B. Bebb, "Photoluminescence in lightly doped epitaxial GaAs-Cd and GaAs-Si," *Journal of Physics and Chemistry of Solids*, vol. 30, pp. 1289-92, 1969.
- [13] J. Noto, Y. Betremieux, R. B. Kerr, H. Zhang, M. Taylor, S. Watchorn, and M. Dorin, "Tandem-Etalon tunable filter for NIR spectral imaging," in *Optical Spectroscopic Techniques and Instrumentation for Atmospheric and Space Research V*. vol. 5157, A. M. Larar, J. A. Shaw, and Z. Sun, Eds. Bellingham: Spie-Int Soc Optical Engineering, 2003, pp. 178-189.
- [14] W. J. Schneller, J. Noto, R. B. Kerr, and R. A. Doe, "Liquid crystal Fabry-Perot etalons," in *Optical Spectroscopic Techniques and Instrumentation for Atmospheric and Space Research V*. vol. 3355 Bellingham: Spie-Int Soc Optical Engineering, 1998, pp. 877-883.
- [15] S. Bull, A. V. Andrianov, I. Harrison, and E. C. Larkins, "The study of strain and defects in high power laser diodes by spectroscopically resolved photoluminescence microscopy," *European Physical Journal-Applied Physics*, vol. 27, pp. 469-473, Jul-Sep 2004.
- [16] J. Tømm and J. Jiménez, *Quantum-Well Laser Array Packaging*: McGraw-Hill Professional; 1 edition, 2006.
- [17] A. Klehr, G. Beister, G. Erbert, A. Klein, J. Maege, I. Rechenberg, J. Sebastian, H. Wenzel, and G. Trankle, "Defect recognition via longitudinal mode analysis of high power fundamental mode and broad area edge emitting laser diodes," *Journal of Applied Physics*, vol. 90, pp. 43-47, 2001.
- [18] P. Lambkin, C. Percival, and B. Corbett, "Reflectivity measurements of intracavity defects in laser diodes," *IEEE Journal of Quantum Electronics*, vol. 40, pp. 10-17, Jan 2004.
- [19] R. Xia, E. C. Larkins, I. Harrison, S. R. A. Dods, A. V. Andrianov, J. Morgan, and J. P. Landesman, "The effect of mounting-induced strain and defect on the properties of AlGaAs 808 nm LDs," *Synthetic Metals*, vol. 127, pp. 255-259, Mar 2002.
- [20] "WWW.BRIGHTER.EU [Project]," <http://www.ist-brighter.eu/tuto7/LARKINS/Larkins.pdf>.
- [21] P. Adamiec, B. Sumpf, I. Rudiger, J. Fricke, K. H. Hasler, P. Ressel, H. Wenzel, M. Zorn, G. Erbert, and G. Trankle, "Tapered lasers emitting at 650 nm with 1 W output power with nearly diffraction-limited beam quality," *Optics Letters*, vol. 34, pp. 2456-2458, Aug 2009.
- [22] B. Sumpf, M. Zorn, R. Staske, J. Fricke, P. Ressel, A. Ginolas, K. Paschke, G. Erbert, M. Weyers, and G. Trankle, "3-W broad area lasers and 12-w bars with conversion efficiencies up to 40% at 650 nm," *IEEE Journal of Selected Topics in Quantum Electronics*, vol. 13, pp. 1188-1193, Sep-Oct 2007.
- [23] M. Zorn, H. Wenzel, U. Zeimer, B. Sumpf, G. Erbert, and M. Weyers, "High-power red laser diodes grown by MOVPE," *Journal of Crystal Growth*, vol. 298, pp. 667-671, Jan 2007.

- [24] M. Leers, K. Boucke, and IEEE, "Cooling approaches for high power diode laser bars," in *58th Electronic Components & Technology Conference, Proceedings* New York: IEEE, 2008, pp. 1011-1016.
- [25] S. C. Auzanneau, M. Calligaro, M. Krakowski, F. Klopff, S. Deubert, J. P. Reithmaier, and A. Forchel, "High brightness GaInAs/(Al)GaAs quantum-dot tapered lasers at 980 nm with high wavelength stability," *Applied Physics Letters*, vol. 84, pp. 2238-2240, Mar 2004.
- [26] A. Gerhardt, J. W. Tomm, R. Müller, A. Bärwolff, D. Lorenzen, and J. Donecker, "Measurement of mounting-induced strain and defects in high-power laser diodes using Fourier-transform photo-current spectroscopy," *Materials Science and Engineering B*, vol. 91-92, pp. 476-480, 2002.
- [27] J. W. Tomm, R. Muller, A. Barwolff, T. Elsaesser, D. Lorenzen, F. X. Daiminger, A. Gerhardt, and J. Donecker, "Direct spectroscopic measurement of mounting-induced strain in high-power optoelectronic devices," *Applied Physics Letters*, vol. 73, pp. 3908-3910, Dec 1998.
- [28] M. Ziegler, F. Weik, J. W. Tomm, T. Elsaesser, W. Nakwaski, R. P. Sarzala, D. Lorenzen, J. Meusel, and A. Kozłowska, "Transient thermal properties of high-power diode laser bars," *Applied Physics Letters*, vol. 89, pp. 263506-3, 2006.
- [29] C. K. Amuzuvi, S. Bull, J. W. Tomm, J. Nagle, E. C. Larkins, B. Sumpf, G. Erbert, N. Michel, and M. Krakowski, "The impact of temperature and packaging-induced strain on current competition and emitter power in laser bars," *Applied Physics Letter*, in preparation to be submitted, 2010.
- [30] C. K. Amuzuvi, S. Bull, J. J. Lim, S. Sujecki, and E. C. Larkins, "Numerical emulation of the degradation of 975nm high power tapered laser bars," in *High Power Diode Lasers and Systems Conference, Coventry (UK) 2009. HPD 2009*, 2009, pp. 1-2.
- [31] J. W. Tomm, R. Muller, A. Barwolff, T. Elsaesser, A. Gerhardt, J. Donecker, D. Lorenzen, F. X. Daiminger, S. Weiss, M. Hutter, E. Kaulfersch, and H. Reichl, "Spectroscopic measurement of packaging-induced strains in quantum-well laser diodes," *Journal of Applied Physics*, vol. 86, pp. 1196-1201, 1999.
- [32] Y. P. Varshni, "Temperature dependence of energy gap in semiconductors," *Physica*, vol. 34, pp. 149-154, 1967.

Chapter 5

By-Emitter Degradation Analysis of High Power Laser Diodes Using the Emulation Tool

This chapter explores the use of laser diode simulation tools to acquire more insight into the degradation of high power laser diodes (HPLD). More specifically, the simulation tool *Speclase*, which was described in chapter 3, will be used to emulate the performance and degradation of laser bars [1]. These emulations will be used in conjunction with the by-emitter degradation analysis.

As the market and applications for high power lasers continue to surge forward, the need to improve the power and reliability of laser bars cannot be overemphasised. This goal can be achieved by the understanding of the physical characteristics and degradation behaviour of bars.

This chapter will demonstrate how our *Speclase* tool [2, 3] is extended to model the behaviour of a laser bar using *Barlase* [4]. We will then better understand how current competition, thermal crosstalk and the level of defects affect the output

power and the degradation of the bar. Since bars are known to degrade faster than single emitters due to thermal crosstalk, current competition and packaging induced strain, *Barlase* can help test postulated degradation processes.

5.1 LabVIEW Control Interface

5.1.1 The *Barlase* control interface

As *Speclase* was designed to simulate single emitters, a control interface (*Barlase*) was developed in LabVIEW to control multiple instances of *Speclase* (one for each emitter) and run these instances simultaneously using a common bias voltage. *Barlase* controls the simulation execution and allows the simulation of multiple emitters under the conditions of either constant bar current or constant bar output power - the two conditions commonly used for aging tests. Parameters such as the defect density, strain and heatsink temperature can be specified for each emitter. The effects of each of these on the operation of individual emitters and full laser bars (L-I characteristics, threshold, efficiency, etc.) can then be investigated.

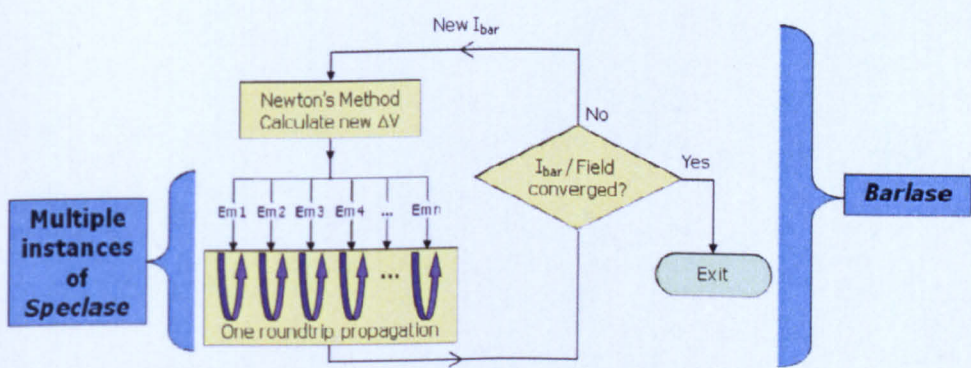


Fig. 5.1 Flow chart showing the communication between *Speclase* and *Barlase*.

Fig. 5.1 depicts the sequence of operation of *Barlase* as a flow chart showing the communication between *Speclase* and *Barlase*. *Barlase* allows a better

understanding how current competition, temperature and the level of defects affect the output power and the degradation rate of the bar. It is known that bars degrade faster than single emitters due to thermal crosstalk, current competition and packaging induced strain. However, these effects and their impact on the interaction of the emitters within the bar is complex [5]. Therefore, *Barlase* can help test postulated degradation processes. *Barlase* has been demonstrated for a hypothetical bar through the emulation of the impact of inhomogeneous defect, temperature and strain distributions.

5.1.2 The laser bar model

In addition to controlling the emitter simulations with *Speclase*, *Barlase* performs the degradation emulation. A simple example of a degradation model is the thermally activated generation of deep level defects or “traps”. The model used to describe this is based on the Arrhenius equation, where the QW trap generation rate is activated by the local QW temperature. The trap generation rate is multiplied by the aging time and the trap density is updated at each aging step. The model is described by the equation [6]:

$$\Delta N_t(x, z) = A \exp\left(\frac{-E_a}{kT_{QW}(x, z)}\right) \Delta t_{aging} \quad , \quad (5.1)$$

where A is the pre-Arrhenius constant, E_a is the activation energy, Δt_{aging} is the aging time, and T_{QW} is the quantum well temperature.

5.2 Overview of the Operation of the LabVIEW Control Interface

Overview of operation

As described previously, *Speclase* is modified to pause at the end of each round trip of the laser cavity and wait for an updated bias voltage to be calculated by *Barlase*'s LabVIEW control interface. An additional input file (*ipcontrol.inp*) is introduced to allow the individual instances of *Speclase* to receive this updated voltage and to allow *Barlase*'s LabVIEW control program to interrogate the current state of the simulation. This file acts as a conduit between *Speclase* and the LabVIEW control interface and both the simulation and control interface regularly monitors this file for each emitter.

The user interface of *Barlase* has the following input parameters:

- File location (i.e. the disk space where the simulation files are located)
- Number of emitters to simulate
- Initial bias voltage guess
- Mode of operation – constant current mode or constant power mode
- Target current/target power
- Number of aging steps
- List of aging times
- Number of simulation currents
- List of simulation currents
- Clamp number – user defined and used to ensure numerical stability in voltage/current
- Pre-Arrhenius factor/activation energy, which are constants.

Given the above information, the program performs the following sequence of operations:

1. Copy the *Speclase* files from the original directory into new directories, 1 per emitter to be simulated
2. Create an *ipcontrol.inp* file for each emitter containing the initial simulation voltage
3. Modify the *Speclase* input files for each emitter (i.e. set different conditions for each emitter)
4. Execute *Speclase* for each emitter
5. Routinely check the *ipcontrol.inp* file for each emitter to see if the current round trip is completed
6. Once the current round trip is completed for all emitters, the values of bias current, output power and optical field convergence (at the back facet) are read from the *ipcontrol.inp* file for each emitter
7. Calculate the total current and power of the bar by summing the values from all emitters
8. Use Newton's method to compare the total current with the target value and calculate an updated voltage if the convergence criteria have not been met.
9. Update the *ipcontrol.inp* file for each emitter with the new voltage
10. Update the *ipcontrol.inp* file for each emitter with a new flag value, so that *Speclase* knows whether to begin another round trip or to stop (if converged) – return to point number 5.

Fig. 5.2 depicts this sequence of operation as a flow diagram.

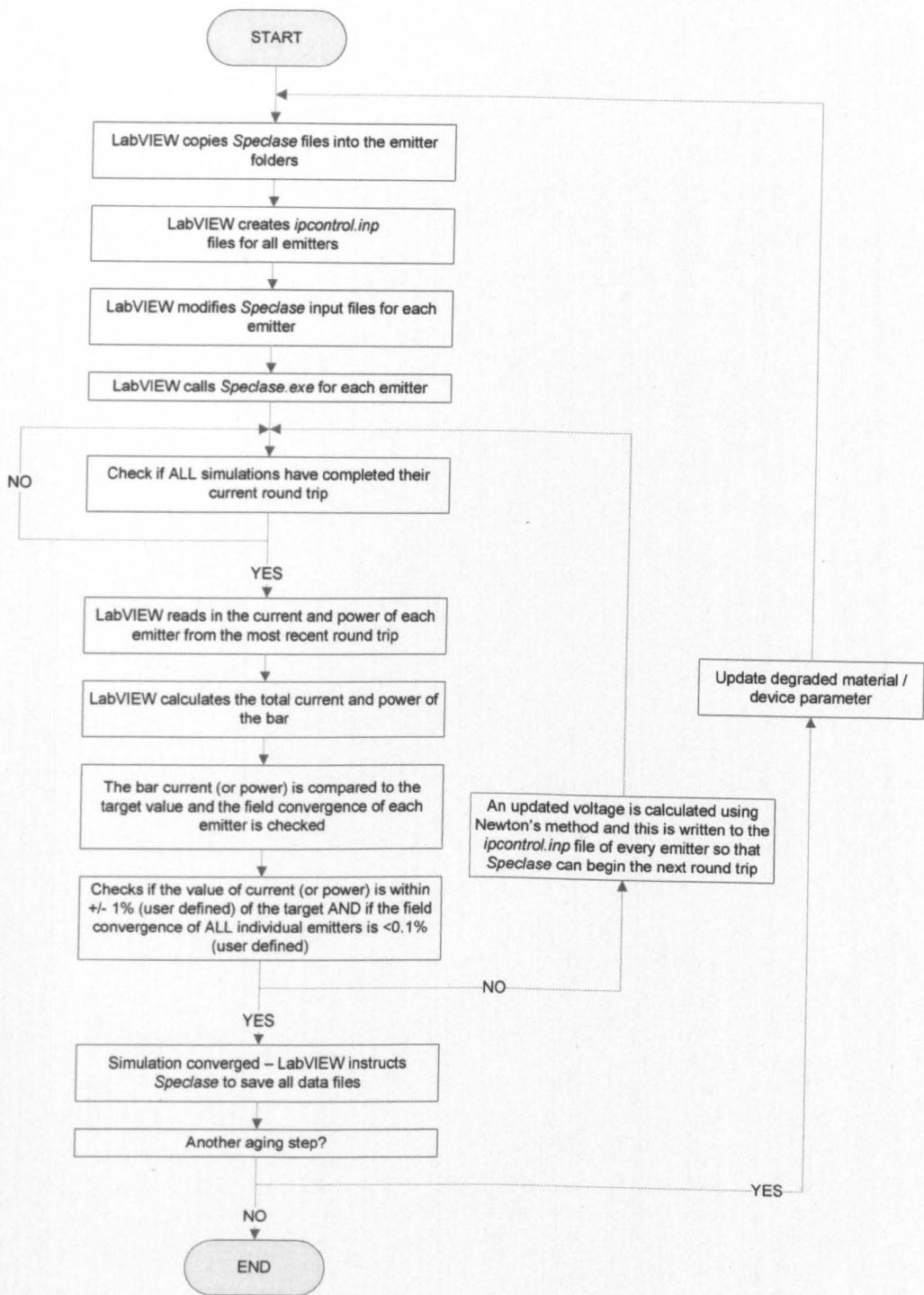


Fig. 5.2 Flow chart of the LabVIEW control program.

Fig. 5.3 shows the front panel of *Barlase*'s user interface showing all the inputs and outputs expected from the program.

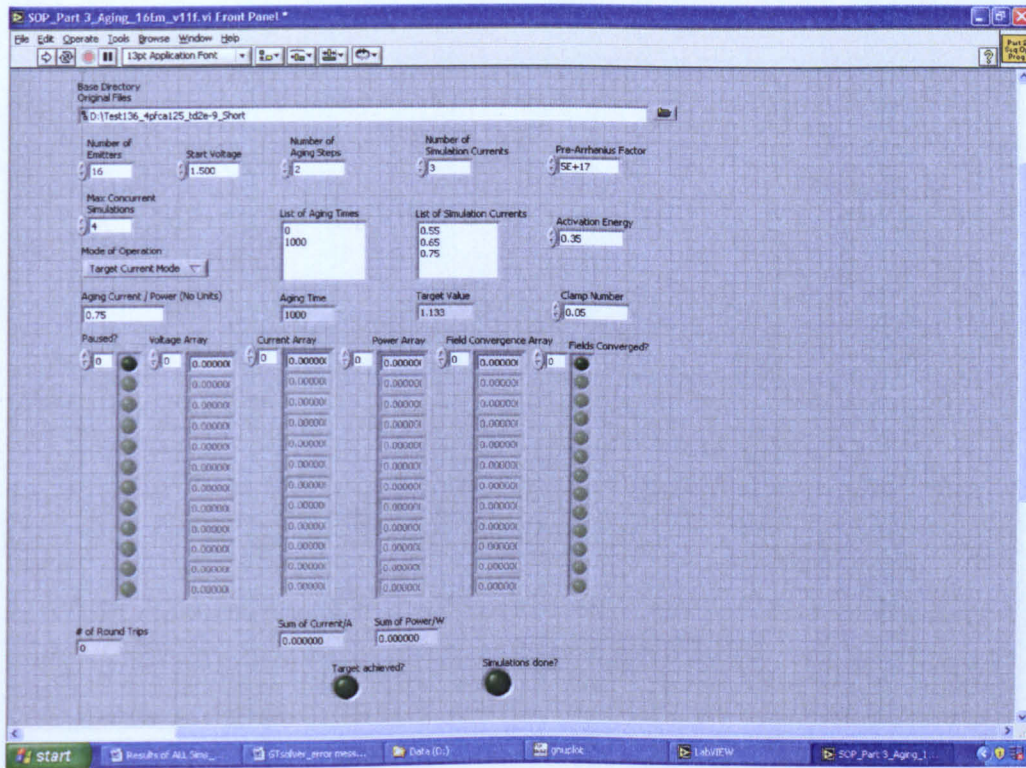


Fig. 5.3 Front panel of the LabVIEW interface control program.

5.3 Testing of the *Barlase* Control Interface

To confirm the correct operation of the *Barlase* control interface, a number of tests were carried out using a hypothetical laser test structure. For all simulations in this report, this standard test structure was selected from those employed in the experimental work in this task. This structure was also selected bearing in mind that an attempt will be made to further emulate the degradation of bars made from “the same epitaxial” structure with similar dimensions. The structure used was the 975 nm narrow-angle ($<1^\circ$) tapered laser from Alcatel Thales III-V Lab. The total length was 2.4 mm, consisting of a 200 μm ridge waveguide and a 2200 μm

tapered amplifier. The front and rear facet reflectivities were 3% and 90%, respectively. The ‘standard’ simulation of this structure assumes a heatsink temperature of 300 K and a trap density in the QW of $2 \times 10^{15} \text{ cm}^{-3}$ (EC-IST Project, POWERPACK) [6]. All of the simulations in the following sections use this structure and the results are referenced to this ‘standard’ structure. Fig. 5.4 shows the laser structure.

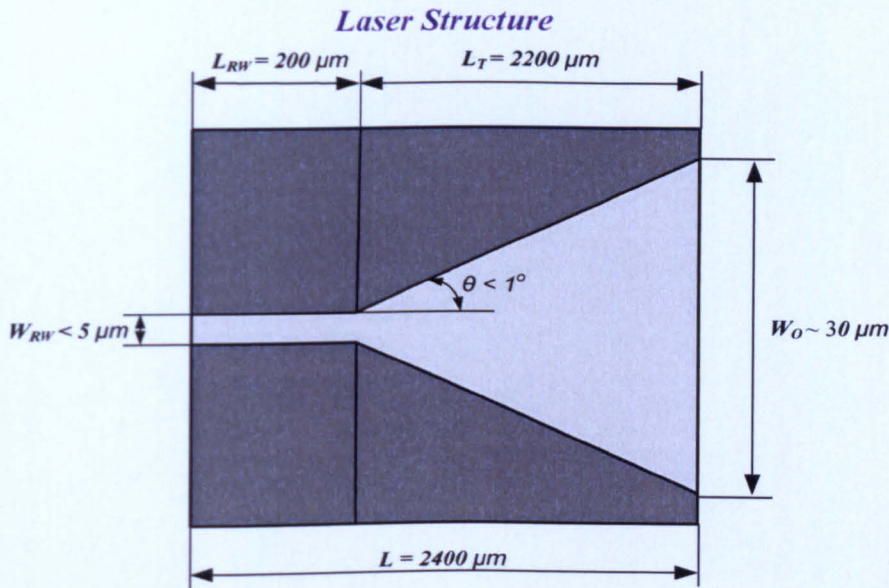


Fig. 5.4 A hypothetical standard 975 nm tapered laser structure.

Test 1: Single emitter simulations were performed with *Barlase*, using the constant current mode of operation. The purpose of this test was to check if there was agreement with results obtained by running *Speclase* alone. Exact agreement was found between these tests, indicating that the LabVIEW program and implementation of Newton’s method were working correctly.

Test 2: Further single emitter tests were also performed to test the constant power mode of operation. In order to do this, the output power from a constant current mode simulation was used as the target power for a constant power mode

simulation to check that it indeed converged to the current of the first simulation. The results of this test are given in Table 5.1. It is interesting to note, however, that significantly more round trips were needed to achieve convergence with the constant power mode simulation. This is acceptable at this time, but future work is required to investigate options to speed up this convergence.

Table 5.1 Data obtained from single emitter simulations performed in constant current and power modes.

	Start voltage (V)	Target current (A)	Target power (W)	Number of round trips	Converged voltage (V)	Converged current (A)	Converged power (W)
Constant Current Mode	2	1	NA	11	1.66137	1.00002	1.06532
Constant Power Mode	2	NA	1.065	19	1.6613	0.99993	1.06506

Test 3: The final tests were performed for multiple emitters to check both the operation of the LabVIEW control program and to investigate the computational resources required for simulating multiple emitters simultaneously. The program was tested for different numbers of emitters (initially set to have identical operating conditions). The results obtained confirmed that the control software worked properly for any user-defined number of emitters. For the current laser structure, up to 12 simulations could be performed simultaneously on a single PC with an Intel 2.4 GHz quad-core processor and 8 GB of RAM. In order to simulate more emitters than this, additional computing resources and modifications to the control software were required to distribute the simulations over the network to several nodes. The examples and discussions that will follow

in this part of the work will be restricted to laser bars with 8 emitters. It takes between 1.5–2 hours to simulate a single emitter laser.

5.3.1 Investigation of some factors affecting laser degradation processes

The principal factors that affect laser degradation are defects (both point defects and line defects), temperature, packaging-induced strain, and inhomogeneous heatsinking (e.g. solder voids, solder flow, etc). To understand how each of these factors affects the operation and degradation of a laser, a number of simulations were performed on a single emitter. These factors were investigated independently. The simulations were performed for a constant bias voltage, as this is the common factor between individual emitters once they are part of a laser bar. In all cases, simulations were attempted at voltages ranging from 1.32 V to 1.60 V at intervals of 0.02 V. The majority of these simulations converged within 10 – 15 round trips.

5.3.1.1 *Effect of introducing defects through nonradiative recombination centres*

To investigate the effects of defects, simulations were performed with different levels of nonradiative recombination in the QW. Simulations were carried out with QW trap densities, N_t , of 2, 4, 10, 20 and 100 times that of the calibrated value, $N_t = 2 \times 10^{15} \text{ cm}^{-3}$ for this standard structure. At this point, *Speclase* did not allow local changes in the trap density within a layer, so that the trap density changes were uniform changes throughout the cavity. (*Speclase* was later modified to accurately represent local degradation processes e.g. trap generation due to local heating.) Fig. 5.5a shows the power-current characteristics and the

evolution of the maximum QW temperature with bias current for each of the trap densities investigated. The P-I curves for the different trap densities show how an increase in the trap density gives rise to an increase in threshold current and a reduction in output power. Fig. 5.5b also shows how the maximum QW temperature increases with both trap density and current.

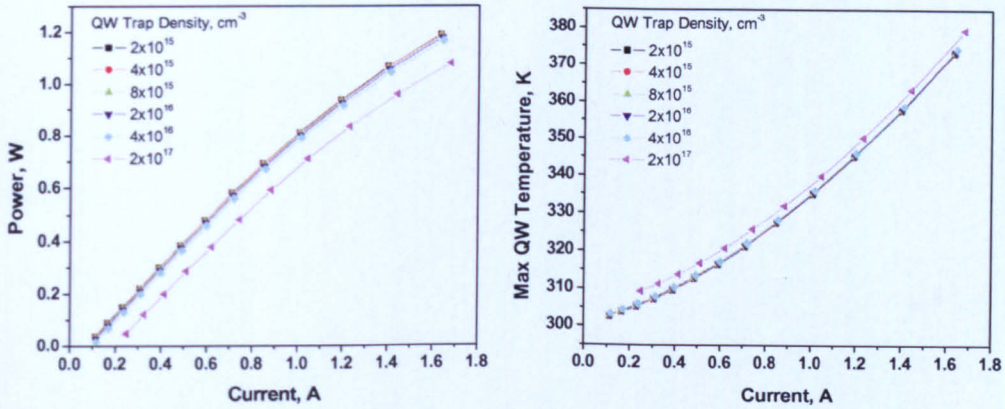


Fig. 5.5 Power-current characteristics (a) and the maximum temperature in the QW (b) as a function of current for simulations with different QW trap densities.

Fig. 5.6 and 5.7 show the equivalent power-voltage/current-voltage characteristics and the evolution of the maximum QW temperature with bias current for each of the trap densities investigated.

The threshold current and slope efficiency were extracted from the P-I curves in Fig. 5.5 and plotted as a function of trap density in Fig. 5.8. For moderate trap densities (N_t up to $2 \times 10^{16} \text{ cm}^{-3}$), the threshold current increases by around 10-15%. At much higher trap densities (N_t up to $2 \times 10^{17} \text{ cm}^{-3}$), the threshold current can more than double. Similarly, for moderate trap densities, the decrease in slope efficiency is less than 1%. However, at higher trap densities, this reduction can be as large as 5%.

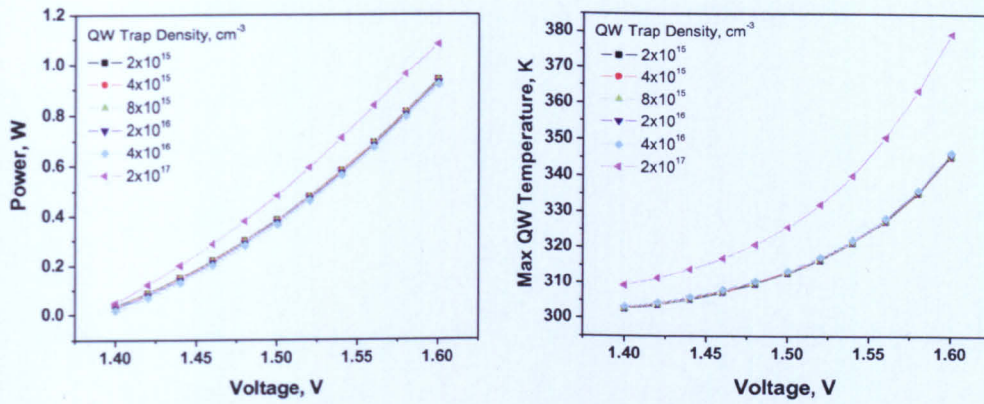


Fig. 5.6 Power-voltage characteristics (a) and the maximum temperature in the QW as a function of voltage (b) for simulations with different QW trap densities.

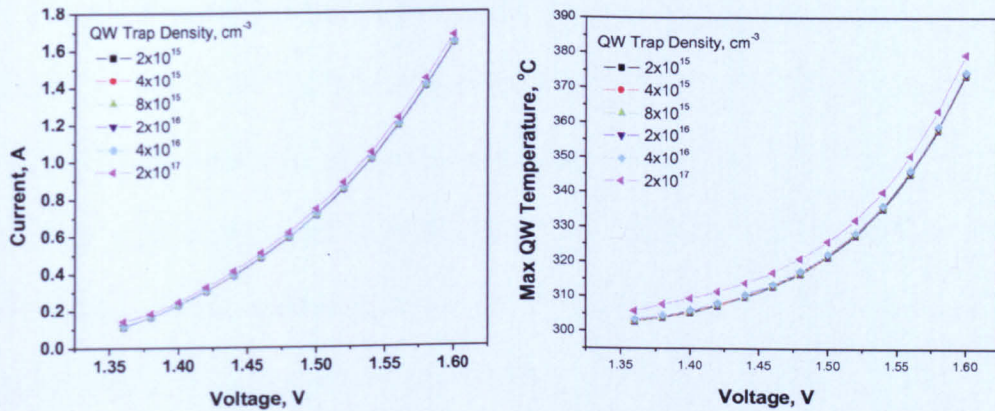


Fig. 5.7 Current-voltage characteristics (a) and the maximum temperature in the QW as a function of voltage (b) for simulations with different QW trap densities.

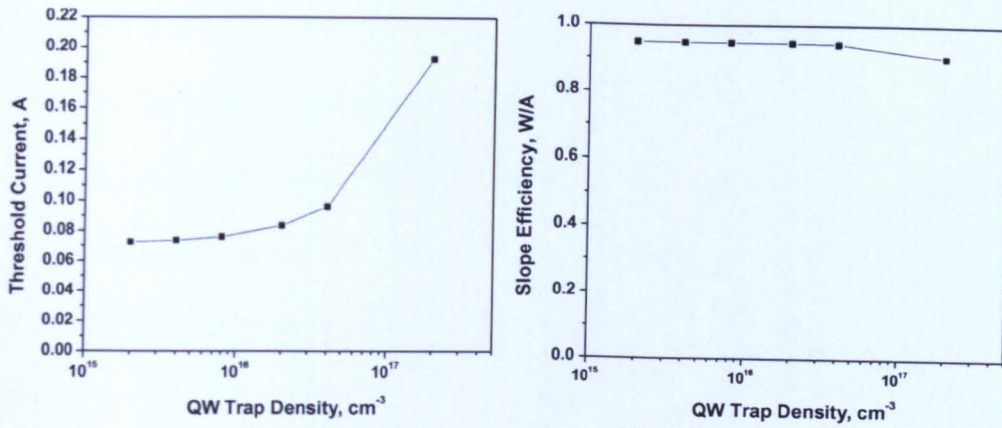


Fig. 5.8 Dependence of threshold current (a) and slope efficiency (b) on the QW trap density.

To see the differences in the simulations, the percentage change (relative to the case with $N_t = 2 \times 10^{15} \text{ cm}^{-3}$) in both bias current and output power are shown in Fig. 5.9. These results are plotted for different bias voltages, as the bias voltage is common to all of the emitters in the laser bar. The percentage change in current for a given voltage is smaller than the percentage change in output power at the same voltage. This may help to explain why simulations converged faster for the constant current mode than for the constant power mode.

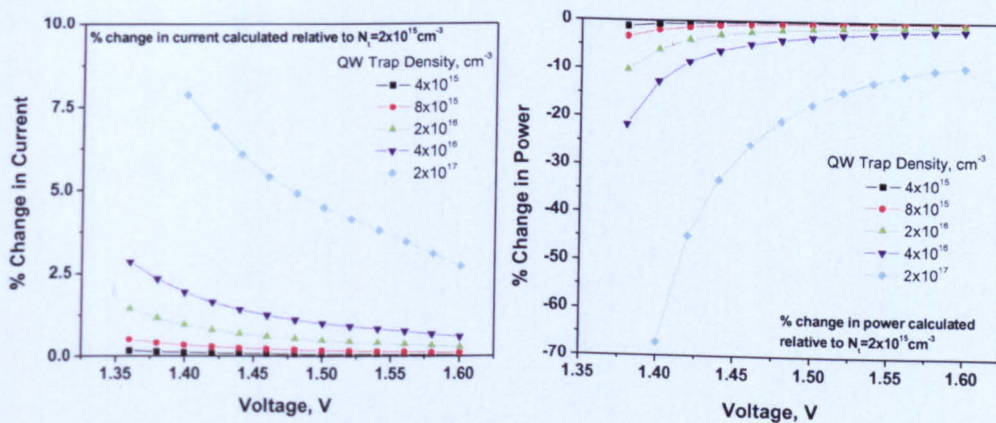


Fig. 5.9 Percentage change in current (a) and output power (b) for simulations with different QW trap densities relative to the standard QW trap density of $2 \times 10^{15} \text{ cm}^{-3}$.

In Fig. 5.9, at a voltage of 1.50 V (this is near the probable operating point of this device, i.e. the device is lasing well above the threshold, but has not yet reached the thermal roll-over point), the bias current increases by up to 1% for moderate trap densities with up to a 4% reduction in output power. For higher trap densities, the current increase is of the order of 5% with the power reduction reaching nearly 20%.

5.3.1.2 Effect of increased heatsink temperature

To investigate the effect of elevated heatsink temperatures (relative to 300 K), simulations were performed at heatsink temperatures of 320 K, 340 K and 360 K. Fig. 5.10 shows the power-current characteristics and the evolution of the maximum QW temperature with bias current for each heatsink temperature. As expected, the P-I curves show an increase in threshold current, a decrease in power and a drop in slope efficiency as the heatsink temperature is increased. Thermal roll-over is observed at high injection currents for all heatsink temperatures. As the heatsink temperature is increased, the point at which thermal roll-over occurs begins to move to lower currents.

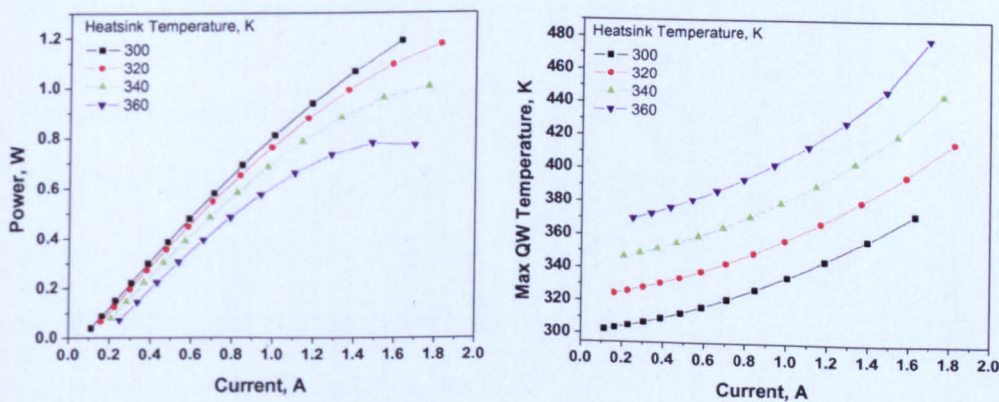


Fig. 5.10 Power-current characteristics (left), the maximum temperature in the QW as a function of current (right).

From the P-I curves in Fig. 5.10, the threshold current and slope efficiency have been extracted and these are plotted as a function of heatsink temperature in Fig. 5.11. As expected, an increase in the threshold current and a decrease in the slope efficiency are observed as the temperature of the heatsink increases.

Increasing the temperature of an emitter from 300 K to 320 K, results in an increase of nearly 25% in the threshold current. For an emitter at 360 K, the threshold current has more than doubled. Clearly, even a small increase in temperature can have a significant impact on the threshold current. The corresponding decreases in slope efficiency are $\sim 2.5\%$ for an emitter at 320 K and 15% for an emitter at 360 K.

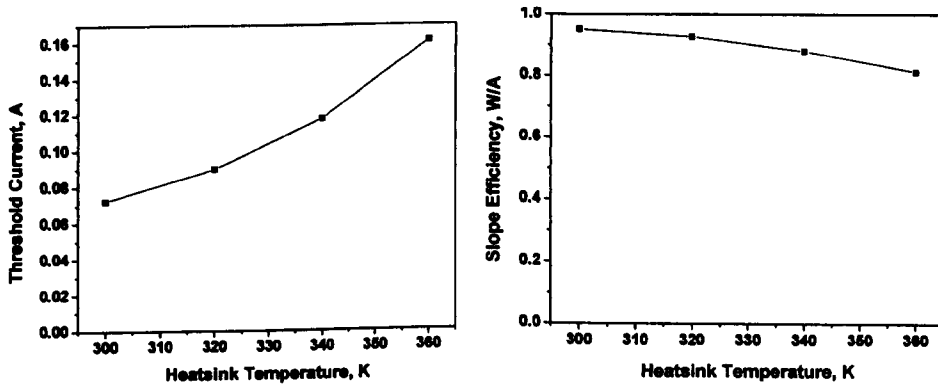


Fig. 5.11 *Graphs showing the dependence of threshold current (a) and efficiency (b) on heatsink temperature.*

This analysis can be misleading, however, since the emitters in a bar are biased with a constant voltage, not a constant current. Hotter emitters will have a lower turn-on voltage, explained earlier in section 4.3.3. Fig. 5.12a-b show the current-voltage and power-voltage characteristics for simulations at different heatsink temperatures. Over the range of heatsink temperatures investigated here, the

current increases by as much as 50% for a fixed voltage of 1.50 V. From the P-V curves, the voltage at which thermal roll-over begins is clearly identifiable. For example, in a laser bar at 1.50 V (Fig. 5.12b), emitters at 300 K and 320 K are operating in their normal operating regimes. However, emitters at 340 K are at the onset of thermal roll-over and emitters at 360 K are operating well past the onset of thermal roll-over.

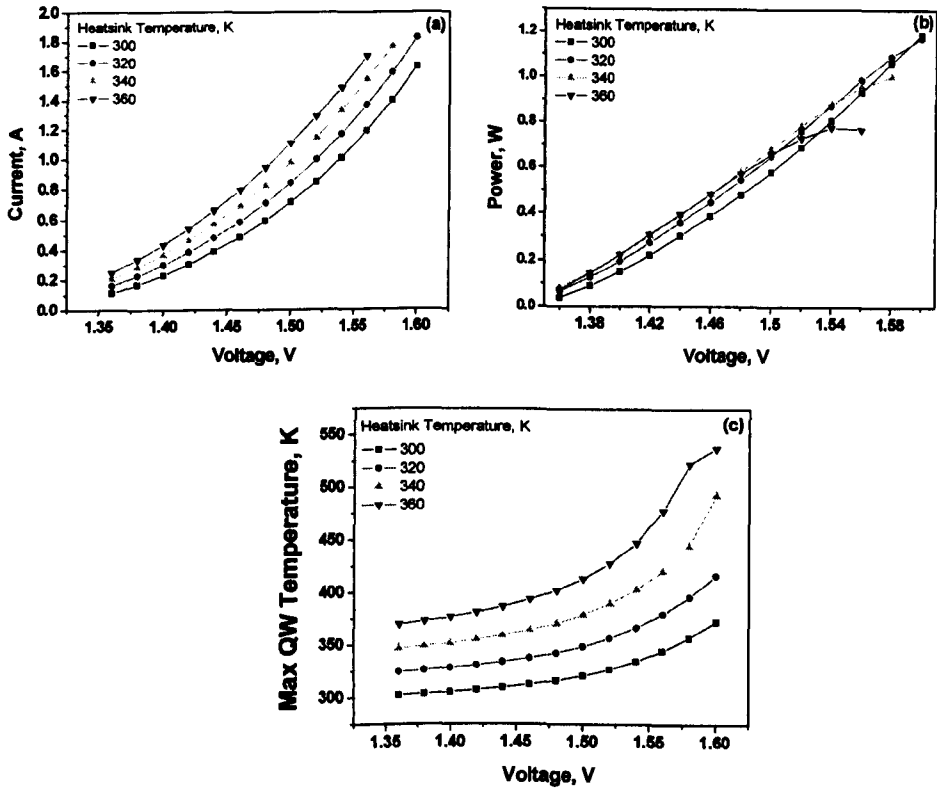


Fig. 5.12 (a) Current-voltage characteristics, (b) power-voltage characteristics, (c) and the maximum temperature in the QW versus voltage for simulations at different heatsink temperatures.

The percentage change in both bias current and output power (relative to a heatsink temperature of 300 K) are shown in Fig. 5.13 as a function of bias voltage. These graphs show the dramatic percentage increases in current and

power as the temperature rises for emitters biased with a fixed voltage. These figures show that current competition becomes an important effect in laser bars where there is an uneven distribution of temperatures between the emitters (a very typical situation). This means that if temperature remains unchecked, it will serve as catalyst for the creation of nonradiative recombination centres, which can nullify the effect of radiative recombination and ultimately kill the laser (Fig. 5.13b).

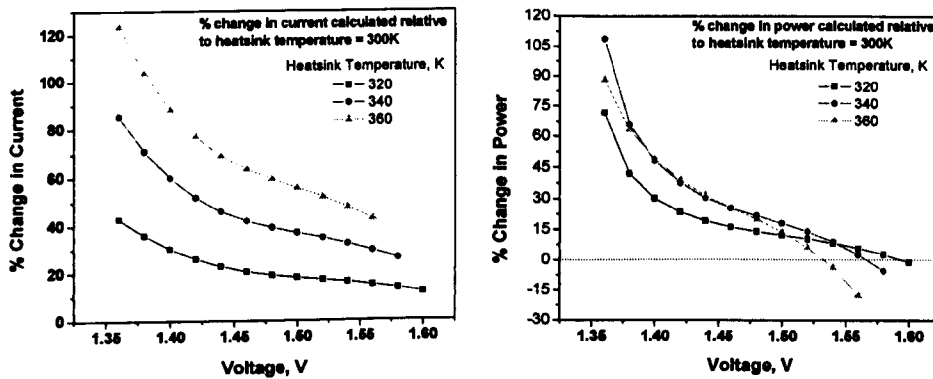


Fig. 5.13 Graphs showing the percentage change in current (left) and power (right) in simulations at different heatsink temperatures relative to the standard heatsink temperature of 300 K.

5.3.1.3 Effect of packaging-induced strain

To investigate the effect of packaging-induced strain, simulations were performed where the QW bandgap energy was increased by 1.5 meV and 3.0 meV to emulate medium and high levels of packaging-induced strain. In order to do this, the gain spectra used in *Speclase* (including differential gain) were recalculated for each of the bandgap energies (strains) investigated. The values investigated were chosen based upon experimental measurements made on a wide range of packaged laser bars (EC-IST Project, POWERPACK) [6]. The typical experimentally measured

increases in the QW bandgap energy are in the range of 1 meV to 5 meV [5, 7, 8], where a 5 meV shift corresponds to compressive strain of $\sim 0.12\%$ [9]. Fig. 5.14 shows the power-current characteristic and the evolution of the maximum QW temperature with bias current for each of the packaging-induced strain levels investigated. A reduction in the bandgap energy is expected to reduce the turn-on voltage of the laser diode. Thus, even though the power-current curves show very little change as a function of strain, the higher strain conditions do indeed cause changes to the operation of a laser biased at a fixed voltage, as shown in Fig. 5.15.

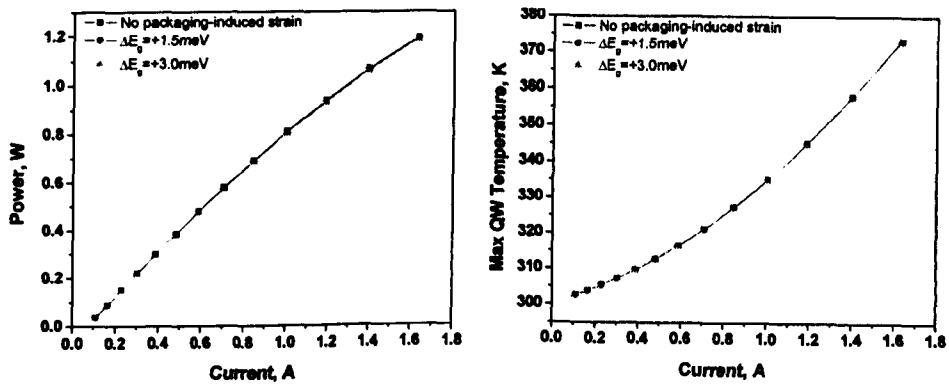


Fig. 5.14 Power-current characteristics (a) and the maximum temperature in the QW as a function of current (b) for simulations with different levels of packaging-induced strain.

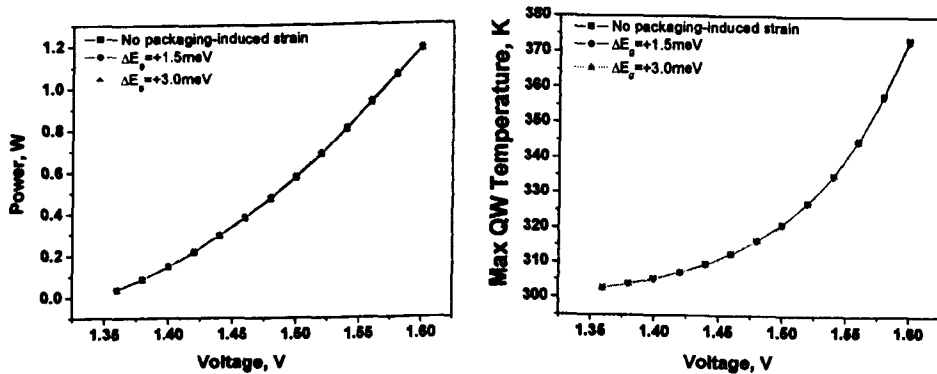


Fig. 5.15 Power-voltage characteristics (a) and the maximum temperature in the QW as a function of voltage (b) for simulations with different levels of packaging-induced strain.

To see the differences in the simulations, the percentage change (relative to the case where there is no packaging-induced strain) in both bias current and output power are shown as a function of bias voltage in Fig. 5.16. From these figures, it is possible to see the differences in the laser operation that are caused by increasing the level of packaging-induced strain. For a bias voltage of 1.45-1.50 V, a high level of packaging-induced strain can reduce the current by up to 1% and the output power by up to 2%.

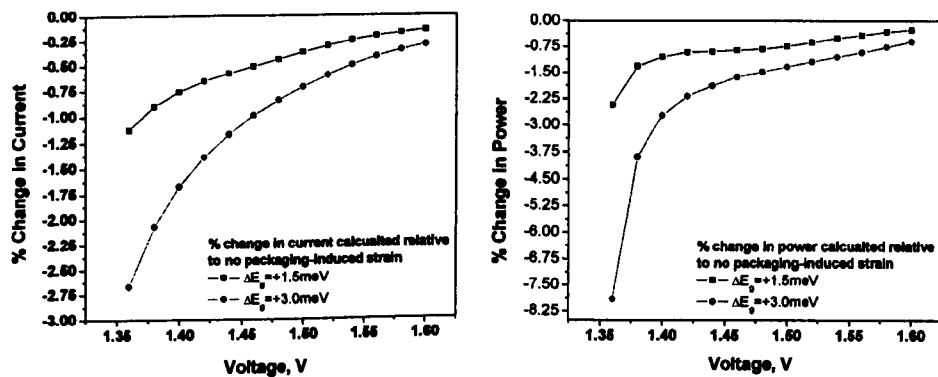


Fig. 5.16 Percentage change in current (a) and power (b) in simulations at different levels of packaging-induced strain relative to the standard case of no packaging-induced strain.

5.3.2 Summary of single emitter simulation scenarios

The results presented in this section show that even simulations of single emitters can provide a great deal of insight into how these emitters will operate in the context of a laser bar. However, it is important to consider their operation with respect to a fixed bias voltage and not with respect to a fixed bias current. The three factors investigated here (defect density, temperature and strain) all affect the operation of the emitter. However, temperature is found to be the most important effect. High levels of defects can also play a significant role. The effects on laser operation of lower levels of defects and packaging-induced strain are smaller, but these are nonetheless important when combined with all of the other factors that can affect laser degradation.

5.3.3 Multi-emitter simulations

Following the single emitter simulations presented in the previous section, multi-emitter simulations (of an 8 emitter bar) were carried out. Note that the pitch between the emitters is not important for these multi-emitter simulations, since the only communication between the emitters in these simulations is only electrical. This means that the emitters are linked only through current/voltage. However, each emitter is independently solved thermally.

Before attempting to carry out the emulation of the degradation processes over time, simulations were performed for a bar at zero aging time. To do this, some variations were introduced across the 8 emitters in the bar. Three commonly encountered scenarios were considered. These include:

1. a statistical fluctuation in the trap density in the QW active region of each of the emitters;
2. a damaged emitter (with a high trap density in the QW active region); and
3. an inhomogeneous temperature profile across the bar.

Each of these scenarios is explained below, together with the results obtained from the simulations. In each case, the results are compared to the ideal case - a reference bar of 8 identical emitters all operating at the same heatsink temperature.

5.3.3.1 Scenario 1: Random low-level of defects distributed across the bar

The first scenario investigated introduced a random low level of defects across the emitters in the bar. From the single emitter simulations, it was observed that increasing the QW trap density from $2\times10^{15}\text{ cm}^{-3}$ to $2\times10^{16}\text{ cm}^{-3}$ caused a reduction in the output power of a few percent. Experimentally, the power between emitters in a new laser bar varies by <5%. The randomised defect level for each emitter was therefore determined by generating a random number between 0 and 1 and multiplying this by $2\times10^{16}\text{ cm}^{-3}$. These new QW trap densities were then used in the simulation input files for the emitters. Fig. 5.17 shows the QW trap density profile and the actual QW trap densities used for the simulations.

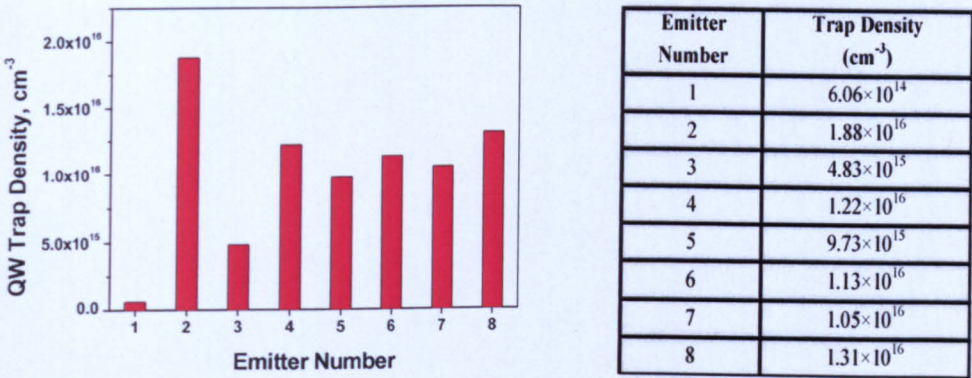


Fig. 5.17 QW trap densities (a) and table showing the values of QW trap densities assigned to each emitter in the bar (b).

Multi-emitter simulations were carried out in constant current mode for bar currents of 2, 4, 6, 8 and 10 A. Fig. 5.18 shows the P-I characteristic of the bar and the P-I characteristics of each of the individual emitters.

The equivalent bar current - voltage characteristic is shown in Fig. 5.19a and the emitter powers versus voltage are shown in Fig. 5.19b. The threshold current and

slope efficiency were calculated for each emitter from the emitter P-I curves in Fig. 5.18b. These quantities are plotted as a function of emitter number in Fig. 5.20. As expected, the threshold current increases and the slope efficiency decreases for emitters with a higher trap density. There is up to a 10% variation in the threshold currents in this example, whilst the variation in slope efficiencies is $<0.3\%$. Fig. 5.20 also shows the simulated values for the “apparent” threshold current and “apparent” slope efficiency of each emitter. These parameters are important for comparison with experimental observations, since the actual threshold currents and slope efficiencies of the individual emitters in a laser bar cannot be measured. The apparent threshold current and apparent slope efficiency can be measured experimentally, but cannot be directly compared with their traditional counterparts. (They are defined similarly to the threshold current and slope efficiency, but use the individual emitter power and the total bar current.)

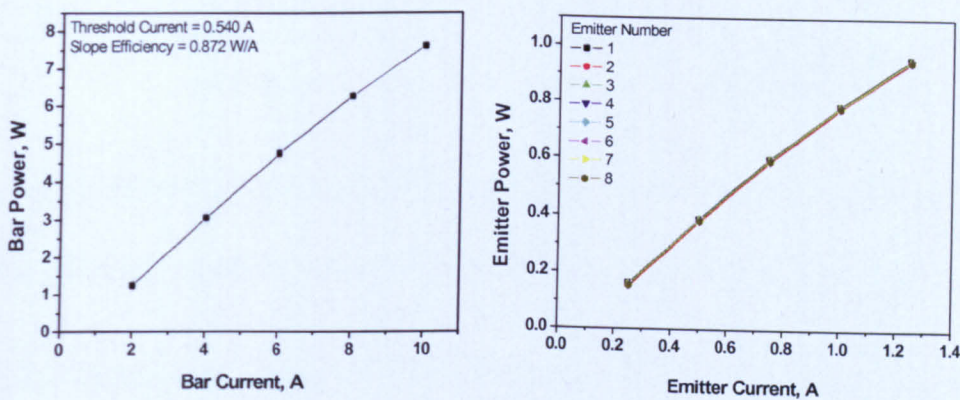


Fig. 5.18 Power-current characteristics of the full bar (left) and of the individual emitters (right).

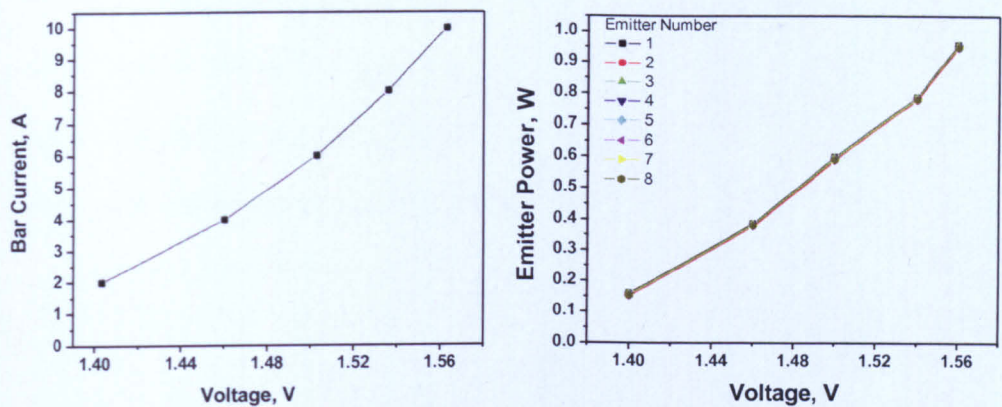


Fig. 5.19 Current-voltage characteristics of the full bar (left) and of the individual emitters (right).

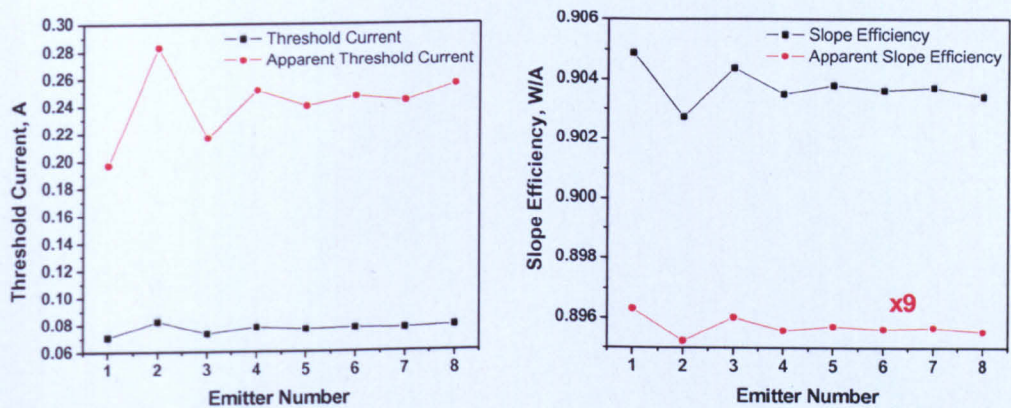


Fig. 5.20 Variation of threshold current (apparent threshold current) (a) and slope efficiency (apparent slope efficiency) (b) of individual emitters.

Fig. 5.21 shows the distribution of current, power and maximum QW temperature for each emitter across the bar for a total bar current of 2 A. Fig. 5.22 shows the same quantities for a total bar current of 10 A.

From the graphs in Figs. 5.21 and 5.22, a correlation can be seen between the currents, powers and maximum QW temperatures of the individual emitters. The emitters with the highest defect densities draw more of the total bar current (meaning there is less available for emitters with fewer defects), but emit less

power because of the higher level of nonradiative recombination. Consequently, these emitters are also hotter. The variations in the emitter current and power across the bar are up to 0.3% and 1.0%, respectively. The variation in the maximum QW temperature of the emitters is ~ 0.5 K.

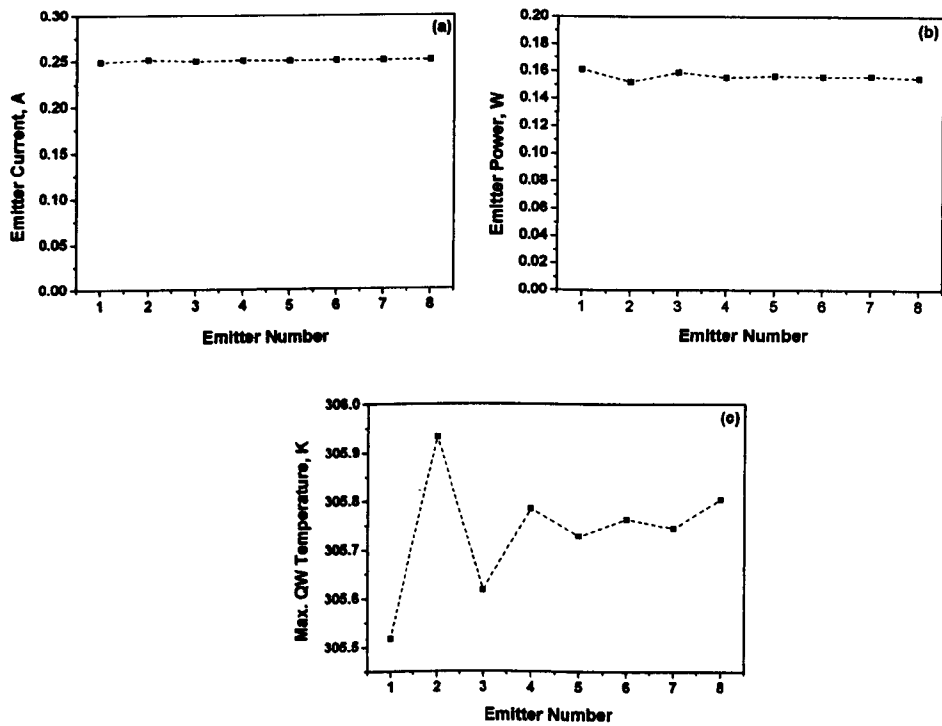


Fig. 5.21 (a) Distribution of the emitter currents, (b) emitter powers and (c) maximum emitter QW temperatures across the bar at a total bar bias current of 2A.

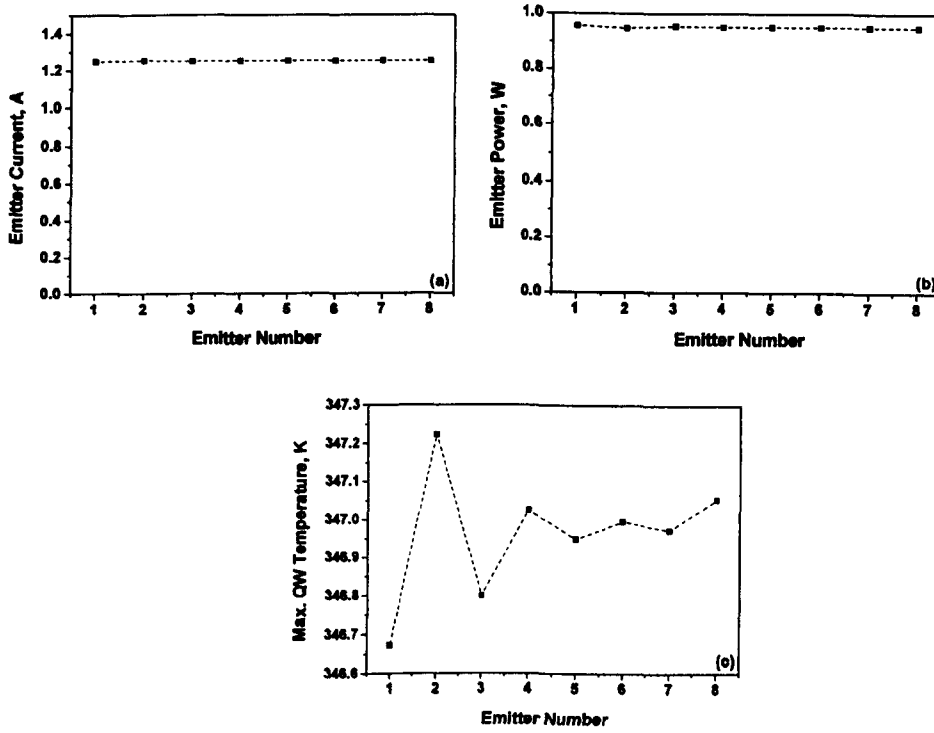


Fig. 5.22 (a) Distribution of the emitter currents, (b) emitter powers and (c) maximum emitter QW temperatures across the bar at a total bar bias current of 10 A.

5.3.3.2 Scenario 2: Damaged single emitter randomly located in the bar

In the second scenario, a high level of defects was introduced in one random emitter in the bar (emitter #3) in order to represent a “damaged” emitter. This level was chosen to be $2 \times 10^{16} \text{ cm}^{-3}$ – an order of magnitude higher than that found in the other 7 emitters. Fig. 5.23a shows the QW trap density profile and Fig. 5.23b shows the actual numbers used for the simulations. Again, multi-emitter simulations were carried out in constant current mode for bar currents of 2, 4, 6, 8 and 10 A.

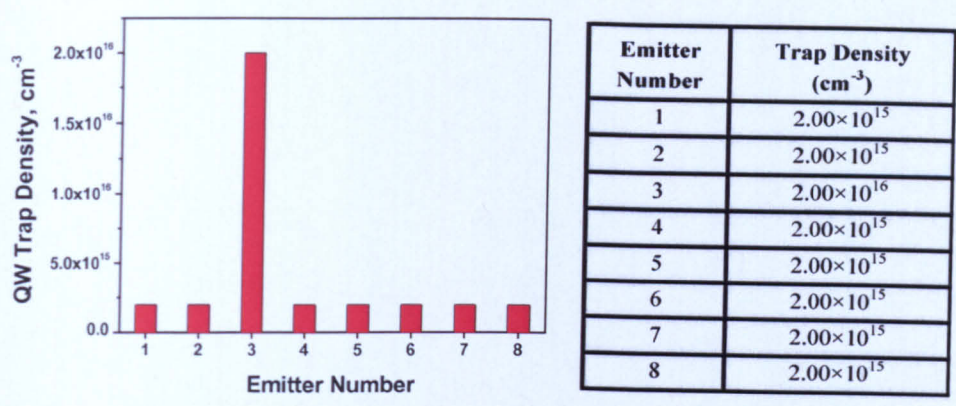


Fig. 5.23 QW trap densities (a) and table showing the values of QW trap densities assigned to each emitter in the bar (b).

Fig. 5.24 shows the P-I characteristic of the bar together with the P-I characteristics and the P-V characteristics of each of the individual emitters. The threshold current (and apparent threshold current) and slope efficiency (and apparent slope efficiency) for the bar are also shown in Fig. 5.25a. The threshold current (and apparent threshold current) and slope efficiency (and apparent slope efficiency) have been calculated for each individual emitter from the emitter P-I curves in Fig. 5.24b. These quantities are plotted as a function of emitter number in Fig. 5.25. The P-I curve of the emitter with the high level of defects (#3) is lower than that of the other emitters, as expected. The threshold current in emitter number 3 is 16% higher, whilst the slope efficiency is only 0.25% lower.

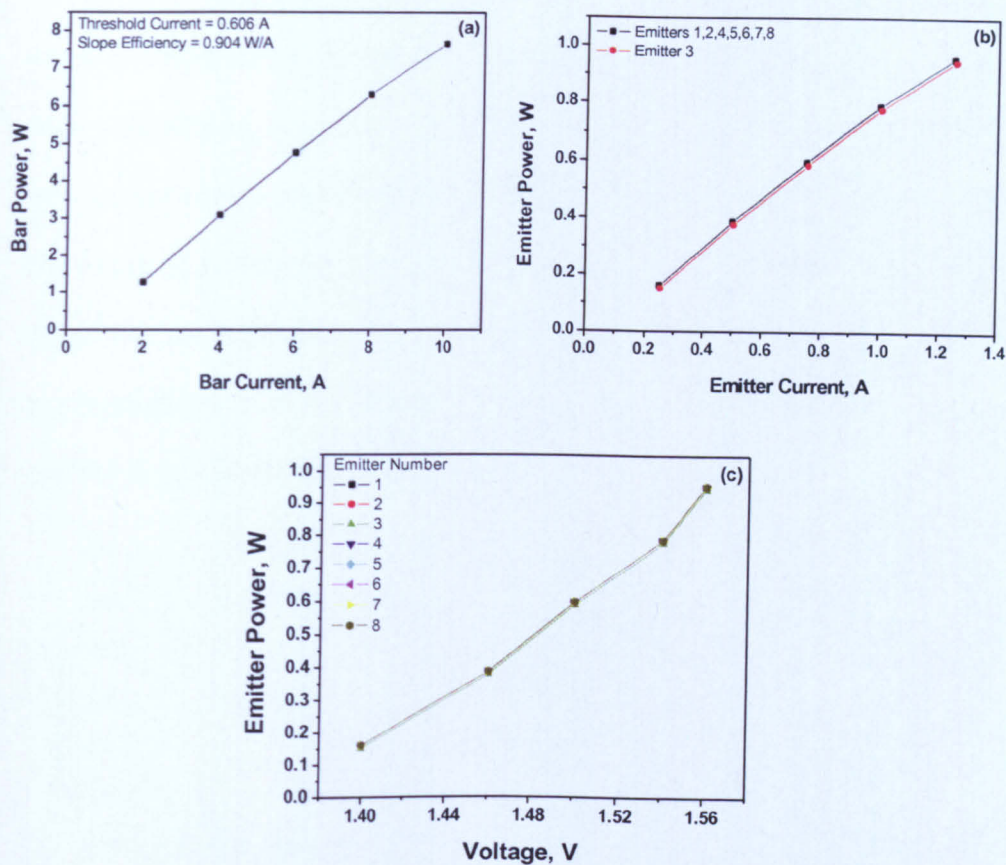


Fig. 5.24 (a) Bar power-current characteristics of the full bar, (b) emitter power-emitter current characteristics, (c) and emitter power-individual emitter voltage characteristics.

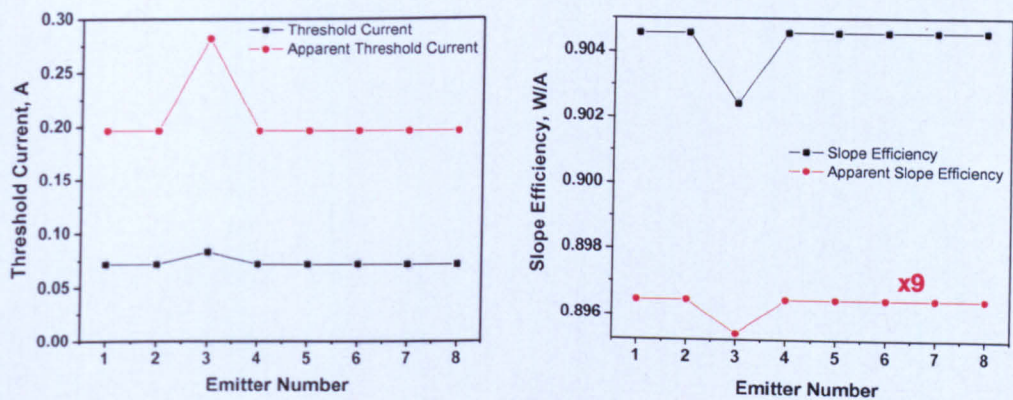


Fig. 5.25 Variation of the threshold current and apparent threshold current (a), and the slope efficiency and the apparent slope efficiency (b) of the individual emitters.

Fig. 5.26 shows the distribution of current, power and maximum QW temperature for each emitter across the bar for a total bar current of 2 A. Fig. 5.27 shows the same quantities for a total bar current of 10 A. From these graphs, the relationship between the current, power and maximum QW temperature of the emitter with the high level of defects can be seen in comparison to the standard emitters. The higher level of defects in emitter number 3 causes its current to be 0.35% higher, its output power to be 1.0% lower and its maximum QW temperature to be just over 0.5 K greater than the other emitters.

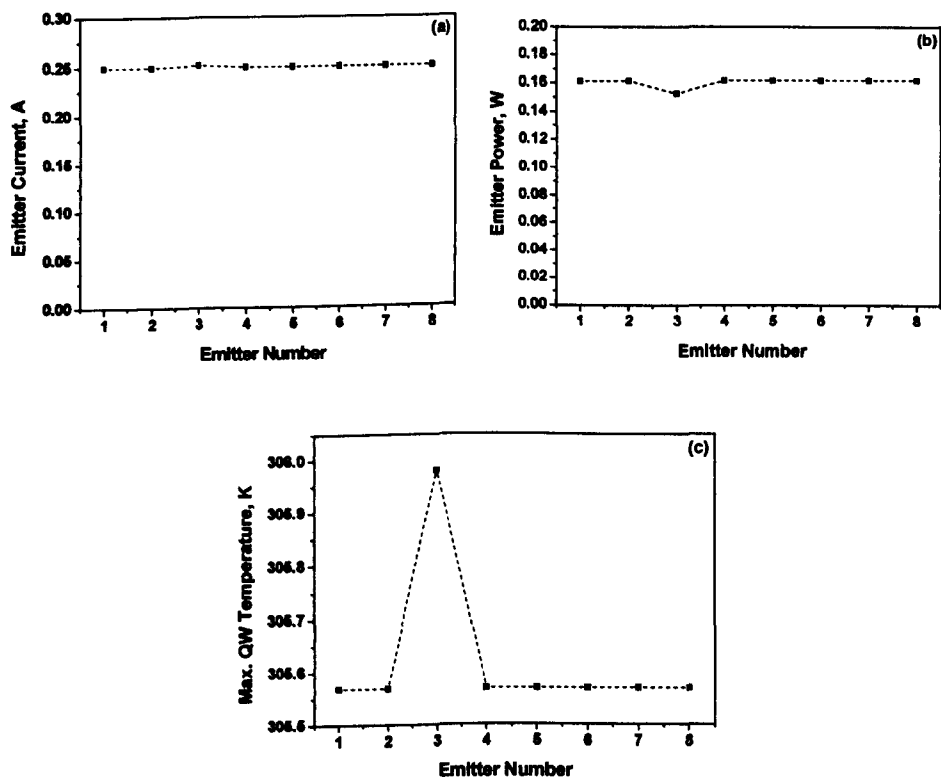


Fig. 5.26 (a) Distribution of the emitter currents, (b) the emitter powers and (c) the maximum emitter QW temperatures across the bar for a total bar bias current of 2 A.

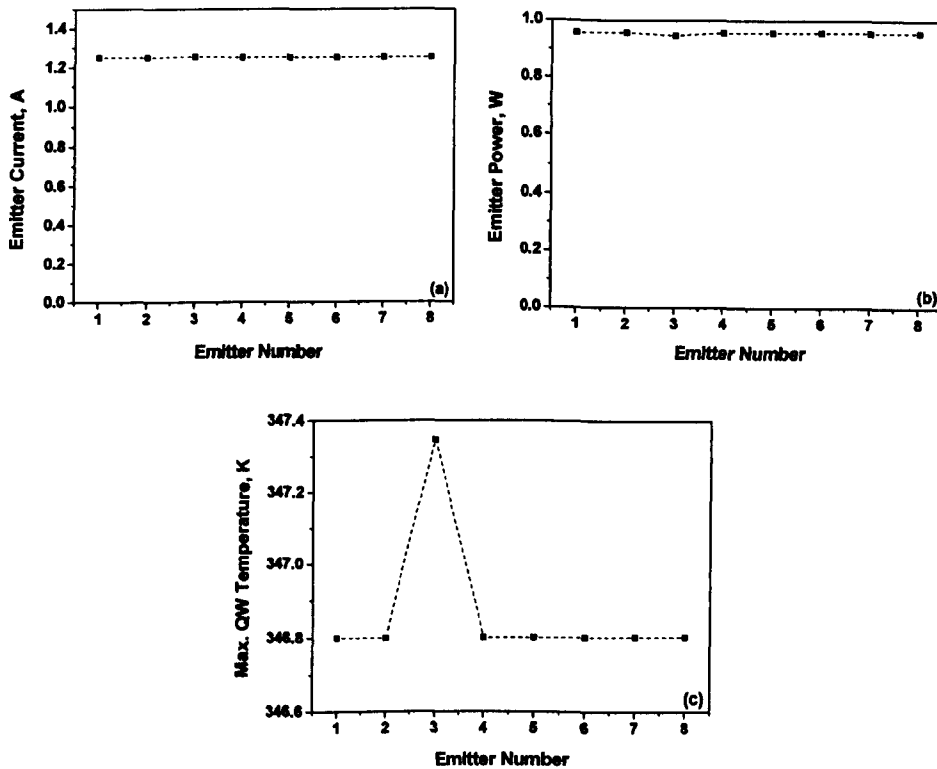


Fig. 5.27 (a) Distribution of the emitter currents, (b) the emitter powers and (c) the maximum emitter QW temperatures across the bar for a total bar bias current of 10 A.

5.3.3.3 Scenario 3: Curved temperature (frown) profile with the maximum temperature at the centre of the bar

The final scenario investigated was the impact of a curved heatsink temperature profile across the bar, with the maximum temperature at the centre of the bar. The edges of the bar were held at 300 K. Temperature variations of this magnitude (up to 30 K) have been measured in high-power laser bars with 25 – 50 emitters operating at high currents (e.g. 30 A – 50 A). Fig. 5.28 shows the assumed heatsink temperature profile and the actual heatsink temperature values used for the simulations.

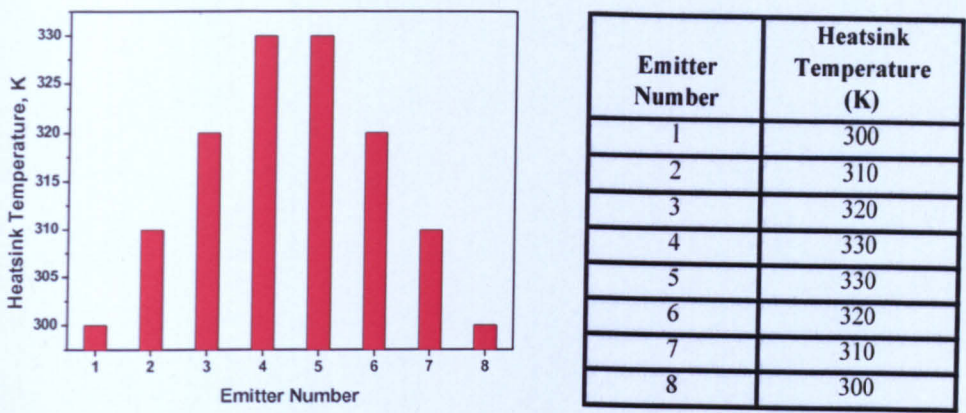


Fig. 5.28 Heatsink temperature profile (a) and table showing the values of heatsink temperatures assigned to each emitter in the bar (b).

Using these values, multi-emitter simulations were carried out in constant current mode for bar currents of 2, 4, 6, 8 and 10 A for a hypothetical 8 emitter bar.

Fig. 5.29 shows the P-I characteristic of the bar together with the P-I characteristics of each of the individual emitters and the P-V characteristics of each of the individual emitters. The threshold current and slope efficiency of the bar are also shown in Fig. 5.30a. From the emitter P-I curves in Fig. 5.29b, the threshold current and slope efficiency have been calculated for each individual emitter. These quantities are plotted as a function of emitter number in Fig. 5.30. The results for the different emitters clearly show an increased threshold current, decreased slope efficiency and earlier onset of thermal roll-over for the hotter emitters. The threshold currents of the individual emitters vary by $\pm 5\%$ from the average value, whilst the slope efficiencies deviate by $\pm(3\% - 5\%)$ from the average value. Nevertheless, the hotter emitters draw more current and emit more power. This can be explained by the fact that the temperature-induced changes in the “apparent” threshold current and the “apparent” slope efficiency are opposite to the changes in the actual threshold current and slope efficiency. This is due to

the temperature induced bandgap reduction, which lowers the turn-on voltage and strongly affects the current competition between emitters, as discussed earlier in section 4.3.3. Strain-induced changes in the bandgap energy are expected to result in similar behaviour of the apparent threshold current and slope efficiency, but this is not expected for increases in the defect or trap density (since this does not change the turn-on voltage of the emitter diode). Finally, this example also shows that temperature is a principal cause of emitter threshold current and slope efficiency variations.

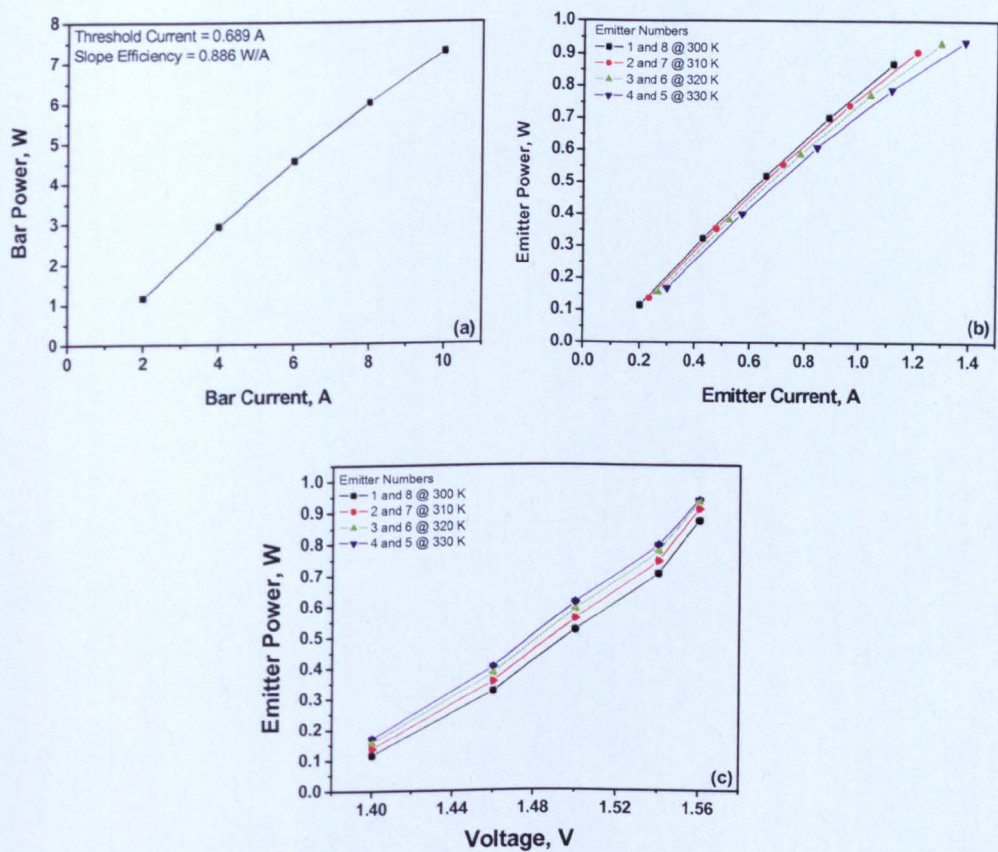


Fig. 5.29 (a) Bar power-current characteristics of the full bar, (b) emitter power-emitter current characteristics, (c) and emitter power-individual emitter voltage characteristics.

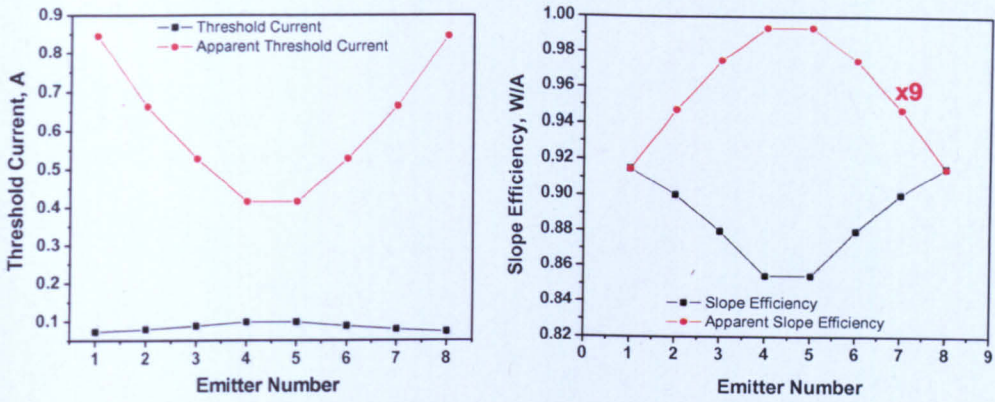


Fig. 5.30 Graphs showing the variation of the threshold current and the apparent threshold current (a), and the slope efficiency and the apparent slope efficiency (b) of the individual emitters.

Fig. 5.31 shows the distribution of current, power and maximum QW temperature across the bar for a total bar current of 2 A. Fig. 5.32 shows the same quantities for a total bar current of 10 A. The horizontal lines in Figs. 5.31 and 5.32 represent the average values of emitter current and power found by dividing the values from the total bar P-I characteristic by the number of emitters. In these graphs, the effects of current competition and the distribution of the power between the emitters are made clear. The emitter currents vary by up to $\pm 10\%$ from the average value, whilst the emitter output powers vary by up to $\pm (3\% - 5\%)$.

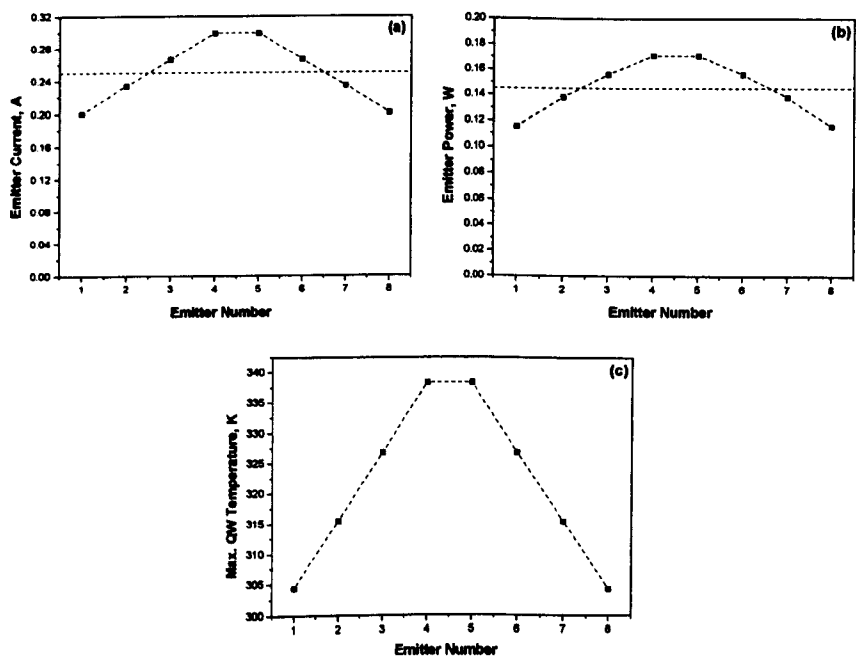


Fig. 5.31 (a) Graphs showing the distribution of the emitter currents, (b) the emitter powers and (c) the maximum emitter QW temperatures across the bar for a total bar bias current of 2 A.

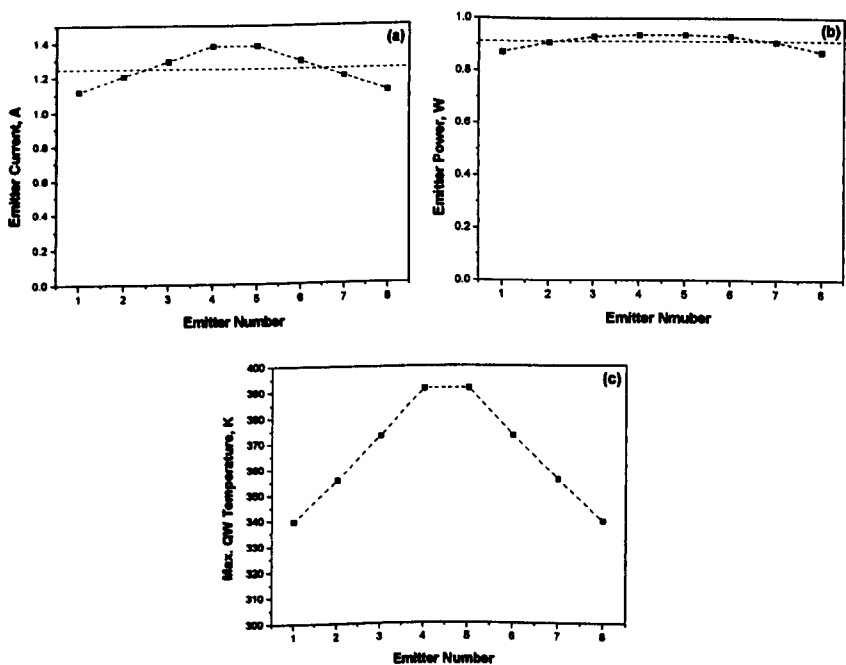


Fig. 5.32 (a) Graphs showing the distribution of the emitter currents, (b) the emitter powers and (c) the maximum emitter QW temperatures across the bar for a total bar bias current of 10 A.

5.3.4 Summary of multiple emitter simulation scenarios

The three cases investigated here using multi-emitter simulations show that variations in the operating conditions and environment of the individual emitters also affect the performance of the other emitters and of the bar as a whole. The introduction of a non-uniform temperature profile caused the most significant change in the bar and emitter operating conditions and in its performance. However, it should be remembered that these scenarios are for devices at the start of the aging process. When all of the relevant effects are combined and allowed to interact over time, high levels of defects are also expected to play a more important role. Indeed, it is well known that the nucleation, propagation and growth of defects increase with temperature. Thus, the rates of defect generation and propagation within emitters are inextricably linked to the temperature profile. Finally, it was shown that the experimentally measurable “apparent” threshold current and “apparent” slope efficiency of the emitters change in the opposite direction to their *actual* threshold current and slope efficiency. This is caused by current competition resulting from a reduction in the turn-on voltage, which is caused by local temperature and/or strain-induced changes in the bandgap energy.

5.3.5 General summary and outlook

This chapter has demonstrated how *Bartase*, can be used to simulate both single emitters and multiple emitter laser bars under a wide range of operation conditions, which (to our knowledge) has not been performed before.

A large number of simulations were performed on single emitters in order to investigate the effects of temperature, defects and packaging-induced strain on the

operation of the laser. The results obtained show that even simulations of single emitters can provide a great deal of insight into how individual emitters will operate within the context of a laser bar – provided the simulation results are considered as a function of bias voltage rather than bias current. Of the factors investigated, temperature was found to have the largest impact, but high defect levels can also play a significant role.

Three initial multiple-emitter scenarios were also investigated to demonstrate the capabilities of *Barlase*. In the three cases investigated, the variations in the operating condition and environments of the individual emitters were seen to affect the performance of the other emitters and of the bar as a whole. In the examples considered here, the introduction of the non-uniform temperature profile caused the most significant changes in the bar and emitter operating conditions and performance. However, it should be remembered that these scenarios were for devices at the start of the aging process. When all of the relevant effects are combined and allowed to interact over time, then high levels of defects are expected to play a more important role. Indeed, it is well known that the propagation and growth of defects increases with increasing temperature. Thus, the rates of defect generation and propagation within the emitters are inextricably linked with the temperature profile of the bar.

References

- [1] C. K. Amuzuvi, J. J. Lim, S. Bull, and E. C. Larkins, "Describing the state-of-the-art laser diode emulation tool," *in preparation to be submitted*, 2010.
- [2] J. J. Lim, S. Sujecki, L. Lang, Z. C. Zhang, D. Paboeuf, G. Pauliat, G. Lucas-Leclin, P. Georges, R. C. I. MacKenzie, P. Bream, S. Bull, K. H. Hasler, B. Sumpf, H. Wenzel, G. Erbert, B. Thestrup, P. M. Petersen, N. Michel, M. Krakowski, and E. C. Larkins, "Design and Simulation of Next-Generation High-Power, High-Brightness Laser Diodes," *IEEE Journal of Selected Topics in Quantum Electronics*, vol. 15, pp. 993-1008, May-Jun 2009.
- [3] J. J. Lim, R. MacKenzie, S. Sujecki, M. Sadeghi, S. M. Wang, Y. Q. Wei, J. S. Gustavsson, A. Larsson, P. Melanen, P. Sipila, P. Uusimaa, A. A. George, P. M. Smowton, and E. C. Larkins, "Simulation of double quantum well GaInNAs laser diodes," in *21st Conference on Semiconductor Integrated Optoelectronics (SIOE)*, Cardiff, WALES, 2007, pp. 259-265.
- [4] C. K. Amuzuvi, J. J. Lim, S. Bull, and E. C. Larkins, "Investigating a hypothetical single emitter/bar using a laser diode emulation tool," *in preparation to be submitted*, 2010.
- [5] S. Bull, J. W. Tomm, M. Oudart, J. Nagle, C. Scholz, K. Boucke, I. Harrison, and E. C. Larkins, "By-emitter degradation analysis of high-power laser bars," *Journal of Applied Physics*, vol. 98, p. 063101, 2005.
- [6] G. P. Agrawal and N. K. Dutta, *Semiconductor Lasers*: Kluwer Academic Publishers; 2nd Revised edition edition, 1993.
- [7] S. Bull, "Photo- and Electroluminescence Microscopy and Spectroscopy Investigation of High Power and High Brightness Semiconductor Laser Diode," *Dissertation, University of Nottingham, United Kingdom*, 2004.
- [8] R. Xia, E. C. Larkins, I. Harrison, S. R. A. Dods, A. Andrianov, J. Morgan, and J. P. Landesman, "Mounting-induced strain threshold for the degradation of high-power AlGaAs laser bars," *IEEE Photonics Technology Letters*, vol. 14, pp. 893-895, Jul 2002.
- [9] J. W. Tomm, A. Gerhardt, T. Elsaesser, D. Lorenzen, and P. Hennig, "Simultaneous quantification of strain and defects in high-power diode laser devices," *Applied Physics Letters*, vol. 81, pp. 3269-3271, Oct 2002.
- [10] M. L. Biermann, S. Duran, K. Peterson, A. Gerhardt, J. W. Tomm, A. Bercha, and W. Trzeciakowski, "Spectroscopic method of strain analysis in semiconductor quantum-well devices," *Journal of Applied Physics*, vol. 96, pp. 4056-4065, Oct 2004.

Chapter 6

Modification of the Emulation Tool for Improved By-Emitter Degradation Analysis

Further work was required to improve the convergence speed of the software and for achieving better use of the computational resources available. *Speclase*, the software tool used by *Barlase* to simulate the individual emitters, needed to be modified in order to accurately represent local degradation processes (e.g. trap generation due to local heating). The modification of *Speclase* was carried out by Dr Jun Lim to run further simulations. The investigation was taken a step further by aging some theoretical laser bars using trap generation caused by local heating, which is what happens during aging. All of the work done in this thesis shows that *Barlase* is capable of performing simulations for multiple emitters (bar simulations) [1]. Attempts will now be made to emulate the degradation of lasers (aging a device) in order to learn more about such devices.

The objective of this work is to use simulation tools to gain a deeper understanding of laser bar degradation at the emitter level by changing the

operating conditions and environments of the individual emitters in a parallel array. The Arrhenius equation is used as a mathematical model for the trap generation rate during the aging of the device.

6.1 Aging Models

The degradation model of lasers has often been described using the Arrhenius equation [2-4]. The Arrhenius equation will therefore be used in the aging process and two models will be implemented to update trap density and temperature as follows:

1. Constant QW trap density based on maximum QW temperature

$$\Delta N_t(x, z) = A \exp(-E_a / kT_{QW_Max}) t_{aging} \quad (6.1)$$

2. Spatially variable QW trap density based on QW temperature distribution

$$\Delta N_t(x, z) = A \exp(-E_a / kT_{QW}(x, z)) t_{aging} \quad (6.2)$$

where:

ΔN_t = Change in trap density, A = Pre-Arrhenius constant, E_a = Activation energy, k = Boltzman constant, t_{aging} = Aging time, T_{QW} = Quantum well temperature

6.2 Spectral Laser Model Enhancement

6.2.1 Spatially variable trap density distribution

It is not physically reasonable to have a constant QW trap density based on the maximum QW temperature. The first model was not physically reasonable and overestimated the degradation rate of the device. Therefore, *Speclase* had to be modified to accept a local trap density distribution, which allows a more realistic and accurate simulation of the degradation behaviour. The modification of the model to accept a local trap density distribution makes it possible for *Barlase* to generate a trap density distribution which evolves as a function of the temperature distribution. Fig. 6.1 shows the uniform and local trap density profiles and the QW temperature profile.

The effect of a local increase in QW temperature profile can be appreciated when single emitter simulations are performed with a uniform trap density distribution as shown in Fig. 6.1a and for a local trap density distribution (Fig. 6.1b). Fig. 6.1b shows a more physically reasonable trap density profile with respect to the local QW temperature profile (Fig. 6.1c). For these simulations, the bias current is 200 mA for a 0.64 degree index guided tapered laser. The temperature profile is in the plane of the QW. The x-axis therefore is the lateral direction and the z-axis is the longitudinal direction.

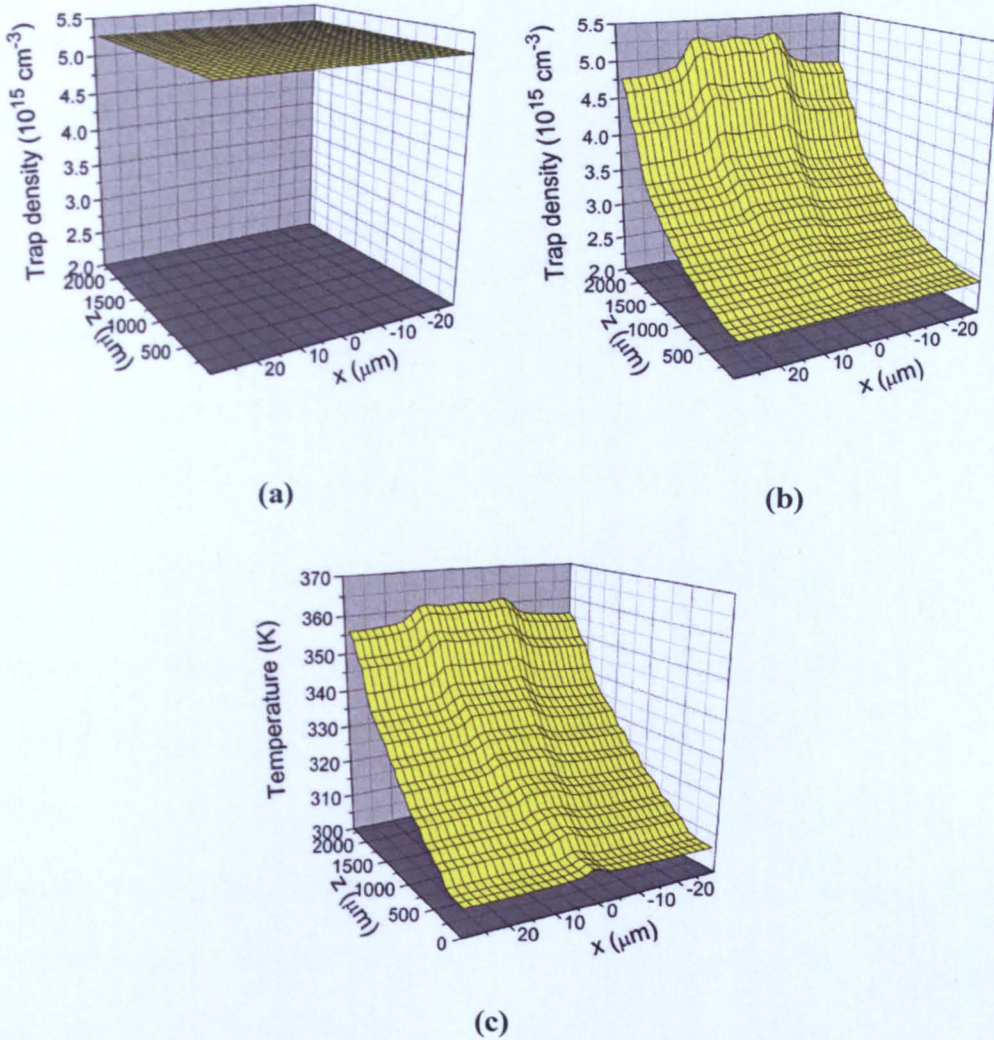


Fig. 6.1 3D plots of (a) uniform trap density (b) local trap density and (c) QW temperature profile.

Once *Speclase* was enhanced to allow for a spatially variable trap density distribution, a more realistic trap distribution was attained, as seen in the 3D plots of Fig. 6.1. The trap density distribution, generated as a function of QW temperature distribution in this case (Fig. 6.1b), allows for a more realistic and accurate simulation of the degradation behaviour, which the earlier case (Fig. 6.1a) had overestimated.

Studies were carried out to do some comparisons using a constant QW trap density and spatially variable QW trap density aging models. This was done to ascertain the operation of the model giving an outline of what is being investigated.

It must be noted at this juncture that the laser structure used throughout in all the case studies that follow is the 975 nm narrow angle tapered emitter described in chapter 5 of section 5.3 (Fig. 5.4) which is un-calibrated. The calibration of a laser bar would be discussed in later parts of this thesis.

6.2.2 Case study 1 (single emitter) – uniform QW trap density

The first case study made to investigate the comparisons for single emitters uses an aging model where the QW trap density is kept constant. The aging was emulated at a constant current of 1.5 A, for aging times up to 10,000 hrs. The parameter being varied is the heatsink temperature at: 300 K, 320 K and 340 K. The emitter power dropped as a function of aging time for different heatsink temperatures of 300 K, 320 K and 340 K. The percentage power drop was calculated and plotted with respect to an unaged emitter.

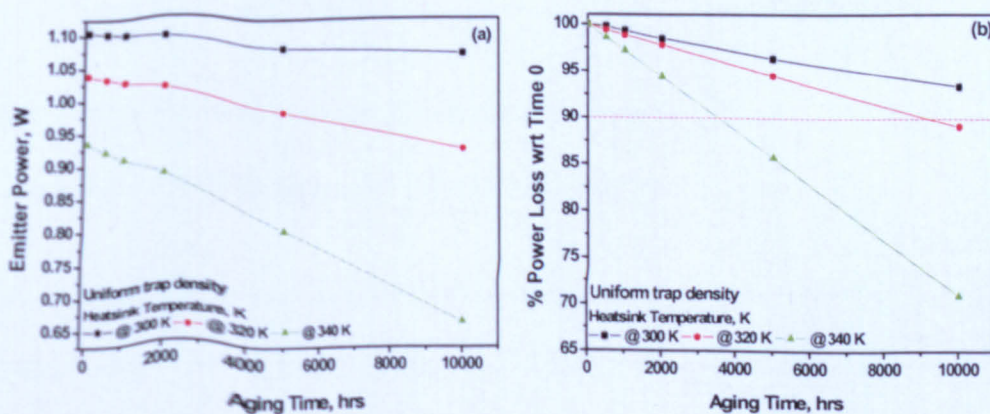


Fig. 6.2 Graphs with uniform trap density for: (a) emitter power versus aging time and (b) % power loss with respect to the unaged emitter.

There is a 10% power loss after ~3,500 hours at 340 K and after ~9,000 hours at 320 K, which is more than the acceptable threshold (10% power loss). This quick rate of degradation can be attributed to the aging model used, which overestimates the rate of degradation.

6.2.3 Case study 2 (single emitter) – local QW trap density

The second case study was to investigate the degradation of the same single emitter using an aging model where the QW trap density depends on the local QW temperature. The aging was emulated for a constant current of 1.5 A, with aging times up to 10,000 hours. The parameter being varied is the heatsink temperature at: 300 K, 320 K and 340 K.

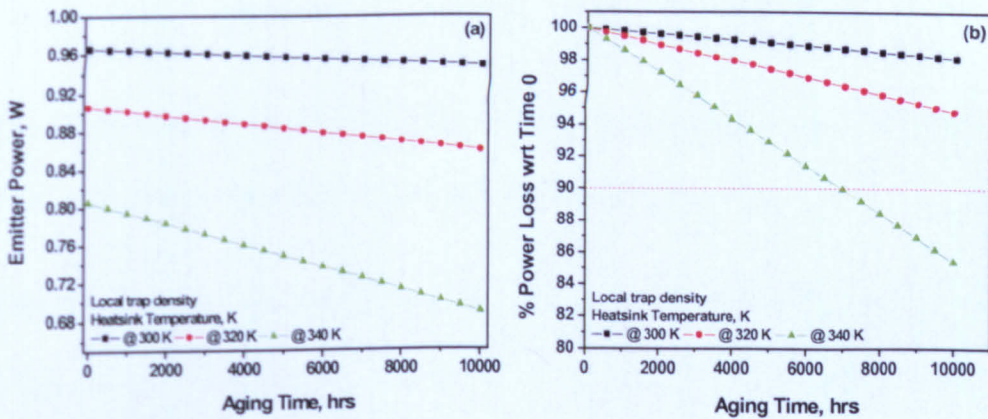


Fig. 6.3 Graphs with local trap density for: a) emitter power versus aging time, (b) % power loss with respect to the unaged emitter.

In Fig. 6.3, power loss occurs with both increased aging time and temperature, as expected. However, the rate of degradation is slower than in case study 1 (power loss during aging). The lower degradation rate is due to the introduction of the local trap density in the model. Devices will survive the targeted 10,000 hour time

at both 300 K and 320 K. However, at 340 K, a 10% power loss occurs at ~7,000 hours.

Evolution of threshold current and efficiency

Fig. 6.4 shows that an increase in the heatsink temperature increases the threshold current and causes a device to degrade more rapidly during aging. There is also a marginal drop in efficiency with increased heatsink temperature.

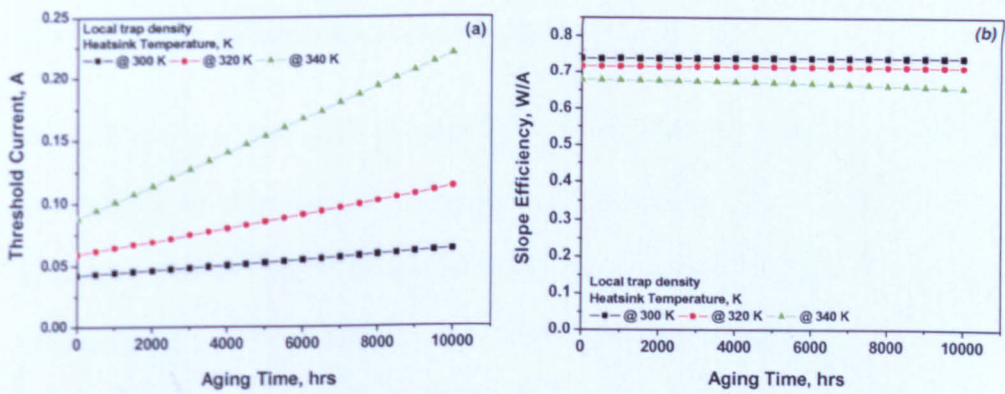


Fig. 6.4 Graphs of: (a) threshold current versus aging time, (b) slope efficiency versus aging time, for a device with a local trap density.

Table 6.1 shows the percentage changes in threshold current and slope efficiency during aging. Table 6.2.3.1 reveals that the increase in threshold current is accompanied by a minimal decrease in the slope efficiency.

Table 6.1 Changes in threshold current and slope efficiency during aging.

% Changes in threshold current and slope efficiency during aging						
Aging Time, Hours	300 K		320 K		340 K	
	Threshold Current, A	Slope Eff., W/A	Threshold Current, A	Slope Eff., W/A	Threshold Current, A	Slope Eff., W/A
1,000	5.20%	0.00%	9.10%	-0.06%	14.90%	-0.23%
5,000	24.90%	-0.07%	45.50%	-0.34%	74.90%	-1.36%
10,000	49.20%	-0.20%	91.60%	-0.75%	151.10%	-3.39%

QW temperature distributions before aging

Temperature continues to be an issue in laser technology. For this reason, the QW temperature distributions are investigated before aging i.e., time zero, with the following results. The QW temperature had a minimum of ~ 305 K and a maximum of ~ 355 K resulting in a QW temperature range of ~ 50 K for a heatsink temperature of 300 K. For a heatsink temperature of 320 K, the QW temperature had a minimum of ~ 355 K and a maximum of ~ 380 K resulting in a QW temperature range of ~ 55 K. Finally, for a heatsink temperature of 340 K, the QW temperature had a minimum of ~ 350 K and a maximum of ~ 410 K resulting in a QW temperature range of ~ 60 K.

Evolution of effects on devices as heatsink temperature and aging times are increased

A comparison was also made between aging before and after the emulation at various aging times (Table 6.2). The effect of temperature on devices show the maximum changes in the QW temperature during aging at various heatsink

temperatures with respect to an unaged device. The evolution of the effect is shown in Table 6.2 as both heatsink temperature and aging times are increased.

Table 6.2 Maximum changes in the QW temperature during aging (K) with respect to time zero.

Maximum changes in QW temperature during aging (K)			
T _{Heatsink} , (K)	500 hours	5,000 hours	10,000 hours
300	0.09	0.85	1.75
320	0.20	2.10	4.25
340	0.50	5.00	10.00

6.2.4 Case study 3 (multiple emitters i.e. bars) – uniform QW trap density

Two multiple emitter scenarios were investigated in this case study, using two different frown shaped heatsink temperature profiles. An eight (8) emitter bar was investigated with maximum central emitter temperatures of 315 K and 330 K, as shown in Figs. 6.5a and b.

One of the most important attributes of *Barlase* is the ability to extract information about the individual emitters in a laser bar. Specifically, the current passing through each emitter is known and the corresponding power emitted by each emitter is also known. It is therefore possible to see the correlation between power loss and temperature for each emitter in the bar.

The third case study was performed to investigate and compare bars using an aging model where the QW trap density is uniform. The aging was emulated for a constant current of 10 A, and aging times up to 10,000 hours. The parameter varied was the heatsink temperature, assuming the initial frown shaped

temperature profiles discussed above. The frown shaped temperature profile is commonly observed for many practical laser bars [5]. Fig. 6.5 show the power loss during aging at the bar level and Fig. 6.6 show the power loss during aging at the emitter level.

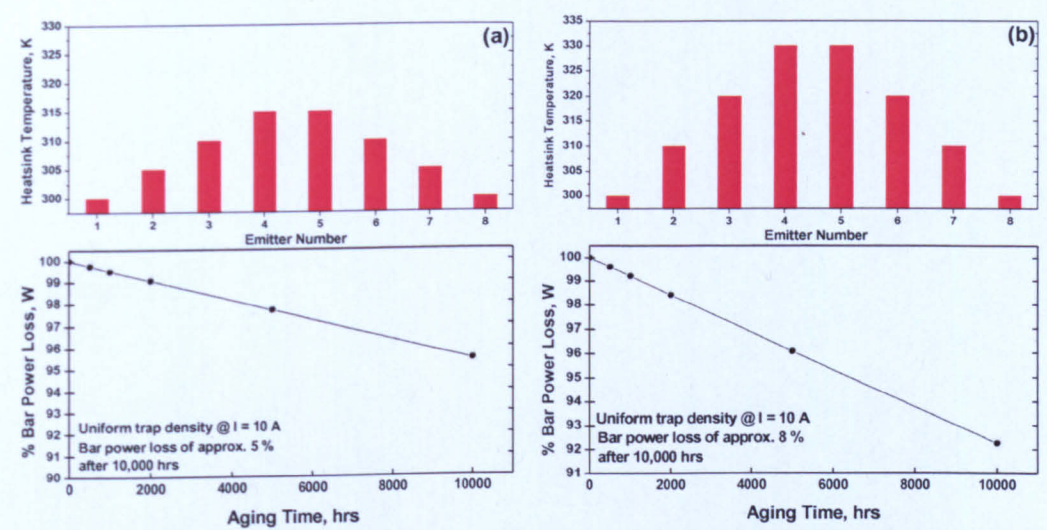


Fig. 6.5 (a) Bar power loss at maximum $T_{Heatsink} = 315\text{ K}$, (b) bar power loss at maximum $T_{Heatsink} = 330\text{ K}$ and their equivalent temperature distributions.

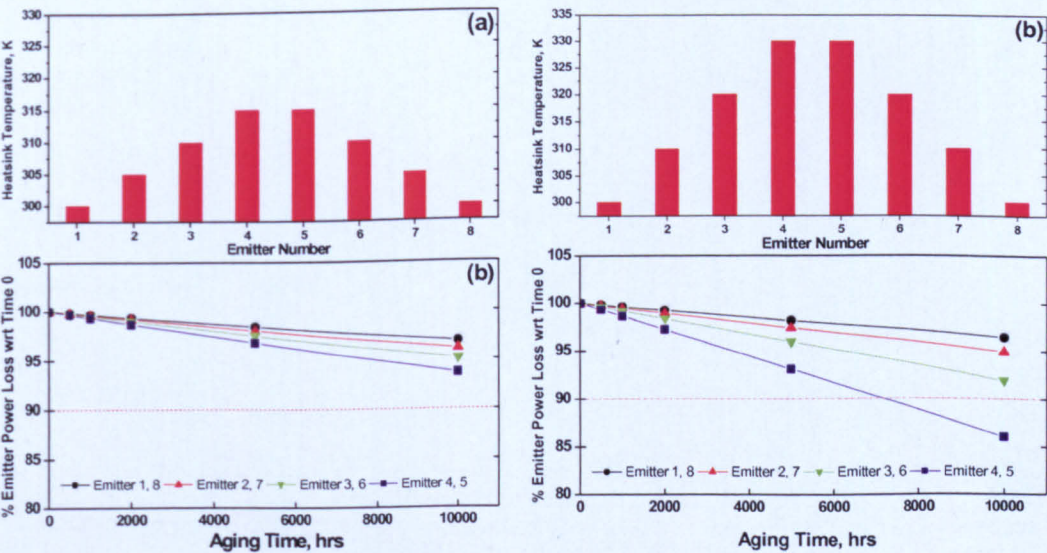


Fig. 6.6 (a) Emitter power losses at maximum $T_{Heatsink} = 315\text{ K}$, (b) emitter power losses at maximum $T_{Heatsink} = 330\text{ K}$.

6.2.5 Case study 4 (multiple emitters i.e. bars) – local QW trap density

The fourth case study investigates the aging of a bar using an aging model where the QW trap density increases according to the local QW temperature. The aging was effected at a constant current of 10 A, with aging time up to 10,000 hours.

An eight (8) emitter bar was investigated for a frown shaped heatsink temperature profile with maximum central temperature of 330 K as shown in Fig. 6.7. Figs. 6.7a and b show the bar power loss and percentage bar power loss with respect to the unaged bar.

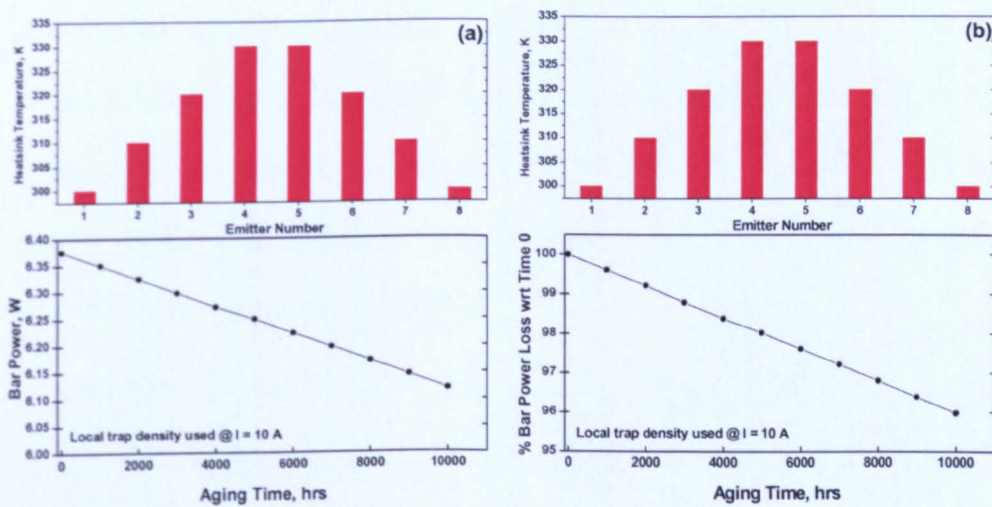


Fig. 6.7 (a) Bar power loss at maximum $T_{\text{Heatsink}} = 330 \text{ K}$, (b) percentage bar power loss at maximum $T_{\text{Heatsink}} = 330 \text{ K}$.

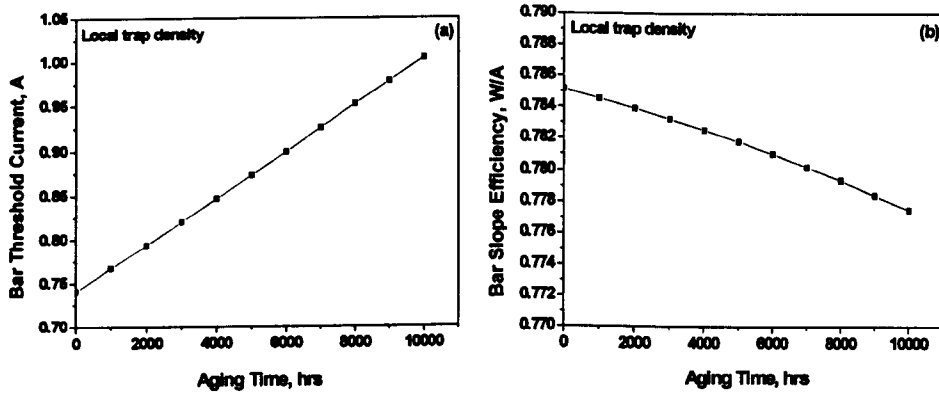


Fig. 6.8 (a) Bar threshold current, and (b) bar slope efficiency at maximum $T_{\text{Heatsink}} = 330 \text{ K}$.

From the results obtained from the comparison of the uniform trap density as against the spatially variable trap density, exaggerated degradation emulation is observed for the case of the uniform trap density. The bar power loss of 4% after 10,000 hours (a factor of 2 higher was predicted with the uniform trap density model) is more consistent with experimental results. In this case, the bar threshold current increased by 35% (Fig. 6.8a), but the bar slope efficiency decreased by only <1% (Fig. 6.8b) after 10,000 hours.

It is worth noting that the hottest emitters draw the most current especially as aging progresses (red circle in Fig. 6.9b for emitters 4 and 5). However, the cooler emitters maintained their current levels even as aging progressed (red circle in Fig. 6.9b for emitters 1 and 8).

Fig. 6.9 shows just small changes of +0.77% and -0.89% in the current distributions between the individual emitters, consistent with the constant current mode of operation.

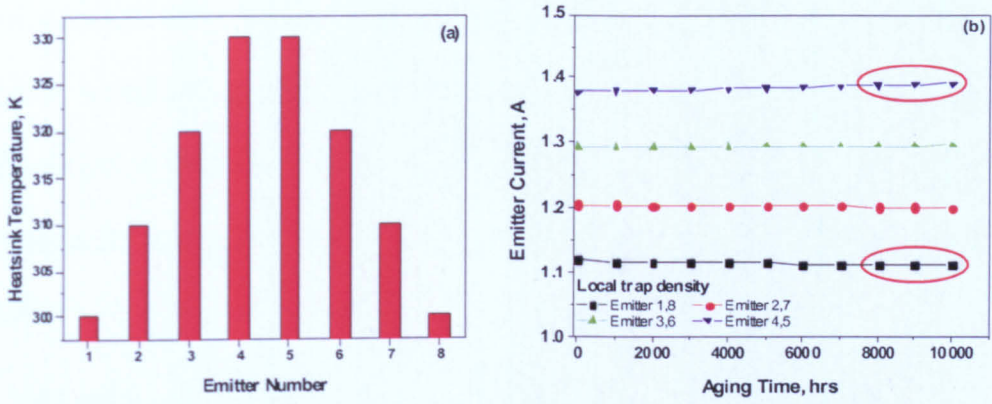


Fig. 6.9 (a) QW temperature profile at maximum $T_{Heatsink} = 330$ K, (b) emitter current at maximum $T_{Heatsink} = 330$ K.

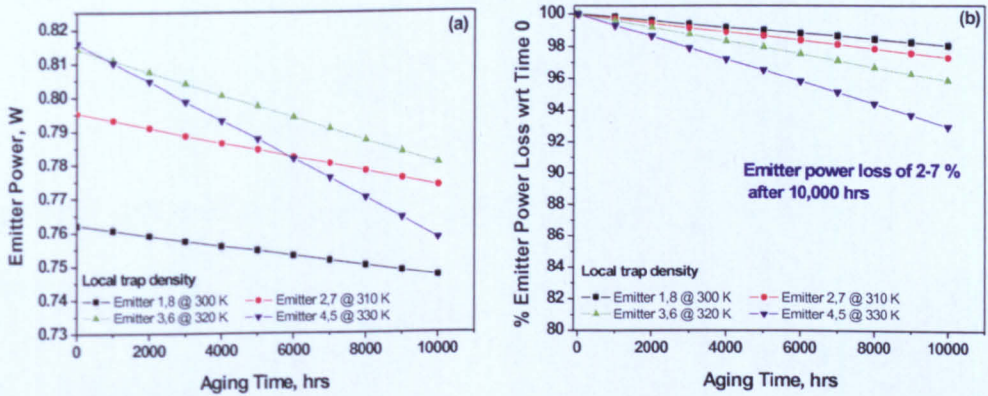


Fig. 6.10 (a) Emitter powers losses at maximum $T_{Heatsink} = 330$ K, (b) percentage emitter power at maximum $T_{Heatsink} = 330$ K.

However, the changes in the emitter power distributions (Fig. 6.10) are more dramatic, with current competition affecting the relative power losses. The power losses for emitters at higher temperatures, say 330 K, is more rapid, intersecting the temperature profiles of emitters at 320 K and 310 K at about 500 hours and 6,000 hours, respectively. It will also intersect the 300 K profile by extrapolation.

The extraction of the threshold current and the slope efficiency at the emitter level (Fig. 6.10) for a heatsink maximum temperature profile of Fig. 6.9a show a

similar trend with the bar level scenario in Fig. 6.8. After 10,000 hours, the emitter threshold currents increased by 14 – 61%, while the emitter slope efficiencies decreased by 0.10 – 2.25%. After 10,000 hours, the bar threshold current went up by 35% while the bar slope efficiency went down by <1% (Fig. 6.11).

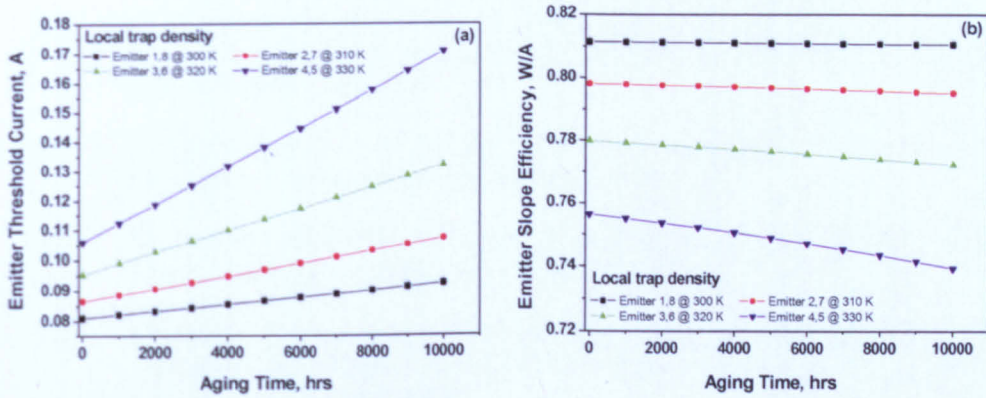


Fig. 6.11 (a) Emitter threshold current and (b) emitter slope efficiency at maximum $T_{\text{Heatsink}} = 330 \text{ K}$.

6.3 Conclusion

The use of *Barlase* has been demonstrated with the aid of a LabView control interface. This has made it possible to perform simulations and degradation emulation of multiple emitters/bars. *Speclase* on its own was designed to operate for a single emitter [6], without the possibility of aging the device. This work developed a means of integrating *Speclase* to work for a bar (*Barlase*), as described in chapter 5.

The simulations performed in this chapter were based on a theoretical tapered laser. The objective was to demonstrate that *Speclase* is successfully synchronised with *Barlase* and able to examine some degradation processes in lasers.

In the next chapter, an attempt is made to emulate the degradation of a real laser bar. This bar is the 975 nm tapered laser bar used in study 2 of chapter 4 in this thesis. Using the P-I experimental data at the unaged level and assuming identical emitters in the bar, the laser is calibrated and used for the emulation.

References

- [1] C. K. Amuzuvi, J. J. Lim, S. Bull, and E. C. Larkins, "Investigating a hypothetical single emitter/bar using a laser diode emulation tool," *in preparation to be submitted*, 2010.
- [2] H. C. Casey and M. B. Panish, *Heterostructure Lasers, Part A: Fundamental Principles*: Academic Press Ltd.; London, 1978.
- [3] M. Fukuda, *Reliability and Degradation of Semiconductor Lasers and LEDs*: Artech House, Boston, first citation in article, 1991.
- [4] K. Hausler, U. Zeimer, B. Sumpf, G. Erbert, and G. Trankle, "Degradation model analysis of laser diodes," *Journal of Materials Science-Materials in Electronics*, vol. 19, pp. S160-S164, 2008.
- [5] C. K. Amuzuvi, S. Bull, J. W. Tomm, J. Nagle, E. C. Larkins, B. Sumpf, G. Erbert, N. Michel, and M. Krakowski, "The impact of temperature and packaging-induced strain on current competition and emitter power in laser bars," *Applied Physics Letter*, *in preparation to be submitted*, 2010.
- [6] C. K. Amuzuvi, J. J. Lim, S. Bull, and E. C. Larkins, "Describing the state-of-the-art laser diode emulation tool," *in preparation to be submitted*, 2010.

Chapter 7

Emulation of the Degradation of a Calibrated 975 nm High Power Tapered Laser Bars

The previous chapter demonstrated how *Barlase* can be used to investigate the degradation of lasers at both the emitter and bar levels [1]. Hypothetical (uncalibrated) laser bars were used to demonstrate the operation of *Barlase* and to better understand the interactions of the emitters within a bar [2]. In this chapter, the first attempt is made to emulate the degradation of real bars, whose performance and degradation was characterised in detail using experimental by-emitter degradation analysis and reported in chapter 4 of this thesis.

The simulation parameters for the constituent laser diodes must first be calibrated to achieve reasonable agreement with the experimental P-I curves of unaged emitters. (This assumes that the bar is made with identical emitters.) The calibrated simulation parameters will then be used to emulate the degradation of the laser.

The aim of this chapter is to demonstrate that *Barlase* really works not only for a fictitious laser bar as demonstrated in the previous chapters, but for a real (calibrated) tapered laser bar as well.

7.1 Structure of the Device Being Studied: 975 nm Tapered Bars Fabricated by Alcatel-Thales III-V Lab.

The device studied is a 16 emitter tapered laser bar with each group of 4 mini-array emitters. The emulation on the bar are performed on one (1) emitter and then scaled up to 4 emitters. Data from the by-emitter studies experiments, presented in chapter 4 (temperature and NIR electroluminescence from defects) extracted at the bar level are used to derive inputs for the simulations. (These data are used because they are the information we know about the bars.) Additional information is available from the apparent threshold current and apparent slope efficiencies of the emitters. The details of the laser structure are given in Fig. 7.1.

The emulated structure used is a 975 nm narrow-angle ($<1^\circ$) tapered laser. The total length is 2.4 mm, consisting of a 200 μm long ridge waveguide and a 2200 μm long tapered amplifier. The front and rear facet reflectivities were 3% and 90%, respectively. The ‘standard’ simulation of this structure assumes a heatsink temperature of 300 K and a QW trap density of $2 \times 10^{15} \text{ cm}^{-3}$. All of the simulations in the following sections use this structure.

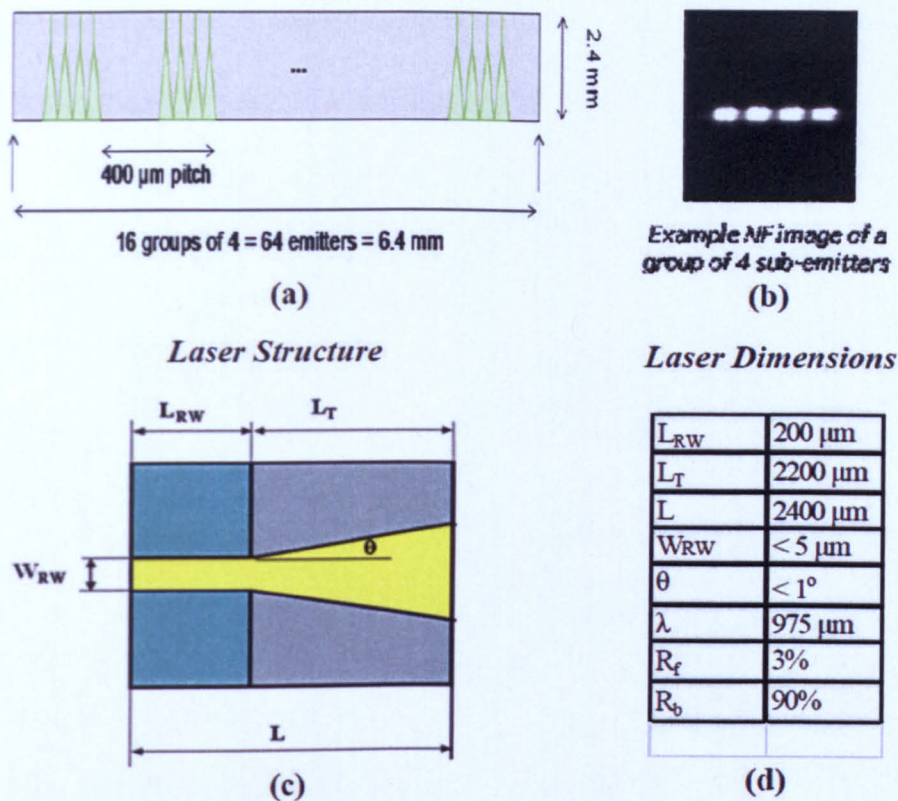


Fig. 7.1 (a) Structure of the investigated laser bar: 16 emitter tapered laser bar with each group of 4 mini-array emitters, (b) NF image of 4 sub-emitter groups, (c) taper structure dimensions and (d) bar dimensions.

7.1.1 Calibration of the laser

The calibration of the 975 nm tapered laser bar involves the determination of a few device parameters which cannot be determined *a priori*. These include: (1) the trap density N_T , (2) the hole absorption cross section, and (3) the QW/waveguide composition. These are determined by performing numerous single emitter simulations and comparing them with that of an “effective” single emitter from an unaged bar. The simulated P-I curves are matched with experimental P-I curves of unaged emitters until reasonable agreement is achieved

between them (Fig. 7.2) [3]. The emulation of degradation is then performed based on the performances of the individual emitters within the bar.

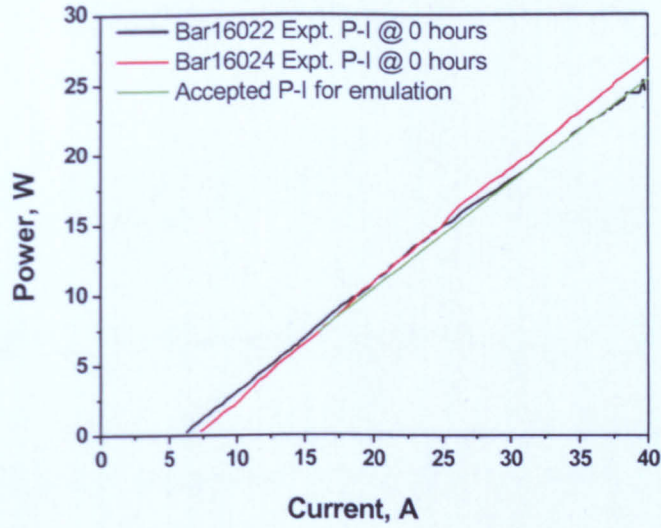


Fig. 7.2 Graphs of the experimental and calibrated (accepted P-I for emulation) laser bar at 0 hours.

7.2 Emulation of the Degradation of a Calibrated Single Emitter

The earlier simulations in chapters 5 and 6 showed that the emulation tool works for bars of emitters which can be simulated by *Speclase*. In this section, single emitter (SE) simulations are performed using the calibrated version using the local trap density model for the 975 nm tapered laser bar. Aging (degradation) of the SE are also emulated for aging times of 0, 500, 1,000, 5,000 and 10,000 hours at temperatures of 300 K, 320 K and 340 K, and at aging currents of 0.50 A, 0.60 A, 0.70 A and 0.80 A. These values were chosen based on the by-emitter experimental analysis values used for the 975 nm bars. Fig. 7.3a and 7.3b show the graphs of emitter output power (W) as a function of aging time (hours) for the three temperatures and power loss versus aging time, respectively. The power loss increases with increasing aging time and temperature.

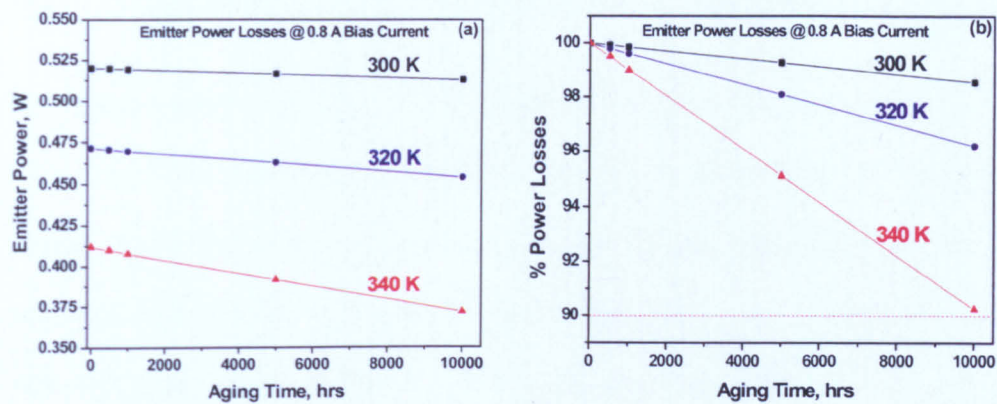


Fig. 7.3 Graphs of (a) emitter output power, (b) % power loss against aging time.

The emulated threshold currents and slope efficiencies for heatsink temperatures of 300 K, 320 K and 340 K are compared at aging times of 0, 500, 1000, 5000 and 10000 hours, respectively. These are shown in Table 7.1. Significant changes occur in the threshold current, but much smaller changes are observed in the slope efficiency. The effect of increasing temperature shows that, the lifetime of HPLDs is intimately linked to operating temperature which ultimately leads to the increase in threshold current.

Table 7.1 Comparison of apparent threshold and slope efficiency.

Aging Time, hours	$T_{\text{heatsink}} = 300 \text{ K}$		$T_{\text{heatsink}} = 320 \text{ K}$		$T_{\text{heatsink}} = 340 \text{ K}$	
	Threshold Current	Slope Efficiency	Threshold Current	Slope Efficiency	Threshold Current	Slope Efficiency
0	0.080 A	0.724 W/A	0.086 A	0.663 W/A	0.109 A	0.598 W/A
500	+0.38 %	-0.03 %	+1.18 %	-0.05 %	+2.40 %	-0.11 %
1,000	+0.76 %	-0.06 %	+2.20 %	-0.12 %	+4.84 %	-0.21 %
5,000	+3.74 %	-0.32 %	+9.48 %	-0.82 %	+24.86 %	-0.96 %
10,000	+7.67 %	-0.59 %	+21.63 %	-1.21 %	+50.73 %	-1.86 %

7.3 Multiple Emitter Degradation Emulation of the Calibrated Bar

A multiple emitter scenario with 8 (eight) emitters was also examined for the calibrated 975 nm tapered laser bar. This was done to demonstrate how the aging model works for a bar, considering also the thermal cross-talk between the emitters. This also shows the role of current competition in bar degradation and the behaviour of the individual emitters during aging. The bar used in this scenario had eight 975 nm tapered emitters connected in parallel. The individual emitters were identical to those used in the SE emulation scenario. The condition used for the emulation of this test scenario was a non-uniform (frown shaped) heatsink temperature distribution. Fig. 7.4a and the table (Fig. 7.4b) show the heatsink temperature profile and the values assigned to each emitter in the bar.

As a test scenario for a real bar degradation, three degradation steps are performed at 0, 5,000 and 10,000 hours at a constant bar current of 6 A. This means that the aging was emulated at a current of 6 A after each of the three degradation steps.

The corresponding bar degradation was emulated for aging times up to 10,000 hours at a constant bar current of 6 A. Figs. 7.5a and 7.5b show the output power and current distributions across the bar with respect to emitter numbers.

Calculated bar power losses of 2% and 4% were recorded at 5000 hours and 10000 hours, respectively. The graphs show that the degradation is faster at the middle of the bar, which corresponds to the hotter emitters (as expected). The reason for this has already been explained in section 4.4.3. As aging progresses and degradation increases, the output power drops at the middle of the bar (Fig. 7.5a).

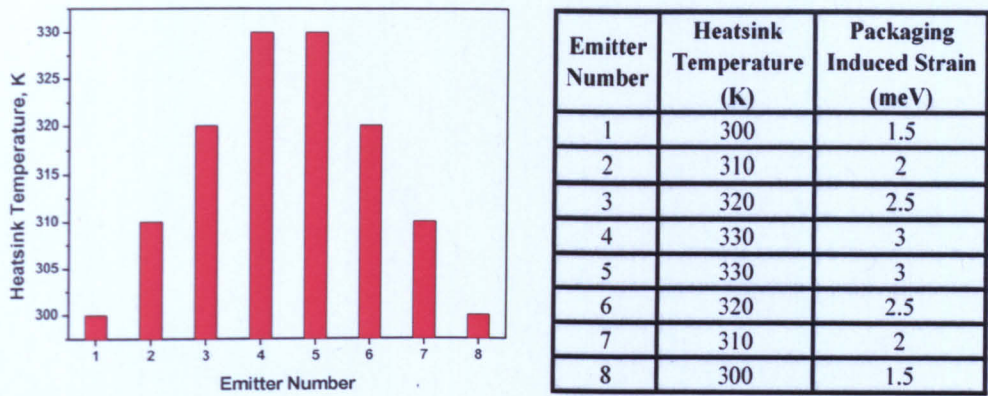


Fig. 7.4 *QW trap densities (a) and table showing the values of QW trap densities assigned to each emitter in the bar (b).*

The next test scenario considered a non-uniform (frown shaped) packaging-induced strain profile with higher strain in the middle of the bar (profile similar to Fig. 7.4a, with strain values in Fig. 7.4b). The inclusion of strain in the emulation tool was not straight forward. It involved changing the lattice constant in *Speclase* and generating a new gain table and updating it after every aging step. This was done in consultation with Dr Jun Lim who developed the *Speclase* tool.

Simulations were performed to verify the effect of strain on a bar under “isothermal”, “thermal” and “thermal + varied heatsink temperature” conditions. In order to approximately account for thermal cross-talk effects, different heatsink temperatures were used for each emitter. (Note: Isothermal condition is a constant-temperature process, accompanied by heat addition or removal from the system at a rate just adequate to maintain the constant temperature. Under thermal conditions, self-heating effects were simulated within each emitter, but thermal cross-talk between emitters is not included.)

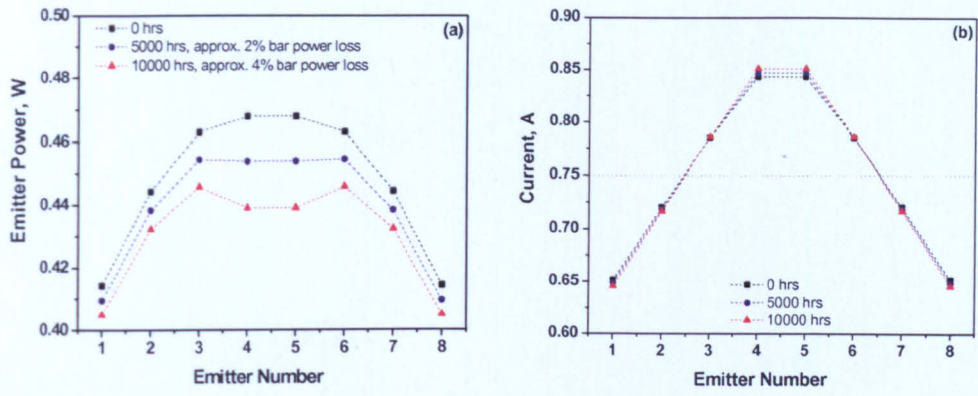


Fig. 7.5 Degradation of a bar using the non-uniform temperature profile and values in Fig. 7.4: (a) Emitter power levels and (b) emitter current competition.

The emulation was performed at a bar current of 6 A for an unaged bar. Figs. 7.6a, b, and c show the output power, current of the strained QW temperature distributions across the bar. All of the conditions used yielded different results. This shows that the effect of strain is important in the operation of high power laser bars. The QW bandgap energy was increased between 1.5 meV to 3.0 meV as shown in Fig. 7.4b.

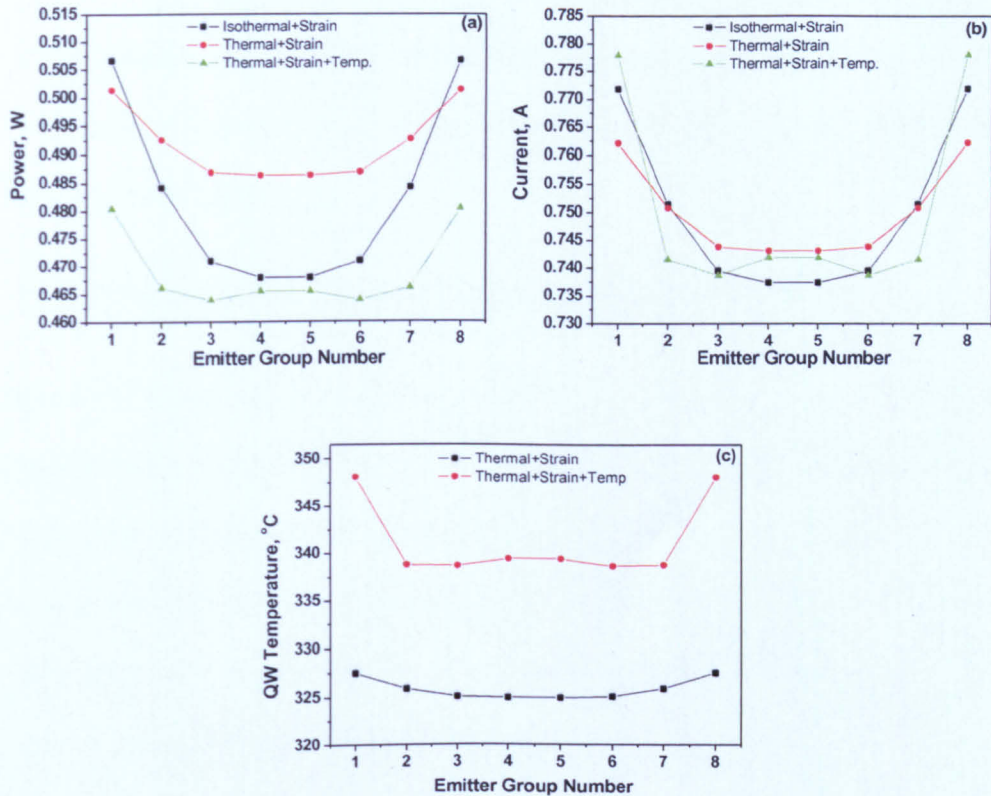


Fig. 7.6 Graphs of: (a) output power, (b) current and (c) QW temperature versus emitter group number at zero aging time (view legend in the graphs for the conditions simulated).

7.4 By-Emitter Emulation of Real Bars (975 nm Laser Bars with 16 Tapered Emitters)

In this section, a first attempt was made to emulate the observed degradation of the actual laser bars discussed in chapter 4 (study 2). Prior to attempting to emulate the degradation of a bar, cognisance was taken of the experimental results attained before, during and after the measurement of the devices. For instance, microscopic photographs were taken before and after measurements to identify damaged emitters. (Some of these pictures are shown in chapter 4.) Also, some measurement results were used to tailor the initial simulation parameters of the

emitters for the emulation of the degradation process. The temperature and the NIR EL signal (defect) profiles for the bars at an aging time of 0 hrs (i.e. unaged) were used as initial input parameters, since they both play a significant role in the degradation of the laser bar.

7.5 Presentation and Analysis of Simulation Results at Time 0

By-emitter measurements were performed on all 4 bars, as the experimental results show in chapter 4. The emulation on the other hand, is only carried out for 2 out of the 4 bars, because 3 of the bars showed similar characteristics, while one is physically damaged at the ends of the bar. Therefore, the 2 bars used for the emulations are one from the 3 which showed similar characteristics (bar 16024) and the one which had damaged ends (bar 16022).

7.5.1 Emulation results (unaged) of bar 16022 (bar physically damaged at two ends)

This bar offers the opportunity to emulate the degradation of a bar which is physically damaged at both ends of the bar, as shown earlier in chapter 4. The by-emitter degradation analysis performed on this bar showed a considerable decrease in power at the ends of the bar (Figs. 4.11 and 4.30), corresponding to emitters number 1 and 16, respectively.

The temperature distribution of the bar (Fig. 7.7a), also gave credence to the considerable drop in power in the end emitters. The poor performances of the two end emitters correlate well with the elevated temperatures in the edge emitter groups (Fig. 7.7a). There was also a higher level of NIR defect luminescence from emitter group number 4. There was some correspondence between the lasing

intensity and the NIR defect EL (i.e. stronger NIR defect EL in the lower power emitters).

When examined carefully, the poor performing emitter groups reveal a correlation with the damage observed by optical microscopy in Fig. 4.12. Weaker emitters within an emitter group are observed by NF imaging for example in Figs. 4.11 and 4.34. Fig. 7.7a and 7.7b show the temperature and NIR defect EL profiles across bar 16022. Also the NIR electroluminescence from defects (which has an inverse relationship with lifetime) was converted into lifetime as an input for the simulation (Fig. 7.7b). The lifetime is calculated, so that the average lifetime is equal to the carrier lifetime of the single emitter used in the calibration of the simulations. It is calculated using the equation $N_t = 1/(k\tau)$, where N_t is the trap density, k is a constant and τ is the lifetime.

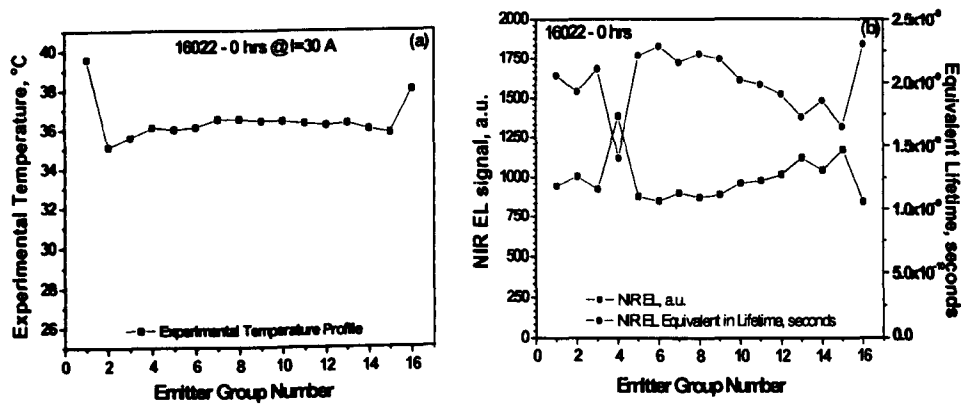


Fig. 7.7 Emulation inputs: (a) Experimental temperature profile against emitter group number in degrees Celsius, (b) NIR EL signal (a.u.) and equivalent lifetime(s) versus emitter number.

The emulation results for the unaged bar (time = 0 hrs) are shown in the figures below for comparison of the experimental and simulated results. The initial results

yielded the distributions of output power, QW temperature and current as shown in Figs. 7.8a, b and c, respectively. The simulated output power in Fig. 7.8a does not correspond well with the experimental results - perhaps due to the physical damage of the end emitters observed by optical microscopy. The correlation between the experimental and simulated temperature profiles (Fig. 7.8b) is better (except for the edge emitters, which are known to be damaged). The profiles are similar in shape, but the magnitudes differ. This discrepancy is due to the fact that the simulated temperature is the QW temperature at the facet, whereas the measured temperature is a spatial average (spatial resolution of camera $\sim 30\ \mu\text{m}$) of the bulk temperature.

The initial simulation result for the output power distribution at time 0 in Fig. 7.8a did not match the measured result – especially at the ends of the bar. More specifically, the simulated power levels at the ends of the bar increase despite the damage i.e. the result of the emulation reveals *the following*:

- high temperature observed for the damaged end emitters
- higher, rather than lower powers observed for damaged end emitters.

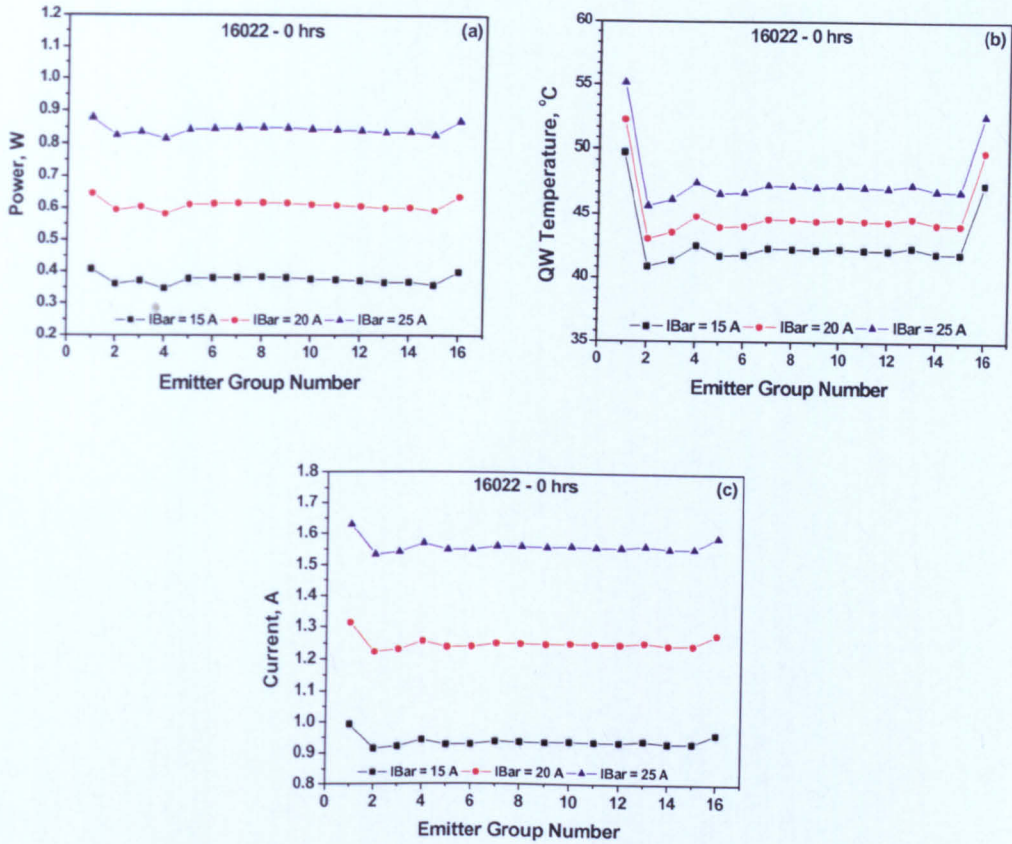


Fig. 7.8 Bar currents of 15 A, 20 A and 25 A: (a) Power, (b) QW temperature and (c) emitter current against emitter group numbers.

The explanation of higher powers at the end emitters even though their temperatures are higher is because those emitters drew more current due to their damaged nature and therefore gave off or emitted more power.

The emulation of the damaged ends of the bar could be improved by deliberately increasing the defect concentration of emitter group numbers 1 and 16 by some factor, say a factor of 3 to represent the damage observed at the facet. The result is a reduction in the power of the edge emitters, giving a better qualitative agreement with the experimental results. Fig. 7.9a shows the modified emulation results of power versus emitter group number for the unaged bar.

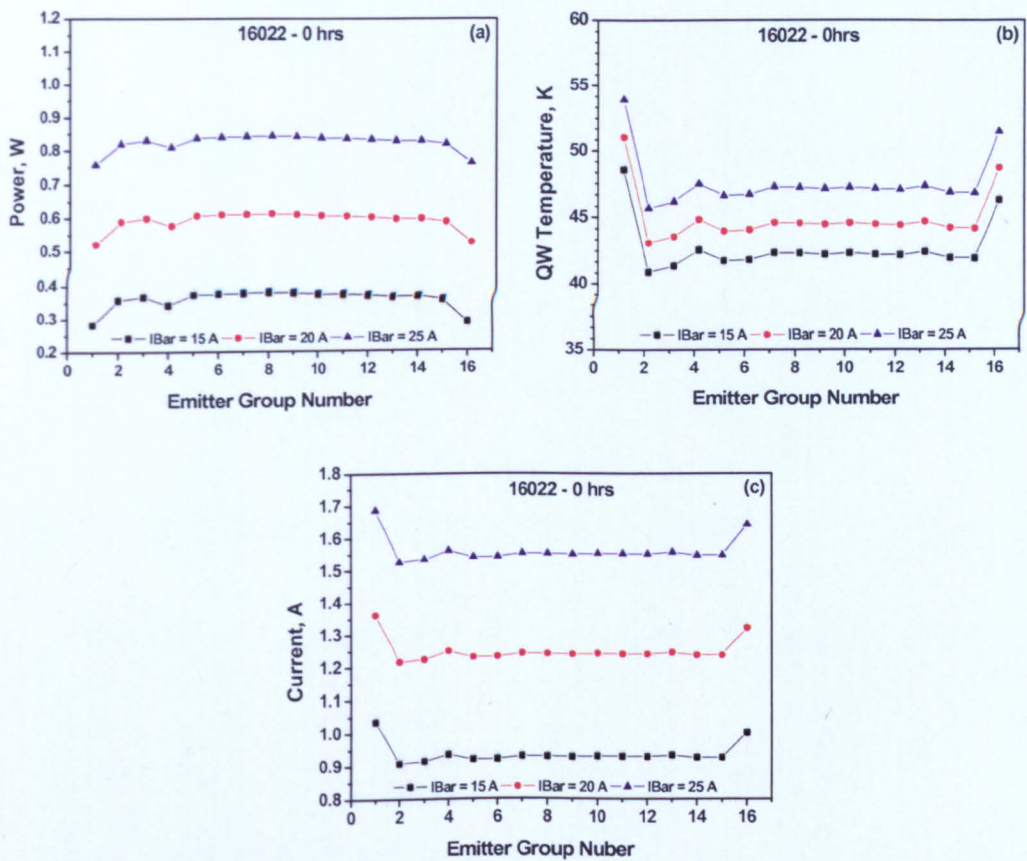


Fig. 7.9 Bar currents of 15 A, 20 A and 25 A: (a) Power, (b) QW temperature and (c) emitter current against emitter group numbers.

Fig. 7.10 compares the output power distributions for the initial emulation and for the case where the defect concentration was increased by a factor of 3. The modified emulation (defect level multiplied by 3 for the edge emitters) shows a drop in the output power distribution of the damaged edge emitters. Other scenarios were investigated for emulating the damaged emitters as follows:

- (1) adjusting the absorption of the mirror (by increasing the absorption), and
- (2) adjusting the reflectivity of the mirror (by reducing it).

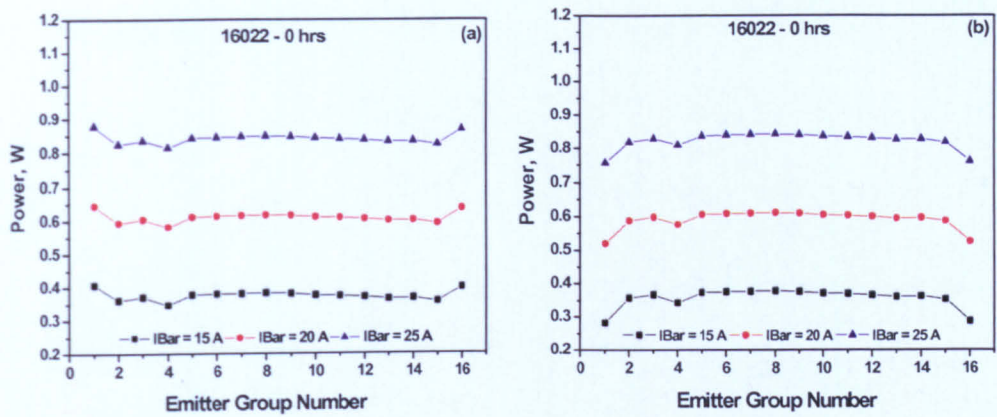


Fig. 7.10 (a) Initial emulation, (b) modified emulation.

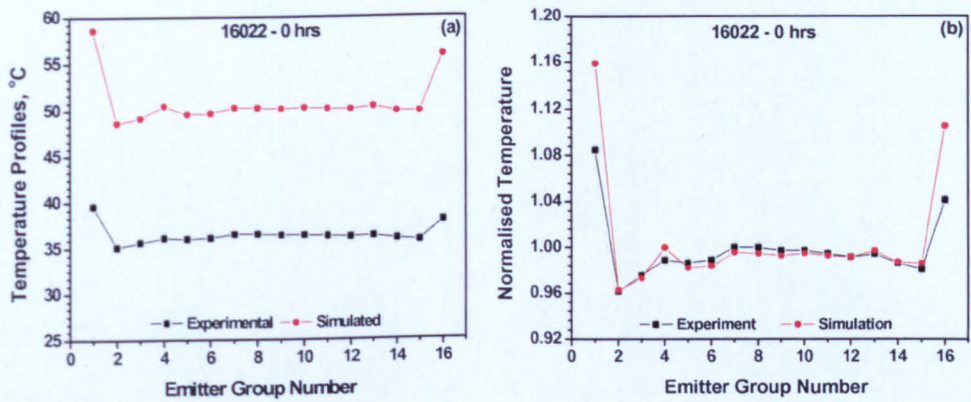


Fig. 7.11 Experimental and simulated temperature profiles of bar number 16022: (a) real temperature, (b) normalised temperature.

A comparison of the temperature distributions shows a similar shape between the experimental and simulated results (Fig. 7.11), but their absolute values differ. As explained earlier, this can be attributed to the limited spatial resolution of the camera ($\sim 30 \mu\text{m}$) which gives a lower (average) temperature. The temperature discrepancy of the damaged emitters suggests that a more complicated representation of the damage is required (e.g., the introduction of a global temperature solver) to address the problem.

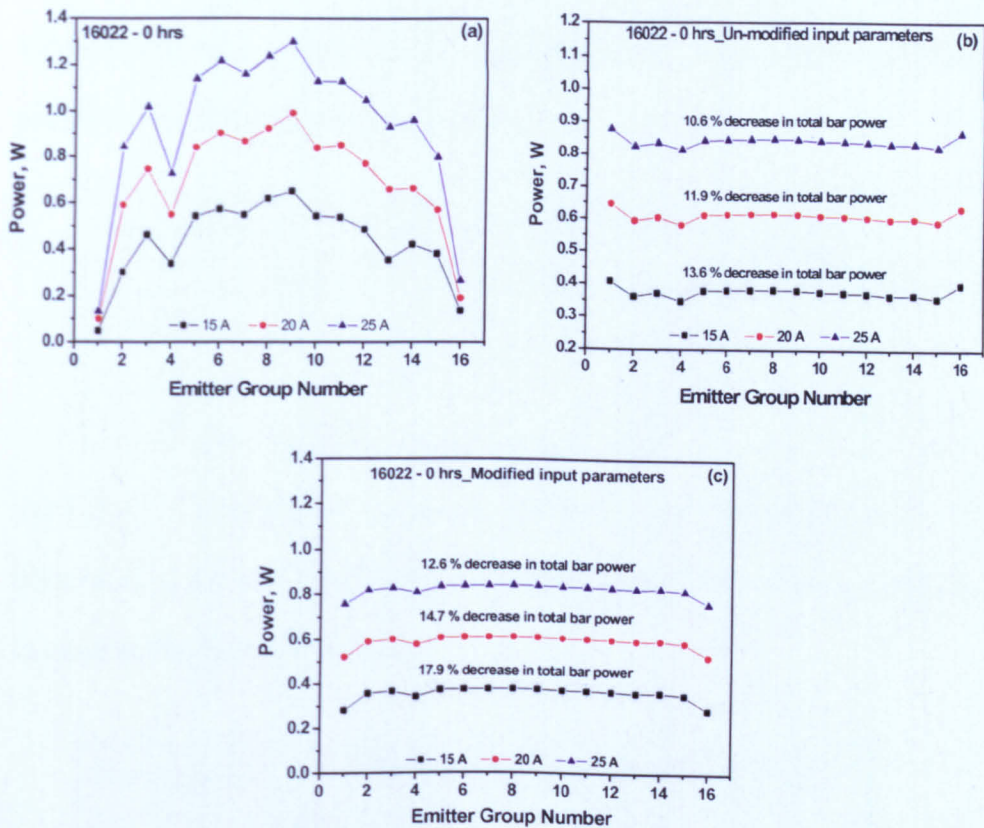


Fig. 7.12 Comparison of power distribution profiles of bar 16022: (a) experimental output power, (b) initial emulated output power without the modification of the input parameters, and (c) initial emulated output power with the modification of the input parameters by increasing defect levels by 3.

Table 7.2 Comparison of the experimental and emulated output power distributions for bar 16022 for the initial emulated output power without the modification of the input parameters.

Bar Current (A)	Total Bar Power (Initial input values)			
	Expt. (W)	Sim. (W)	Error (W)	Error (%)
15	6.95	6.01	0.94	13.6
20	11.09	9.77	1.32	11.9
25	15.06	13.47	1.60	10.6

Table 7.3 Comparison of the experimental and emulated output power distributions for bar 16022 with the modification of the input parameter by increasing the defect level by 3.

Bar Current (A)	Total Bar Power (Modified input values)			
	Expt. (W)	Sim. (W)	Error (W)	Error (%)
15	6.95	5.71	1.24	17.9
20	11.09	9.46	1.63	14.7
25	15.06	13.17	1.90	12.6

Strong disagreement is observed between the measured and the emulated power distribution profiles, when the initial input values extracted from the experimental results are used for the emulation. However, the percentage error between the total bar output power of the experimental result and the simulated result is 13.6 % for 15 A and 10.6 % for 25 A (Fig. 7.12b), as presented in Table 7.2. This deviation may not be too bad at this stage of the work. The percentage error is higher when a deliberate effort is made to bring down the output powers at the edge of the emitters, since we know they are damaged and could not have given off more power. The error in this case as shown in Fig. 7.12c is presented in Table 7.3.

The strong disagreement may also be attributed to the damage at the edges of the bar, affecting the emulated degradation behaviour. The power and temperature discrepancies in the damaged emitters suggest that a more complicated representation of the damage is required (e.g. the mirror facet reflectivity and absorption losses may need to be adjusted). Furthermore, the introduction of a global temperature solver may be needed to address this problem.

7.5.2 Emulation results (unaged) of bar 16024

This is the bar from the 3 which showed similar characteristics from the by-emitter analysis. The bar is therefore a representative bar for the 3 bars which showed similar characteristics.

The graphs showing the 16 emitter temperature profile and the NIR EL distribution profiles obtained from experiments are given in Fig. 7.7. The data from the experiments are used as a first step as inputs for the emulation to determine the degradation profile for the simulations.

Fig. 7.7b also shows the equivalent NIR EL which represents the defect levels in the bar. These defect levels are re-expressed as equivalent lifetimes and used as defect inputs for the simulation.

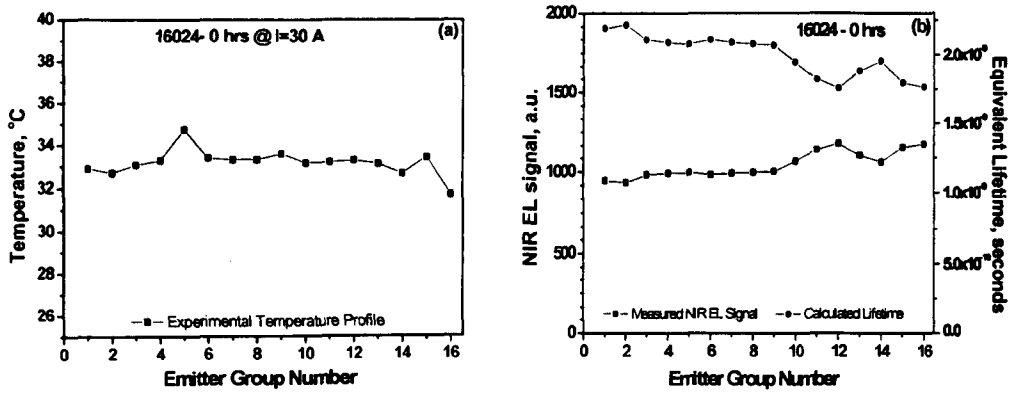


Fig. 7.13 Emulation inputs: (a) Experimental temperature profile against emitter group number in degrees celsius, (b) NIR EL signal (a.u.) and equivalent lifetime (s) against emitter group number.

The emulation results for the unaged bar (time = 0 hrs) are shown in the figures below for comparison of the experimental and emulated results. The initial results yielded the distributions of output power, QW temperature and current shown in Fig. 7.14a, b and c, respectively. The output power and current drawn increases with increasing trap density (Fig. 7.14a and c), as expected. Also, the higher currents in emitter group numbers 5 and 15 are as a result of their higher temperatures. The simulated output power in Fig. 7.14a does not correspond well with the experimental results. The correlation between the experimental and simulated temperature profiles (Fig. 7.8b) is better in this case. This is expected since the experimental temperature is set as input for the heatsink temperature profile. The agreement therefore must not be over-emphasised. The profiles are similar in shape, but their magnitudes differ. Once again, much of the discrepancy is due to the fact that the simulated temperature is the QW temperature, whereas the measured temperature is a spatial average (spatial resolution of camera ~30

μm) of the bulk temperature. There is good agreement between the normalised experimental and simulated temperature profiles, Fig. 7.15b.

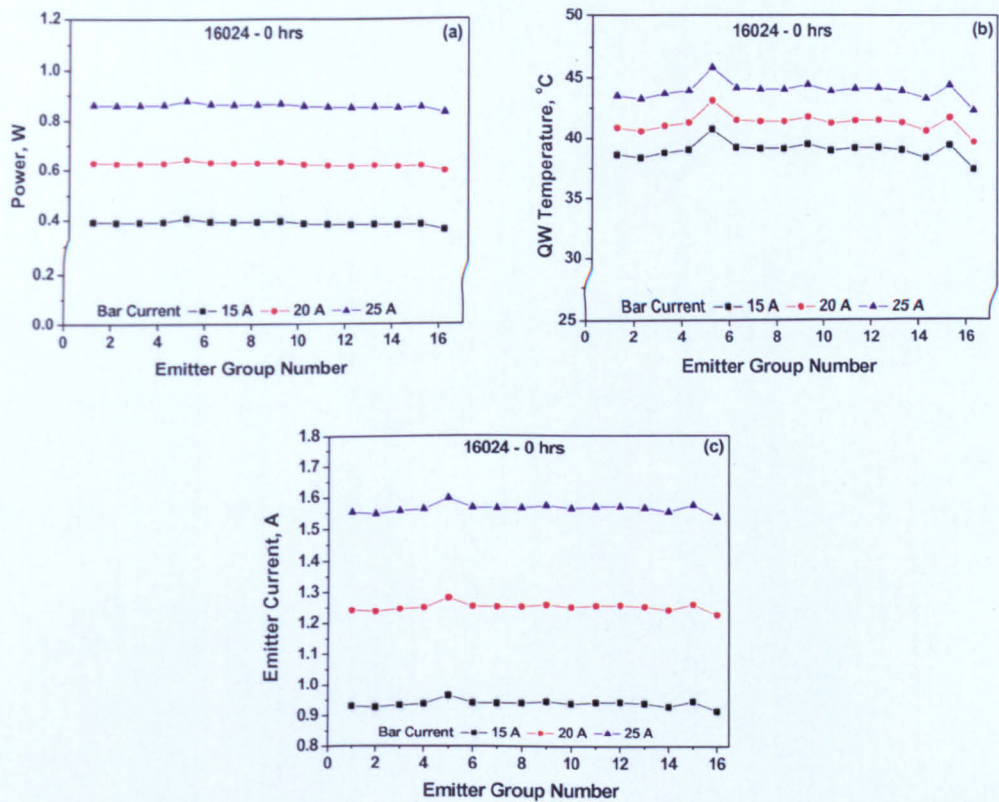


Fig. 7.14 Bar currents of 15 A, 20 A and 25 A: (a) Power, (b) QW temperature and (c) emitter current against emitter group numbers.

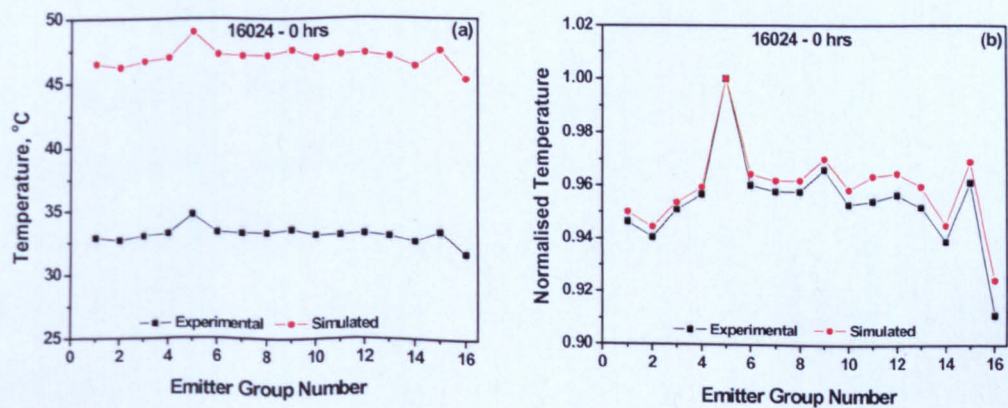


Fig. 7.15 Experimental and simulated temperature profiles of bar number 16024; (a) real temperature, (b) normalised temperature.

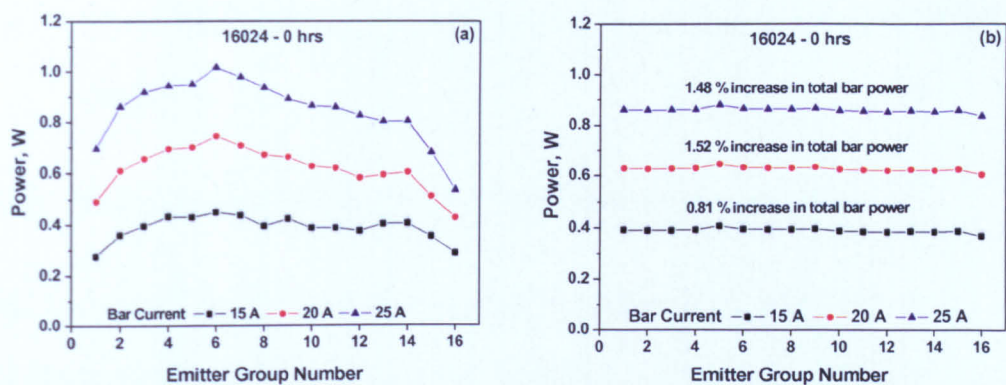


Fig. 7.16 Comparison of power distribution profiles of bar 16024: (a) experimental output power, (b) simulated output power.

Table 7.4 Comparison of the output power distributions for bar 16024.

Bar Current (A)	Total Bar Power			
	Expt. (W)	Sim. (W)	Error (W)	Error (%)
15	6.18	6.23	0.05	0.81
20	9.87	10.02	0.15	1.52
25	13.55	13.75	0.20	1.48

In this bar also, the normal frown shaped profile of the output power distribution is absent in the emulation results as observed in Fig. 7.16. As already explained, the agreement between the shapes of the experimental and simulated profiles is not great, but the total bar powers given in Fig. 7.16b are comparable and far closer than for bar 16022 (where physical damage was evident). The only reason that can be attributed to this is the absence of a noticeable damage to this bar through optical microscopy. See Table 7.4 above for the numerical comparisons of the output power distribution between the experimental and simulated results.

7.6 The Enhancement of the Emulation Tool Using A Global Thermal Solver

7.6.1 Bar emulation enhancement using a global thermal solver

The bar emulation model was enhanced by including a global thermal solver (GTS) to model the thermal crosstalk between emitters. The enhancement was once again carried out by Dr Jun Lim. This was done by *alternating between the electrical-optical solver applied for each of the emitters and the heat diffusion equation applied to the entire bar, including the substrate and heatsink*. The GTS solves the heat flow equation:

$$\text{div}(-\kappa(T) \text{grad } T) = H, \tag{7.1}$$

where κ is the thermal conductivity and H is the heat source distribution. The heat flow equation is also solved using Newton's method. Fig. 7.17 demonstrates the flow diagram of the bar emulation tool showing the electro-opto-thermal communication between the solvers.

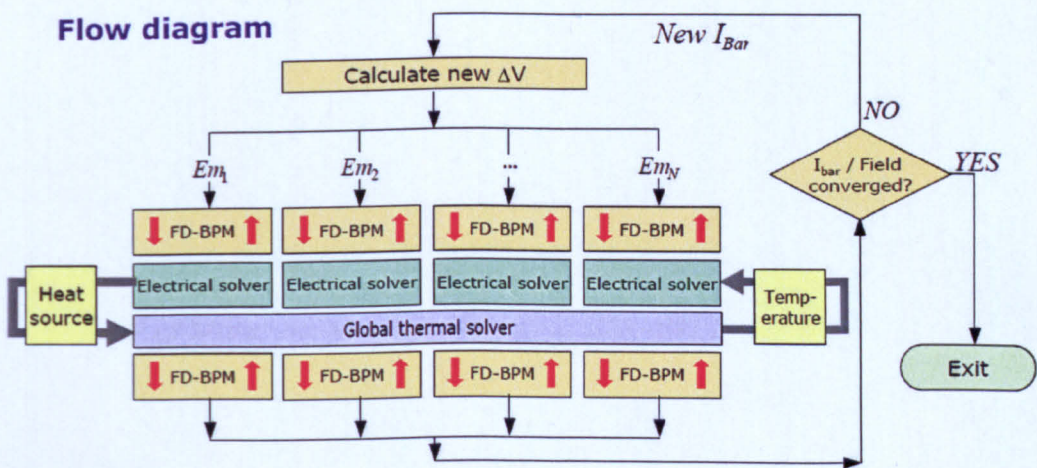


Fig. 7.17 Flow diagram of the global thermal solver showing the electro-optical communication in the bar emulation tool (courtesy of Dr Jun Lim).

The analysis is initiated at the rear facet and the optical field is propagated a distance to the next electrical slice, yielding a new photon density distribution. The new photon distribution is used to obtain the new carrier and potential distributions in the cavity. These new carrier profiles are used to update the lateral gain and refractive index distribution for the optical propagation to the next electrical slice [9].

The electrical solver also calculates the heat sources from the individual emitter simulations and supplies them to the global thermal solver. The heat sources include the Joule heating, nonradiative recombination heating, free carrier absorption heating and capture heating. The thermal distribution is updated by the GTS at each electro-thermal slice. The GTS calculates the temperature distribution for the entire 2D cross-section of the bar by solving the heat flow equation (Eq. 7.1). The global thermal distribution will be saved until the next instance of the electrical solver is called at that position. The thermal distribution is used to update all the variables in the electrical solver, which depend on temperature. These include the bandgap energy, the carrier mobilities, gain, recombination rates and carrier density.

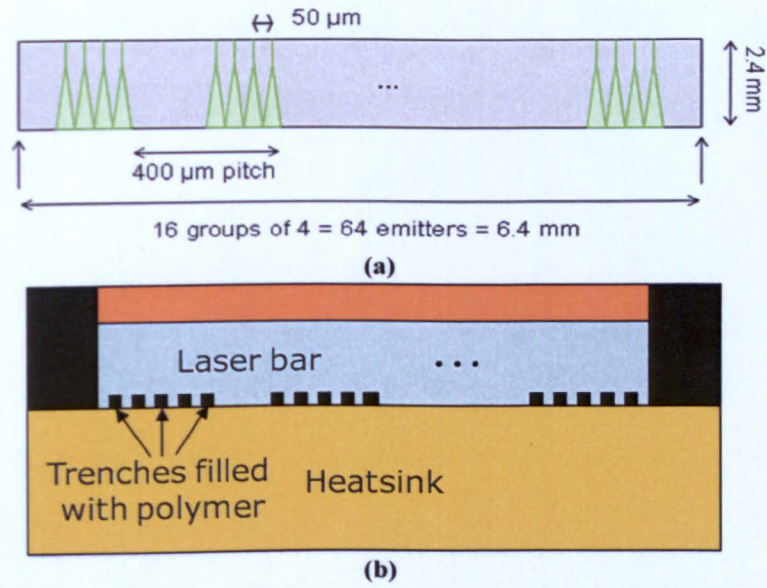


Fig. 7.18 (a) Top view of bar and (b) transverse cross section of the bar.

The thermal conductivities of the different materials in the bar are supplied to the GTS. These materials include the epitaxial structure, the heatsink, the metal contacts, and the polymer used to fill the etched trenches of the ridge-waveguide. Fig. 7.18 shows the top view and the transverse cross section of the 975 nm tapered laser bar. The Fox-Li iterations are performed for each emitter until convergence is achieved in the output power.

The operations of the GTS can be summed up as follows:

- For each emitter group, electro-optical simulations are performed on 1 emitter.
- The heat source distribution is calculated and supplied to the global thermal solver. Identical heat sources are used for each emitter in the group.

- The temperature distribution for the entire bar is solved and the average temperature for an emitter in the group is calculated and fed back to *Speclase*. The global thermal solver includes all 64 emitters.

7.6.2 Analysis and observations made

The GTS has definitely brought an improvement in the bar emulation model judging from the output current/power profiles in Fig. 7.19. Clearly defined frown shaped profiles are exhibited by the output current and power. However, the maximum variation in power is only about 0.75% which is very small compared to experimental results ~50 – 60%.

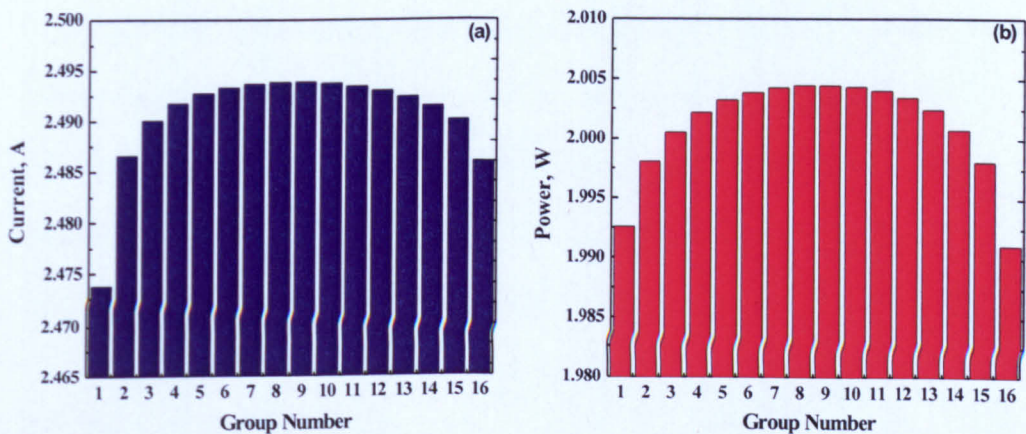


Fig. 7.19 (a) Current and (b) power versus emitter group numbers.

Higher currents were drawn and consequently more power emitted towards the center of the bar compared to the edge [1, 10]. The temperature at the front facet is higher and has a stronger curvature than at the back facet, which is expected (Fig. 7.20). This is because the front facet is the part of the laser array which draws more current and is more exposed to local heating of the laser mirrors [11]. The lifetime of high-quality GaAs-based lasers is often no longer limited by

failures in the bulk semiconductor, but rather by degradation processes in the susceptible mirror facets [12]. Light absorption (especially at the front facet), and the recombination current density increase with temperature, due to local thermal shrinkage of the bandgap energy. The bandgap shrinkage in turn, is caused by heat from the recombination current [13]. Thermal runaway in semiconductor lasers (which is as a result of facet heating) leads to catastrophic damage and occurs predominantly at the front facet. It is generally believed that thermal runaway is a positive feedback process initiated by heat created from intense nonradiative recombination [14]. This feedback, which occurs at certain output powers, leads to a rapid temperature increase that result in local melting of the active material and catastrophic damage of the laser front facet.

Various experiments, among them facet temperature measurements for ultra high-power operation have provided evidence that in arrays, the front facets are significantly affected by device operation mainly due to front facet heating [15]. Therefore, it is not surprising that the front facet (Fig. 7.20a) has a higher temperature than the back facet (Fig. 7.20b).

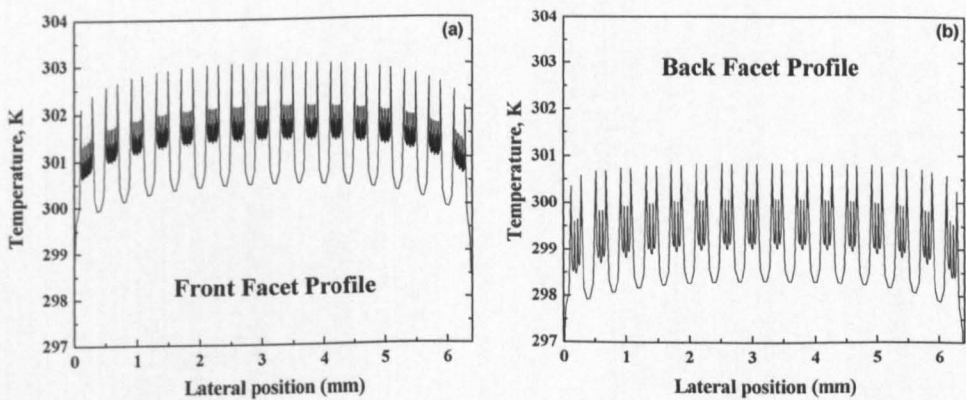


Fig. 7.20 (a) *Front facet temperature profile of the bar* and (b) *back facet temperature profile of the bar.*

The variations though, in the current and power (Fig. 7.19) is less pronounced than what pertains in the experimental results. The reasons for this could be investigated in further work on this thesis.

7.7 Summary

Emulation has been attempted for real bars, whose performance and degradation have been characterised in detail using by-emitter degradation analysis. Although the simulated output power profile did not correspond well with the experimental power profile, there was good agreement between the total output power of the bar. Better correlation was observed between the experimental and the simulated temperature profiles. This was expected since the experimental temperature was set as input for the heatsink temperature profile. The agreement therefore must not be over-emphasised. The bar emulation model was enhanced by including a global thermal solver to model effectively the thermal crosstalk between emitters. Emulations using this model showed a clearly defined frown shaped profile in the output current and power profiles but the change was minimal. As the emulation of laser bar degradation has not been attempted before, this work is still at a very early stage. Therefore, further work is needed to achieve better agreement in the output current/power profiles and to better the model.

References

- [1] C. K. Amuzuvi, S. Bull, J. J. Lim, S. Sujecki, and E. C. Larkins, "Numerical emulation of the degradation of 975nm high power tapered laser bars," in *High Power Diode Lasers and Systems Conference, Coventry (UK) 2009. HPD 2009*, 2009, pp. 1-2.
- [2] C. K. Amuzuvi, J. J. Lim, S. Bull, and E. C. Larkins, "Investigating a hypothetical single emitter/bar using a laser diode emulation tool," *in preparation to be submitted*, 2010.
- [3] J. J. Lim, S. Sujecki, L. Lang, Z. C. Zhang, D. Paboeuf, G. Pauliat, G. Lucas-Leclin, P. Georges, R. C. I. MacKenzie, P. Bream, S. Bull, K. H. Hasler, B. Sumpf, H. Wenzel, G. Erbert, B. Thestrup, P. M. Petersen, N. Michel, M. Krakowski, and E. C. Larkins, "Design and Simulation of Next-Generation High-Power, High-Brightness Laser Diodes," *IEEE Journal of Selected Topics in Quantum Electronics*, vol. 15, pp. 993-1008, May-Jun 2009.
- [4] S. Selberherr, *Analysis and Simulation of Semiconductor Devices*: Wien, New York: Springer, 1984.
- [5] S. Selberherr, "Device Modeling and Physics," *Physica Scripta*, vol. T35, pp. 293-298, 1991.
- [6] M. R. Pinto, C. S. Rafferty, and R. W. Dutton, *PISCES-II User's Manual*: Stanford Electron. Labs., Stanford, CA, 1984.
- [7] R. E. Bank, D. J. Rose, and W. Fichtner, "Numerical-methods for semiconductor-device simulation," *IEEE Transactions on Electron Devices*, vol. 30, pp. 1031-1041, 1983.
- [8] O. E. Akcasu, "Convergence properties of Newton's method for the solution of the semiconductor transport-equations and hybrid solution techniques for multidimensional simulation of VLSI devices," *Solid-State Electronics*, vol. 27, pp. 319-328, 1984.
- [9] S. Sujecki, L. Borruel, J. Wykes, P. Moreno, B. Sumpf, P. Sewell, H. Wenzel, T. A. Benson, G. Erbert, I. Esquivias, and E. C. Larkins, "Nonlinear properties of tapered laser cavities," *IEEE Journal of Selected Topics in Quantum Electronics*, vol. 9, pp. 823-834, May-Jun 2003.
- [10] C. K. Amuzuvi, S. Bull, J. W. Tamm, J. Nagle, E. C. Larkins, B. Sumpf, G. Erbert, N. Michel, and M. Krakowski, "The impact of temperature and packaging-induced strain on current competition and emitter power in laser bars," *Applied Physics Letter*, *in preparation to be submitted*, 2010.
- [11] G. Chen and C. L. Tien, "Facet heating of quantum-well lasers," *Journal of Applied Physics*, vol. 74, pp. 2167-2174, Aug 1993.
- [12] A. Moser, "Thermodynamics of facet damage in cleaved AlGaAs lasers," *Applied Physics Letters*, vol. 59, pp. 522-524, 1991.

- [13] R. Schatz and C. G. Bethea, "Steady-state model for facet heating leading to thermal runaway in semiconductor-lasers," *Journal of Applied Physics*, vol. 76, pp. 2509-2521, Aug 1994.
- [14] C. H. Henry, P. M. Petroff, R. A. Logan, and F. R. Merritt, "Catastrophic damage of $\text{Al}_x\text{Ga}_{1-x}\text{As}$ double-heterostructure laser material," *Journal of Applied Physics*, vol. 50, pp. 3721-3732, 1979.
- [15] J. W. Tomm, E. Thamm, A. Barwolff, T. Elsaesser, J. Luft, M. Baeumler, S. Mueller, W. Jantz, I. Rechenberg, and G. Erbert, "Facet degradation of high-power diode laser arrays," *Applied Physics a-Materials Science & Processing*, vol. 70, pp. 377-381, 2000.

Chapter 8

Conclusions and Further Study

Introduction

Four main contributions can be credited to this thesis. Firstly, the characterisation of the high power laser diode devices at The University of Nottingham before and after aging and the analysis of the corresponding results. Secondly, the developments of a software control interface in LabVIEW to control *Speclase*, which lead to the development of *Barlase*. Thirdly, the validation of *Barlase* using a hypothetical laser bar to emulate the experimentally-observed degradation behaviour, including the investigation of defects, temperature, packaging-induced stress and current competition between the emitters. The fourth contribution was the use of *Barlase* to emulate the degradation of a real bar. In this section, the main results and conclusions are summarised. The thesis concludes with suggestions for further work.

Experimental Assessment of Laser Degradation

Firstly, in depth characterisation studies were carried out on two different laser bars, captured as studies 1 and 2 in chapter 4 of this thesis.

Study 1: Red laser bars (FBH)

All three of these bars exhibited reasonably uniform power emission, with variations of ~6% between emitters – even after 700 hours of aging. A slightly frown-shaped profile was evident in the profile of the emitter powers across the unaged bars. After aging, the frown-shaped profile tended to turn into a smile-shaped profile, with the centre emitters providing less power. The frown-shaped power profile of the unaged bars is a result of the higher temperature of the centre emitters compared to those at the edges of the bar [1]. Nevertheless, both the power variation across these bars and the subsequent power loss during aging was quite small in these devices. Furthermore, the shift in the PL transition energy of the substrate was very small (<0.3 nm), indicating that the packaging induced strain is very homogenous across the bar. Furthermore, the strain induced shift in the substrate PL did not change appreciably during aging. These observations are consistent with a good soldering process and the excellent reliability achieved with these bars.

Study 2: 975 nm tapered laser bars (3-5 Lab)

A general correlation can be observed between the temperature and power distributions of undegraded bars. Once again, the power distributions of the bars typically have frown-shaped profiles, so that higher emission power was observed for the emitters at the middle of the bar [1]. At the same time, the typical temperature profile of the bars was also frown-shaped [2]. At first glance, this

correlation between the temperature and power profiles seems surprising. For example, it is well established that *the threshold current of a laser increases and its external quantum efficiency decreases as the temperature increases*. Nevertheless, this correlation between the temperature and power profiles is correct and can be understood as follows: The emitters at the center of the bar are hottest because they are being heated by neighbouring emitters. The bandgap energy (E_g) decreases with temperature. This means that the turn-on voltage of the emitter drops as E_g decreases, so that hotter emitters turn on earlier (i.e. at a lower voltage).

The peak emission wavelength of the GaAs substrate, measured by micro-PL measurements, has a smile-shaped profile. Thus, packaging induced strain increases the bandgap of the substrate near the middle of the bar. A correlation between power and packaging induced strain is expected using the arguments made for the correlation between the emitter temperature and power. Unfortunately, the apparent correlation has the wrong dependence on temperature – the power should decrease at the centre of the bar. This is because the strain-induced changes in the bandgap energies of the QW and of the confinement layer are only $\sim 0.7\text{--}1$ meV. Thus, the strain-induced bandgap energy change is dominated by the larger temperature-induced changes – which have the same shape, but change in the opposite direction.

All of the bars considered (16022–16025) show a significant aging induced change in the profile of the peak PL emission wavelength from the substrate. These strain profile changes are unusually large compared to other previously observed bars, so it is believed that this was caused by numerous voids in the solder.

Emitters with poor performance in unaged bars were often found to correlate with damage observed by optical microscopy and PLM/ELM at the facet. Emitters which degraded during aging (noticeable drop in output power) often showed either a marked increase in near-infrared electroluminescence from defects or a marked increase in temperature. This suggests that there may be two different manifestations (or even causes) of defect degradation – one due to radiative deep level defects and one due to nonradiative recombination.

Finally, in this study, bar 16024 and especially bar 16023 deserve special attention. Both bars show a smile-shaped profile in the PL emission wavelength of the substrate, which indicates that the profile of the packaging induced strain is typical for the soldering process used. In these bars, the profiles of the bandgap energies of the InGaAs QW and InGaAsP confinement region do not correlate with the substrate PL shift. The only reasonable explanation for this behaviour is a compositional variation in the epitaxial material of these bars. The observed increase in the bandgap energy would only require an increase of ~ 0.004 in the phosphorus mole fraction or a decrease of ~ 0.002 in the indium mole fraction across the 6.4 mm wide bar. Finally, the point defect density also appears to increase linearly across these bars, as seen from their near-infrared electroluminescence profiles. This is also consistent with the linear change in composition and pseudomorphic strain.

Development of the Bar Emulation Tool, *Barlase*

Secondly, the software control interface developed in LabVIEW to control *Speclase* led to the development of *Barlase*. *Speclase* was first used to emulate single emitter scenarios. Simulations were performed on single emitters to better understand the effects of temperature, defects and packaging-induced strain on the constant voltage operation of the emitter. The early results presented showed that even simulations of single emitters provided a great deal of insight into how these emitters will operate in the context of a laser bar. Of the three factors investigated, temperature was found to be the most important effect, but high defect levels and strain also played a significant role. The effects on laser operation of lower levels of defects and packaging-induced strain are smaller, but these are nonetheless important when combined with all of the other factors that affect laser degradation. Nevertheless, the actual impact on the performance of the emitters in a bar is more complex, due to current competition and thermal cross talk.

Validation of *Barlase*

Multiple-emitter simulations were also performed on hypothetical laser bars, providing better insight into the role of defects, self-heating and packaging-induced strain on the performance of a laser bar. Three initial multiple-emitter scenarios were considered to test the capabilities of *Barlase* and the control interface. Of the three cases investigated, non-uniform heatsink temperature and strain profiles (frown shaped) caused the most significant changes in the bar and emitter performance. However, these were initial conditions for the devices at the start of the aging process. Subsequently, when all of the relevant effects are combined and allowed to interact, over time, high levels of defects then play a

significant role in degradation. As the propagation and growth of defects can be increased by temperature, the rates of defect generation and propagation within emitters are inextricably linked to the emitter temperatures. Hotter emitters were found to draw more current and hence produce more power. Conversely, emitters with greater packaging-induced strain drew less current and produced less power. Finally, it was shown that the experimentally measurable “apparent” threshold current and “apparent” slope efficiency of the emitters change in the opposite direction to their *actual* threshold current and slope efficiency. Many of these counter-intuitive observations can be understood by considering the change in bandgap energy, which changes the turn-on voltage of the emitters and significantly affects the current competition between them.

The test of *Barlase* continued using a modified and improved emulation tool which accurately represented local degradation processes (e.g. trap generation due to local heating). Investigations went a step further by aging some theoretical laser bars using trap generations due to local heating which gave a better picture of what happens during aging.

Degradation Emulation of a Real Laser Bar

Finally, *Barlase* was used to emulate the degradation of a real bar.

Emulation of bar degradation (975 nm tapered laser bars (3-5 Lab))

These are bars whose performance and degradation had been characterised in detail using by-emitter degradation analysis [3]. Although the simulated output power profile did not correspond well with the experimental power profile, but there was good agreement for the combined output power of the bar. Better correlation was observed between the experimental and the simulated temperature

profiles. This was expected, since the experimental temperature was set as the input for the heatsink temperature profile. The agreement therefore must not be over-emphasised. The bar emulation model was enhanced by including a global thermal solver to model the thermal crosstalk between the emitters. Emulations using this model showed a clearly defined frown shaped profile in the output current and power profiles, but the change was much smaller than expected. As the emulation of laser bar degradation has not been attempted before, this work is still at a very early stage. Therefore, further work is needed to achieve better agreement in the output current/power profiles and to better the model.

This thesis has also demonstrated how the state-of-the-art simulation tool, Speclase can be used by *Barlase* to emulate a real bar. To the best of our knowledge, this is the first time a laser bar has been simulated and its degradation behaviour emulated.

Further Work

As already made known in this thesis, this is the first time to our knowledge that a high power laser diode has been emulated at the by-emitter level of a laser bar. What has been learnt at this stage of the use of this emulation tool at this stage is therefore good, but more needs to be done to improve upon it.

The global thermal solver brought some improvements in the results obtained at time zero (unaged bar) and the frown shaped power profile expected was realised to some extent but the variation was small. The following may be considered to improve upon the profile already obtained:

- altering the thermal resistivity of the substrate and
- lowering the thermal conductivity of the solder may help.

It must be noted that prior to aging the emulated bar, a good agreement must be reached between the experimental and emulated results for the unaged bar. The aging model used to perform the test simulations in chapter 6 to age the bars was a simple one and will need to be upgraded after agreement is achieved with the experimental results. In my opinion, a multi-disciplinary approach is needed involving not only electrical and material science engineers but chemical, mechanical, electro-mechanical engineers and mathematicians may all be involved in arriving at an aging model.

For instance, the current aging model used to emulate the degradation in chapter 6 underestimates the complexity of what actually happens in the laser bar during aging. Further work will therefore be needed to include other factors such as packaging-induced strain, defects, etc.

References

- [1] C. K. Amuzuvi, S. Bull, J. J. Lim, S. Sujecki, and E. C. Larkins, "Numerical emulation of the degradation of 975nm high power tapered laser bars," in *High Power Diode Lasers and Systems Conference, Coventry (UK) 2009. HPD 2009*, pp. 1-2, 2009.
- [2] C. K. Amuzuvi, S. Bull, J. W. Tomm, J. Nagle, E. C. Larkins, B. Sumpf, G. Erbert, N. Michel, and M. Krakowski, "The impact of temperature and packaging-induced strain on current competition and emitter power in laser bars," *Applied Physics Letter*, in preparation to be submitted, 2010.
- [3] S. Bull, J. W. Tomm, M. Oudart, J. Nagle, C. Scholz, K. Boucke, I. Harrison, and E. C. Larkins, "By-emitter degradation analysis of high-power laser bars," *Journal of Applied Physics*, vol. 98, p. 063101, 2005.

Appendix

List of Publications

The following papers have been published based on the results of the work described in this thesis:

- C. K. Amuzuvi, S. Bull, J. J. Lim, S. Sujecki, and E. C. Larkins, "Numerical emulation of the degradation of 975 nm high power tapered laser bars," in *High Power Diode Lasers and Systems Conference, Coventry (UK) 2009. HPD 2009*, 2009, pp. 1-2.
- S. Bull, C. K. Amuzuvi, T. J.W., X. R., L. J.J., S. S., and L. E.C., "By emitter degradation analysis in high power laser bars: Experiment and emulation," in *High Power Diode Lasers and Systems Conference, Coventry (UK) 2008. HPD 2008*, 2008.
- C.K. Amuzuvi, S. Bull, J.W. Tomm, J. Nagle, E.C. Larkins, B. Sumpf, G. Erbert, N. Michel, and M. Krakowski, "The impact of temperature and packaging-induced strain on current competition and emitter power in laser bars" *Applied Physics Letter*, *in preparation to be submitted October 2010*.

- J.W. Tomm, C.K. Amuzuvi, S. Bull, J. Nagle, and E.C. Larkins, “The effect of facet heating and the evolution with aging”, *in preparation to be submitted October 2010*.
- C. K. Amuzuvi, J. J. Lim, S. Bull, and E. C. Larkins, “Describing the state-of-the-art laser diode emulation tool” *in preparation to be submitted October 2010*.
- C. K. Amuzuvi, J. J. Lim, S. Bull, and E. C. Larkins, “Investigating a hypothetical single emitter/bar using a laser diode emulation tool” *in preparation to be submitted October 2010*.